Silicon Carbide – Nanostructured Ferritic Alloy Composites for Nuclear Applications

Kaustubh Krishna Bawane

Dissertation submitted to the faculty of the Virginia Polytechnic Institute and State University in partial fulfillment of the requirements for the degree of

Doctor of Philosophy
in
Materials Science and Engineering

Kathy Lu (Chair)
Xian-Ming Bai
William T. Reynolds
Scott W. Case

December 6, 2019
Blacksburg, Virginia

Keywords: Nanostructured ferritic alloys, silicon carbide, metal matrix composite, high temperature corrosion, in-situ irradiation damage

Silicon Carbide – Nanostructured Ferritic Alloy Composites for Nuclear Applications

Kaustubh Krishna Bawane

Abstract

Silicon carbide and nanostructured ferritic alloy (SiC-NFA) composites have the potential to maintain the outstanding high temperature corrosion and irradiation resistance and enhance the mechanical integrity for nuclear cladding. However, the formation of detrimental silicide phases due to reaction between SiC and NFA remains a major challenge. By introducing a carbon interfacial barrier on NFA (C@NFA), SiC-C@NFA composites are investigated to reduce the reaction between SiC and NFA. In a similar way, the effect of chromium carbide (Cr_3C_2) interfacial barrier on SiC (Cr_3C_2@SiC) is also presented for Cr_3C_2@SiC-NFA composites. Both the coatings were successful in suppressing silicide formation. However, despite the presence of coatings, SiC was fully consumed during spark plasma sintering process. TEM and EBSD investigations revealed that spark plasma sintered SiC-C@NFA and Cr_3C_2@SiC-NFA formed varying amounts of different carbides such as $(Fe,Cr)_7C_3$, (Ti,W)C and graphite phases in their microstructure. Detailed microstructural examinations after long term thermal treatment at 1000^{o}C on the microstructure of Cr_3C_2@SiC-NFA showed precipitation of new $(Fe,Cr)_7C_3$, (Ti,W)C carbides and also the growth of existing and new carbides. The results were successfully explained using ThermoCalc precipitation and coarsening simulations respectively.

The oxidation resistance of 5, 15 and 25 vol% SiC@NFA and Cr_3C_2@SiC-NFA composites at 500-1000^{o}C temperature under air+45%water vapor containing atmosphere is investigated. Oxidation temperature effects on surface morphologies, scale characteristics, and cross-sectional microstructures were investigated and analyzed using

XRD and SEM. SiC-C@NFA showed reduced weight gain but also showed considerable internal oxidation. Cr_3C_2@SiC-NFA composites showed a reduction in weight gain with the increasing volume fraction of Cr_3C_2@SiC (5, 15 and 25) without any indication of internal oxidation in the microstructure. 25 vol% SiC-C@NFA and 25 vol% Cr_3C_2@SiC-NFA showed over 90% and 97% increase in oxidation resistance (in terms of weight gain) as compared to NFA. The results were explained using the fundamental understanding of the oxidation process and ThermoCalc/DICTRA simulations.

Finally, the irradiation performance of SiC-C@NFA and Cr_3C_2@SiC-NFA composites was assessed in comparison with NFA using state-of-the-art TEM equipped with in-situ ion irradiation capability. Kr^{++} ions with 1 MeV energy was used for irradiation experiments. The effect of ion irradiation was recorded after particular dose levels (0-10 dpa) at 300^{o}C and 450^{o}C temperatures. NFA sample showed heavy dislocation damage at both 300^{o}C and 450^{o}C increasing gradually with dose levels (0-10 dpa). Cr_3C_2@SiC-NFA showed similar behavior as NFA at 300^{o}C. However, at 450^{o}C, Cr_3C_2@SiC-NFA showed remarkably low dislocation loop density and loop size as compared to NFA. At 300^{o}C, microstructures of NFA and Cr_3C_2@SiC-NFA show predominantly 1/2<111> type dislocation loops. At 450^{o}C, NFA showed predominantly <100> type loops, however, Cr_3C_2@SiC-NFA composite was still predominant in ½<111> loops. The possible reasons for this interesting behavior were discussed based on the large surface sink effects and enhanced interstitial-vacancy recombination at higher temperatures. The molecular dynamics simulations did not show considerable difference in formation energies of ½<111> and <100> loops for NFA and Cr_3C_2@SiC-NFA composites. The additional Si element in the SiC-NFA sample could have been an important factor in determining the dominant loop types. SiC-C@NFA composites showed heavy dislocation damage during irradiation at 300^{o}C. At 450^{o}C, SiC-C@NFA showed high dislocation damage in thicker regions. Thinner regions near the edge of TEM samples were largely free from dislocation loops. The precipitation and growth of new (Ti,W)C carbides were observed at 450^{o}C with increasing irradiation dose. $(Fe,Cr)_7C_3$ precipitates were largely free from any dislocation damage. Some Kr bubbles were observed inside $(Fe,Cr)_7C_3$ precipitates and at the interface between α-ferrite matrix and carbides ($(Fe,Cr)_7C_3$, (Ti,W)C). The results were discussed using the fundamental understanding of irradiation and ThermoCalc simulations.

Silicon Carbide – Nanostructured Ferritic Alloy Composites for Nuclear Applications

Kaustubh Krishna Bawane

General Audience Abstract

With the United Nations describing climate change as ‘the most systematic threat to humankind’, there is a serious need to control the world’s carbon emissions. The ever increasing global energy needs can be fulfilled by the development of clean energy technologies. Nuclear power is an attractive option as it can produce low cost electricity on a large scale with greenhouse gas emissions per kilowatt-hour equivalent to wind, hydropower and solar. The problem with nuclear power is its vulnerability to potentially disastrous accidents. Traditionally, fuel claddings, rods which encase nuclear fuel (e.g. UO_2), are made using zirconium based alloys. Under ‘loss of coolant accident (LOCA) scenarios’ zirconium reacts with high temperature steam to produce large amounts of hydrogen which can explode. The risks associated with accidents can be greatly reduced by the development of new accident tolerant materials. Nanostructured ferritic alloys (NFA) and silicon carbide (SiC) are long considered are leading candidates for replacing zirconium alloys for fuel cladding applications. In this dissertation, a novel composite of SiC and NFA was fabricated using spark plasma sintering (SPS) technology. Chromium carbide (Cr_3C_2) and carbon (C) coatings were employed on SiC and NFA powder particles respectively to act as reaction barrier between SiC and NFA. Microstructural evolution after spark plasma sintering was studied using advanced characterization tools such as scanning electron microscopy (SEM), electron backscattered diffraction (EBSD), transmission electron microscopy (TEM) and energy dispersive spectroscopy (EDS) techniques. The results revealed that the Cr_3C_2 and C coatings successfully suppressed the

formation of detrimental reaction products such as iron silicide. However, some reaction products such as $(Fe,Cr)_7C_3$ and (Ti,W)C carbides and graphite retained in the microstructure. This novel composite material was subjected to high temperature oxidation under a water vapor environment to study its performance under the simulated reactor environment. The degradation of the material due to high temperature irradiation was studied using state-of-the-art TEM equipped with in-situ ion irradiation capabilities. The results revealed excellent oxidation and irradiation resistance in SiC-NFA composites as compared to NFA. The results were discussed based on fundamental theories and thermodynamic simulations using ThermoCalc software. The findings of this dissertation imply a great potential for SiC-NFA based composites for future reactor material designs.

Dedication

To my mom and dad, Shalini and Krishna Bawane

To my sister, Kiran Bawane

Acknowledgment

First and foremost, I would like to express my sincere gratitude to my advisor Prof. Kathy Lu for her patience, support, and guidance throughout this project. It is because of her valuable insights, suggestions that I could complete my dissertation. Under her guidance, I learned how to define a research problem, finding a solution and write an outline for the work. Her hypothesis-driven research methods have been extremely useful for me and had a great impact on the way I approach a research problem. I admire her diligence at work, analytical thinking and passion for research which has been a constant source of motivation for me throughout my Ph.D. work.

I would like to thank my committee member and research collaborator Prof. Xian-Ming Bai for his helpful discussions on my irradiation work. He has also performed molecular dynamics simulations to explain some unique phenomena observed in my work. I am grateful to my committee members, Prof. William T. Reynolds and Prof. Scott W. Case for their constant support and valuable insights and suggestions on my work. I would like to express my deep sense of indebtedness to Prof. Reynolds for his help in solving some administrative obstacles related to my research internship at Oak Ridge National Laboratory (ORNL).

I would like to express my sincere appreciation for Dr. Meimei Li, Dr. Wei-Ying Chen and Dr. Jing Hu from Argonne National Laboratory for helping me with data collection, analysis on their state-of-the-art in-situ ion irradiation facility (IVEM-Tandem). I am thankful to both of you for your valuable comments and discussion on my analysis of TEM results collected at your facility. I would also like to thank Mr. Peter Baldo and Mr. Edward Ryan for providing support during the in-situ ion irradiation experiment at Argonne National Laboratory.

I am thankful to Dr. Christopher Winkler, Mr. Stephen McCartney and Ms. Ya-Peng Yu from Nanoscale Characterization and Fabrication Laboratory (NCFL) at Virginia Tech for training me on transmission electron microscopy (TEM), TEM sample preparation techniques, scanning electron microscopy and electron backscattered

diffraction (EBSD) techniques. I am grateful to Dr. Abdullah Alomari from Prof. K. L. Murty's lab from North Carolina State University (NCSU) for their help with the twin-jet electropolishing apparatus for TEM sample preparation. I wish to thank Mr. Hesham Elmkharram for training me on X-ray diffraction (XRD), differential scanning calorimetry (DSC) techniques and help with the installation of new high-temperature tube furnace in the lab.

My special thanks to Dr. Thak Sang Byun (currently at Pacific Northwest National Laboratory) and Dr. David Hoelzer from Oak Ridge National Laboratory for providing high energy ball milled nanostructured ferritic alloy (NFA) powder.

The financial support from the Office of Nuclear Energy of the Department of Energy (DOE) under grant number DE-NE-0008264 is greatly appreciated. In-situ ion irradiation study was supported by the Rapid Turnaround Experiment (RTE) award from Nuclear Science User Facilities (NSUF).

My heartfelt gratitude goes to Dr. Lauren Garrison, Weinberg fellow and research staff at ORNL for giving me a wonderful opportunity to SHINE project as an internship student. I would like to thank Dr. John Echols for his constant support and encouragement during my work at ORNL. I would also like to thank Dr. Chad Parish, Dr. Boopathy Kombaiah, Dr. Wei-Cheng Zhong for training me on a focused ion beam (FIB) technique for TEM sample preparation and nanoindentation instrument. I am grateful to Dr. Maxim Gussev and Dr. Sumit Bahl for training me on SEM-EBSD instruments and EBSD data analysis.

I would like to extend my unlimited thanks to all my former and present colleagues Dr. Fengyu Shen, Dr. Kaijie Ning, Dr. Michelle Gervasio, Dr. Ruixin Ma, Dr. Lixia Wang, Ni Yang, Alex Jannisek, Hongfei Ju, Donald Erb, Rezawana Islam, Lingchen Kong, Advaith Rau, Dr. Yi Je Cho, and Dr. Sanjay Kumar for their constant support and making my experience enjoyable.

I would like to express my gratitude for all my professors and staff members in the MSE department and especially Kim Grandstaff, Amy Hill, Cindy Perdue, Prof. Thomas Staley and Prof. Carlos Suchicital for their generous help.

My gratitude and appreciation are also extended to all my previous advisors: Prof. Dipankar Banerjee from Indian Institute of Science, Bangalore, Dr. Dheepa Srinivasan from General Electric India Technology Center, Bangalore (now at Pratt and Whitney, Bangalore), Prof. Narendra B. Dhokey from College of Engineering, Pune and Prof. Kaustubh N. Kulkarni from Indian Institute of Technology, Kanpur. All these people have played an instrumental role in shaping my career and significantly influenced my overall personality.

I would like to extend my sincere thanks to all my friends, my parents and my sister for their patience, love and constant support.

Contents

List of Figures

List of Tables

Attribution

A number of colleagues aided with different steps of this work related to sample preparations, processing, characterization, and writing/editing the manuscripts. A brief description of their contribution is as follows:

Chapter 2: Mr. Zhihao Hu, M.S. student (now, the Ph.D. candidate in the Department of Statistics, Virginia Tech) conducted experiments to develop carbon coating on NFA powder particles. Dr. Kaijie Ning, postdoc (now, a research scientist at Alfred University, NY, USA) planned sintering experiments and also prepared SiC and C@NFA mixed powders with different volume fractions. I analyzed SPS sintered samples using SEM, XRD and Vickers hardness tester, Archimedes density method. Dr. Kaijie Ning served as lead author for the paper. I contributed partially to the writing and the editing of the manuscript. Prof. Kathy Lu (Professor, Virginia Tech) served the corresponding author of the paper and was involved in the editing of the manuscript.

Chapter 3: Mr. Hongfei Ju, M.S. student (now, M.S. student at Arizona State University) conducted experiments to develop chromium carbide coating on SiC powder particles. Dr. Kaijie Ning planned sintering experiments and also prepared SiC and C@NFA mixed powders with different volume fractions. I analyzed SPS sintered samples using SEM, XRD and Vickers hardness tester, Archimedes density method. Dr. Kaijie Ning served as lead author for the paper. I contributed partially to the writing and the editing of the manuscript. Prof. Kathy Lu served the corresponding author of the paper and was involved in the editing of the manuscript.

Chapter 4: I performed all the experiments and characterization in this manuscript. I also wrote the manuscript and served as lead author. Prof. Kathy Lu served as the corresponding author and was involved in the editing of the manuscript.

Chapters 5 and 6: I performed all the oxidation experiments and characterization. I also wrote two manuscripts and served as lead author in both. Dr. Kaijie Ning and Prof. Kathy

Lu served as the corresponding author and were involved in the editing of both manuscripts.

Chapters 7 and 8: I performed the in-situ TEM characterization during irradiation. Dr. Wei-Ying Chen (Staff scientist, Argonne National Laboratory, IL, USA) and Dr. Jing Hu (Postdoc, Argonne National Laboratory, IL, USA) trained me on TEM and also assisted with problems during the experiment. Mr. Edward Ryan and Mr. Peter Baldo assisted with the ion accelerator instrument needed for irradiation. I wrote two manuscripts and served as lead author in both. Prof. Xian-Ming Bai (Assistant Professor, Virginia Tech) performed molecular dynamics simulations to explain experimental results. Prof. Bai also assisted in editing both manuscripts and also wrote section 8.5.4 related to simulations he performed. Dr. Meimei Li (Staff scientist, Argonne National Laboratory, IL, USA) assisted with editing both manuscripts. Prof. Kathy Lu served as the corresponding author and was involved in the editing of both manuscripts.

Chapter 1

Introduction

Nuclear reactors are very expensive to set-up, however, can provide electricity at very low operational costs as well as with significantly lower CO_2 emissions [1, 2]. These factors, especially the later one, appeals a lot to the governments seeking to reduce greenhouse gas emission owing to worldwide climate change concerns and also diversifying energy assets in wake of depleting fossil fuel resources [3, 4]. CO_2 emission (kg CO_2-eq./kWh) for nuclear power is on a par with hydro and wind energy sources, and almost negligible as compared to fossil fuel sources such as coal, oil and natural gas [5]. A major impediment in the growth of the nuclear industry is its high perceived risk, as the high energy density of nuclear reactors (100 times greater than typical fossil fuel based power) also makes it disastrous in the events of accidents [3, 4, 6]. Due to the controversial nature of nuclear power, countries like Germany, Switzerland are leading the efforts to completely phase out nuclear energy from their grids especially after the 2011 Fukushima catastrophe [2, 7, 8]. Despite this, nuclear power remains popular in several energy hungry nations (especially China and India) which are looking to decrease their fossil fuel import bills and move towards cleaner energy sources [2, 4, 8]. In the wake of the considerable number of power plants are currently being constructed or planned or undergoing upgradation in recent years, it is important to provide higher safety features and intelligent accident tolerant designs to prevent another Fukushima like tragedy [3-5, 8, 9].

1.1. Background and a brief history

Nuclear fission reactors derive its energy from controlled fission reaction triggered by neutron bombarding nuclei of large fissile atoms such as U^{235} and Pu^{239} [2, 10, 11]. In this process, the U^{235} or Pu^{239} splits into lighter atomic nuclei, γ-rays, α, β particles and several other neutrons which makes the reaction self-sustaining and generate a large amount of energy [2]. This energy can be used for electricity generation or propelling naval ships and submarines by using heat

exchangers and steam turbines [10-12]. Irrespective of design, all nuclear reactors contain fuel elements, moderator, control rods, coolants and heat exchanger/turbine assembly.

Neutrons generated during fission reaction plays a very important role to sustain it. These neutrons are known as fast neutrons because of their high kinetic energy (~2 MeV) and speed (~13500 km/s) [2, 13]. However, in order to keep the reactor running, these neutrons must be slowed down (also known as thermal neutrons with kinetic energy~0.025 eV and velocity~2.2 km/s), because the probability of interaction with nuclei (neutron scattering cross section) increases with decreasing neutron energy [2, 13, 14]. Moderator materials composed of lighter elements is used in the reactor to slow down these neutrons by repeated elastic scattering events. Therefore, moderator materials should have high neutron scattering cross section. It is also desirable for moderator materials to have low neutron absorption cross section in order to achieve enough number of neutrons for self-sustaining fission reaction [2, 14, 15]. Currently, light water, heavy water, graphite, beryllium and lithium fluoride are used as moderators in nuclear reactors [15].

In addition to achieving self-sustaining nuclear fission, it is also important to control the rate of chain reaction within desirable limits. Control rods are used in the reactor to achieve the optimized quantity of neutrons to ensure the safe and efficient operation of the reactor. Therefore, ideal control rod materials must possess a high neutron absorption cross section and should not transmute further into fissile materials [2, 16]. Materials such as cadmium, cobalt, boron, indium, europium, samarium or dysprosium are suitable for control rod applications [17]. Ag-In-Cd alloys, boron carbide, hafnium diboride, and dysprosium titanate are commonly used as control rods in commercial nuclear reactors [16, 18]. Besides controlling chain reaction, control rods are also used in normal and emergency reactor shutdown systems (SCRAM) [19].

Coolants are fluid materials that are circulated through the reactor core to transfer energy to heat exchangers. Light water, heavy water, molten salts, molten lead, helium, and CO_2 are commonly used coolants for nuclear reactors [2, 10, 15]. Several reactor designs have been developed over the years to efficiently harness this energy. The evolution of nuclear reactors can be divided into 4 segments, Generation I (prototype nuclear reactors, 1950-1970), Generation II (commercial light water reactors, pressurized heavy water reactors, gas cooled reactors, 1970-1995), Generation III/III+ (advanced light water reactors, 1995-2030) and Generation IV (future

advanced reactor concepts, 2030+) [20, 21]. Generation IV designs such as molten salt reactor (MSR), supercritical water reactor (SCWR), very high temperature reactor (VHTR) and gas/lead/sodium cooled fast reactors are currently under developmental stages [20, 22, 23]. Currently, majority of the operating reactors in the world are light water reactors (369 out of 450) belonging to Gen II and Gen III technologies [24].

1.1.1. Light water reactors (LWR)

Light water reactors (LWR) are nuclear reactors which use light water (H_2O) as coolant/moderator as opposed to heavy water (D_2O, e.g., pressurized heavy water reactor, PHWR). Light water exhibits excellent neutron scattering cross section, but higher neutron absorption cross section. Therefore, to ensure sustained chain reaction, enriched UO_2 fuel is needed in LWRs, in contrast with natural UO_2 fuel for PHWRs [2, 14]. There are two commercially available designs for LWRs, the first pressurized water reactor (PWR) and boiling water reactor (BWR). PWR constitutes the majority of LWRs around the world.

In pressurized water reactor (PWR), water in the primary coolant loop is heated using fuel elements in the core to around 600 K. The pressure in the loop is kept at 15 MPa which is high enough to prevent it from boiling at this temperature. The heat from the primary coolant loop is used to boil water in the heat exchanger to form steam at 560 K temperature and 7 MPa pressure which is similar to conventional fossil fuel generators. Control rods in PWR are made of B_4C or Ag-In-Cd clad stainless steel [11, 16].

In boiling water reactor (BWR) reactor, water in the core is allowed to boil and form steam at 560 K temperature and 7 MPa pressure which can be directly used for running steam turbines. The exhaust steam from turbines is allowed to condense into the water which is recirculated back to the reactor [11, 16]. Since water near the reactor core is contaminated with radionuclide traces, radiation shielding for turbines is important in BWR [10].

1.1.2. Importance of nuclear fuel cladding

Nuclear fission reaction generates hazardous α, β particles, radionuclides, and radioactive waste products. Nuclear fuel claddings are used in reactor physically and chemically isolate fuel from surrounding coolant/moderator. Fuel cladding tube along with fuel pellets is also known as fuel rod or fuel element [2, 25, 26]. The fuel assembly is composed of numerous fuel rods (~49 to 300). Fuel rods consist of UO_2 fuel pellets (diameter~1 cm, height~1.5 cm) enclosed in the cladding tube (height~4-5 m). Typical reactor core (~1100 MWe, light water reactor) contains over 193 fuel assemblies with ~50000 fuel rods and ~18 million fuel pellets [27].

Since the unhindered movement of thermal neutrons through the core is important to sustain the nuclear reaction, fuel cladding must be transparent to neutrons (i.e. low neutron absorption cross section). In addition to this, fuel cladding should possess high resistance to irradiation induced damage, corrosion resistance under aggressive coolant environment at high operating temperatures (~300^{o}C for LWR), good chemical compatibility with fuel and coolant and excellent mechanical and structural integrity at reactor temperatures [9, 14, 28]. All these design constraints significantly limit the set of suitable materials for fuel cladding. Materials such as stainless steels [10, 29-32], zirconium alloys[11, 12, 26] , beryllium alloys [33], magnesium alloys [34] and silicon carbide [24, 35] are commonly used for fuel claddings applications.

Currently, zirconium alloys are used for cladding applications in light water reactors. Zirconium possesses significantly low neutron absorption cross section as compared to stainless steel [36, 37]. The high cost of zirconium and presence of neutron absorbing hafnium impurity in the early days was a major hurdle for its large scale use [11, 37]. With the advent of Kroll's process and other new purification and processing techniques, engineers were able to build thicker claddings without significant loss of neutrons. Nuclear reactors with zirconium claddings could operate at around 1% lower fuel enrichment which led to significant cost reductions [11]. Zirconium also shows very good high temperature strength, corrosion and irradiation resistance at operating temperature. Various zirconium alloys with alloying elements such as Sn, Fe, Nb, etc. have been developed over the years to improve its high temperature strength, creep resistance and corrosion properties [11, 14, 37]. The use of zirconium claddings in nuclear reactors has significantly improved the rate of cladding failures from 1/100 in 1960 to $1/10^5$ in 2005 [38]. Due

to all these remarkable properties, zirconium has enjoyed a monopoly in the light water reactors market to this date. However, in recent years, due to more aggressive operating conditions, power uptakes, longer cycle lengths and accident conditions there have been increased corrosion related failures in zirconium claddings [15].

1.2. Motivation and objectives

1.2.1. Limitations of Zirconium alloy fuel claddings

Despite being a very reliable choice for LWR claddings under normal operating conditions, the major problems with zirconium show up during accident scenarios. Zirconium tends to react exothermically with steam at high temperatures (~1000°C). The heat generated during reaction also makes it autocatalytic which results in a dangerous rise in the amount of hydrogen gas in the reactor (see Eq. 1.1) [11, 39].

$$\mathrm{Zr(s) + 2H_2O(g) = ZrO_2(s) + 2H_2(g) + 586\,kJ/mol\ of\ Zr} \qquad (1.1)$$

During accident conditions such as 'loss of coolant accident (LOCA)' or 'station blackout event (SBO)', primary coolant supply is often obstructed. Even with emergency shutdown (SCRAM) of nuclear reactors using control rods, the core of the reactor keeps on producing heat due to decay of short live isotopes formed after fission [39]. Therefore, it becomes difficult to contain the rise of temperature in reactors without coolants. The heat from core vaporizes all the water in the reactor, which then reacts with zirconium cladding to form the ZrO_2 layer according to Eq. 1.1. The ZrO_2 layer does slow down the reaction to some extent but eventually fails because of its brittle nature. Damaged ZrO_2 layer again exposes the metal underneath leading to continuous reaction with steam. Therefore, with the heat coming from fuel as well as exothermic oxidation eventually melts the cladding [39, 40].

Zirconium reacts with water/steam during normal operating conditions (~300^{o}C) as well, however the amount of hydrogen and rate of reaction is much smaller than elevated temperatures [14]. At these temperatures, hydrogen produced is picked up by zirconium cladding to form brittle hydride phases. Zirconium hydride formation can lead to cladding failures via embrittlement. Zirconium hydride formed near the cladding surface often acts as crack initiation points. Therefore, hydride embrittlement is one of the major issues which determines the longevity of zirconium claddings [14, 15, 41].

1.2.2. Recent attempts to address the challenges

Recent efforts to solve the problems with zirconium alloy claddings can be grouped into two categories. First, modification of zirconium alloy claddings which includes alloying, coating, metal ceramic hybrid cladding systems [41-44]. Second, the substitution of zirconium alloys with other suitable materials. The leading candidates for cladding are advanced stainless steel, ODS alloys, SiC and its composites and MAX phases, etc [2, 32, 41, 45].

From the industry's point of view, modification of current zirconium alloys is considered a better choice as it doesn't significantly change zirconium-UO_2 fuel design. Also licensing requirements and regulatory hurdles will be much easier to deal with modified Zr alloys as compared to completely new material. Currently, thermal sprayed coatings of SiC and MAX phases like Ti_3SiC_2 and Ti_3AlC_2 on zirconium cladding are under development. Due to superior high temperature oxidation properties of these coatings, hydrogen formation in zirconium claddings during LOCA conditions can be suppressed. These coatings can also significantly reduce hydrogen pickup under normal operating conditions by forming a diffusion barrier, therefore, improving the longevity of claddings [41].

Recently, hybrid structures of SiC-ceramic matrix composites (CMCs) and zirconium cladding have been proposed and under development [46]. SiC based outer layer provides much better oxidation resistance as compared to zirconium alloy. Therefore, such material can deal with hydrogen pickup during normal operating conditions and hydrogen formation during LOCA conditions [46].

Nanostructured ferritic alloys (NFAs), a special type of oxide dispersion strengthened (ODS) ferritic steels, are considered as a promising nuclear cladding material for both nuclear fission and fusion reactor systems [47-51]. The combination of properties, such as resistance to high temperature corrosion, irradiation, void swelling, and creep as well as high temperature strength makes NFAs very attractive for nuclear applications [29, 32, 52, 53].

Silicon carbide (SiC) is also widely considered as another desirable cladding material for nuclear reactors. It exhibits high irradiation resistance, excellent high temperature strength, slow oxidation kinetics, and high chemical stability [28, 35, 54-56]. SiC and its composites are being intensively studied for their use in fusion reactors, LWR fuel claddings, and high temperature gas reactors.

1.2.3 Proposed solution and hypothesis

Silicon carbide possesses very attractive neutronic and high temperature properties to replace zirconium alloy claddings. However, the development of hermetic seals (or end caps) with acceptable high temperature strength, irradiation, and corrosion properties along with reliable joining techniques are some of the major challenges for SiC-based claddings [2, 41]. In addition to this, the inherent brittleness of SiC is problematic during mechanical interaction between fuel pellets and cladding [2].

The nanostructured ferritic alloy also shows impressive irradiation and creep properties at high temperatures. NFA derives its corrosion resistance from the protective Cr_2O_3 layer. Therefore, the amount of Cr affects its high temperature corrosion properties. Pint et. al. [55] stated that steels should have at least 20% Cr content in order to have a stable and protective chromia layer in high temperature steam environments. NFAs with around 9-12% Cr may still show acceptable corrosion resistance at normal LWR operating conditions (~300^{o}C), however rapid breakaway oxidation during LOCA (~1000^{o}C) can seriously damage the performance of cladding [57, 58].

In this work, composites of the nanostructured ferritic alloy (NFA) and silicon carbide is proposed as a potential cladding material. Considering the excellent properties of both NFA and SiC, such composite is expected to provide good high temperature mechanical performance, strong

oxidation and irradiation tolerance, and improved manufacturability. Fig 1.1 shows the proposed microstructural design of gradient SiC-NFA composites with SiC on the outer side and NFA on the inner side of the cladding tube. Outer SiC surface can provide much better oxidation properties as compared to NFA in both normal and accident conditions. While the inner layer of NFA can allow the use of conventional metal joining techniques for hermetic seals, thus improving its reliability. Unlike thermal sprayed coatings, the outer SiC surface is expected to be much denser and better attached to the rest of the cladding. This project aims at exploring benefits of the addition of SiC in the NFA matrix and also the development of single step powder based manufacturing of such gradient composites, therefore reducing additional processing costs.

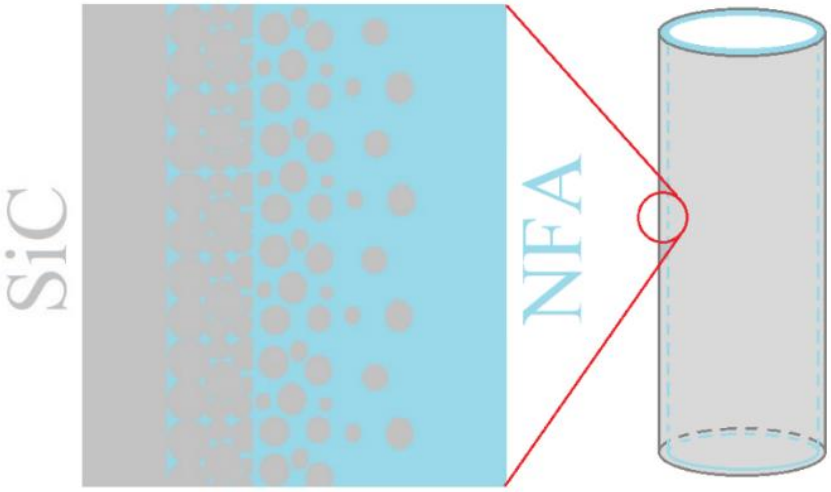

Fig. 1.1. Schematic of proposed microstructural design.

1.2.4. Objectives

In order to study the processing and microstructure behavior of this gradient composite, first separate composites with different volume fractions of SiC and NFA are studied (e.g. 5, 15, 25,….95 vol% SiC in NFA). This dissertation particularly focuses on spark plasma sintered NFA (0 vol% SiC) and 5, 15, 25 vol% SiC-NFA composites. This work will also focus on high temperature oxidation and irradiation properties of these composites under the simulated nuclear reactor environment. The objectives of this work are as follows:

1) There is a need to identify effective reaction barrier layers to control the reaction between SiC and NFA during sintering. Also, suitable processing methods for coating these reaction barrier materials on SiC or NFA powder particles needs to be developed. In this dissertation, C and Cr_3C_2 coatings on NFA and SiC powders are identified as possible reaction barrier materials. This dissertation will study the microstructural evolution of NFA and 5-25 vol% SiC-NFA composites with C and Cr_3C_2 reaction barrier layers. Long term thermal stability of these microstructures during heat treatment at elevated temperatures will also be studied. This dissertation also aims to develop thermodynamic, diffusion and precipitation simulation methods using ThermoCalc/DICTRA/PRISMA software respectively. These simulations are expected to predict phases and other microstructural aspects such as precipitation and coarsening of phases during sintering and subsequent heat treatments.
2) This dissertation will also address high temperature corrosion behavior of spark plasma sintered NFA and SiC-NFA composites in water vapor environments. The oxidation mechanism will be assessed using advanced microstructural characterization techniques as well as simulation methods based on ThermoCalc.
3) Finally, the irradiation behavior of NFA and SiC-NFA composites will be studied using state-of-the-art TEM equipped with in-situ ion irradiation capabilities. This effort will focus on the fundamental understanding of dislocation evolution in SiC-NFA in comparison with NFA and other existing materials from literature.

1.3. Literature review

1.3.1. Physical metallurgy of Nanostructured ferritic alloys (NFA)

The microstructure of nanostructured ferritic alloys (NFA) consists of highly dense and uniformly distributed oxide (e.g., yttria, titania, Y-Ti-O complex, etc.) nanoclusters (size ~2-6 nm, density~10^{23} m^{-3}) in ultra-fine grained (< 1 μm) ferritic steel matrix [59, 60]. These nanoclusters act as an impediment to dislocation climb and glide to improve both high temperature strength and creep resistance. They also contribute towards the improvement of irradiation properties by acting as a sink for irradiation induced defects. Nanoclusters provide an enormous surface area for nucleation of helium bubbles during neutron irradiation. Therefore, the formation of a large density of small helium bubbles at an oxide-matrix interface ensures significantly less void swelling as compared to the sample with large helium bubbles with small density [30, 60]. These nanoclusters have shown very high thermal stability even up to near melting temperatures (~1300^{o}C) [61]. Typically, NFA contains more than 12 wt% Cr to maintain ferritic grains till melting temperature. Recently NFAs with around 9 wt% Cr have been developed to intentionally introduce partial phase transformation (α→γ at grain boundaries allows enhanced diffusion) which significantly improves diffusion bonding between grains. As a result, 9 wt% Cr NFAs have shown enhanced fracture toughness as compared to >12 wt% Cr NFAs [59].

Traditional processing of NFAs involves mechanical alloying of ferritic steel and Y_2O_3 powders and consolidation using thermomechanical treatments (TMT) such as hot extrusion followed by rolling. The mechanical alloying process forces Y_2O_3 to dissolve in the ferritic steel matrix, which then nucleates as nanoclusters of Y_2O_3 or Y-Ti-O complex during the consolidation process. The thermomechanical treatments used for consolidation tends to produce highly anisotropic microstructures. Kasada et al. [62] showed highly anisotropic microstructures in ODS ferritic steels processed using hot extrusion process.

Spark plasma sintering (SPS) has recently emerged as an alternative technique to consolidate NFA powders to almost full density. SPS process uses electric current in combination

with high pressure to sinter the powders. EBSD image of 14 YWT processed using SPS shows a bimodal and isotropic microstructure as compared to hot extruded counterparts [63].

1.3.2. Silicon carbide in nuclear industry

Silicon carbide has existed in the nuclear industry for over 50 years. SiC is used for coating TRISO fuel (e.g. gas reactors) to retain fission products inside or to prevent fuel damage at high temperatures where steam might be present in the coolant. SiC based claddings are primarily considered for applications in very high temperature reactors (VHTR) and fast reactors (gas cooled, lead cooled) and fusion reactors. In LWRs, SiC based cladding can allow high fuel burnup, power uprates, longer cycle lengths and better performance during LOCA events as compared to zirconium alloy cladding [15, 64]. In order to improve mechanical properties (especially fracture toughness), SiC is often used in the form of SiC-fiber reinforced SiC ceramic matrix composites (SiC_f/SiC CMC) [65].

1.3.3. High temperature oxidation behavior in reactor environment

NFA relies on the protective Cr_2O_3 layer for its high temperature oxidation resistance. However, a water vapor environment is known to damage this Cr_2O_3 protective layer and promote the formation of non-protective Fe rich oxides [57, 58]. The harsh moisture-containing environments can also cause accelerated chromium loss due to the formation of volatile $CrO_2(OH)_2$ [66-68]. This process leads to a phenomenon called ‘breakaway oxidation’ where the chromia scale is replaced by a non-protective Fe-rich scale [58, 69]. The detrimental effect of water vapor on high temperature corrosion resistance of various steels is widely reported in the literature [54, 57, 58, 67, 69-76]. Ehlers et. al. [69] found that a higher H_2O/O_2 ratio in the atmosphere promotes the formation of a non-protective Fe-rich layer on 9 wt% Cr P91 ferritic steel at high temperatures. The double layer scale formation with an internal Cr-rich and external Fe-rich layer is observed in previous studies on water vapor/steam oxidation of Fe-Cr alloys [57, 58, 69, 77, 78]. Ishitsuka et. al. [79] studied steam oxidation resistance of Si-containing Fe-9Cr alloy and reported that the low

oxidation rates in the high Si-containing alloy are attributed to the formation of amorphous SiO_2 at the scale and metal interface. Fujikawa et. al. [80] reported that silicon enrichment in the internal spinel phase layer greatly reduces the ionization of Fe and its diffusion in the oxide layer during high temperature steam oxidation.

Oxidation kinetics of SiC is almost 2 to 3 orders of magnitude slower than zirconium based alloys even up to very high temperatures (such as LOCA~1000^{o}C) [28]. In the absence of water vapor SiC shows two types of oxidation behavior: passive and active. Passive oxidation occurs when oxygen activity is sufficient to form a protective SiO_2 layer. While active oxidation leads to the formation of volatile SiO (thereby, mass loss) as a result of the insufficient activity of oxygen [35]. Pourbaix diagram in Fig. 1.2 shows SiC oxidation reactions in the presence of water vapor at LWR conditions (300^{o}C and 15 MPa). It can be observed that SiO_2 layer forms during all the reactions. However, this SiO_2 reacts again with water vapor to form volatile $Si(OH)_4$, thus leading to mass loss (see Eq. 1.2) [81].

$$SiO_2\ (s) + 2H_2O\ (g) \rightarrow Si(OH)_4\ (g) \qquad (1.2)$$

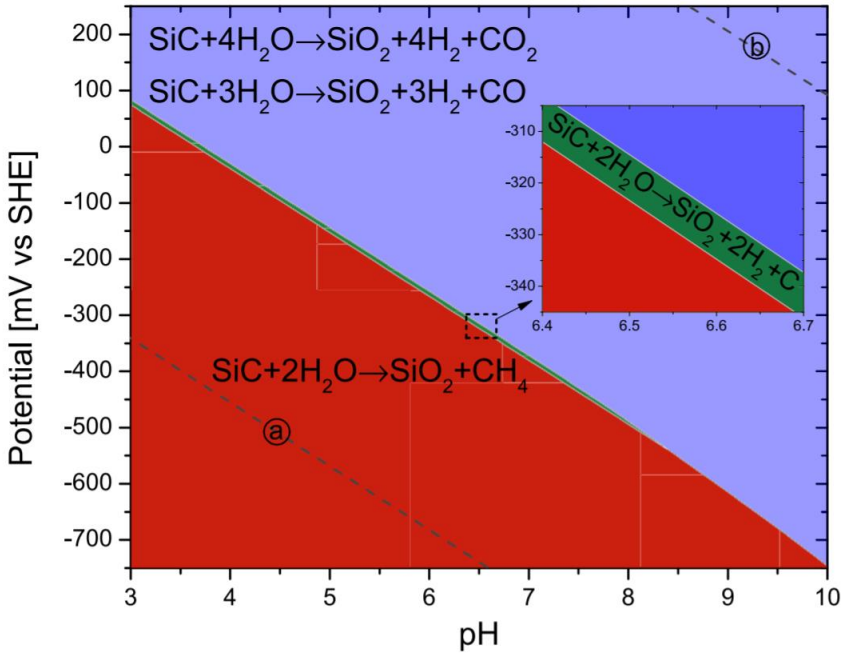

Fig. 1.2. Pourbaix diagram of SiC in water at LWR conditions, i.e., 300^{o}C and 15 MPa [81] (Reprinted from Journal of Nuclear Materials, 465, Terrani K. A., Yang Y., Kim Y. J., Rebak R., Meyer H. M., Gerczak T. J., Hydrothermal corrosion of SiC in LWR coolant environments in the absence of irradiation, 488-498, Copyright (2015), with permission from Elsevier).

1.3.4. Irradiation effects on fuel cladding materials

Cladding materials are subjected to continuous neutron irradiation during reactor operation. Neutron interaction with cladding material can adversely affect both mechanical and corrosion properties. The types of possible neutron interactions include scattering, knock-on damage, and ionization. The knock on damage occurs when neutrons bombard and transfer their energy to the nucleus of the atom (from cladding). Therefore, the atom gets displaced from its original position in lattice when the neutron of sufficient energy hits it. This displaced atom is called the primary knock on atom (PKA). As PKA travels in lattice it displaces several other atoms (or secondary knock-on atom) in its path. These subsequent collisions are collectively also as 'cascade event'. Therefore, cascade events lead to formation of several vacancies and interstitials also known as 'Frenkel pair'. Most of these vacancies and interstitials annihilate each other as a

result of thermal energy generated due to atomic friction during cascade events. However, some Frenkel pair stays back in the material as irradiation induced defects [82, 83].

Irradiation induced damage can be expressed in terms of 'displacement per atom (dpa)'. The 'dpa' is commonly used as a measure of irradiation dose. The rate of damage or dpa/s is given as follows [83]:

$$\frac{\text{dpa}}{\text{s}} = \frac{\text{No. of displacements}}{\text{Number density of target atoms} \times \text{cm}^3 \times \text{s}} = \int_{E_{min}}^{E_{max}} \sigma_d(E_n).\phi(E_n).dE_n \qquad (1.3)$$

Where, E_n = energy of neutron required to displace atom,

E_{min} and E_{max} = minimum and maximum energy of neutrons,

$\sigma_d(E_n)$ = displacement cross section (see equation 2),

$\phi(E_n)$ = neutron flux $= \frac{\text{No. of neutrons with energy } E_n}{\text{cm}^2 \times \text{s}}$.

$$\sigma_d(E_n) = \int_{T_{min}}^{T_{max}} \sigma(E_n).\upsilon(T).dT \qquad (1.4)$$

where, T_{min} and T_{max} = minimum and maximum energies transferred from neutrons to target atom

$\sigma(E_n)$ = collision cross section of neutron with energy E_n

$\upsilon(T)$ = number of displacements per primary knock − on atom

The quantity and type of irradiation induced defects depend on a variety of factors such as neutron energy, irradiation time, temperature and the material itself. The interstitial mobility is comparatively higher than that of vacancies. Therefore, the defects which cannot annihilate often forms separate vacancy and interstitial clusters. Coarsening of these defect clusters as a result of further cascade events eventually leads to the formation of dislocation loops. These dislocation loops can act as an impediment to the movement of other dislocations, which often results in the degradation of mechanical properties (hardening, embrittlement, etc.) [83-85].

Irradiation temperature can affect the defect behavior in the material. Due to the higher availability of thermal energy, most Frenkel pairs can recombine leading to the lower density of total defects. Higher temperature improves mobility of vacancies which can cluster together to form voids and bubbles. The formation of voids adversely affects the mechanical properties of the material [82, 86].

Neutron and ion irradiation studies on iron alloys have shown the formation of two kinds of dislocations with Burgers vector b=a/2<111> and b=a<100> [84]. Relative quantities and sizes of these dislocations strongly depend on alloying and irradiation temperature. During neutron irradiation of pure iron, b=a/2<111> is mostly observed at room temperature [87, 88], however at temperatures above 300^{o}C, b=a<100> becomes predominant [89, 90]. Recent ion irradiation studies have shown that b=a/2<111> type dislocations are highly mobile while b=a<100> dislocations are almost immobile. Fe-Cr alloys show a strong affinity to the formation of Cr-interstitial clusters mainly along with b=a/2<111> type dislocation. This leads to a decrease in the mobility of b=a/2<111>. Therefore, Cr addition can influence relative fraction of b=a/2<111> and b=a<100>. However, the exact correlation between Cr content and proportions of these dislocations has not been fully established yet [84].

SiC shows varying responses to neutron irradiation mainly depending on temperature and dose levels. SiC shows an exponential increase in void swelling with irradiation below 150^{o}C. Below this critical temperature, strain accumulation due to defects causes the amorphization of SiC. However, above 150^{o}C swelling only reaches a saturation level with increasing irradiation dose. This saturation level shows a decreasing trend with the temperature, due to the higher availability of thermal energy for defect recombination. Neutron and ion irradiation between 150^{o}C and 1000^{o}C temperature have shown the formation of point defects and Frank loops. Above

1200ºC and dose levels >10 dpa, vacancy diffusion becomes predominant, leading to the significant increase in void swelling. Voids adversely affect mechanical properties and decrease thermal conductivity. In cladding materials, high thermal conductivity is important to ensure efficient transfer heat from fuel to coolant [82, 86, 91].

1.3.5. Review on SiC containing metal matrix composites

Metal matrix composites (MMCs) can show significant improvement in modulus, thermal stability and mechanical behavior as compared to parent metals. Most common MMCs include reinforcements such as carbides (SiC, B_4C, TiC), oxides (Al_2O_3, SiO_2), nitrides (Si_3N_4, AlN), carbon (nanotubes, graphene, fibers) in aluminum, magnesium, copper and steel matrix. In order to achieve stable dispersion of reinforcements, solubility, diffusivity and interfacial energy between reinforcements and matrix must be minimum [92]. However, it is not always possible to find a compatible matrix and reinforcements for particular applications due to so many design constraints. In such situations, reinforcements can be coated with compatible material. The coating can act as an interfacial barrier between matrix and reinforcements to achieve favorable bonding properties. Steel and SiC react at elevated temperature to form silicides, carbides and carbon [93-95]. The formation of brittle silicide phases degrades the mechanical performance of SiC/steel composites. The reaction can also completely consume SiC reinforcement, leaving only undesirable reaction products in the microstructure. Mani et. al.[96] has successfully demonstrated the use of electroless Co coating on SiC as an interfacial barrier for SiC and Fe-Co alloys.

Chapter 2

Spark Plasma Sintering of SiC and NFA using Carbon as Interfacial Barrier Layer

2.1. Abstract

Silicon carbide and nanostructured ferritic alloy (SiC-NFA) composites have the potential to maintain the outstanding irradiation resistance and enhance the mechanical integrity of nuclear cladding. By introducing a carbon reaction barrier on NFA (C@NFA), SiC-C@NFA composites are investigated in order to reduce the reaction between SiC and NFA in this work. The densities of the spark plasma sintered (SPS) SiC-C@NFA composites show an increasing trend with the SiC content to almost 100% dense. Although the SiC phase is absent, the Vickers hardness of the composites reaches 436-638 kgf/mm^2. The reaction leads to two types of regions in the composites, the NFA matrix, and the micro-sized carbon enrich region, both of which contain extra Si element. The SiC-C@NFA composites show much improved microstructures and phases compared to the SiC-NFA composite without any coating. The SPS sintered SiC-C@NFA composites offer a new promising system for nuclear cladding.

2.2. Introduction

The major processing challenge during the fabrication of NFA-SiC composites is the reactions between Fe (the base element of NFA) and SiC, confirmed by experiment [97-99] and simulation [100]. The reactions start with the decomposition of SiC, then the formation of silicides (e.g. Fe_3Si, FeSi and $FeSi_2$) and carbides (e.g. Fe_3C). For example, Pelleg produced Fe-SiC composites using pressureless sintering and hot isostatic pressing (HIP) in the temperatures range of 900^{o}C to 1100^{o}C, finding a large amount of pearlite and iron silicides [98]. Shen et al. confirmed that several products, Fe_3C (a component of pearlite), Fe(Si), Fe_3Si, Fe_2Si, and C, come from different

reactions between Fe and SiC [99]. To successfully fabricate SiC-NFA composites, reactions between NFA and SiC must be prevented. The reactions between NFA and SiC were also confirmed by our previous studies [101, 102].

In order to avoid/reduce the reactions between SiC and NFA, applying a carbon coating on NFA can be promising. This is because carbon does not react with SiC and the solubility of carbon in α-Fe is very small (0.022 wt% [103]). Carbon is also an outstanding nuclear material, which has been used as a moderator and reflector in fission reactors, because of its physical and chemical stabilities in high temperature irradiation environments, especially for its very low neutron absorption cross-section [2]. Our purpose to introduce a carbon layer on the NFA particles (C@NFA) in the fabrication of the SiC-C@NFA composites is to maintain the original SiC and NFA, each of which offers its own benefits for the nuclear application, while the carbon coating as the reaction barrier layer will not compromise or degrade the expected functions of the SiC and NFA. The nanoscaled Y-Ti oxide nanoclusters (~2-5 nm) in the NFA [104] have extraordinary stabilities up to a high temperature of 1400^{o}C. The designed SiC-C@NFA composites with the intended sintering temperature of 850-1250^{o}C (in our previous work [101, 105]) will not alter the Y-Ti oxide nanoclusters. More importantly, the interphase boundaries in the composites can still act as the sinks for the recombination of the irradiation-induced defects [106].

In this work, a carbon coating introduced on NFA (C@NFA) particles was used to prevent the reactions between SiC and NFA. The composites have the compositions of 5 vol% SiC-95 vol% C@NFA, 15 vol% SiC-85 vol% C@NFA, and 25 vol% SiC-75 vol% C@NFA. The effectiveness of the coating is assessed based on the pressureless sintering of SiC-C@NFA and then SPS sintering followed by various characterizations. Although the effectiveness in avoiding the reactions between SiC and NFA is compromised due to the high difficulty of producing a perfect carbon coating layer, the improvement is obvious based on the microstructures of the as-sintered SiC-C@NFA composites. Furthermore, the fundamental investigation based on the thermodynamic simulation from the Thermo-Calc software offers in-depth understanding and scientific knowledge about the proposed system.

2.3. Materials and methods

2.3.1. Carbon coating on NFA (C@NFA) particles

First, sucrose ($C_{12}H_{22}O_{11}$, 99%, Alfa Aesar, Ward Hill, MA) was dissolved in ethanol (C_2H_5OH, Decon Laboratories, Inc., King of Prussia, PA). Then, NFA powder (D50=~20 μm; Lab made NFA, Fe-9Cr-2W-0.4Ti-0.2V-0.12C-0.3Y_2O_3 [59, 107]) was poured into the ethanol solution. After that, the ethanol solution with the NFA powder was heated on a hot plate to 60^{o}C while stirring to make sure that sucrose was uniformly precipitated on the surface of individual NFA particles during the ethanol evaporation process. After the ethanol solution was evaporated, the NFA powder with the coating was ground to improve homogeneity. The molar ratio of Fe and C was controlled at 4:1. To convert sucrose on the surface of the NFA powder into carbon, the NFA powder was thermally treated at 400^{o}C for 1 hr under Ar atmosphere. The heating rate was controlled at 5^{o}C/min. The sucrose was fully decomposed during this treatment, leaving only a carbon film on the surface of the NFA (C@NFA) particles. The C@NFA particles were mounted in epoxy and then carefully polished to examine the cross-section of the coated powders. The quality and thickness of the carbon coating on NFA particles were examined by scanning electron microscopy (FEI FEG-ESEM Quanta600, FEI Company, Hillsboro, OR, USA).

2.3.2. Pressureless sintering of SiC-C@NFA composites

In order to assess the effectiveness of the carbon coating as a reaction barrier, pressureless sintering was carried out for two composites of 10 vol% SiC-90 vol% C@NFA and 30 vol% SiC-70 vol% C@NFA. The carbon coated NFA powder was mixed with a SiC powder (D50=~0.5 μm, SiC UF-15, H. C. Starck, Goslar, Germany) by grinding the mixture in a mortar for 20 mins. Then the mixed powders were cold pressed at ~103 MPa for 5 mins. The pressed green bodies had a cylindrical shape with 12.7 mm diameter and 4 mm thickness. The green samples were pressurelessly sintered in a furnace under Ar atmosphere at 850^{o}C, 1050^{o}C, and 1250^{o}C for 1 hr.

The sintered SiC-C@NFA samples were examined by X-ray diffraction (XRD, PANalytical B. V., Almelo, Netherlands).

2.3.3. SPS sintering of SiC-C@NFA composites

For spark plasma sintering (SPS), the C@NFA and SiC powder were mixed in three different volume ratios, namely 5 vol% SiC-95 vol% C@NFA, 15 vol% SiC-85 vol% C@NFA, and 25 vol% SiC-75 vol% C@NFA. A 30 vol% SiC-70 vol% NFA composite without coating was also sintered for comparison. After mixing the composite powders in a mortar for 30 mins, the densification process was carried out by SPS (SPS Nanoceramics LLC, Morton Grove, IL) at two different temperatures of 850^{o}C and 950^{o}C with the same heating/cooling rate of 50°C/min, applied pressure of 100 MPa, and holding time of 10 mins.

The SPS sintered SiC-C@NFA composites were examined by X-ray diffraction (XRD). The densities of the composites were measured by the Archimedes method. For the relative density estimation, the theoretical density comes from the full density of the assumed SiC-NFA composites without reaction. The polished surface of the composites was evaluated by optical microscopy (BH2-HLSH, Olympus Inc, Japan) and scanning electron microscopy (FEI FEG-ESEM Quanta600, FEI Company, Hillsboro, OR). Vickers hardness measurement was carried out by a hardness tester (LV700AT, LECO, St. Joseph, MI). Fifteen indentations were performed for each sample with a pyramid shaped diamond indenter. Considering the composition distribution in the as-sintered composites, a relatively large load of 3 kg was utilized in order to reduce the potential errors. Elemental maps were further obtained using energy-dispersive X-ray spectroscopy (EDS) attached to the same SEM.

2.4. Results and discussion

2.4.1 Characterization of C-coating on NFA

The carbon coating around the spherical NFA particles can be seen in Fig. 2.1a. Since the particles are embedded in the epoxy matrix during polishing, the coating layer is much clearer on the lower left side. The high magnification SEM image in Fig. 2.1b shows that the thickness of the carbon coating is 200-400 nm.

The effectiveness of the coating is initially assessed by pressureless sintering of SiCC@NFA at 850^{o}C, 1050^{o}C, and 1250^{o}C. Fig. 2.2a shows the XRD patterns of the pressureless sintered 10 vol% SiC- 90 vol% C@NFA and 30 vol% SiC-70 vol% C@NFA composites, and the XRD patterns of the as received NFA and SiC powders and the C@NFA powder are included in Fig. 2.2b. After coating carbon on the NFA surface, the C@NFA powder has the same α-Fe phase as the as-received NFA powder. Due to the small amount and the possibly amorphous phase of the coated carbon, the XRD pattern does not show any peak from carbon. At the lower sintering temperatures of 850^{o}C and 1050^{o}C, the peaks reveal the presence of SiC and NFA, meaning that the carbon coating is effective in preventing the reactions between SiC and NFA. However, at the sintering temperature of 1250^{o}C, the reactions lead to the presence of Fe_3Si peaks, but without the SiC peaks for both composites. This is because the Fe atoms become more mobile at the sintering temperature of 1250^{o}C. During the Fe diffusion process, the carbon coating is broken and the NFA particles come in contact with SiC, leading to reactions. Thus, the carbon coating is not effective in preventing reactions at ≥1250^{o}C.

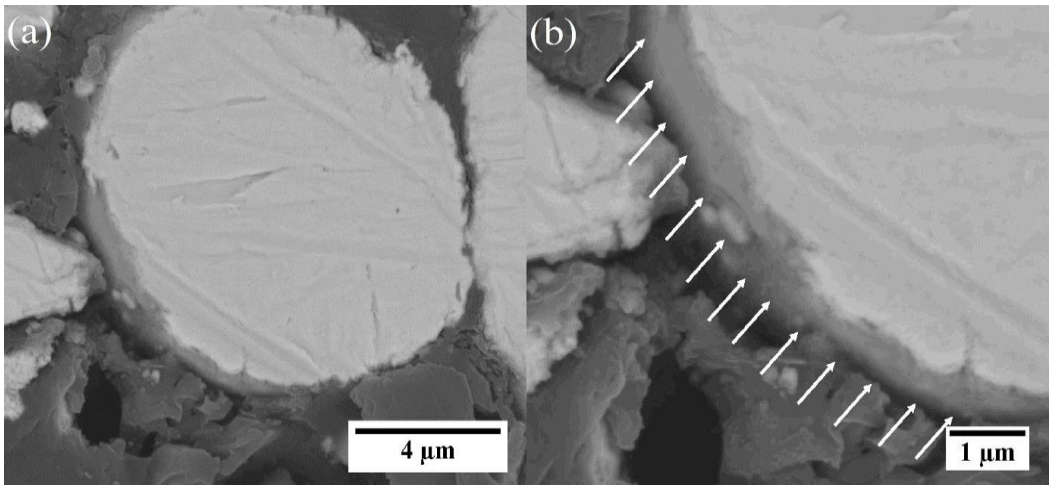

Fig. 2.1. SEM images of the C@NFA particle cross-section showing the carbon coating layer (courtesy: Dr. Kaijie Ning – co-author in this manuscript).

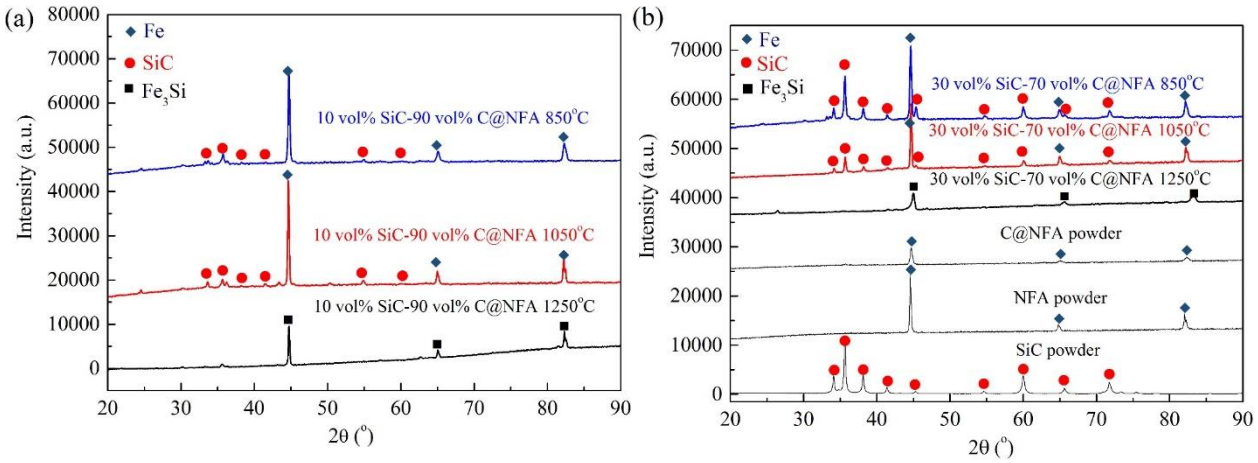

Fig. 2.2. (a) XRD patterns of the 850ºC, 1050ºC, and 1250ºC sintered 10 vol% SiC-90 vol% C@NFA composites, (b) XRD patterns of the 850ºC, 1050ºC, and 1250ºC sintered 30 vol% SiC-70 vol% C@NFA composites, as well as the NFA, SiC, and C@NFA powders.

2.4.2. Relative density and hardness of SPS sintered composites

Fig. 2.3a shows the relative densities of the SPS sintered SiC-C@NFA composites at 850^{o}C and 950^{o}C. The higher temperature sintered composites show higher relative densities, meaning that high temperature enhances the densification. Meanwhile, the relative densities increase with the SiC content in the composites, indicating that SiC accelerates densification. This is caused by the decomposition of SiC and the diffusion of Si into the NFA as to be discussed in later sections.

Fig. 2.3b shows the Vickers hardness of the SPS sintered SiC-C@NFA composites at 850^{o}C and 950^{o}C. There are different trends for the composites at different sintering temperatures. For the 850^{o}C sintered composites, the hardness increases with the addition of SiC to the NFA matrix. For the 950^{o}C sintered composites, the hardness shows a slight decrease with the SiC content. As known, the mechanical properties are affected by both density and composition [108]. On one hand, high density should lead to higher hardness. On the other hand, the decomposition of SiC leads to a solid solution of Si in the NFA matrix. Considering the low solubility of C in ferritic steel (BCC α-Fe, maximum solubility for C is 0.022 wt% at 723^{o}C [109]) and its aggregation observed in Figs. 2.7f and 2.7i, diffusion of Si into the NFA matrix is the major factor in influencing the mechanical behavior of the composites. Accordingly, the hardness decrease is modest at 950^{o}C sintering condition as shown in Fig. 2.3b. For the lower sintering temperature of 850^{o}C, the decomposition of SiC and diffusion of Si into the NFA matrix are relatively weak, and the hardening is believed to be mainly from the relative density effect. Thus, the hardness keeps increasing with the density of the 850^{o}C sintered composites. For the higher sintering temperature of 950^{o}C, the decomposition of SiC and diffusion of Si into the NFA matrix are more extensive, which degrades the hardness of the 950^{o}C sintered composites.

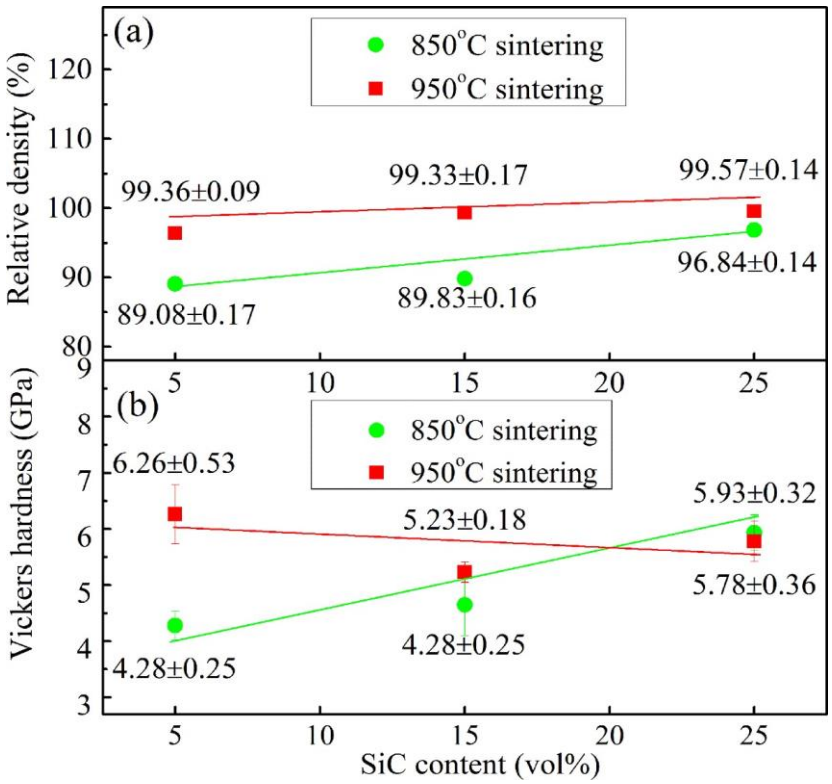

Fig. 2.3. Relative density (a) and Vickers hardness (b) of the SPS sintered SiC-C@NFA composites at 850°C and 950°C.

2.4.3. Phase, microstructure and composition evolution during SPS sintering

Fig. 2.4 shows the XRD patterns of the SiC-C@NFA composites sintered at 850°C and 950°C. At 850°C sintering, all the composites (5 vol% SiC-95 vol% C@NFA, 15 vol% SiC-85 vol% C@NFA, and 25 vol% SiC-75 vol% C@NFA) show only the α-Fe phase, which is the same as the as-received NFA powder in Fig. 2.2b. With the increase of the SiC content, the XRD peaks of the α-Fe phase slightly shift to higher angles. However, none of the SiC peaks can be detected, even for the composites with the maximum SiC content of 25 vol%. Potential reaction products of Fe_3Si are not seen either. The right shift of the α-Fe XRD peaks for all the composites is due to the diffusion of Si into the NFA lattice, which will be explained based on the elemental compositions in Fig. 2.7.

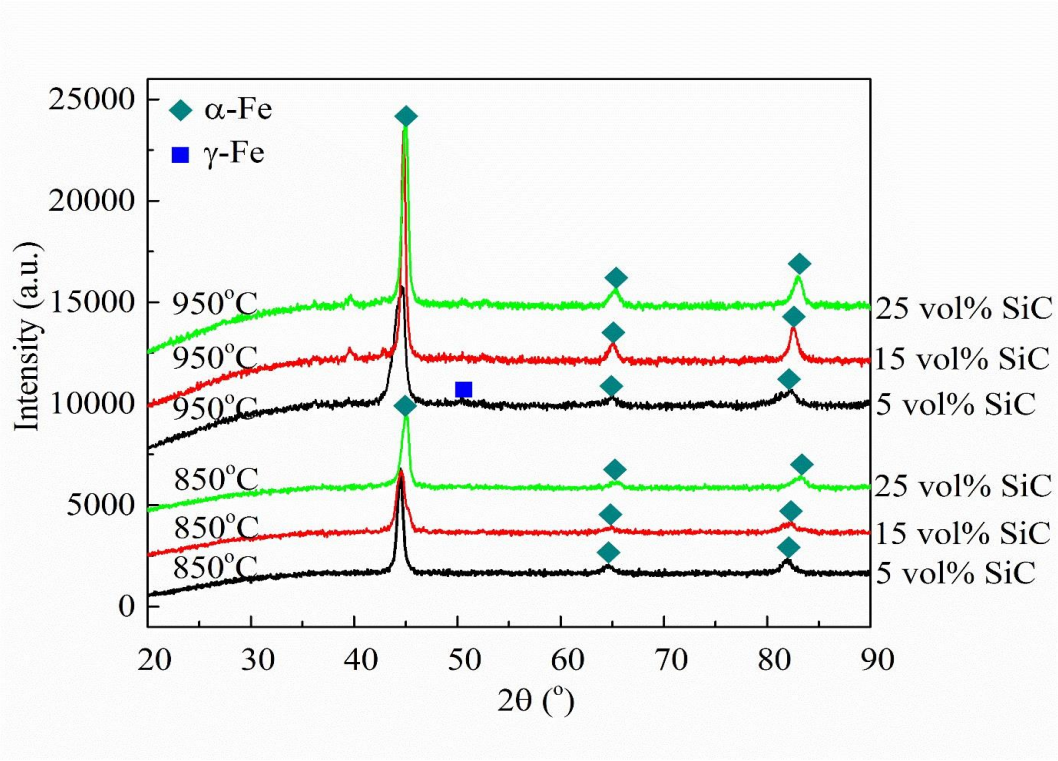

Fig. 2.4. XRD patterns of SPS sintered SiC-C@NFA composites at 850°C and 950°C.

At 950°C sintering, all the composites continue to maintain the major α-Fe phase, similar to the 850°C sintered samples. Minor γ-Fe phase is observed in the 5 vol% SiC content sample. The appearance of the minor γ-Fe phase at the sintering temperatures of ≥950°C has been confirmed from our previous work [110]. In the two high SiC content samples (15 vol% and 25 vol%), the γ-Fe phase is not observed. This is because the diffusion of Si into the NFA matrix hinders the Fe α→γ phase transformation [110]. Still, no SiC peaks are identified. The right shift of the XRD peaks is also observed as for the 850°C sintered composites, which is again attributed to the Si diffusion into the NFA lattice. The lattice parameters for all the composites are calculated by the following equation and plotted in Fig. 2.5.

$$a = \frac{\lambda.\sqrt{h^2 + k^2 + l^2}}{2\sin\theta} \qquad (2.1)$$

where *a* is lattice constant; *h*, *k*, *l* are Miller indices; θ is diffraction angle; λ is wavelength (1.5406 Å in this study). For both 850 and 950ºC sintered composites, the lattice constant decreases with the increase of the SiC content. As known, the atomic radii [111] for Fe and Si are 1.40 Å and 1.10 Å, respectively, and the lattice parameter of Fe-Si alloys decreases with increasing Si content [112]. Thus, Si, which diffuses into the NFA lattice, should lead to the decrease of the lattice constant. As a matter of fact, the diffusion of Si into the NFA matrix is demonstrated in the elemental composition study of Figs. 2.7a and 2.7e.

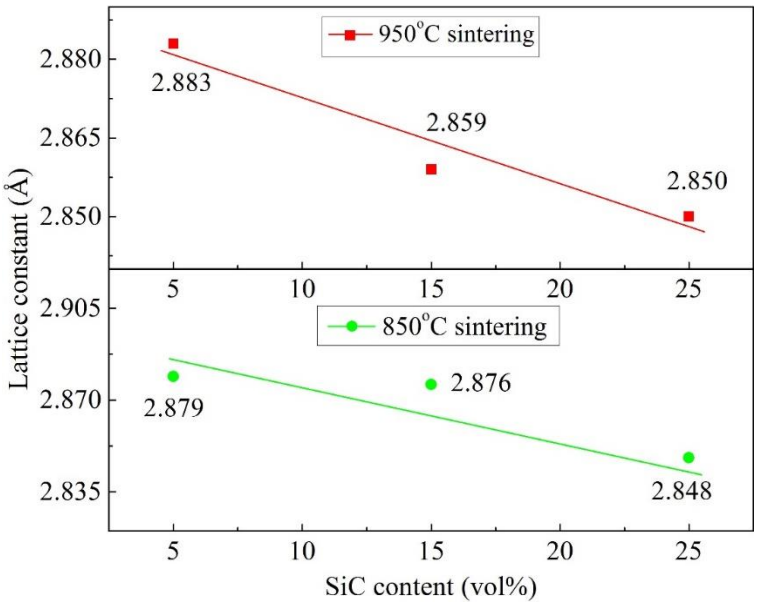

Fig. 2.5. Lattice parameters of the 850ºC and 950ºC sintered SiC-C@NFA composites.

Figs. 2.6a, 2.6b and 2.6c show the optical images for the 850ºC sintered composites. For the 5 vol% SiC-95 vol% C@NFA composite in Fig. 2.6a, the round shape is from the NFA grains, which has a lighter contrast. Between the NFA grains are the grain boundaries. The dark regions are the reaction products between the NFA and SiC particles. For the 15 vol% SiC-85 vol% C@NFA composite in Fig. 2.6b, due to the further increase of the SiC content in the matrix, the distance between the NFA grains is larger because more SiC particles occupy the space among the NFA grains, which leads to more reaction products among the NFA grains. For the 25 vol% SiC-

75 vol% C@NFA composite in Fig. 2.6c, the NFA grains are even more separated from the reaction products.

The optical images of the 950ºC sintered 5 vol% SiC-95 vol% C@NFA, 15 vol% SiC85 vol% C@NFA, and 25 vol% SiC-75 vol% C@NFA composites are shown in Figs. 2.6d, 2.6e and 2.6f, respectively. These images have the similar trend as the 850ºC sintered composites in Figs. 2.6a-2.6c. With the increase of the SiC content in the composites, the distance between the NFA grains increases. The NFA grains are randomly distributed in the matrix with further distance for the 25 vol% SiC-75 vol% C@NFA composite as shown in Fig. 2.6f. Some rust (oxidation of the NFA phase) shows as the dark contrast areas for the 15 vol% SiC-85 vol% C@NFA sample in Fig. 2.6e.

Figs. 2.6g and 2.6h further show the backscattered SEM images of the 25 vol% SiC-75 vol% C@NFA composite sintered at 850ºC. The bright contrast areas in Fig. 2.6g represent the NFA rich region, which contains the higher atomic number elements of Fe and Cr. The darker contrast areas represent the original SiC rich regions, which contain more low atomic number elements of Si and C. The high magnification image of Fig. 2.6h shows a large NFA grain with rough edges. This is attributed to the interactions between the NFA and SiC particles. There is extensive interaction at the NFA grain surface during the sintering process. Also, a bright edge along the NFA grain is observed. This is due to the accumulation of some higher atomic number element, which is proven to be Cr by elemental mapping in Figs. 2.7a and 2.7c.

Fig. 2.7a shows an observation covering both the NFA matrix and the reaction region. The high contrast species are more visible in the form of rough lines on the edge of the reaction region. In the reaction region at the bottom of Fig. 2.7a, dark colored species is embedded, which has a similar contrast to that of the NFA matrix region on the top of Fig. 2.7a. The EDS elemental maps are shown in Figs. 2.7b-2.7e. The NFA matrix region is rich in Fe and Cr but deficient in Si as shown in Figs. 2.7b, 2.7c, and 2.7e, respectively. On the edge of the reaction region, there is an enrichment of Cr, which matches with the high contrast edge in Figs. 2.6h and 2.7a. At the bottom of Fig. 2.7a, more Si and Fe elements and less Cr element are observed from Figs. 2.7e, 2.7b and 2.7c, respectively. Along the edge of the reaction region, where the bright phases are dominant, the deficiency of Si is evident, probably due to the low solubility of Si in the Cr-rich alloy.

However, the C element is enriched in the discrete dark regions, the NFA matrix region also has C element.

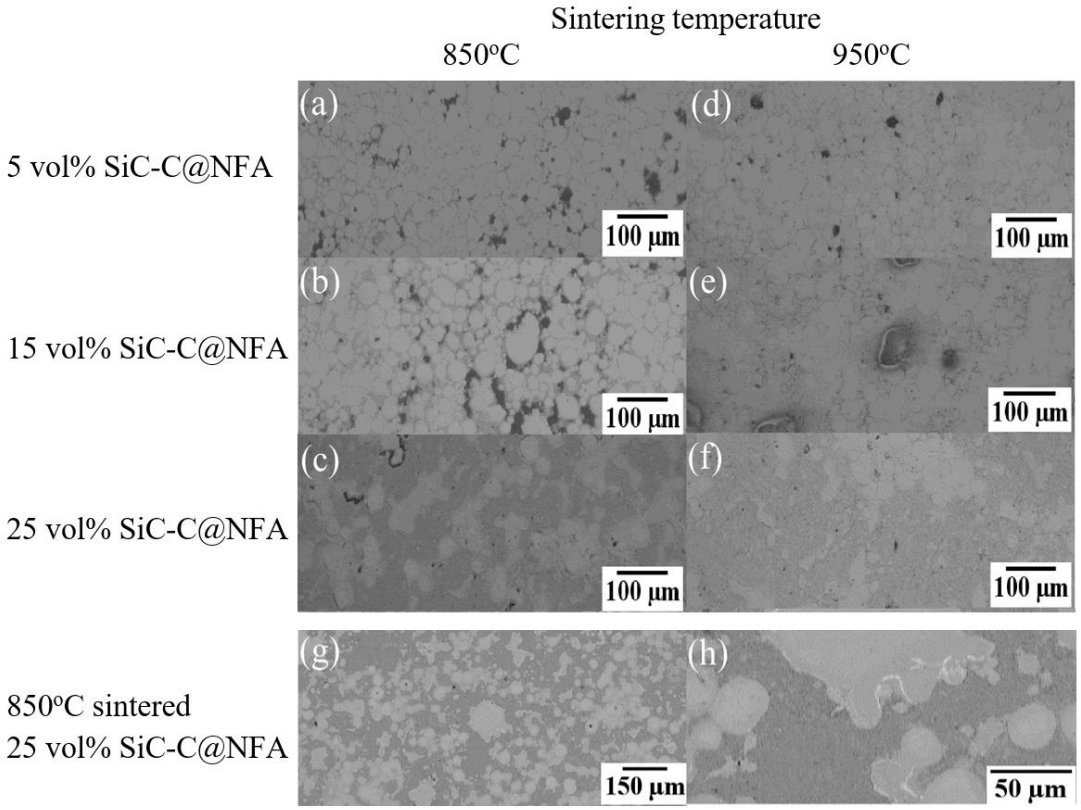

Fig. 2.6. Optical (a-f) and backscattered SEM images (g-h) of the SPS sintered SiC-C@NFA composites.

The elemental distribution in the reaction region (at the bottom of Fig. 2.7a) consists of bright and dark contrast phases. The SEM image with high magnification in Fig. 2.7f further reveals that the dark phases have elongated shapes embedded in the bright phase. The size of the dark phase is in the range of 0.5-1.5 µm. Based on Fig. 2.7i, these darker phases are C-rich and Fe- and Si-deficient. The bright phase areas are Fe-, Cr-, and Si-rich as shown in Figs. 2.6g, 2.6h and 2.6j, respectively. The dissolution of Si into the NFA matrix lattice is the main reason for the right peak shift of the XRD patterns in Fig. 2.4.

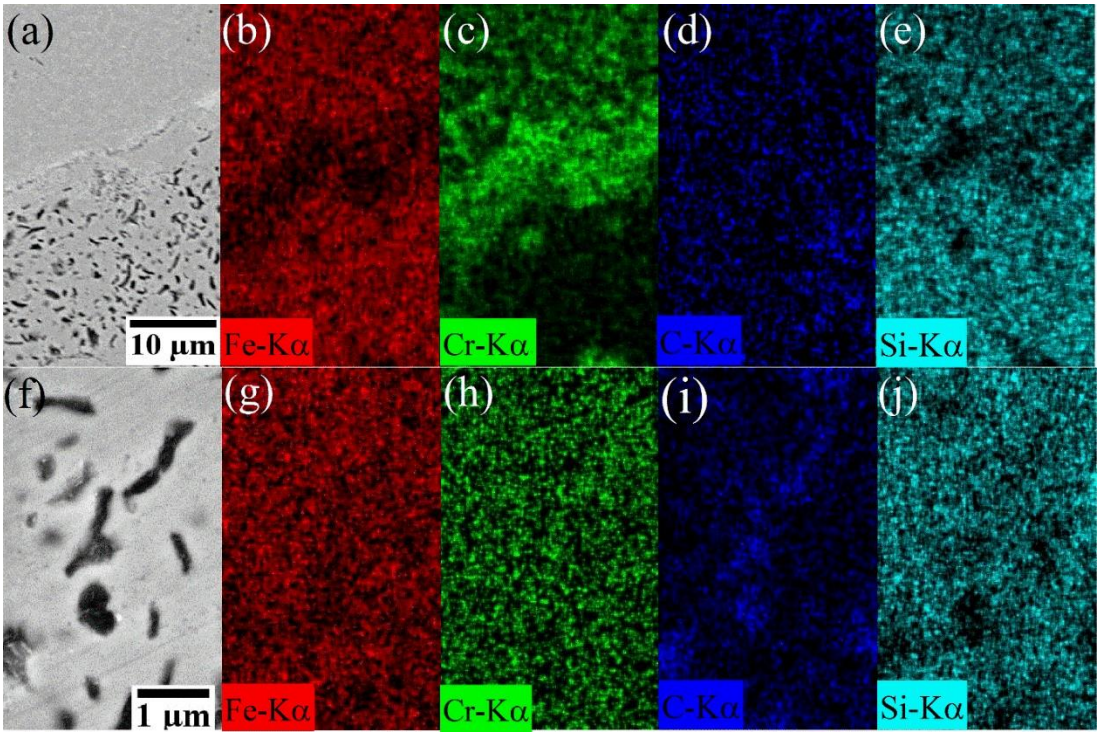

Fig. 2.7. SEM image and elemental maps of the SPS sintered 25 vol% SiC-75 vol% C@NFA composites at 950^{o}C.

2.4.4. Comparison between SiC-C@NFA and SiC-NFA composites

The XRD patterns of the 30 vol% SiC-70 vol% NFA composite sintered without any coating on the NFA particles are shown in Fig. 2.8 in order to compare with the SiC-C@NFA composites. The major reaction phase Fe_3Si and some other unknown impurity phases can be observed. However, both SiC and NFA phases are absent. For the current SiC-C@NFA composites, although the SiC peaks are not observed in Fig. 2.4, the reaction product Fe_3Si is not observed, meaning that the C reaction barrier can prevent extensive reactions between SiC and NFA.

The SiC-C@NFA composites demonstrate the ability to maintain the original phases of NFA (α-Fe, BCC) with a slight shrinkage of the lattice (Figs. 2.4 and 2.5), while the SiC-NFA composite without coating has a significant amount of Fe_3Si (Fig. 2.8) due to the strong reactions

between SiC and NFA. The SiC-C@NFA composite has clear NFA grains; although reaction regions are also identified, and micron-sized C-rich phase is produced in the reaction region, the extent of the reaction between SiC and NFA is more constrained. In the SiC-NFA composites, the detrimental Fe_3Si phase forms the matrix phase; and a lamellar phase and another second phase are also created after the reactions. Therefore, the C coating barrier is effective in reducing the reactions of the SiC-NFA composite.

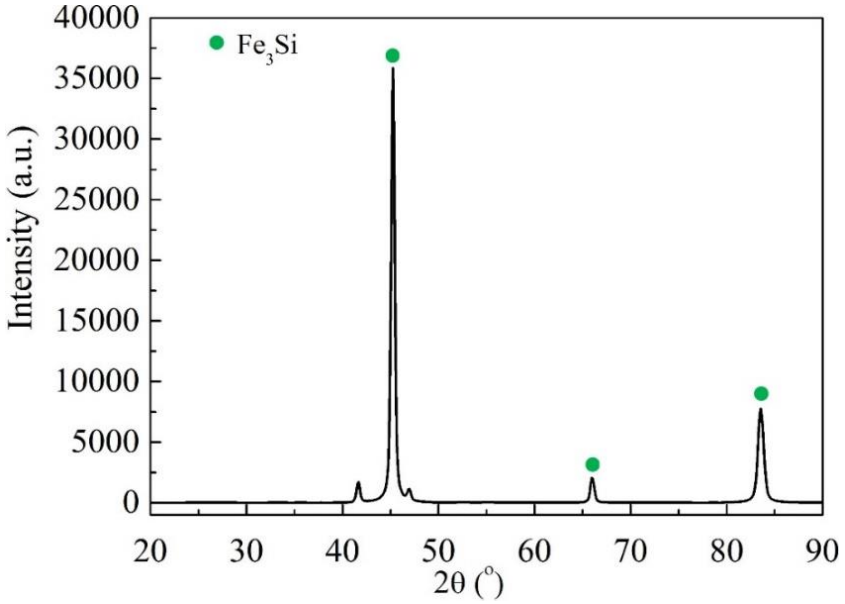

Fig. 2.8. XRD patterns of the 30 vol% SiC-70 vol% NFA composite without the carbon coating barrier.

2.4.5. Fundamental understanding of SiC-C@NFA composites

After the SPS sintering at 850 and 950°C, the composites with 5 vol% SiC-95 vol% C@NFA, 15 vol% SiC-85 vol% C@NFA, and 25 vol% SiC-75 vol% C@NFA compositions maintain the same crystal structure as α-Fe. No new phases of FeSi, Fe_2Si, or Fe_3Si are produced. Before the SPS sintering (Fig. 2.9a), NFA particle (D50=~20 μm) packing serves as the framework and the SiC particles (D50=~0.5 μm) fill the interstitial sites of the NFA particles.

After sintering, the NFA particles grow to become the dense matrix with low Si diffusion, while the reaction regions form from the reaction between NFA and SiC, and hence are composed of Fe with diffused Si grains and C-enriched aggregates. The cause of C-rich aggregation is because of its low solubility and low diffusion coefficient in ferritic steel. The diffusion distance *l* can be calculated by the following equation [113]:

$$l = \sqrt{6Dt} \tag{2.2}$$

where *D* is diffusion coefficient, and *t* is time. At 800ºC, the diffusion coefficients for C and Si in ferritic steel are 1.0×10^{-16} cm^2/s [114] and 0.76×10^{-8} cm^2/s [115], respectively. The SPS sintering time for all the composites is 10 mins. According to Eq. (2.2), the diffusion distances for C and Si are 0.006 μm and 52.3 μm, respectively. This means that, after the reaction from the SiC decomposition, C is extremely hard whereas Si is extremely easy to diffuse into the NFA matrix.

2.5. Conclusions

In this work, C@NFA particles are made by precipitating sucrose on NFA particles followed by pyrolysis. SPS sintering of SiC-C@NFA composites with 5 vol%, 15 vol%, and 25 vol% SiC is carried out at 850ºC and 950ºC. Densification of the SiC-C@NFA composites is enhanced by increasing the temperature and the SiC content. The hardness increases with the SiC content at 850ºC but decreases with the SiC content at 950ºC. All the composites have the major α-Fe phase without the presence of the SiC phase. In the reaction region, the Si element diffuses into NFA while C-enriched aggregates form. Although the break-down of the carbon coating layer during the sintering process compromises the ability to prevent the reactions between SiC and NFA, the SiC-C@NFA composites show 4-7 Gpa hardness and much improved phase retention compared to the composite without any coating. The fundamental interactions between Fe and SiC are explained based on phase diagram and Gibbs free energy. Fabrication of the SiC-NFA composites by introducing a carbon barrier offers a new strategy for nuclear cladding materials.

Chapter 3

Spark Plasma Sintering of SiC and NFA using Chromium Carbide as Interfacial Barrier Layer

3.1. Abstract

Silicon carbide and nanostructured ferritic alloy (SiC-NFA) composites are expected to be remarkable candidates for nuclear cladding materials. However, SiC and NFA reactions during sintering have been a challenging problem to address. A Cr_3C_2 coating on SiC particles is introduced as a reaction barrier layer to fabricate novel Cr_3C_2@SiC-NFA composites in this work. The composites of 5 vol% Cr_3C_2@SiC-95 vol% NFA, 15 vol% Cr_3C_2@SiC-85 vol% NFA, and 25 vol% Cr_3C_2@SiC-75 vol% NFA achieve >96% densities under spark plasma sintering (SPS) at 950^{o}C and have the Vickers hardness of 5-6 GPa. The main phase for the composites maintains the original α-Fe structure of the NFA composition. Although the NFA matrix with silicon diffusion and carbon-rich aggregates are detected, the much improved microstructures in the composites indicate the positive effects of the Cr_3C_2 coating as the reaction barrier. The Cr_3C_2@SiC-NFA composites are expected to be promising cladding materials in harsh nuclear environments.

3.2. Introduction

The novelty of this work is to introduce a Cr_3C_2 barrier layer on SiC particles (Cr_3C_2@SiC powder) to prevent the SiC-NFA reactions during sintering. SiC and Cr_3C_2 [116] can coexist at sintering temperatures up to 1300^{o}C. In addition, Cr_3C_2 has very low solubility in ferritic steel below 627°C and tends to precipitate from saturated α-Fe (BCC) solid solution [117]. Compared to our prior work [101, 102], this work emphasizes the influence of the Cr_3C_2 barrier layer on the microstructural and mechanical evolution of the SiC-NFA composites. The effectiveness of the

Cr_3C_2 coating layer as a reaction barrier was demonstrated based on pressureless sintering of the Cr_3C_2@SiC-NFA composites. Three different Cr_3C_2@SiC-NFA composites (5 vol% Cr_3C_2@SiC-95 vol% NFA, 15 vol% Cr_3C_2@SiC-85 vol% NFA, and 25 vol% Cr_3C_2@SiC-75 vol% NFA) were further made by spark plasma sintering (SPS) and characterized based on density, Vickers hardness, microstructure, phase, and elemental compositions. The Cr_3C_2@SiC-NFA composites with high density, improved microstructure, and high hardness are expected to have promising cladding applications for nuclear reactors.

3.3. Materials and methods

The Cr_3C_2 coating layer on SiC particles was developed through a melt salt coating approach followed by high temperature reduction. First, SiC powder (D50=~0.5 μm, SiC UF15, H. C. Starck, Goslar, Germany) and chromium nitride powder ($Cr(NO_3)_3$•$9H_2O$, 98.5% purity, Alfa Aesar, Ward Hill, MA) were mixed with a ratio of 5:1 in water and kept at 60^{o}C for 30 mins in a water bath with stirring. During this process, $Cr(NO_3)_3$ was dissolved into the solution. After 10 mins of vibratory milling, the suspension was kept at 450^{o}C for 2 hrs in a muffle furnace to completely evaporate the water. A Cr_2O_3 coating layer was thus obtained on individual SiC particles (denoted as Cr_2O_3@SiC). The reduction process was conducted at 1300^{o}C for 1 hr in a mixed atmosphere of methane and argon with the methane: argon ratio of 2:1. Thus, a final Cr_3C_2 coating layer was obtained on the surface of SiC particles (denoted as Cr_3C_2@SiC), and the thickness was designed to be ~15 nm from our calculation. After mixing the Cr_3C_2@SiC powder with the NFA powder (D50=~20 μm, Fe-9Cr2W-0.4Ti-0.2V-0.12C-0.3Y_2O_3 [107]), green bodies of the 30 vol% Cr_3C_2@SiC-70 vol% NFA composite with a size of 12.7 mm diameter and 4 mm thickness were prepared by cold pressing at ~103 MPa and then pressureless sintering to 1050^{o}C and 1250^{o}C in Ar atmosphere for 1 hr.

Cr_3C_2@SiC-NFA composites were also obtained using SPS with three different compositions including 5 vol% Cr_3C_2@SiC-95 vol% NFA, 15 vol% Cr_3C_2@SiC-85 vol% NFA, and 25 vol% Cr_3C_2@SiC-75 vol% NFA. Before sintering, the corresponding Cr_3C_2@SiC and NFA powders were mixed for 30 mins manually in a mortar. The densification was achieved by

SPS (SPS Nanoceramics LLC, Morton Grove, IL) at two different temperatures of 850ºC and 950ºC with the same heating/cooling rate (50 °C/min), applied pressure (100 MPa), and holding time (10 mins).

The phase and morphology of the as-prepared Cr_3C_2@SiC powders and the pressureless sintered Cr_3C_2@SiC-NFA composites were examined by X-ray diffraction (XRD, PANalytical B. V., Almelo, Netherlands) and scanning electron microscopy (FEI FEG-ESEM Quanta600, FEI Company, Hillsboro, OR, USA). The densities of the SPS sintered Cr_3C_2@SiC-NFA composites were measured using the Archimedes method. Their phases were identified by XRD. The polished surfaces of the composites were examined by optical microscopy (BH2-HLSH, Olympus Inc, Japan) and SEM. The Vickers hardness was measured by a hardness tester (LV700AT, LECO, St. Joseph, MI) under a load of 3 kg. The elemental compositions and maps were obtained from the polished surfaces using energydispersive X-ray spectroscopy (EDS) attached on the SEM.

3.4. Results and discussion

3.4.1. Characterization of Cr_3C_2 coating on SiC

Fig. 3.1a shows the XRD patterns of the Cr_2O_3 coated SiC (Cr_2O_3@SiC) powder and Cr_3C_2 coated SiC (Cr_3C_2@SiC) powder. After the thermal treatment in air, Cr_2O_3 phase is obtained from the decomposition of $Cr(NO_3)_3$ according to:

$$4Cr(NO_3)_3 \rightarrow 2Cr_2O_3 + 12NO_2 \uparrow + 3O_2 \uparrow \quad (3.1)$$

With the reduction in the methane and argon mixture, Cr_2O_3 converts to Cr_3C_2 according to:

$$3Cr_2O_3 + 13CH_4 \rightarrow 2Cr_3C_2 + 9CO \uparrow + 26H_2 \uparrow \quad (3.2)$$

Meanwhile, a small carbon peak can be found at ~26°, resulting from the decomposition of methane during the reduction process according to:

$$CH_4 \rightarrow C + 2H_2 \uparrow \quad (3.3)$$

By using the Rietveld method [118], the weight ratios for SiC, Cr_3C_2, and C are calculated from their XRD patterns to be 59.8 wt%, 18.6 wt%, and 21.6 wt%, respectively. The thickness of the Cr_3C_2 coating on the individual SiC particle is also evaluated to be 13 nm according to the weight ratio, which agrees with the designed thickness of 15 nm. Since the Cr_2O_3@SiC powder is loose during the thermal treatment, the reducing gas can easily penetrate the entire powder and lead to the deposition of decomposed C on the SiC particle surfaces as well. Fig. 3.1b shows the XRD patterns of the pressureless sintered Cr_3C_2@SiC-NFA composites at 1050°C and 1250°C. For the 1050°C sintered sample, the Cr_3C_2 coating is effective in preventing the reactions between SiC and NFA. Both SiC and NFA phases can be observed without any other phases derived from the reactions. However, at 1250°C sintering temperature, the Cr_3C_2 coating is no longer effective in preventing the reactions. The unknown new phase cannot be identified for now. Thus, when the sintering temperature exceeds 1050°C, the coating layer is broken, allowing the reactions between SiC and NFA.

Fig. 3.2 shows the morphology of the as-received SiC powder, Cr_2O_3@SiC powder, and Cr_3C_2@SiC powder. The as-received SiC powder shows flaky shapes with sharp edges (Fig. 3.2a). After the $Cr(NO_3)_3$ thermal decomposition, the SiC particle surface is coated with a thin Cr_2O_3 layer (Fig. 3.2b), which is comprised of Cr_2O_3 nanoparticles. Fig. 3.2c shows the SiC powder after the reduction process. The SiC particles are coated by tiny Cr_3C_2 particles, which have relatively larger sizes than the Cr_2O_3 particles. A thin coating layer can be found between the small particles, which likely included some decomposed carbon and should play a role in preventing the reactions between SiC and NFA particles because of the extremely low solubility of carbon in α-Fe (0.022 wt% [109]).

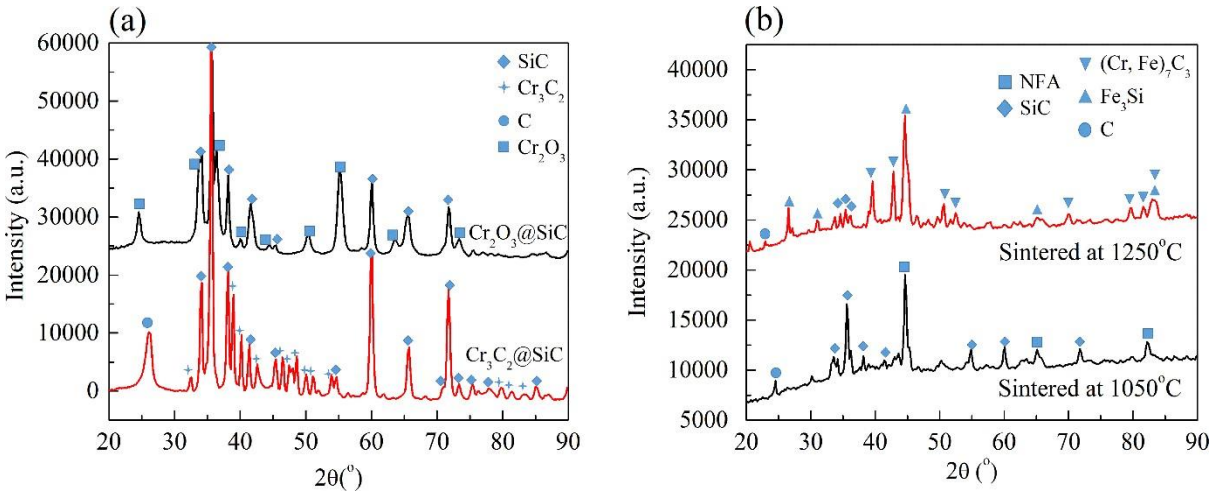

Fig. 3.1. XRD patterns of Cr2O3@SiC and Cr3C2@SiC powders (a) and the pressureless sintered 30 vol% Cr3C2@SiC-70 vol% NFA composite (b) at different temperatures.

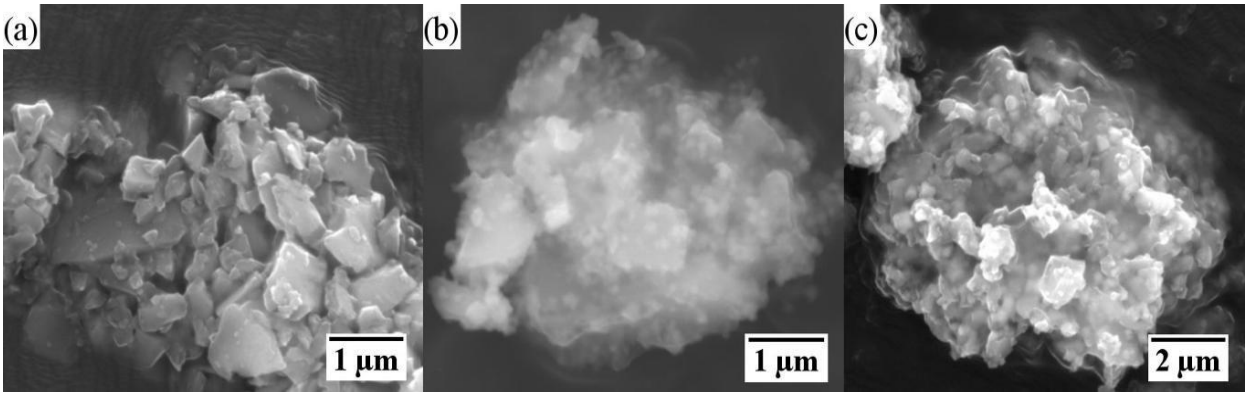

Fig. 3.2. SEM images of as-received (a) SiC powder, (b) Cr2O3@SiC powder, and (c) Cr3C2@SiC powder (courtesy: Dr. Kaijie Ning – co-author in this manuscript).

3.4.2. Relative density and Vicker's hardness

Table 3.1 lists the relative density and Vickers hardness of the composites SPS sintered at 850°C and 950°C. At 850°C, the 5 vol% Cr_3C_2@SiC-95 vol% NFA composite has a relatively low density of 93.22±0.13%. When the Cr_3C_2@SiC content increases to 15 vol%, the composite

density rapidly increases to 99.73±0.11%. The 25 vol% Cr_3C_2@SiC-75 vol% NFA composite has the highest relative density of 103.16±0.14%. The relative density slightly higher than 100% is due to the reactions between SiC and NFA during the SPS sintering process. The diffusion of Si into the NFA matrix (see Fig. 3.7) contributes to the lattice volume shrinkage (see Table 3.2) of the composite and thus causes higher relative density. At 950^{o}C SPS sintering temperature, the relative density for the 5 vol% Cr_3C_2@SiC95 vol% NFA composite is 96.74±0.06%, which is much higher than that at 850^{o}C SPS sintering. This means that higher sintering temperature benefits the densification of the Cr_3C_2@SiC-NFA composites with the lower Cr_3C_2@SiC content. However, for the other two composites with higher Cr_3C_2@SiC contents at 15 vol% and 25 vol%, their relative densities maintain the same levels as those of the 850^{o}C sintering condition. Both of them approach full density and are less dependent on the sintering temperature. It is believed that the reactions between SiC and NFA promote elemental diffusion and enhance the densification of the composites.

Vickers hardness of the Cr_3C_2@SiC-NFA composites in Table 3.1 shows a different trend for the two sintering temperatures. For the 850^{o}C sintered composites, the hardness increases with the Cr_3C_2@SiC content, rising from 5.00±0.23 GPa for the 5 vol% Cr_3C_2@SiC-95 vol% NFA sample, to 5.16±0.14 GPa for the 15 vol% Cr_3C_2@SiC-85 vol% NFA sample, and further to 5.82±0.21 GPa for the 25 vol% Cr_3C_2@SiC-75 vol% NFA sample. The SiC content plays a key role in the hardness increase. Even though the SiC phase is not detected in the XRD patterns (see Fig. 3.3), the density keeps increasing with the Cr_3C_2@SiC content at 850^{o}C (Table 3.1). Thus, it can be stated that higher Cr_3C_2@SiC content leads to higher composite density and thus higher Vickers hardness. However, the hardness values of the 950^{o}C sintered samples show slight fluctuation with a basically decreasing trend, from 6.33±0.33 GPa for the 5 vol% Cr_3C_2@SiC-95 vol% NFA composite to 6.03±0.15 GPa for the 25 vol% Cr_3C_2@SiC-75 vol% NFA composite. The changing trend of the hardness is not related to the relative density as for the 850^{o}C sintered samples. Combining with the XRD patterns from Fig. 3.3, it can be seen that reactions between SiC and NFA happen for all these composites. The Si diffusion from SiC to the NFA matrix strongly depends on the SiC content within the composites, and the ratio of Si/Fe (see Fig. 3.7) in the NFA matrix keeps increasing with the SiC content. It has also been reported that the Si solute compromises the hardness of an iron matrix [108]. As a result, the slightly decreasing hardness for the Cr_3C_2@SiC-NFA composites at 950^{o}C is likely due to the reactions between SiC and NFA

and the Si diffusion to the NFA matrix. As a cladding material for nuclear reactors, the traditional zirconium based alloy developed for Gen I-III reactors has the Vickers hardness of 3.2-4.2 GPa [119]. New cladding materials for future Gen IV reactors are various ODS steels with Vickers hardness as follows: 14Cr-ODS~3.6-3.8 GPa [120], 14YWT (14Cr-ODS)~ 3.5-3.7 GPa [121], Eurofer ODS (9Cr)~3.2-4.2 GPa [122], Eurofer 97 (9Cr)~2.1-2.2 GPa [123], ODS RAF (14Cr)~4.5-5.0 GPa [124], European ODS (14Cr)~4.5 GPa [122]. In this study, our sintered Cr_3C_2@SiC-NFA composites have the Vickers hardness of 5-6 GPa, which is much higher than the zirconium based alloy and ODS steels, indicating its promising potential as a cladding material for nuclear reactors.

Table 3.1. Relative density and hardness of 850^{o}C and 950^{o}C sintered Cr_3C_2@SiC-NFA composites.

Sintering temperature (^{o}C)	Samples	Relative density (%)	Hardness (GPa)
850^{o}C	5 vol% Cr_3C_2@SiC-95 vol% NFA	93.22±0.13%	5.00±0.23
	15 vol% Cr_3C_2@SiC-95 vol% NFA	99.73±0.11%	5.16±0.14
	25 vol% Cr_3C_2@SiC-95 vol% NFA	103.16±0.14%	5.82±0.21
950^{o}C	5 vol% Cr_3C_2@SiC-95 vol% NFA	96.74±0.06%	6.33±0.33
	15 vol% Cr_3C_2@SiC-95 vol% NFA	99.46±0.10%	5.25±0.34
	25 vol% Cr_3C_2@SiC-95 vol% NFA	103.87±0.12%	6.03±0.15

3.4.3. Phase compositions

Fig. 3.3 shows the XRD patterns of the SPS sintered Cr_3C_2@SiC-NFA composites at 850°C and 950°C. At 850°C sintering, all the three samples show just the peaks of the α-Fe phase, which conforms to the NFA BCC structure. However, the peaks shift to higher angles for all the composites. With more SiC content in the composite, the peaks shift more significantly to higher angles. At 950°C sintering, the main phase is α-Fe with a small amount of γ-Fe, which is present in the lowest SiC content sample, 5 vol% Cr_3C_2@SiC-95 vol% NFA. Previous work from our group on the SiC-NFA composite sintering shows that an increase of SiC content in the composite hinders the phase transformation of Fe α→γ [110]. Thus in the two composites with higher SiC contents of 15 vol% and 25 vol%, the γ-Fe phase is absent. Meanwhile, the SiC phase is absent for all the composites and the peak shift to higher angles is also obvious, similar to the 850°C sintered samples. With the increase of the SiC content, the extent of the peak shift is greater.

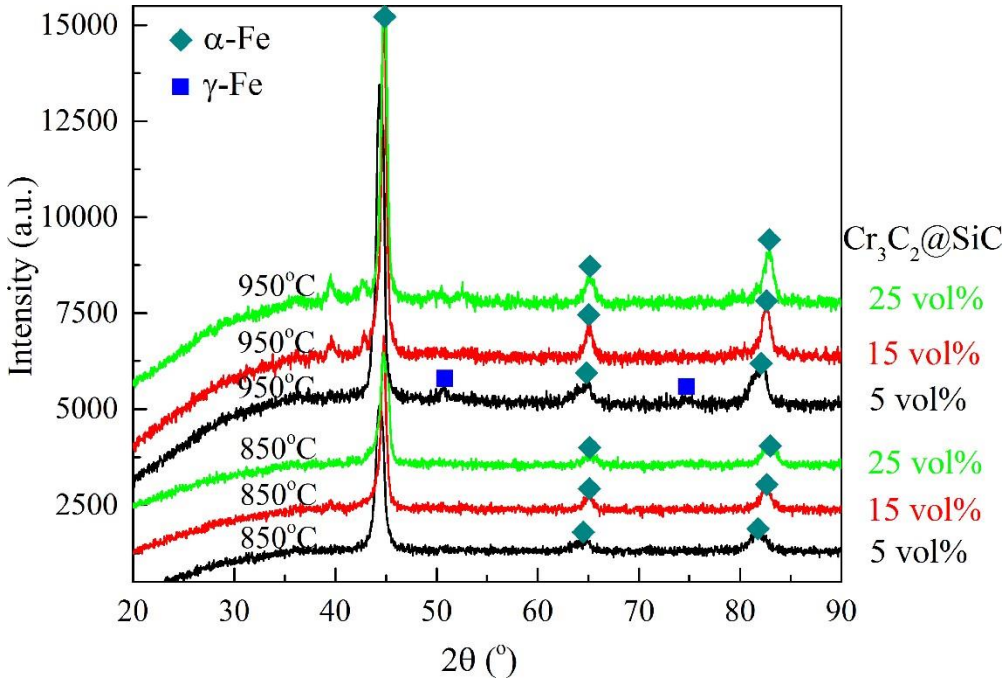

Fig. 3.3. XRD patterns of the SPS sintered Cr_3C_2@SiC-NFA composites at 850°C and 950°C.

Table 3.2 lists the lattice parameters for the SPS sintered Cr_3C_2@SiC-NFA composites at 850°C and 950°C. For both 850°C and 950°C sintering temperatures, the composites show the decreasing trend of the lattice constants with the SiC contents, the lattice constants for the 25 vol% Cr_3C_2@SiC-75 vol% NFA composite shrink about 0.1% compared to those of the 5 vol% Cr_3C_2@SiC-95 vol% NFA composite. Based on the elemental composition study, the diffusion of Si to the NFA matrix leads to the shrinkage of the NFA lattice constant. It is also known that Si has a slightly smaller atomic size (1.10 Å) than Fe (1.40 Å) [111]. Thus, the strain induced by the unit cell shrinkage (if there is any) in the sintered Cr_3C_2@SiC-NFA composites should be beneficial, as indicated from the improved Vickers hardness in Table 3.1. Meanwhile, SPS sintering temperature affects the lattice parameters of the sintered composites as well. The composites that sintered at 950°C have smaller lattice parameters than those at 850°C. This is because at higher sintering temperature, the diffusion for Si is more intensive than at lower temperature, as demonstrated from Fig. 3.7. The 950°C sintered composites exhibit much higher Si/Fe ratios in the NFA matrix than the 850°C sintered composites.

Table 3.2. Lattice constant (a) of 850°C and 950°C sintered Cr_3C_2@SiC-NFA composites.

Sintering temperature (°C)	Samples	2θ (°)	Lattice constant, 'a' (Å)
850°C	5 vol% Cr_3C_2@SiC-95 vol% NFA	44.41	2.883
	15 vol% Cr_3C_2@SiC-95 vol% NFA	44.76	2.861
	25 vol% Cr_3C_2@SiC-95 vol% NFA	44.85	2.856
950°C	5 vol% Cr_3C_2@SiC-95 vol% NFA	44.43	2.881
	15 vol% Cr_3C_2@SiC-95 vol% NFA	44.80	2.859
	25 vol% Cr_3C_2@SiC-95 vol% NFA	44.83	2.857

3.4.4. Microstructural evolution

Figs. 3.4a, 3.4b and 3.4c show the surface images of the polished 5 vol% Cr_3C_2@SiC-95 vol% NFA, 15 vol% Cr_3C_2@SiC-85 vol% NFA, and 25 vol% Cr_3C_2@SiC-75 vol% NFA composites sintered at 850^{o}C, respectively. After polishing, the surfaces for all the composites look dense; no pores are observed. The dark contrast regions are the SiC-rich regions, which are more apparent in Figs. 3.4b and c due to higher SiC contents in the composites. Besides, there is a less bright region surrounding the dark center, as a core-shell structure. The core should be SiC-rich and the shell should be the inter-diffusion region between SiC and NFA. Since there are only very few SiC cores left, there are no SiC peaks in the XRD patterns (Fig. 3.3). Figs. 3.4d, 3.4e, and 3.4f show the surface images of the polished 5 vol% Cr_3C_2@SiC-95 vol% NFA, 15 vol% Cr_3C_2@SiC-85 vol% NFA, and 25 vol% Cr_3C_2@SiC-75 vol% NFA composites sintered at 950^{o}C, respectively. The surfaces for all the samples look rather dense. In the 5 vol% Cr_3C_2@SiC-95 vol% NFA composite (Fig. 3.4d), there is no contrast difference from different phases. For the 15 vol% Cr_3C_2@SiC-85 vol% NFA (Fig. 3.4e) and 25 vol% Cr_3C_2@SiC-75 vol% NFA (Fig. 3.4f) composites, the boundaries around the roundish microstructure features can be seen. However, the core-shell microstructures are not as visibly identified as for the 850^{o}C sintered composites in Figs. 3.4b and 3.4c. Moreover, the dark contrast of the roundish microstructures in the 25 vol% Cr_3C_2@SiC-75 vol% NFA composite (Fig. 3.4f) is much more obvious than those of the 15 vol% Cr_3C_2@SiC-85 vol% NFA composite (Fig. 3.4e). In comparison, the 950^{o}C sintered composites have more uniform microstructures compared to the 850^{o}C sintered composites. This is because the sintering temperature affects the SiC decomposition and the diffusion of Si in the NFA matrix. At 950^{o}C sintering temperature, the Si element diffuses more extensively and distributes more homogeneously in the NFA matrix.

Detailed backscattered SEM images for the 25 vol% Cr_3C_2@SiC-75 vol% NFA sample are shown in Fig. 3.5. The overall distribution of the SiC-rich regions with dark contrast can be observed in Fig. 3.5a, and the bright shell-like structures around the SiC rich regions are also observed. These microstructures are reminiscent of the core-shell structure in Figs. 3.4b and 3.4c. The core structure is from the SiC-rich region, and the shell structure is from the transition region, which is affected by the reactions between SiC and NFA as well as the Si diffusion to the NFA

matrix. On the edge of the shell structure, there is a much brighter layer, which is identified to be a Cr-rich region from the EDS measurement in Fig. 3.6. The microstructure near the NFA matrix boundary at a higher magnification is shown in Fig. 3.5b. The left side of the boundary is the NFA matrix, which consists of many small sized primary grains. On the boundary, a 4 μm thick narrow region with small-sized dark spots is found. On the right side of the boundary, the larger-sized dark spots distribute (Fig. 3.5c) in a bright phase, which is believed to have the same main elemental composition as the NFA matrix.

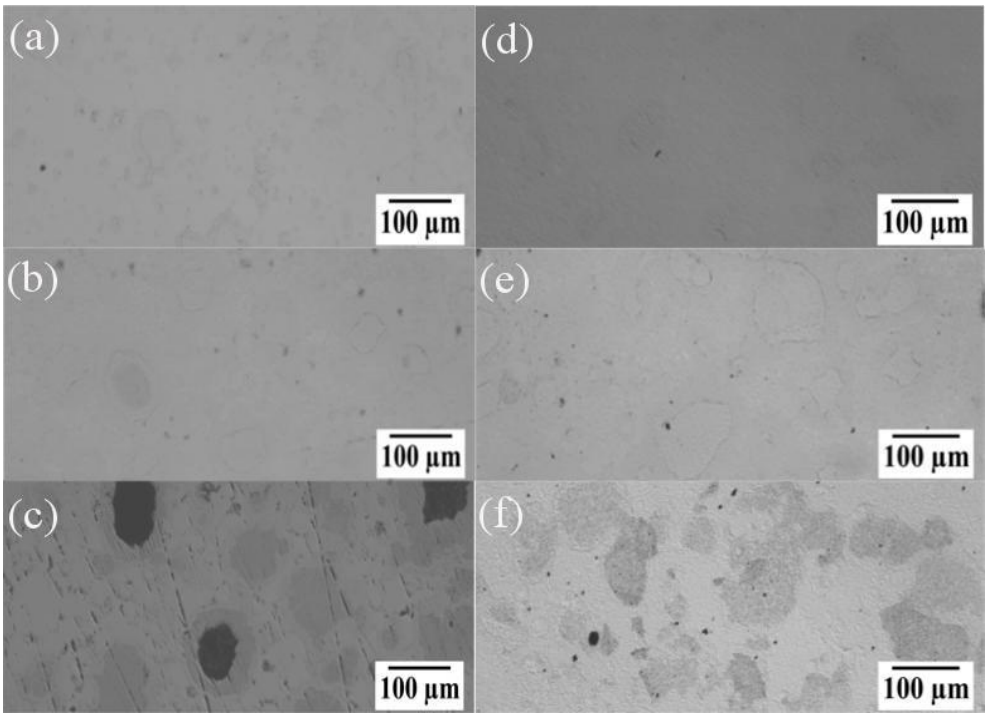

Fig. 3.4. Optical images of the polished Cr_3C_2@SiC-NFA composites sintered at 850°C and 950°C.

The elemental distributions around the NFA matrix boundary are shown in Fig. 3.6. On the boundary, the bright region is Cr-rich (Fig. 3.6c) but Fe- and Si-deficient (Figs. 3.6b and e). On the left side of the boundary, both Fe and Cr are rich as shown in Figs. 3.6b and 3.6c. Fig. 3.6e indicates that Si has diffused into the NFA matrix from the SiC-rich area. In the SiC-rich area, although Fe and Si elements are dominant as shown in Figs. 3.6b and e, Cr is clearly observed based on Fig. 3.6c, which partly derives from the Cr_3C_2 coating on SiC. Since the NFA matrix has

much lower melting point (~1500°C) than that of SiC (2700°C), during the SPS sintering under 100 MPa pressure, the Cr_3C_2 layer may be broken and the quick diffusion of NFA into the SiC-rich region could lead to the reactions between them. Finally, the bright contrast backbone with the black spots is formed as shown in Fig. 3.5c.

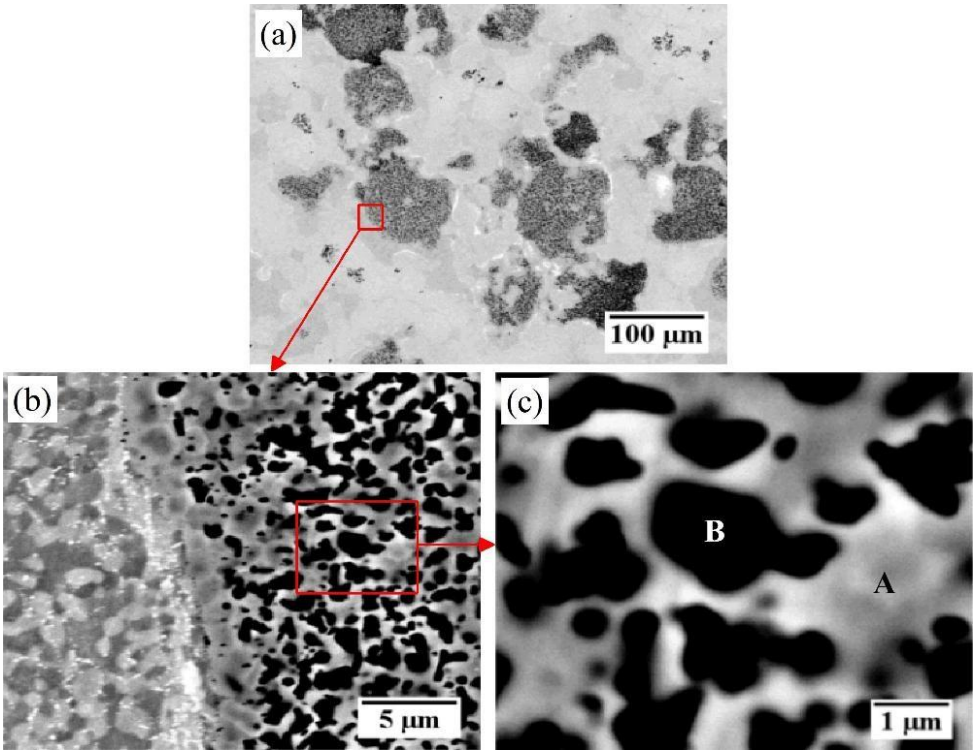

Fig. 3.5. Backscattered SEM images of the 25 vol% Cr_3C_2@SiC-75 vol% NFA sample sintered at 950°C.

Based on the above analysis, the SPS sintered Cr_3C_2@SiC-NFA composites show two regions, the intact NFA matrix region and the reaction region with discrete carbon-rich aggregates. Although there are no reaction phases observed in the XRD patterns as shown Fig. 3.3, the absence of SiC peaks confirms that the reactions have occurred. The decomposition of SiC leads to the diffusion of Si into the NFA matrix and the aggregation of carbon as demonstrated in Fig. 3.5c and Table 3.2. Fig. 3.7 shows the Si/Fe ratios in the NFA matrix and the reaction region (bright phase) for the 850°C and 950°C sintered samples. For the 850°C sintered samples in Fig. 3.7a, the

Si/Fe ratios in the NFA matrix stay constantly at ~0.010. This means that the diffusion of Si into the NFA matrix is relatively slow at 850^{o}C. However, in the reaction region, the Si/Fe ratios are high and increase with the SiC content in the composites. For the 5 vol% SiC sample, the Si/Fe ratio in the reaction region is 0.059, ~6 times higher than that of the NFA matrix. For the 25 vol% SiC sample, the Si/Fe ratio in the reaction region is 0.196, ~20 times higher than that of the NFA matrix. This means that the diffusion of Si in the bright phase of the reaction region can be easily affected by the SiC content in the composites at 850^{o}C. Meanwhile, the Si diffusion in the NFA matrix is restricted. For the 950^{o}C sintered samples in Fig. 3.7b, the Si/Fe ratios in the NFA matrix and the bright reaction region are different from those of the 850^{o}C sintered samples. In both regions, the Si/Fe ratios consistently increase with the SiC content. In the NFA matrix, the 5 vol% SiC sample has the Si/Fe ratio of 0.012, which is slightly higher than that of 850^{o}C sintered sample. With the SiC content increase, the Si/Fe ratios increase to 0.025 for the 15 vol% SiC sample and 0.080 for the 25 vol% SiC sample, respectively, which are 2-8 times higher than that of the 850^{o}C sintered samples. Thus, higher sintering temperature causes more intensive diffusion of Si into the NFA matrix. Similar to the 850^{o}C sintered samples, the Si/Fe ratios in the bright phase of the reaction region for the 950^{o}C sintered samples keep increasing from 0.077 to 0.121 and to 0.161 with the SiC contents. Meanwhile, the Si/Fe ratios are slightly lower than those of the 850^{o}C sintered sample as observed for the 15 vol% and 25 vol% SiC samples. Since more Si has diffused into the NFA matrix, it is reasonable that less Si is located in the reaction region.

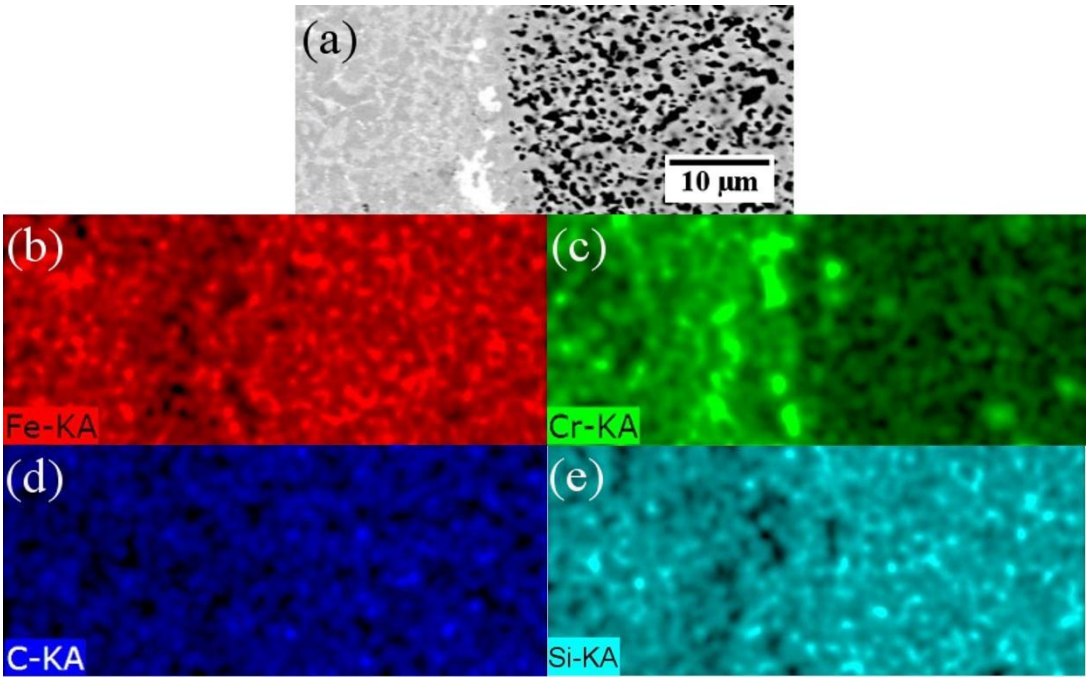

Fig. 3.6. Elemental distribution around the NFA grain boundary for the 950ºC sintered 25 vol% Cr_3C_2@SiC-75% vol% NFA sample.

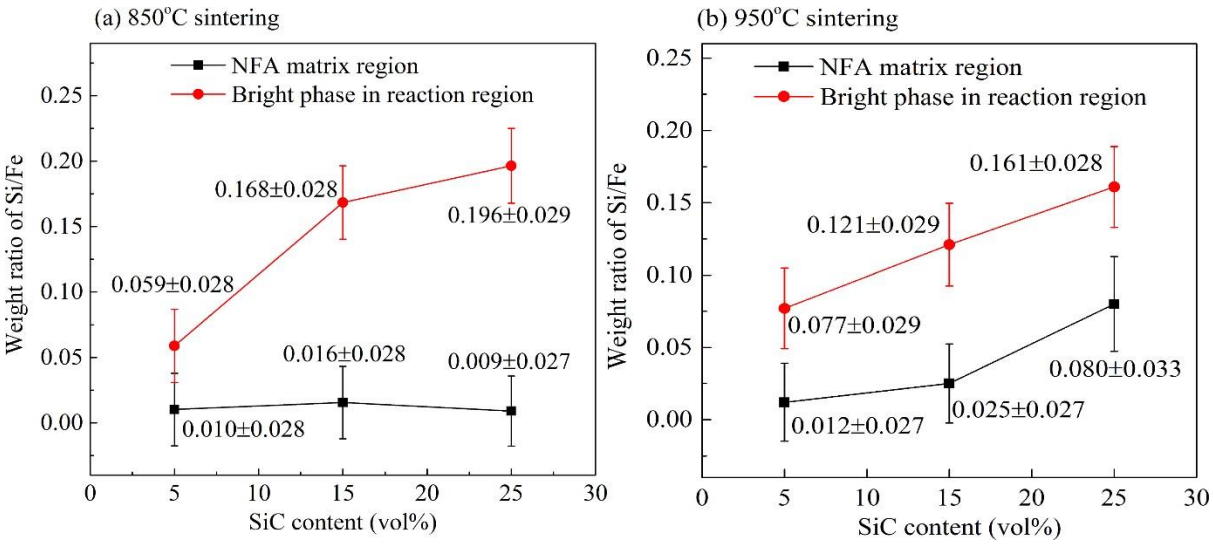

Fig. 3.7. Si/Fe ratios in the NFA matrix region and reaction region for 850ºC (a) and 950ºC (b) sintered composites.

3.5. Conclusions

In this study, a Cr_3C_2 coating is introduced as a reaction barrier layer to fabricate novel Cr_3C_2@SiC-NFA composites. The composites with various SiC contents consolidated under SPS sintering have much improved microstructures compared to that of the composite without the coating barrier. At 850^{o}C, the densification and hardness of the composites benefit from the increase of the SiC content. At 950^{o}C, the densification is enhanced by more SiC content, while the hardness is compromised slightly. The Cr_3C_2@SiC-NFA composites maintain the main phase of BCC α-Fe and have a hardness of 5-6 GPa. The increase of the SiC content leads to the decrease of the lattice constant and also hinders the Fe α→γ phase transformation. The Si element from the decomposition of SiC diffuses into the NFA matrix, while the C aggregates due to its low solubility in NFA. The Si/Fe ratios in the NFA matrix and reaction region are dependent on both the sintering temperature and the SiC content in the composites. The as-sintered Cr_3C_2@SiC-NFA composites are expected to have promising cladding applications for nuclear reactors.

Chapter 4

Microstructure Evolution for Nanostructured Ferritic Alloy with and without Chromium Carbide Coated SiC at High Temperatures

4.1. Abstract

This work focuses on fundamental understanding of microstructure evolution of nanostructured ferritic alloy (NFA) and 25 vol% Cr_3C_2 coated SiC(Cr_3C_2@SiC)-NFA composite during spark plasma sintering at 950°C and the following thermal treatment at 1000°C. A unique bi-phase microstructure with distinct Cr-rich and Si-rich phases has been observed for the 25 vol% Cr_3C_2@SiC-NFA composite, while for the NFA sample, the traditional large grain microstructure remains. Grain sizes are significantly smaller for the 25 vol% Cr_3C_2@SiC-NFA composite compared to those for the pure NFA, which can be attributed to the presence of grain boundary phases in the composite sample. During the thermal treatment, microstructure features can be directly correlated with the dissolution kinetics and phase diagrams calculated using Thermo-Calc/DICTRA/PRISMA®.

4.2. Introduction

Spark plasma sintered NFA and SiC-NFA composites with and without reaction barriers (Cr_3C_2 and carbon) were explored in our previous research [110, 125-127] for nuclear reactor claddings. A Cr_3C_2 coating on SiC particles (Cr_3C_2@SiC) and a carbon coating on NFA (C@NFA) particles were created in order to suppress the formation of detrimental reaction products such as iron silicides (Fe_3Si, FeSi) [126, 127]. Our earlier work reported density, hardness, and preliminary microstructural characterization of spark plasma sintered (SPS) Cr_3C_2@SiC-NFA composites with various Cr_3C_2@SiC volume fractions. These composites showed excellent mechanical and high temperature oxidation and irradiation properties [127-129]. With combined properties of NFA and

SiC, they can serve as a promising candidate for fuel cladding to replace existing zirconium based alloys.

This chapter reports detailed microstructural characterization and comparison of the pure NFA and Cr_3C_2@SiC-NFA composite after the SPS sintering. Microstructural evolution during prolonged thermal treatment at 1000^{o}C is also discussed. Phase evolution and precipitate formation are evaluated using Thermo-Calc/DICTRA/PRISMA simulations.

4.3. Materials and Methods

The NFA powder was prepared using high energy ball milling of a ferritic steel powder (Fe-9Cr-2W-0.4Ti-0.2V-0.18C) with 0.3 wt% Y_2O_3 in an argon atmosphere (average size ~15 μm, ball milling was performed at Oak Ridge National Laboratory). SiC particles (Grade UF-15, α-SiC, ~1.25 μm average size, H.C. Starck, Karlsruhe, Germany) were coated with Cr_3C_2 using a melt salt method followed by reduction treatment at high temperatures. The NFA and 25 vol% Cr_3C_2@SiC powder were mixed and densified using spark plasma sintering (SPS) at 950^{o}C with a heating/cooling rate of 50^{o}C/min, applied pressure of 100 MPa, and holding time of 10 minutes. Detailed procedures of creating the Cr_3C_2 coating on SiC and sintering the pure NFA and Cr_3C_2@SiC-NFA composite are reported in previous chapter.

The SPS densified NFA and 25 vol% Cr_3C_2@SiC-NFA composite were treated at 1000^{o}C in an argon atmosphere for 50 hours. The thermal treatment was performed in a tube furnace (1730-20 HT Furnace, CM Furnace Inc., Bloomfield, NJ) with a gas flow of ~1.2 $L \cdot min^{-1}$ at 1 atm pressure.

Microstructures were analyzed using scanning electron microscopy in the backscattered mode (FEG E-SEM QUANTA600, FEI Company, Hillsboro, OR, USA) and the compositions were analyzed using energy dispersive spectroscopy (Bruker EDS). An electron backscatter diffraction detector (TSL/EDAX/EBSD attached to a focused ion beam microscope (FIB), Helios Nanolab, FEI Company, Hillsboro, OR, USA) was used to characterize grain size and grain size distribution. The EBSD measurements were performed using a 20 kV beam (probe current = 11 nA) with a 70^o tilt angle to the horizontal axis. The EDAX Team software was used to collect data

and the OIM analysis software was used for post processing and data analysis without the problem of interconnecting grains from participates. EBSD maps were cleaned using grain dilation routing with default parameters (grain tolerance angle ~5^{o} and minimum grain size ~2 pixels).

STEM-EDS analysis was performed using scanning transmission electron microscopy (JEOL 2100 attached with an EDS detector). The samples for the STEM-EDS analysis were obtained by cutting a thin sample section (~400 μm) using a Beuhler Isomet low speed saw. The section was then gently polished with diamond papers (~1 μm size) up to ~60 μm thickness. Final thinning was carried out using a Fischione 1010 low angle ion mill under a 3 kV argon ion beam, a 5 mA current, and a 12^{o} incident angle. The JEOL TEM was also used to acquire electron diffraction patterns from various phases. CrystalMaker and CrysTBox software were used for phase identification based on diffraction pattern analysis.

ThermoCalc® software was used to calculate the phase diagram of the NFA and SiC system. The Si and C elements were simultaneously varied in the same amount in the NFA alloy to mimic addition of SiC. The DICTRA module in ThermoCalc was used to simulate the dissolution of spherical SiC particles in NFA at the sintering temperature of 950^{o}C. Diffusion profiles of important elements (Fe, Cr, Si, and C) were plotted against the distance from the SiC-NFA interface to estimate the amount of SiC dissolution. Finally, the formation of new precipitates and their sizes after sintering and thermal treatment were estimated using TTT diagram and PRISMA module in ThermoCalc. The Y and O elements were not considered for simulation because Y-rich nanoclusters should have formed much before dissolution of Cr_3C_2@SiC in NFA owing to supersaturation (of Y and O in NFA) during mechanical alloying itself. Since SiC dissolved into the NFA very fast (as to be shown later in Fig. 4.7) and the amount was much higher (25 vol%) than the Y_2O_3 content (0.3 wt%), the impact of the Y_2O_3 nanoclusters in the SiC dissolution was ignored. TCFE9 and MOBFE4 databases were used for all these calculations.

4.4. Results and discussion

4.4.1. Microstructural evolution during spark plasma sintering

Fig. 4.1 shows the SEM micrographs of the spark plasma sintered NFA and 25 vol% Cr_3C_2@SiC-NFA samples. The NFA sample shows mainly equiaxed grains along with some pores at the grain boundaries; there are no visible secondary phases, as indicated in Fig. 4.1a. The microstructure of the 25 vol% Cr_3C_2@SiC-NFA sample shows fine light gray precipitates (P1) in a dark gray matrix as shown in Fig. 4.1b. The precipitates (P1) form interconnected structures, possibly due to their large volume fraction and coalescence of adjacent growing precipitates during the spark plasma sintering process. Very fine and bright precipitates (P2) can also be seen throughout the microstructure (Fig. 4.1b). The dark phase (pointed out by the green arrow) in Fig. 4.1b is a graphite precipitate as identified in previous chapter. The P1 and P2 precipitates are identified as M_7C_3 and MC type carbides and will be discussed in detail in Chapter 4. All these precipitates, P1, P2, and graphite, are a result of reactions between the NFA and Cr_3C_2@SiC particles during the spark plasma sintering, as to be discussed in Chapter 4. It should be mentioned that Y-Ti-O-rich precipitates (or clusters) are present in the NFA and 25 vol% Cr_3C_2@SiC-NFA samples. However, they are too fine to be visible in these images. Previous research on various ODS/NFA alloys have shown that very fine (2-4 nm) Y-rich nanoclusters (such as Y-Ti-O) are only visible from high magnification TEM images with certain imaging conditions or using atom probe tomography. Examples are the work of Massey et al. [130], which showed no oxide clusters under TEM and EDS but the opposite through atom probe tomography, as well as Kishimoto et al.'s [131] work on 14CrYWTi alloy, which showed no oxide clusters in a low magnification bright field TEM image, but with dark field imaging under high magnification showed the presence of the nanoclusters. Since Y-Ti-O nanoclusters are not the focus of this study, these experiments were not performed. Previous research on the same NFA alloy has reported the presence of 2-4 nm Y-Ti-O nanoclusters with a high number density (~10^{24} m^{-3}). Recent work on spark plasma sintered 9Cr [132] and 14Cr [63, 133] ODS alloys have reported fine Y-Ti-O nanoclusters in the microstructures. It is fair to assume that both NFA and Cr_3C_2@SiC-NFA composites reported here

contain fine Y-Ti-O nanoclusters. In addition, extensive studies on the functions of these clusters have been carried out before [59, 134] and will not be discussed here.

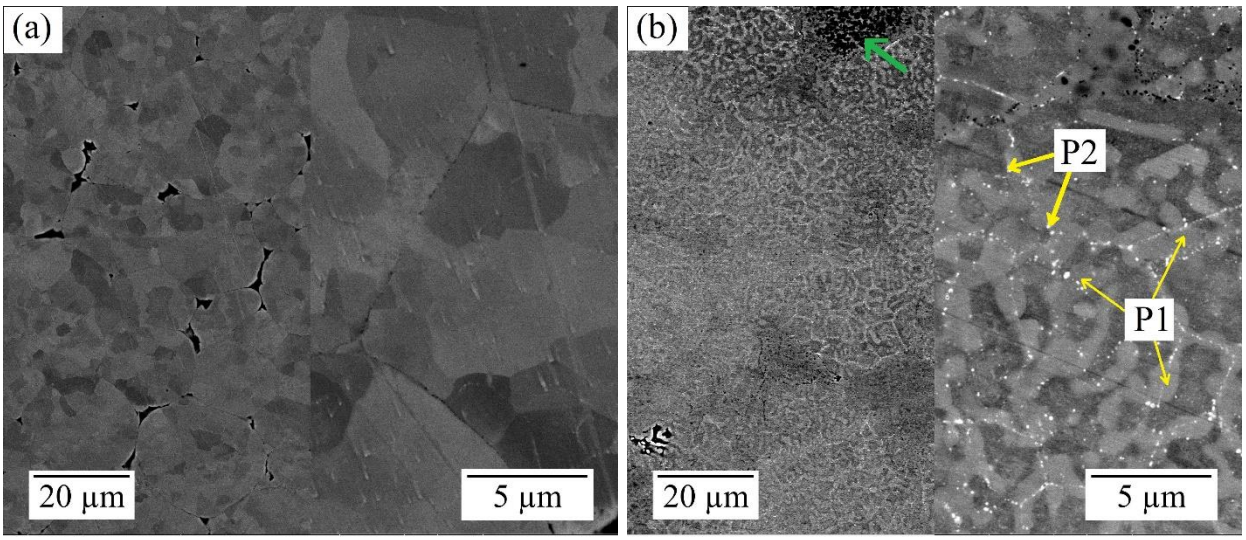

Fig. 4.1. SEM micrographs of (a) NFA and (b) 25 vol% Cr_3C_2@SiC-NFA composite after the SPS sintering (the right side is the magnified image of the left side for each sample).

Fig. 4.2a shows the EBSD inverse pole figure (IPF) map of the SPS sintered NFA specimen. The grain size is on average ~15 μm but the microstructure has a mixture of very large grains (~45 μm) and plenty of small grains (4-5 μm). Such a bimodal grain size distribution has been previously observed in various SPS sintered ODS alloys [132, 135-142]. The behavior is attributed to variations in dislocation density and heterogeneous distribution of Y-Ti-O nanoclusters, which create heterogeneous grain boundary pinning effects and also local variations in heat distribution due to the joule heating effect during the SPS process [136, 141, 143]. The IPF map in Fig. 4.2a shows no preferential grain orientation and almost fully recrystallized grains with no remnants of dendritic microstructures from the starting powder. Figs. 4.2b and 4.2c show the IPF maps of α-ferrite and M_7C_3 grains of the 25 vol% Cr_3C_2@SiC-NFA composite respectively. There is no preferential grain orientation for the α-ferrite grains. The size of the α-ferrite grains is much smaller (~3 μm) compared to that of the NFA sample (~15 μm). The overall smaller size grains in the 25 vol% Cr_3C_2@SiC-NFA composite can be attributed to the strong pinning effect

due to the significant precipitation of the P1 and P2 phases as a result of the reactions between NFA and Cr_3C_2@SiC during the spark plasma sintering. Fig. 4.2c shows that the interconnected worm-like structure of the M_7C_3 (or P1) precipitates consists of small (1-1.5 μm) sized equiaxed grains with no preferential orientation. Fig. 4.2d shows the EBSD phase map of the 25 vol% Cr_3C_2@SiC-NFA composite with the α-ferrite and M_7C_3 phases. The shape and size of the α-ferrite and M_7C_3 phases correspond well with the dark gray and light gray regions in the SEM image as shown in Fig. 4.1b respectively.

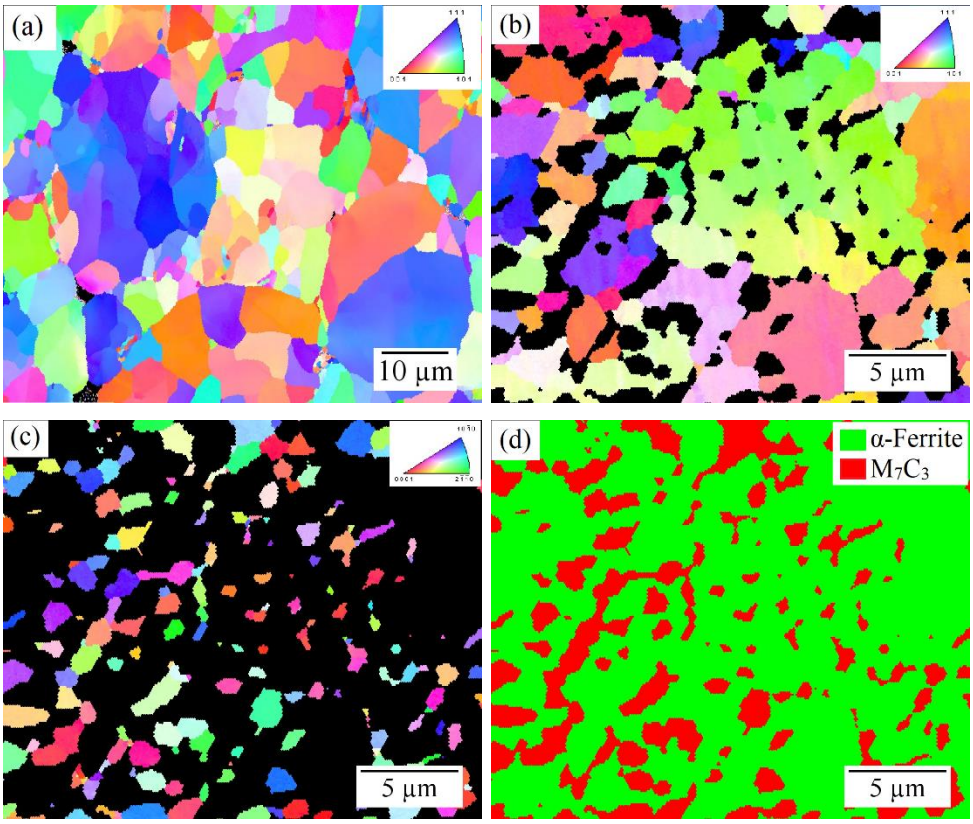

Fig. 4.2. (a) IPF map of the NFA sample; IPF maps of (b) α-ferrite grains and (c) M_7C_3 grains, and (d) phase map of the 25 vol% Cr_3C_2@NFA-SiC composite after the SPS sintering.

4.4.2. Effect of thermal treatment on microstructures

Fig. 4.3 shows the microstructures of the NFA and 25 vol% Cr_3C_2@SiC-NFA composite after the thermal treatment at 1000ºC for 50 hours. The NFA sample (Fig. 4.3a) shows equiaxed grains, similar to those observed before the thermal treatment (Fig. 4.1a). The 25 vol% Cr_3C_2@SiC-NFA composite after the treatment (Fig. 4.3b) shows dark gray NFA (ferrite) grains, light gray P1 precipitate, and fine bright P2 precipitate, similar to those before the thermal treatment (Fig. 4.1b). The major change is the grain sizes. Fig. 4.4 shows the size and volume fraction of the precipitates (P1, P2) before and after the 1000ºC treatment measured using ImageJ software (grey scale method was used for volume fraction measurement). The sizes of the P1 and P2 precipitates show 110% and 108% increases, respectively, after the thermal treatment at 1000ºC. The volume fractions of the P1 and P2 precipitates show 37.5% and 75% increases respectively. Therefore, the thermal treatment at 1000ºC has resulted in significant coarsening and potentially more nucleation of the existing precipitates (P1 and P2). In both cases, the amount of the P2 phase (MC) is significantly less than that of the P1 phase (M_7C_3).

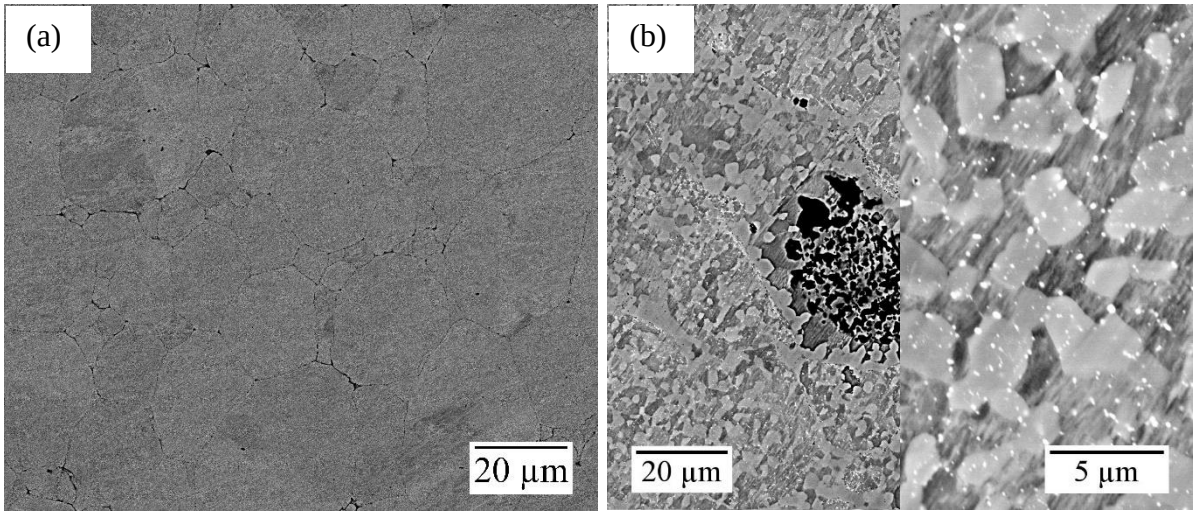

Fig. 4.3. SEM micrographs of (a) NFA and (b) 25 vol% Cr_3C_2@SiC-NFA composite after the thermal treatment at 1000ºC for 50 hours (the right part is the magnified image of the left part).

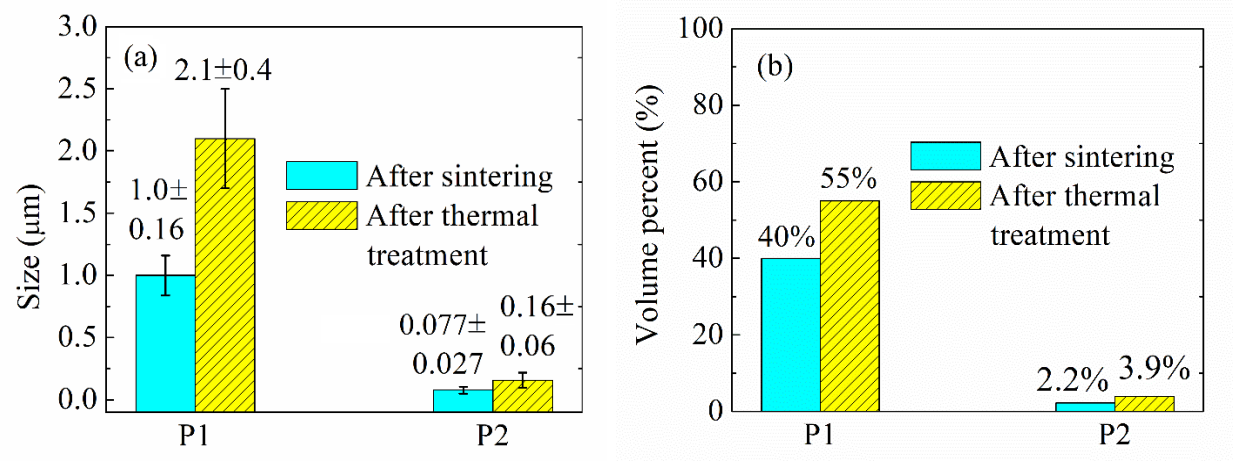

Fig. 4.4. (a) Size and (b) volume fraction of P1 and P2 precipitates before and after the 1000ºC thermal treatment for 50 hours.

Fig. 4.5 shows the STEM bright field images of the 25 vol% Cr_3C_2@SiC-NFA composite after the thermal treatment at 1000ºC for 50 hours. The bright region is Fe-rich (Fig. 4.5b). This phase is similar to the dark grey NFA grains in the corresponding SEM images (Figs. 4.1b and 3b). The dark region in Fig. 4.5 can be correlated with the P1 precipitate in the SEM images in Figs. 4.1b and 4.3b. The diffraction patterns corresponding to the bright region (NFA) and dark region (P1) in Fig. 4.5 are shown in Figs. 4.6a and 4.6b respectively. The patterns are indexed by comparing with the simulated patterns from the CrysTBox and CrystalMaker^{TM} software and Figs. 4.6a and 4.6b are consistent with standard NFA and M_7C_3 crystallographic files (.cif files available on the Crystallography Open Database (COD) website). The NFA region has been indexed as an α-ferrite phase, while the P1 phase is identified as a M_7C_3 phase, which is consistent with the EBSD results from Fig. 4.2c. The EDS mappings in Figs. 4.5a and 4.5b show that the M_7C_3 phase is rich in both Fe and Cr. Therefore, the composition of the P1 precipitates should be $(Fe,Cr)_7C_3$.

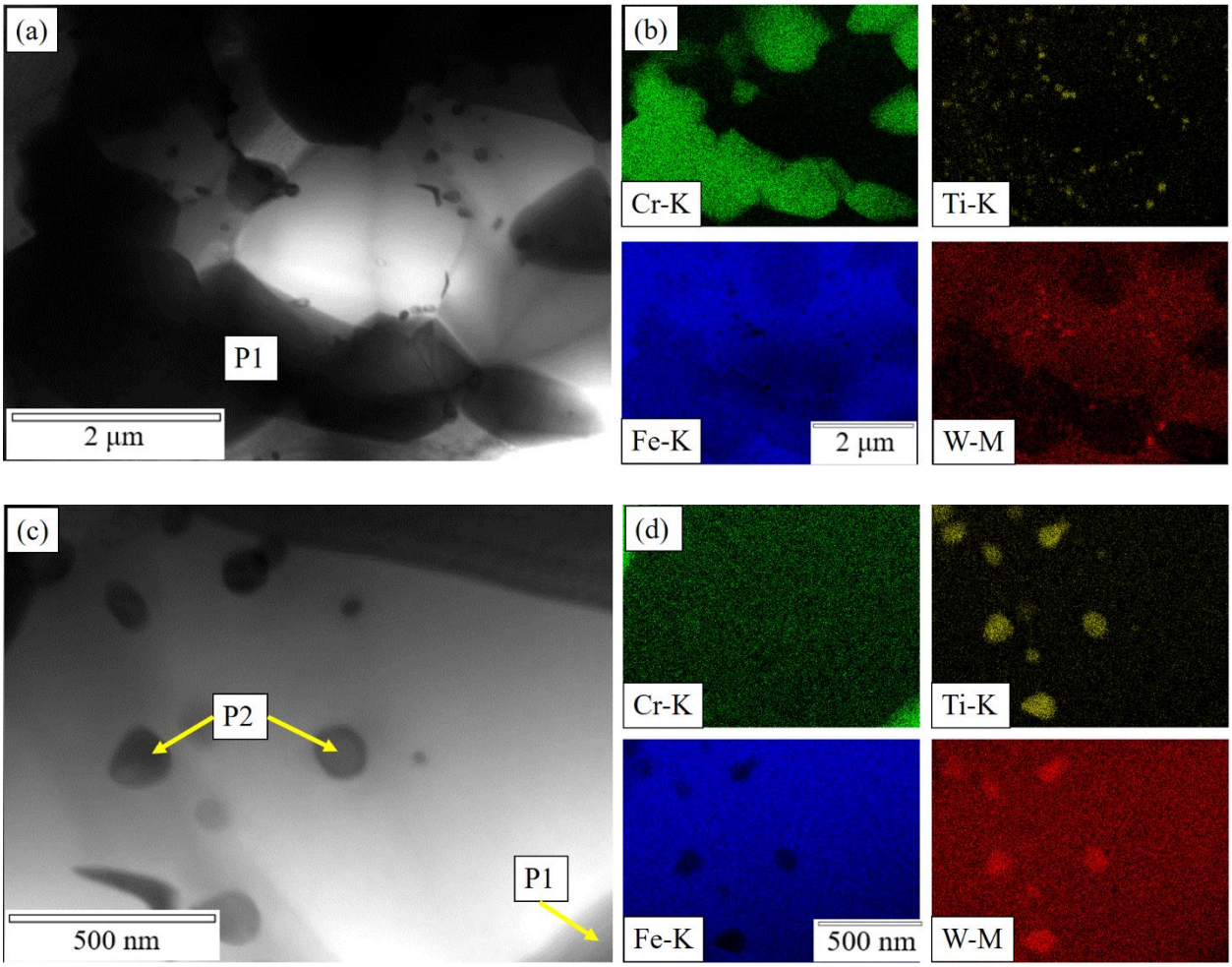

Fig. 4.5. STEM-BF images (a, c) with corresponding EDS mappings (b, d) for the Cr_3C_2@SiC-NFA composite after the 1000°C treatment for 50 hours.

Some fine precipitates can be observed in both the bright and dark regions as shown in Figs. 4.5a and 4.5b. This phase is made up of the bright fine precipitates (P2) observed in Figs. 4.1b and 4.3b. The EDS analysis shows Ti- and W-enrichment in these precipitates. The W-enrichment explains the bright contrast in the SEM images (Figs. 4.1b and 4.3b). These precipitates are believed to be (Ti,W)C, i.e. MC type carbides [144]. It should be mentioned that the presence of the M_7C_3 and MC carbide phases has been previously reported for various ODS and ferritic alloys [144-147]. STEM images in Fig. 4.5 is at low magnification.

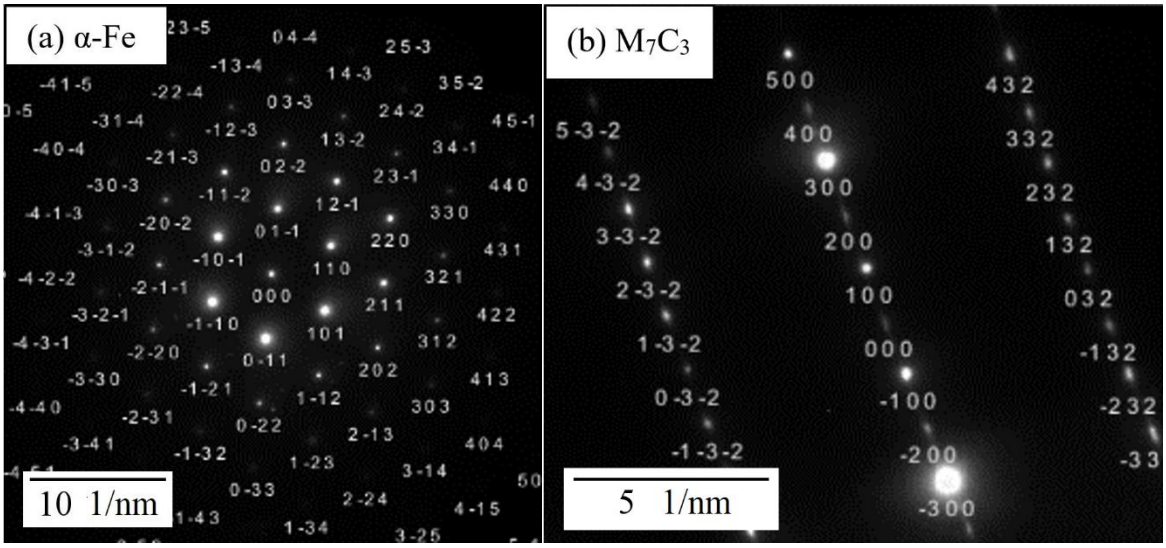

Fig. 4.6. (a) Diffraction pattern from the bright area, (b) diffraction pattern from the dark area (P1) in Fig. 5a.

4.4.3. Fundamental understanding of microstructural evolution

Fig. 4.1b shows that the spark plasma sintering process has resulted in complete dissolution of the Cr_3C_2@SiC powder and formation of new phases such as $(Fe,Cr)_7C_3$, (Ti,W)C, and graphite. The reactions between SiC and NFA after the coating dissolution can be divided into two steps. The first step is dissociation of SiC into Si and C, according to Eq. (4.1). The dissociated Si and C atoms diffuse into NFA, thus forming Si- and C-containing supersaturated NFA. This supersaturated NFA then leads to the precipitation of graphite, M_7C_3, and MC phases as shown in Fig. 4.1b.

$$SiC \rightarrow Si_{NFA} + C_{NFA} \tag{4.1}$$

The dissolution kinetics of SiC has been studied using the DICTRA® software package as shown in Fig. 4.7. Within only 400 seconds, a significant amount of SiC region has dissolved (~4.3 μm thick) in the NFA at 950°C. This behavior is driven by the high diffusivities (2.37×10^{-13} m^2/s and 1.31×10^{-10} m^2/s) of Si and C respectively in the α-ferrite matrix. Since the original SiC particle size was around 1-2 μm, all the SiC particles should have dissolved in the NFA matrix. Therefore,

it can be assumed that supersaturated NFA with homogeneous Si and C compositions has formed at a sintering temperature of 950ºC according to Eq. (4.1). Figs. 4.8a-4.8d show diffusion behaviors of important elements (Fe, Cr, Si, and C respectively) in this system. Diffusion behavior of Si and C in Figs. 4.8b and 4.8d clearly shows significant penetration inside the NFA matrix after SiC dissolution (around ~20 μm for Si and ~60 μm for C).

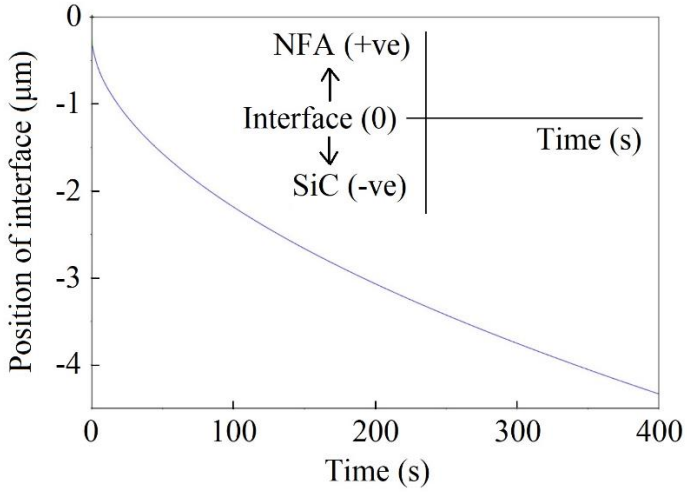

Fig. 4.7. Dissolution kinetics of SiC in the NFA matrix at a sintering temperature of 950ºC.

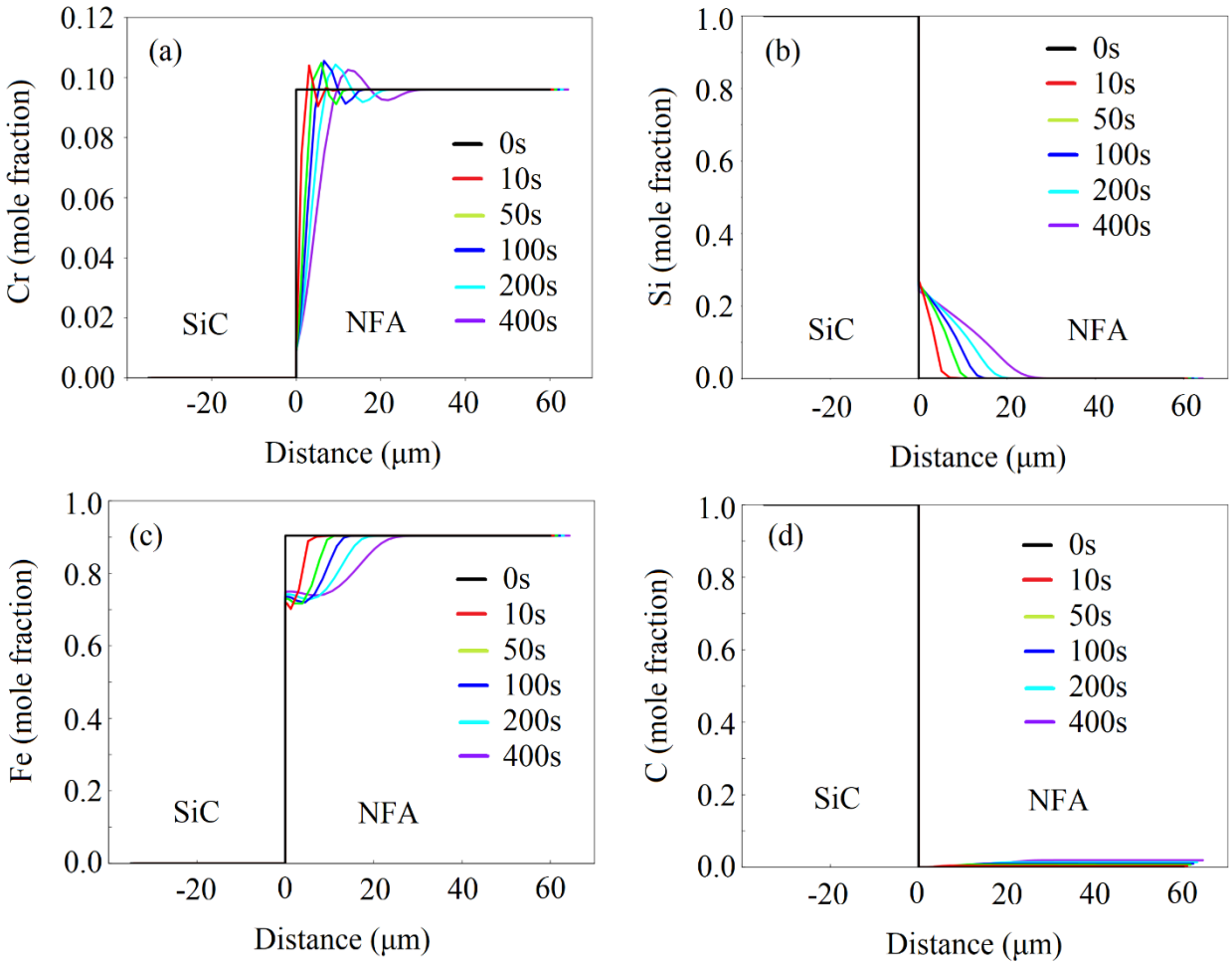

Fig. 4.8. Diffusion behaviors of (a) Cr, (b) Si, (c) Fe, and (d) C based on the ThermoCalc-DICTRA simulations during sintering at 950°C.

The second step involves formation of equilibrium phases from the newly homogenized composition. This leads to the precipitation of graphite, $(Fe,Cr)_7C_3$, and (Ti,W)C phases according to the reaction in Eq. (4.2). The phase diagram of the Cr_3C_2@SiC-NFA composite in Fig. 4.9 confirms the formation of these phases. The precipitation of the secondary phases from the supersaturated NFA can be visualized using the phase diagram in Fig. 4.9 and the TTT diagram in Fig. 4.10. It shows the presence of NFA (α-ferrite with dissolved Si), graphite, and carbides $(Fe,Cr)_7C_3$ and (Ti,W)C. This observation correlates well with the results from our previous work where Si dissolved α-ferrite and graphite were observed using SEM-EDS [127]. The phase diagram was constructed using the ThermoCalc console mode, where the Cr_3C_2@SiC content in

the NFA was varied rather than only varying a single element. The TTT diagram in Fig. 4.10 shows that all the precipitates form almost instantaneously ($<10^{-2}$ s) at 950°C (during the sintering) as well as during the thermal treatment at 1000°C.

$$\text{NFA (supersaturated with Si and C)} \rightarrow \text{NFA (Si)} + (\text{Fe, Cr})_7\text{C}_3 + (\text{Ti, W})\text{C} + \text{C} \qquad (4.2)$$

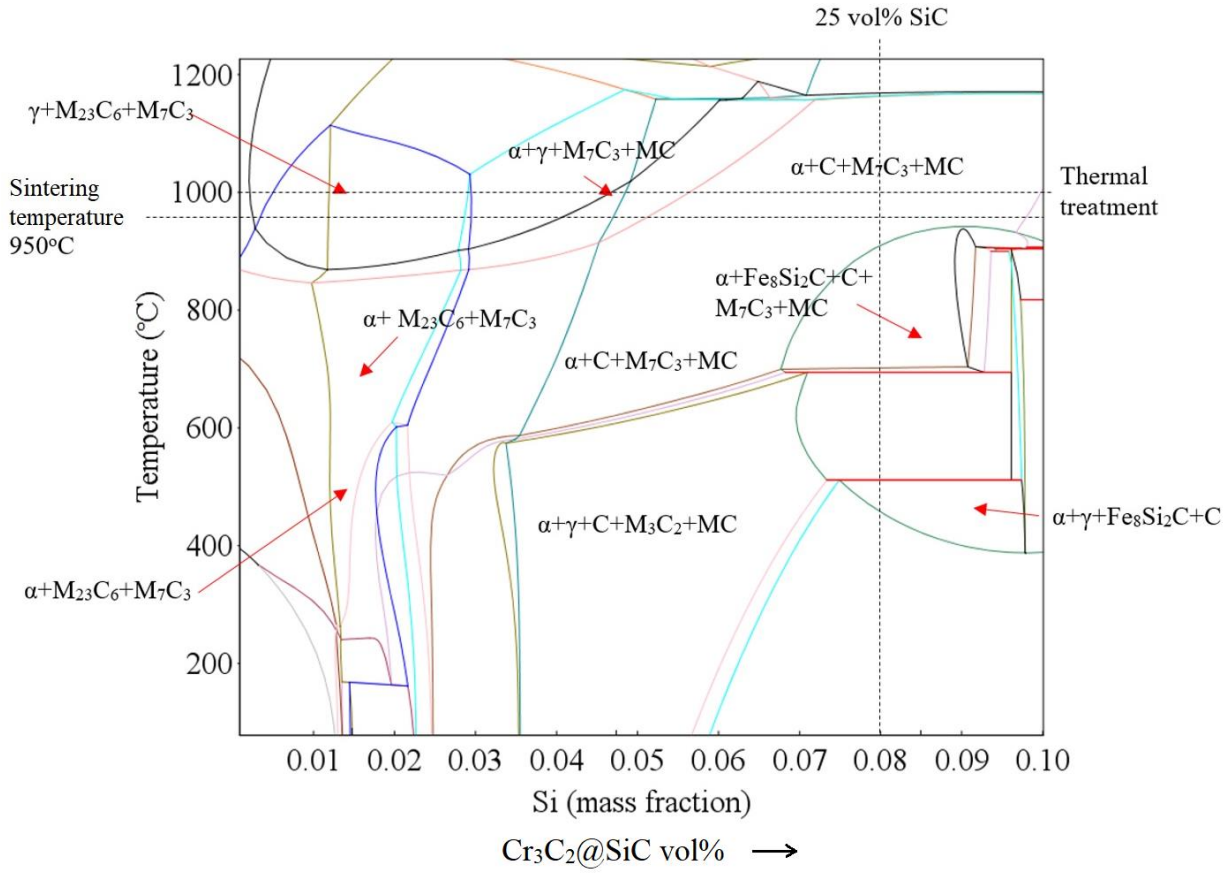

Fig. 4.9. Phase diagram of the Cr_3C_2@SiC-NFA system.

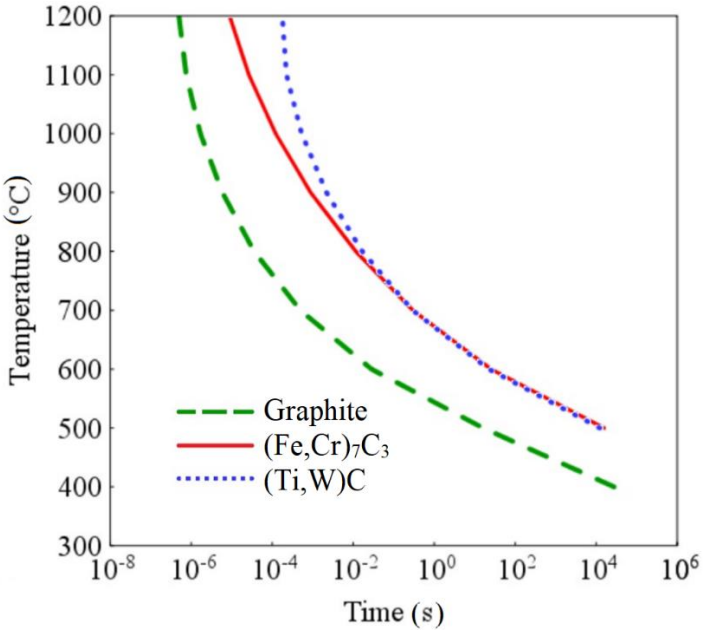

Fig. 4.10. TTT diagram of graphite, $(Fe,Cr)_7C_3$, and (Ti,W)C phases for the 25 vol% Cr_3C_2@SiC-NFA composite.

In Fig. 4.4, both the size and volume fraction of the M_7C_3 and MC type precipitates increase after the 1000°C thermal treatment. This means that the thermal treatment has resulted in coarsening of the precipitates formed during the SPS sintering along with potential nucleation of new $(Fe,Cr)_7C_3$ and (Ti,W)C type precipitates based on the TTT diagram in Fig. 4.10. Precipitation simulations were carried out at 1000°C using the PRISMA module of the ThermoCalc software to estimate the size of the M_7C_3 and MC carbides after the thermal treatment. The simulated sizes of the $(Fe,Cr)_7C_3$ and (Ti,W)C type carbides match reasonably well with the experimental results as shown in Fig. 4.11. Fig. 4.12a and 4.12b shows SEM micrographs of Cr_3C_2@SiC-NFA composites after thermal treatment at 1000°C for 25 and 75 hours respectively. The precipitate sizes after 25 and 75-hour treatment are also plotted in Fig. 4.11. However, the estimated sizes of the $(Fe,Cr)_7C_3$ and (Ti,W)C type precipitates before the thermal treatment (or after sintering) are much smaller than the actual sizes in Fig. 4.4. This means local overheating and enhanced diffusion under the electric current in the SPS sintering must have accelerated the nucleation and growth of these precipitates, since the ThermoCalc software cannot consider the electric field effect. This process can be visualized using enhanced mass transport from an electromigration theory in Eq. (4.3).

$$J_i = -\frac{D_i C_i}{RT}\left[\frac{RT\ \partial\, ln\, C_i}{\partial x} + Fz^* E\right] \tag{4.3}$$

where J_i is the flux of the diffusing species i, D_i is the diffusivity of the species, C_i is the concentration of the species, F is Faraday's constant, z^* is the effective charge on the diffusing species, E is the field, R is the gas constant, and T is temperature [148].

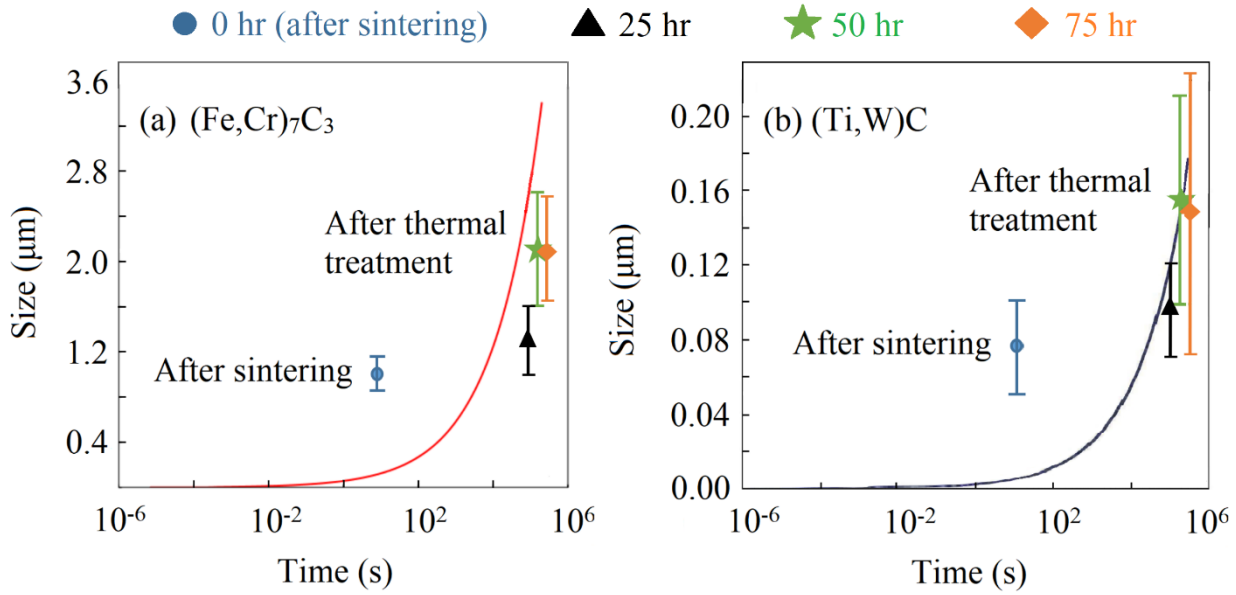

Fig. 4.11. ThermoCalc PRISMA simulations of the size of (a) $(Fe,Cr)_7C_3$ and (b) (Ti,W)C precipitates and the corresponding experimental values after the sintering and thermal treatment (Data points with error bars show experimental values, which are also reported in Fig. 4.4a; curve plots show simulation results.

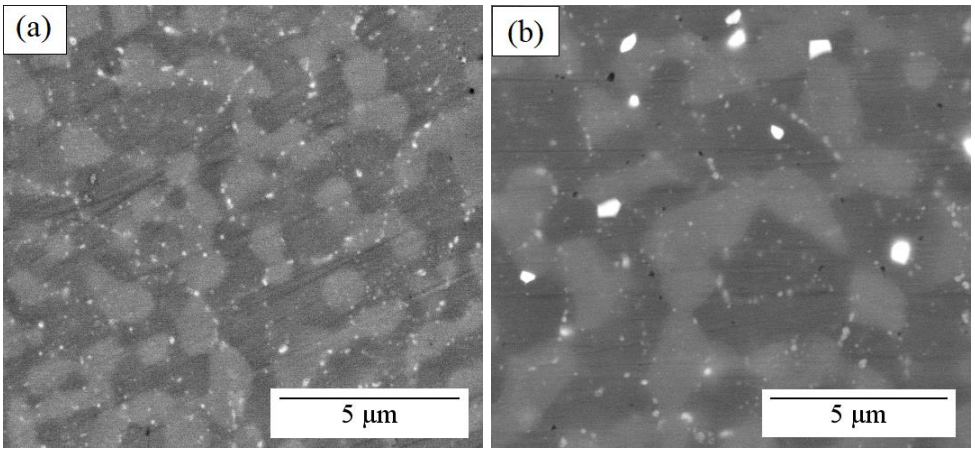

Fig. 4.12. SEM micrographs of Cr_3C_2@SiC-NFA composites after thermal treatment at 1000°C for (1) 25 hours and (b) 75 hours.

Coarsening of the $(Fe,Cr)_7C_3$ and (Ti,W)C precipitates can be visualized based on the Ostwald ripening equation:

$$r^3 - r_o^3 = \frac{8\gamma c \upsilon^2 D}{9RT} t = kt \tag{4.4}$$

Where r and r_o are the radii of the precipitate before and after the thermal treatment respectively. γ is surface energy, c is the solubility of the precipitate, D is the diffusivity of the precipitate, R is gas constant, T is temperature, ν is the molar volume of the precipitate, t is time, and k is coarsening rate coefficient.

For the $(Fe,Cr)_7C_3$ and (Ti,W)C precipitates, the coarsening rate coefficient k can be calculated using the ThermoCalc-DICTRA module as shown in Fig. 4.13. The estimated sizes of the $(Fe,Cr)_7C_3$ precipitates after the 1000°C treatment for 25, 50 and 75 hours are 1.19 μm, 1.33 μm, and 1.44 μm, while experimental values are 1.3±0.3 μm, 2.1±0.4 μm, and 2.2±0.5 μm respectively. Similarly, the estimated sizes of the (Ti,W)C precipitates after the 1000°C treatment for 25, 50 and 75 hours are 0.147 μm, 0.181 μm, and 0.205 μm, while experimental values are 0.095±0.03 μm, 0.16±0.5 μm, and 0.15±0.08 μm respectively. The simulated sizes of both $(Fe,Cr)_7C_3$ and (Ti,W)C precipitates are reasonable close to size range observed during experiments.

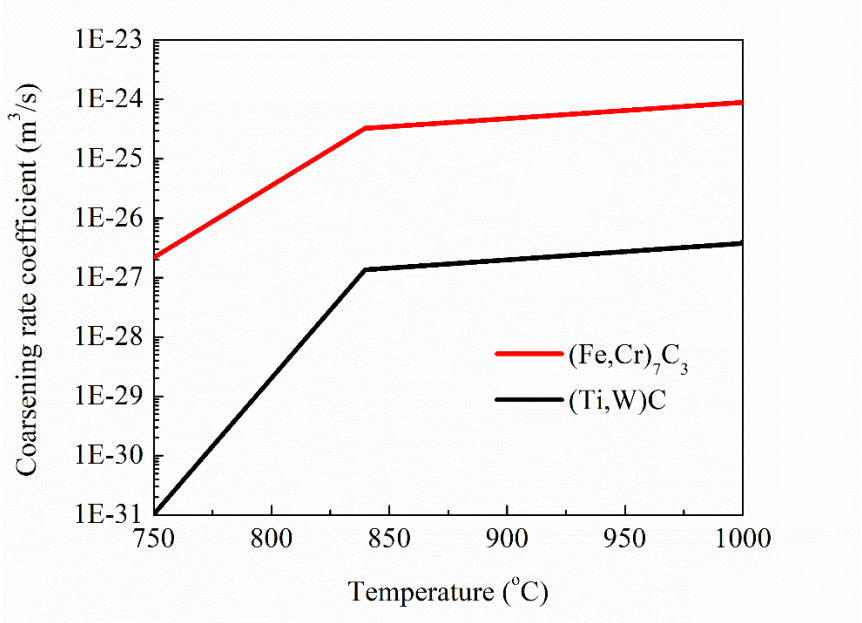

Fig. 4.13. ThermoCalc DICTRA simulations of the coarsening rate coefficient of the $(Fe,Cr)_7C_3$ and (Ti,W)C precipitates.

4.5. Conclusions

Microstructural evolutions of spark plasma sintered NFA and 25 vol% Cr_3C_2@SiC-NFA composite before and after the thermal treatment at 1000°C for 50 hours were studied. The grain sizes for the 25 vol% Cr_3C_2@SiC-NFA composites are far smaller than those for the NFA sample (2 μm vs. 12 μm). The 25 vol% Cr_3C_2@SiC-NFA composite shows a large amount of $(Fe,Cr)_7C_3$ and (Ti,W)C carbides in the microstructure along with the α-ferrite (NFA) matrix. The precipitates $(Fe,Cr)_7C_3$ and (Ti,W)C show considerable increase in size and volume fraction after the 1000°C thermal treatment. The microstructural evolution of the 25 vol% Cr_3C_2@SiC-NFA composite during the SPS sintering and after the thermal treatment was explained using the ThermoCalc phase diagram and diffusion/precipitation simulations. The coarsening rate of the precipitates ($(Fe,Cr)_7C_3$ and (Ti,W)C) calculated using the ThermoCalc DICTRA module matches well with the experimental results.

Chapter 5

High Temperature Oxidation Behavior of Silicon Carbide – Carbon Coated Nanostructured Ferritic Alloy Composites in Air+Water Vapor Environment

5.1. Abstract

Oxidation behavior of silicon carbide (SiC) - carbon coated nanostructured ferritic alloy (C@NFA) composites was investigated in an air+45 vol% H_2O atmosphere at 500-1000^oC. All the composites show an oxidation structure with an outer Fe-rich layer and an inner Cr-rich layer, as well as internal oxidation along grain boundaries. Oxidation resistance increases with SiC addition. The corresponding fundamental mechanism is proposed. The improved oxidation resistance for the higher SiC content composites is attributed to a delay in 'breakaway oxidation' due to improved kinetics for the formation of dense Cr_2O_3 and SiO_2 protective layers.

5.2. Introduction

Fuel cladding materials experience harsh oxidation conditions in water vapor containing nuclear environments [55, 149, 150]. High temperature oxidation resistance is critical to the safe and long term operation of nuclear stations [31]. Especially at the coolant loss condition during the accident, the cladding material must be able to withstand the high temperatures up to 1000^oC without compromising its strength and ductility. Understanding the oxidation behavior for the cladding material at higher temperature water vapor condition is a critical step for developing accident tolerant cladding material. It is known that a protective chromia (Cr_2O_3) layer imparts high oxidation resistance to Fe-Cr alloys. However, water vapor environment is known to promote oxidation of Cr rather than forming an external protective chromia layer [57, 58]. The harsh moisture-containing environments can also cause accelerated chromium loss due to the formation

of volatile $CrO_2(OH)_2$ [66, 67, 69, 76]. This process leads to a phenomenon called 'breakaway oxidation' where chromia scale is replaced by a non-protective Fe-rich scale [58, 69]. The adverse effect of water vapor on corrosion resistance of various steels at high temperature is widely reported in literature [54, 57, 58, 67, 69-75]. Pint et. al. [55] stated that steels should have at least 20% Cr content in order to have a stable and protective chromia layer in high temperature steam environments. Ehlers et. al. [69] found that higher H_2O/O_2 ratio in the atmosphere promotes the formation of a non-protective Fe-rich layer on 9 wt% Cr P91 ferritic steel at high temperatures. The double layer scale formation with an internal Cr-rich and external Fe-rich layer is observed in previous studies on water vapor/steam oxidation of Fe-Cr alloys [57, 58, 69, 77, 78]. Ishitsuka et. al. [79] studied steam oxidation resistance of Si-containing Fe-9Cr alloy and reported that the low oxidation rates in the high Si-containing alloy are attributed to the formation of amorphous SiO_2 at the scale and metal interface. Fujikawa et. al. [80] reported that silicon enrichment in the internal spinel phase layer greatly reduces the ionization of Fe and its diffusion in the oxide layer during high temperature steam oxidation.

This work focused on the effects of thermal treatment on the NFA and SiC-C@NFA composites at 500-1000^{o}C in air+45 vol% H_2O vapor environment. The oxidation resistance was studied based on weight change and oxidized layer thickness. The oxide layer microstructures, phase compositions, and surface morphologies were characterized and investigated. The overall oxidation mechanism was elucidated from a thermodynamic point of view.

5.3. Materials and methods

Chapter 2 has detailed the preparation method, density, and microstructural evolution of the SiC-C@NFA composites. In brief, carbon coated NFA powder (C@NFA, NFA with a composition of Fe-9Cr-2W-0.4Ti-0.2V-0.12C-0.3Y_2O_3) was mixed with 5, 15, and 25 vol% SiC powder and then densified using spark plasma sintering (SPS) at 850^{o}C and 950^{o}C for 10 minutes with pressure of 100 MPa and heating/cooling rate of 50 ^{o}C/min.

In this work, the pure NFA and 5-25 vol% SiC-C@NFA composites were thermally treated in an air+45 vol% H_2O atmosphere. The composite samples were cut into size of 5 mm×5 mm×3

mm and surfaces were polished using SiC papers (grit size: 180, 400, 600, 800, 1200) and alumina suspension (size: 1 μm) before thermal treatment. It was carried out in a tube furnace (1730-20 HT Furnace, CM Furnace Inc., Bloomfield, NJ) at temperatures of 500°C, 750°C, and 1000°C for 50 hours. The air+45 vol% H_2O atmosphere was generated by passing air through a water jar before it reached the tube furnace. The water in the jar was maintained at 80°C and generated the saturated vapor pressure of 355 mmHg, which corresponded to ~45 vol% of water vapor. The weight changes of the samples were tracked using a balance before and after the thermal treatment in air+45 vol% H_2O atmosphere. Normalized weight changes with respect to sample areas were obtained for all the samples.

The phase compositions of the oxidized sample surfaces were examined using an X-ray diffractometer (XRD, PANalytical B.V., Almelo, Netherlands) with Cu-Kα radiation at an operating condition of 45 kV/40 mA. Scanning electron microscopy (SEM, FEG ESEM QUANTA600, FEI Company, Hillsboro, OR, USA) was performed to characterize the surface morphology and cross section microstructure of the oxidation layers. Elemental distributions along the cross section of the oxide layers were analyzed using an energy dispersive spectrometer (EDS) (model of BRUKER) attached to the SEM.

The oxidation behavior of the samples was studied based on the Thermo-Calc® software. The corresponding phase diagrams and elemental diffusion coefficients (D_{Cr} and D_{Fe}) at the thermal treatment conditions were obtained. The average elemental compositions in each composite were calculated by considering contributions from SiC, C-coating, and NFA.

5.4. Results and discussion

5.4.1. Physical changes

Fig. 5.1 shows the effect of SiC addition on the mass changes for the 850°C and 950°C sintered pure NFA and 5-25 vol% SiC-C@NFA composites during the thermal treatment in air+45 vol% H_2O atmosphere. There are three major factors that contribute to the mass changes during the oxidation process: oxide layer formation, oxide layer spallation, and volatile species formation

and depletion. The oxide scale formation contributes to the mass gain due to oxygen uptake during metal-oxygen reaction. The difference in thermal expansion coefficients between the oxide scale and the substrate at high temperatures results in the oxide layer spallation and concurrent mass loss. The chemical reactions between the oxide layer and the atmosphere (more specifically H_2O vapor) also lead to the formation of volatile species such as metal hydroxide, which again contribute to the mass loss.

As shown in Fig. 5.1a, the 850°C sintered pure NFA and 5-25 vol% SiC-C@NFA composites after the thermal treatment in air+45 vol% H_2O at 500°C and 750°C have significantly less mass gains (0.4-15 mg/cm^2) compared to that of the 1000°C treated composites except for the 25 vol% SiC composites. (The marginal increase in the mass gain for the 850°C sintered 15 vol% SiC-C@NFA composite after the 500°C thermal treatment is probably because of sample quality variation derived from sintering, and it does not alter the overall trend in this work). For the 500°C thermal treated samples, the 25 vol% SiC-C@NFA sample shows the lowest mass gain of 0.38 mg/cm^2 as compared to 1.15 mg/cm^2 for the pure NFA. While for the 750°C thermally treated samples, the mass gain decreases from 14.6 mg/cm^2 for the pure NFA to 4.5 mg/cm^2 for the 25 vol% SiC-C@NFA. The mass gains after the 1000°C thermal treatment show considerable decrease from 111.9 mg/cm^2 for the pure NFA to 8.5 mg/cm^2 for the 25 vol% SiC-C@NFA. Less than 1/10 of the mass gain for the 25 vol% SiC-C@NFA composite than that for the pure NFA means that the high SiC with 25 vol% addition significantly improves oxidation resistance of the SiC-C@NFA composites. All the 950°C sintered pure NFA and 5-25 vol% SiC-C@NFA composites show negligible mass gains after the 500°C and 750°C thermal treatments (0.03-3.5 mg/cm^2) as shown in Fig. 5.1b. There is no obvious correlation with the SiC addition in the samples. The 950°C sintered samples also show better oxidation resistance than the 850°C sintered samples at the same thermal treatment condition. The 950°C sintered pure NFA and 5-25 vol% SiC-C@NFA composites show decreasing trend in mass gain similar to the 850°C sintered composites after the 1000°C treatment. The mass gain for the 950°C sintered pure NFA is comparable to that of the 850°C sintered condition (~107 vs ~ 111.9 mg/cm^2 respectively) after the 1000°C treatment. However, the 950°C sintered 5 and 15 vol% SiC-C@NFA composites have much lower mass gains (84.5 vs 23.2 mg/cm^2) than that of the 850°C sintered 5 and 15 vol% SiC-C@NFA composites (111.7 vs 86.2 mg/cm^2). The 950°C sintered 25 vol% SiC-C@NFA composite shows significantly lower mass gain (7.8 mg/cm^2) compared to that of the pure NFA

(107 g/cm^2) as well as that of the 5 and 15 vol% SiC composites (84.5 and 23.2 g/cm^2) during the 1000ºC treatment. The 950ºC sintered samples have better oxidation resistance than the 850ºC sintered samples at the same treatment condition, which is attributed to the higher densities derived from the sintering temperature. As discussed in section 2.4.2 in Chapter 2, the higher sintering temperature of 950ºC produces higher relative density for the same composition sample. The denser samples tend to have fewer defects, which can hinder oxidant diffusion and benefit the oxidation resistance.

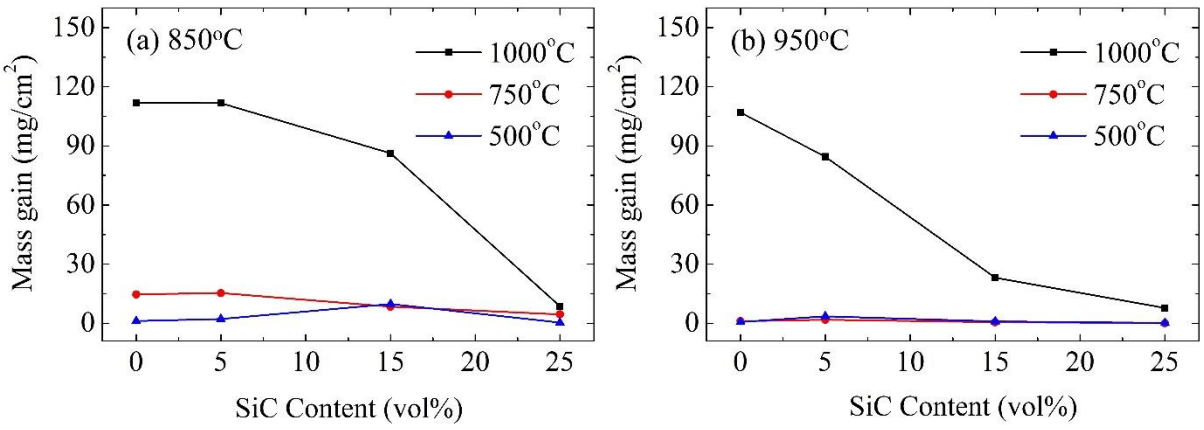

Fig. 5.1. Effect of SiC addition on mass gain for the air+water vapor thermal treated pure NFA and 5-25 vol% SiC-C@NFA composites after 850ºC (a) and 950ºC (b) sintering. (The error bars for all samples are within ± 0.38 mg/cm^2).

5.4.2. Phase composition

Fig. 5.2 shows the XRD patterns of the 850ºC and 950ºC sintered pure NFA and 5-25 vol% SiC-C@NFA composites after the thermal treatments. All the samples show mainly hematite phase after the thermal treatment between 500-1000ºC. For the 500ºC thermal treatment condition, the pure NFA and 5-25 vol% SiC-C@NFA composites show the hematite phase without preferential growth. For the 750ºC thermal treatment condition, the XRD peaks of the (300) plane from the hematite phase in the pure NFA and SiC-C@NFA composites have higher intensity,

meaning that the hematite phase has preferential growth along the (300) plane. For the 1000ºC thermal treatment condition, the pure NFA and 5 vol% SiC-C@NFA composite show preferential growth of the hematite phase along the (600) plane, while the 15 vol% and 25 vol% SiC-C@NFA composites have no preferential growth of the hematite phase. The same phenomenon has been observed in previous work from our group with 0-5 vol% SiC-NFA composites (without any coating) after the thermal treatment in air+45 vol% H_2O at 500-1000ºC [151]. The 15 vol% and 25 vol% SiC-C@NFA composites without the preferential growth of hematite after the 1000ºC thermal treatment indicate higher oxidation resistance capability compared to the pure NFA and 5 vol% SiC-C@NFA composite. This is also reflected by the lower mass gain (Fig. 5.1) and smaller thickness of the oxidized layer (Fig. 5.10). Due to the thinner oxide layer for the 15 vol% SiC-C@NFA composite after the 1000ºC treatment, the magnetite phase beneath the hematite top layer can be observed from the XRD pattern as shown in Fig. 5.2a. The 25 vol% SiC-C@NFA composites shows minor phase shift in hematite peaks as compared to pure NFA, 5 and 15 vol% SiC-C@NFA composites. This corresponds to presence of protective Cr rich oxide phase in addition to Fe_2O_3.

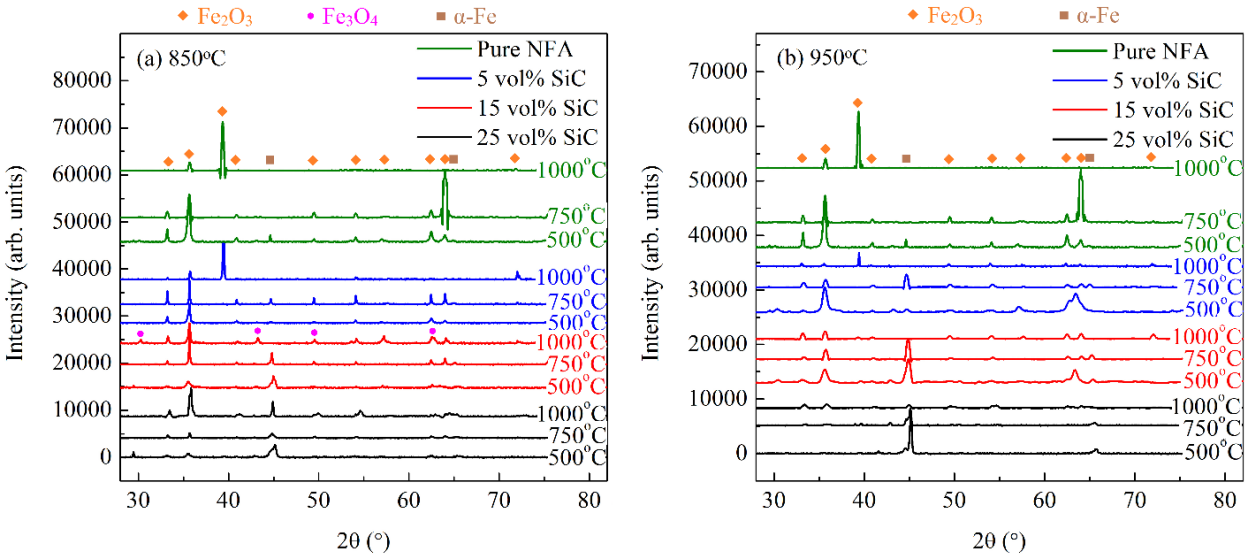

Fig. 5.2. XRD patterns of the 850ºC and 950ºC sintered pure NFA and 5-25 vol% SiC-C@NFA composites after the air+water vapor thermal treatment at 500ºC, 750ºC, and 1000ºC.

5.3.3. Surface morphology

The surface morphologies of the 850°C and 950°C sintered pure NFA and 5-25 vol% SiC-C@NFA composites after the thermal treatment in air+45 vol% H_2O at 500-1000°C are shown in Fig. 5.3 and Fig. 5.4 respectively. All the 850°C sintered samples show morphologies similar to 950°C, therefore discussion is omitted here for brevity. After the 500°C treatment, the pure 950°C sintered NFA as well as the 5 and 15 vol% SiC-C@NFA composites have similar fine and continuous flake-like microstructures as shown in Figs. 5.4a-5.4d, which is believed to be the hematite phase as identified from the XRD analysis (Fig. 5.2). The 25 vol% SiC-C@NFA composite does not show the flake-like microstructures, different from the 0-15 vol% SiC composites. Instead, bright contrast regions with a rough surface and dark contrast regions with a flat surface can be observed. As discussed earlier based on the mass gain in Fig. 5.1 and the XRD patterns in Fig. 5.2, the 25 vol% SiC-C@NFA composite has stronger oxidation resistance, which is directly responsible for the different surface morphology compared with those of the pure the NFA and the 5-15 vol% SiC composites at the same thermal treatment condition. Due to the higher SiC addition in the 25 vol% SiC-C@NFA composite, the dark contrast regions are believed to be very thin oxidation layers, which result from the SiC rich region in the composites. Similar surfaces can be found when comparing the same sample before and after thermal treatment [152]. The bright contrast regions have higher oxidation resistance than the dark contrast regions due to the rough surface. The hematite phase is much smaller compared to that in the pure NFA and 5-15 vol% SiC-C@NFA composites, so the flake structures cannot be observed.

Figs. 5.4e-5.4h show the oxide morphologies of the pure NFA and 5-25 vol% SiC-C@NFA composites after the thermal treatment in air+45 vol% H_2O at 750°C. The pure NFA sample exhibits a flat and porous oxidation layer as shown in Fig. 5.4e. The 5-25 vol% SiC-C@NFA composites show island-like structures scattered in the oxidation layer. The number of the islands is much lower for the 25 vol% SiC-C@NFA composite compared to the 5 and 15 vol% SiC-C@NFA composites. This means lower oxidation damage for the 25 vol% SiC composite, consistent with the mass gain results in Fig. 5.1. The 5 vol% and 25 vol% SiC-C@NFA samples show a flake structure, while the 15 vol% composite shows more faceted structure for the island regions even though some small flake residuals can also be observed in the faceted areas. We

believe that the faceted structure derives from the further growth of the flake structure, possibly because of some unexpected contamination on the sample surface, which accelerates the morphology change. For the 850^{o}C sintered samples, the 15 vol% SiC composite has the same flake structure as that of the 5 vol% and 25 vol% composites, as given in the Fig. 5.3.

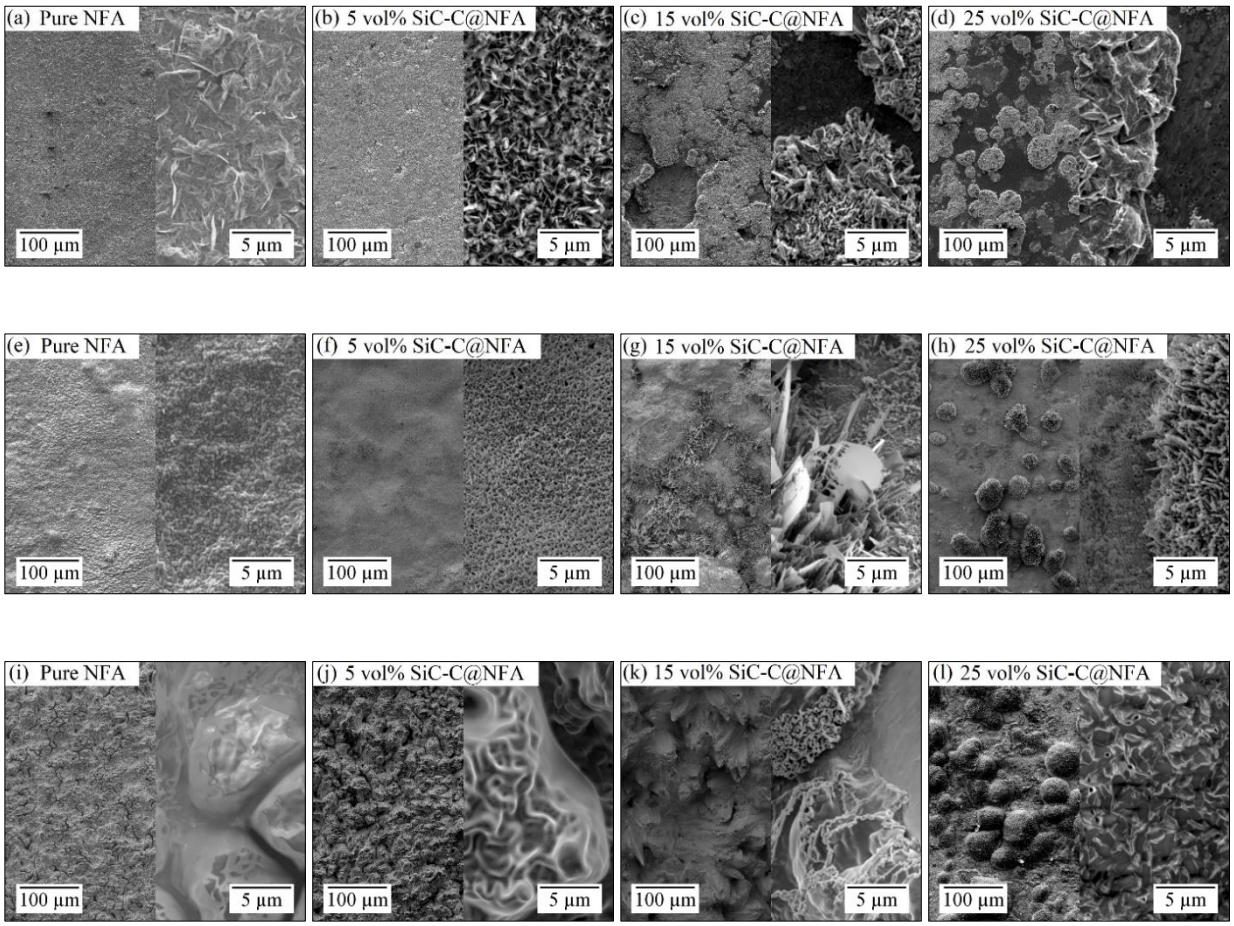

Fig. 5.3. Surface morphologies of the 850^{o}C sintered pure NFA and SiC-C@NFA composites after the water vapor thermal treatment at 500^{o}C (a-d), 750^{o}C (e-h), and 1000^{o}C (i-l).

The oxide morphologies of the pure NFA and 5-25 vol% SiC-C@NFA composites after the thermal treatment in air+45 vol% H_2O at 1000^{o}C are shown in Figs. 5.4i-5.4l. The pure NFA as well as the 5 vol% and 15 vol% SiC-C@NFA composites show preferentially grown ridge-type structure with cracks and microchannels. The ridge size in the 5 vol% SiC-C@NFA composite is

larger than that in the pure NFA sample. The 15 vol% SiC-C@NFA composite also shows oriented ridge structure, but slightly different from the preferential orientation in the pure NFA and 5 vol% SiC-C@NFA composites. The 25 vol% SiC-C@NFA composite shows the island-like structure with preferentially oriented flakes growing on it. Since the pure NFA as well as the 5-15 vol% SiC-C@NFA composites have considerably higher mass gain than the 25 vol% SiC-C@NFA composite, the ridge-type structure should be an indication of more extensive oxidation. The presence of cracks and microchannels in the ridge type structure is likely to promote further oxidation by allowing short circuit paths for oxidizers (O_2 and H_2O).

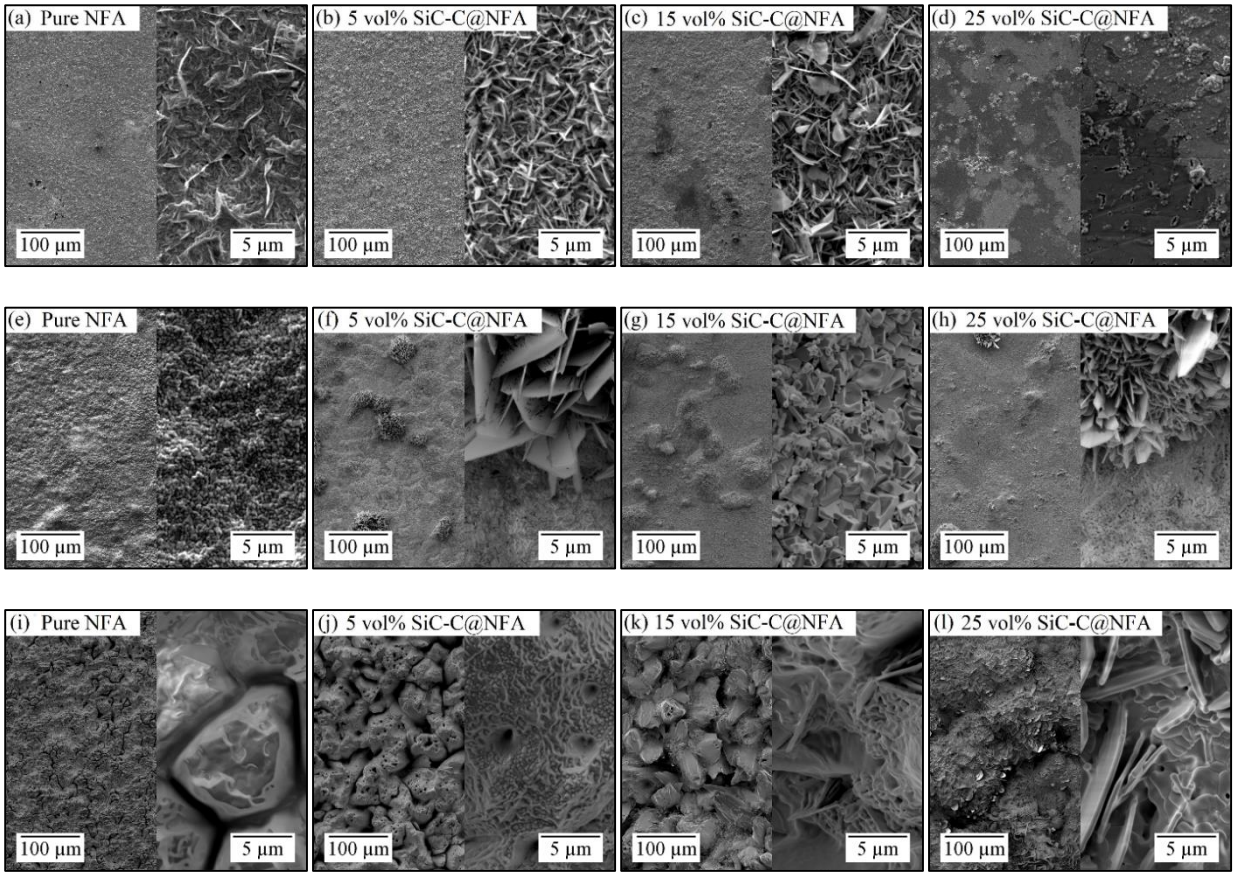

Fig. 5.4. Effect of SiC addition on the surface morphologies of the 950°C sintered pure NFA and the 5-25 vol% SiC-C@NFA composites after the air+water vapor thermal treatment at 500°C (a-d), 750°C (e-h), and 1000°C (i-l). (Right image is the magnified version of left image).

5.3.4. Oxide layer structure

Figs. 5.5 and 5.6 shows the cross-section microstructures of the 850^{o}C and 950^{o}C sintered pure NFA and 5-25 vol% SiC-C@NFA composites after the thermal treatment in air+45 vol% H_2O at 1000^{o}C. Since, 850^{o}C sintered samples have similar morphologies (see Fig. 5.5), discussion is omitted for brevity. The 950^{o}C sintered pure NFA sample shows three distinct layers with a total layer thickness of ~1715 μm as shown in Fig. 5.6a. The 5 vol% and 15 vol% SiC-C@NFA composites show a similar three-layer structure with the thicknesses at ~1080 μm and ~487 μm, respectively, as shown in Figs. 5.6b and 5.6c respectively. The thickness of the entire oxide layer for the 25 vol% SiC composite is ~108 μm, which again demonstrates the strong oxidation resistance of the composite, matching with its lowest mass gain as shown in Fig. 5.1. The outermost layers in the pure NFA and 5-15 vol% SiC-C@NFA composites are identified as Fe_2O_3 based on the XRD analysis from Fig. 5.2b. The middle layers should be magnetite Fe_3O_4, which tends to locate close to the outer hematite as determined for a 9Cr steel [69]. The inner layer contains three different phases for pure NFA but four different phases for SiC-C@NFA composites. The specific phase composition in the inner layer of SiC-C@NFA composite samples is further explored to be a mixture of $FeCr_2O_4$, Fe_3O_4, $(Fe,Si)_2W$ (laves), and Fe_2SiO_4, as to be discussed based on the EDS maps in Fig. 5.9a. While inner layer of pure NFA was composed of $FeCr_2O_4$, Fe_3O_4 and Fe_2W (laves) due to absence of Si in the system. For the 25 vol% SiC-C@NFA composite (Fig. 5.6d), there is no obvious layered structure as that for the pure NFA and 5-15 vol% SiC-C@NFA composites. Due to its strong oxidation resistance, the internal oxide region is minimal and overlaps with the inner layer. The outer Fe_2O_3 layer and the middle Fe_3O_4 layer, which are more obvious around the island surface, will be discussed based on the EDS maps in Fig. 5.8d. Unlike the pure NFA sample, each composite shows an internal oxidation layer, extending beyond the inner oxide layer, which will be discussed in details next. The internal oxidation layer in the 25 vol% SiC-C@NFA has the smallest thickness of ~90 μm. Due to the 5 vol% and 15 vol% SiC-C@NFA composites have the internal oxidation over entire sample thickness, and their thickness of internal oxidation layer is observed to be similar at ~1500 μm. However, 15 vol% SiC-C@NFA sample is expected to have thinner internal oxidation layer due stronger resistance from more SiO_2 and Cr_2O_3 protection as explained in detail in later sections.

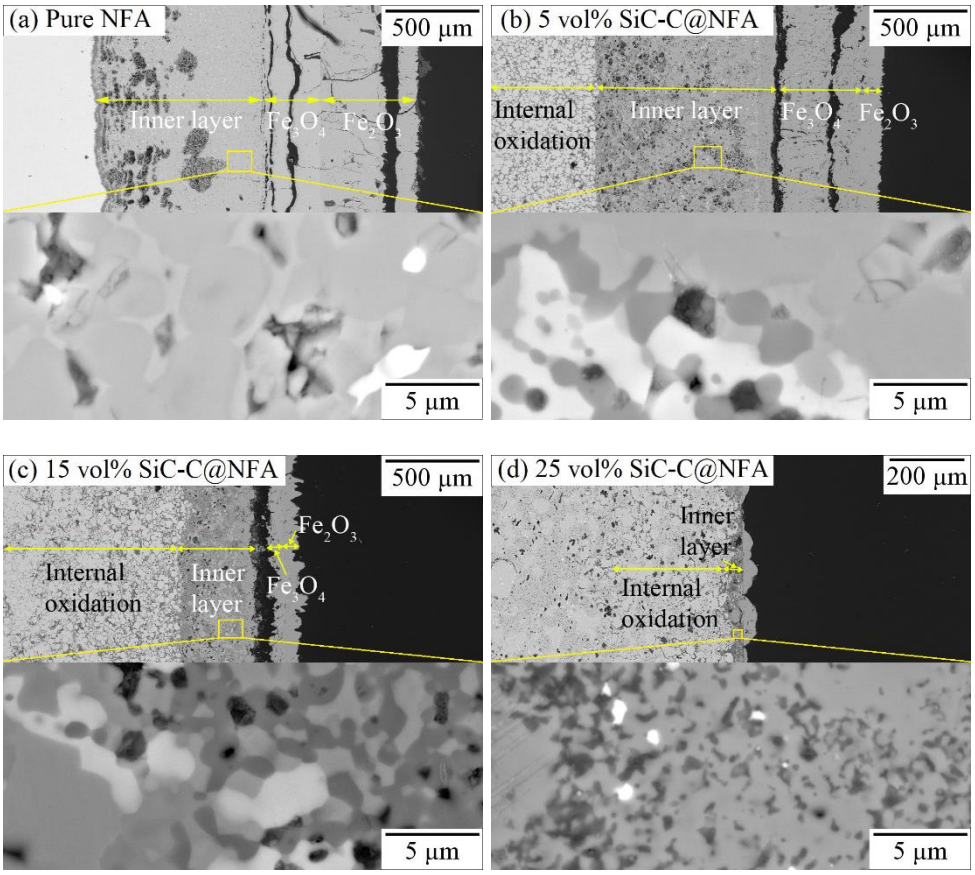

Fig. 5.5. Cross section microstructures of the 850°C sintered pure NFA (a), 5 vol% SiC-C@NFA (b), 15 vol% SiC-C@NFA (c), and 25 vol% SiC-C@NFA (d) after the water vapor thermal treatment at 1000°C.

Fig. 5.7 and 5.8 shows the elemental distributions of the oxide layer cross sections for 850°C and 950°C sintered NFA and 5-25 vol% SiC-C@ NFA composites. The 850°C sintered samples have similar elemental distributions along the cross section oxide layers (see Fig. 5.7) and are omitted in the discussion for brevity. For the 950°C sintered pure NFA and 5-15 vol% SiC-C@ NFA composites (Figs. 5.8a-5.8c), the oxide layer is composed of an outer Fe-rich region and an inner Cr-rich region. O is present in both regions. Combined with the earlier discussion, it can be derived that the outer Fe-rich region in the Fig. 5.8 is covered with an outer layer of Fe_2O_3 and a middle layer of Fe_3O_4 in Fig. 5.6, as both phases are Fe-rich. The Fe_3O_4 layer has been shown to exist beneath the top Fe_2O_3 phase layer after oxidation treatment in the 9Cr steel [69]. The phases in the Cr-rich inner layer for the 15 vol% SiC-C@NFA composite (Fig. 5.9a) are further identified

as $FeCr_2O_4$, Fe_3O_4, $(Fe,Si)_2W$, and Fe_2SiO_4. The EDS maps of the 25 vol% SiC-C@NFA composite are shown in Fig. 5.8d. The discontinuous outer layer close to surface is predominantly Fe-rich and O-rich. Some islands have Cr-, Fe-, O- enrichment (indicated by white dashed arrows in Fig. 5d). As shown from the XRD patterns in Fig. 2, only Fe_2O_3 is identified in the 25 vol% SiC-C@ NFA composites, thus, the surface layer on the island should be the same Fe_2O_3 structure, possibly with some $(Fe,Cr)_2O_3$ phase. Beneath the island surface, there is an Fe-rich and Cr deficient region (indicated by yellow dashed arrows), which is believed to be the discontinuous middle Fe_3O_4 phase layer. In other regions, a discontinuous surface layer (indicated by the red arrow) with Fe-, O-enrichment and Cr-deficiency is believed to be the Fe_2O_3 phase. Following the Fe_3O_4 middle layer beneath the island, there is a thin, Cr-rich inner layer, the same as the inner layer of the 5-15 vol% SiC-C@ NFA composites. The inner layer is also discontinuous and spreads to the internal oxidation layer, as described in Fig. 5.6d. A Cr enriched layer can be seen at the interface between the inner layer and the substrate (indicated by the blue dashed arrow). The formation mechanism for the layered structure with different phases will be discussed in later sections.

The EDS maps of the inner layer for the 950^{o}C sintered 15 vol% SiC-C@NFA composite after the thermal treatment in air+45 vol% H_2O at 1000^{o}C are shown in Fig. 5.9a. The bright contrast Fe-, Si- and W-rich phase (red arrow) is possibly $(Fe,Si)_2W$. Similar $(Fe,Si)_2W$ phase was also identified by Abe et. al. [153]. The dark contrast phase (yellow arrow) is Fe-, Si- and O-rich and from Fe_2SiO_4 (which is derived from the reaction given in Eq. (5.5). The gray contrast is composed of two different phases, first Fe-, Cr- and O-rich phase (blue arrow) and second Fe- and O-rich (green arrow) and therefore it is possibly a mixture of Fe_3O_4 and $FeCr_2O_4$ [69]. The internal oxidation region is investigated by focusing on the 950^{o}C sintered 15 vol% SiC-C@NFA composite after the 1000^{o}C treatment as shown in Fig. 5.9b. The internal oxidation occurs predominantly on the NFA grain boundaries of the composites. Apart from the Si-rich oxide along the boundaries within the internal oxide region, a Cr-rich oxide is also observed. These Si-rich and Cr-rich oxides are believed to be a mixture of SiO_2 and Cr_2O_3, which promote the oxidation resistance. The formation mechanisms for such oxides will be discussed later.

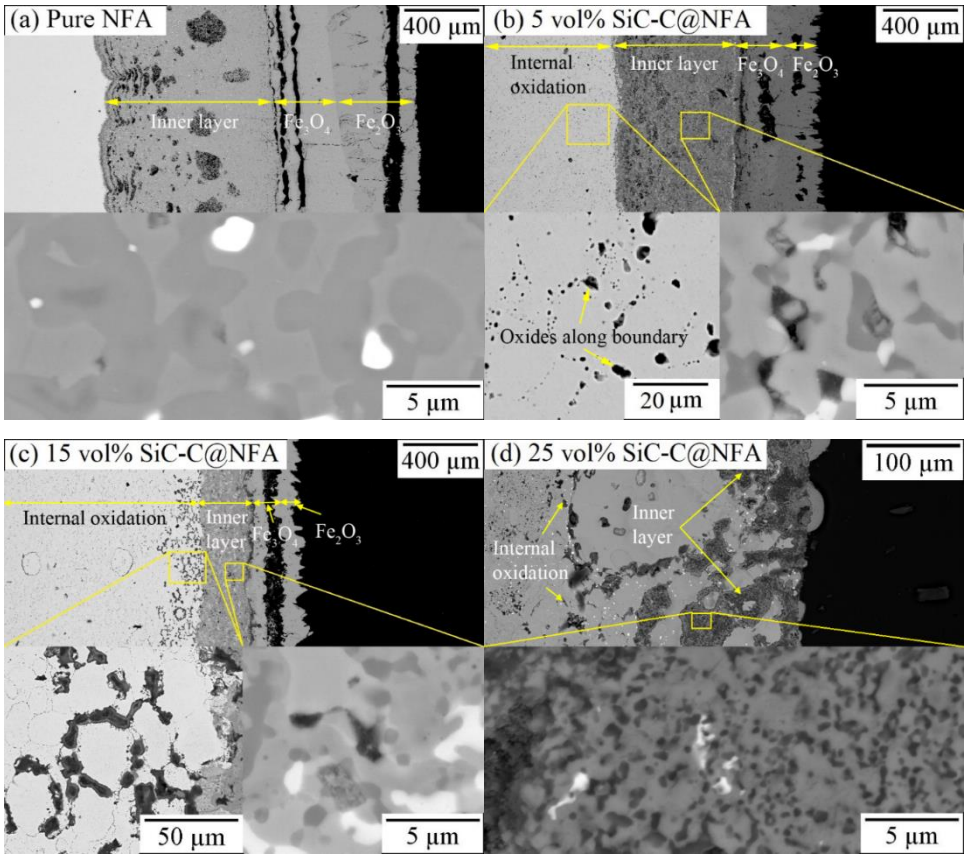

Fig. 5.6. Cross section microstructures of the 950°C sintered (a) pure NFA, (b) 5 vol% SiC-C@NFA, (c) 15 vol% SiC-C@NFA, and 25 vol% SiC-C@NFA after the air+water vapor thermal treatment at 1000°C.

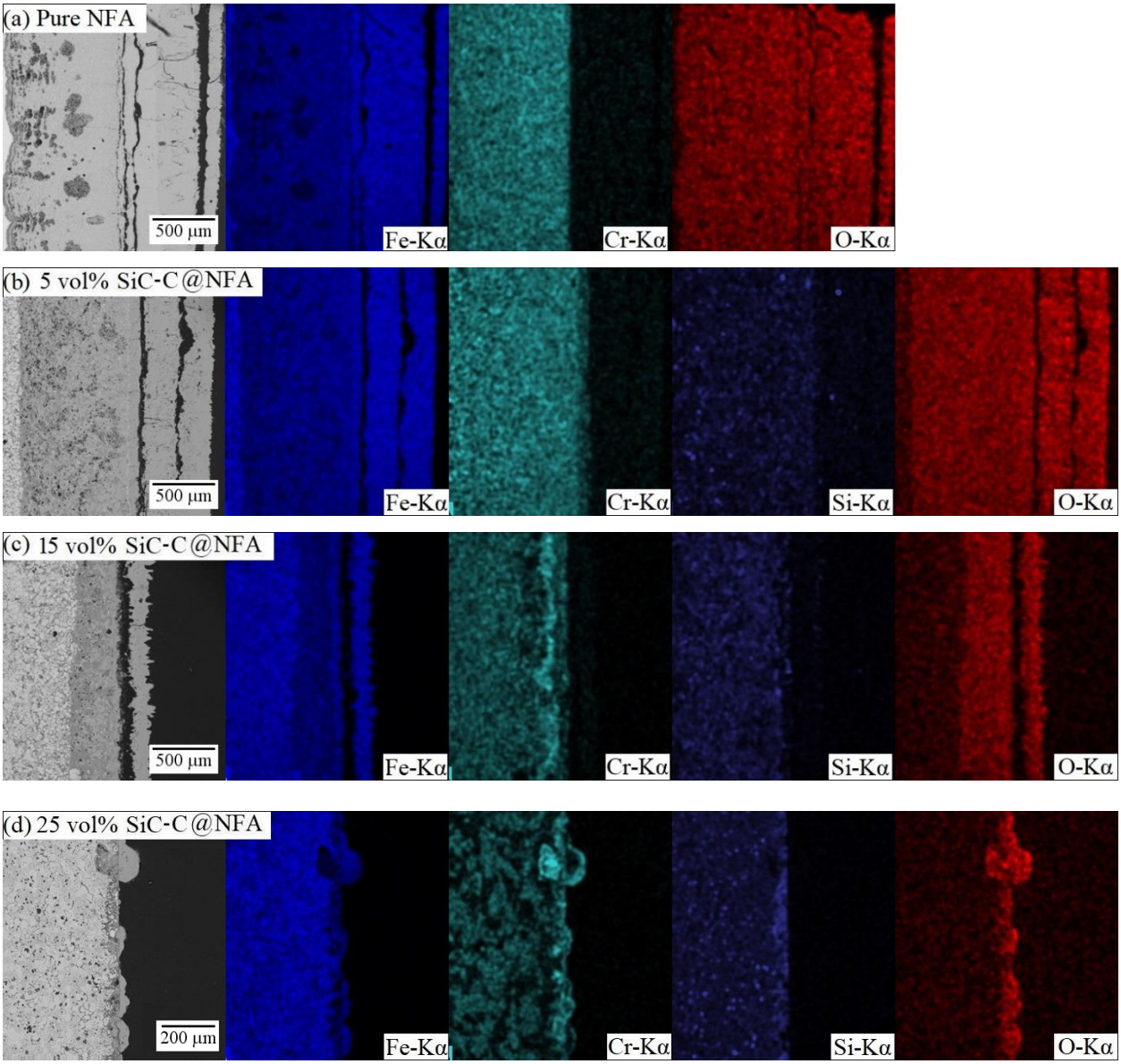

Fig. 5.7. EDS maps of the oxide layer of the 850ºC sintered (a) pure NFA, (b) 5 vol%, (c) 15 vol%, (d) 25 vol% SiC-C@NFA composites with the water vapor treatment at 1000ºC.

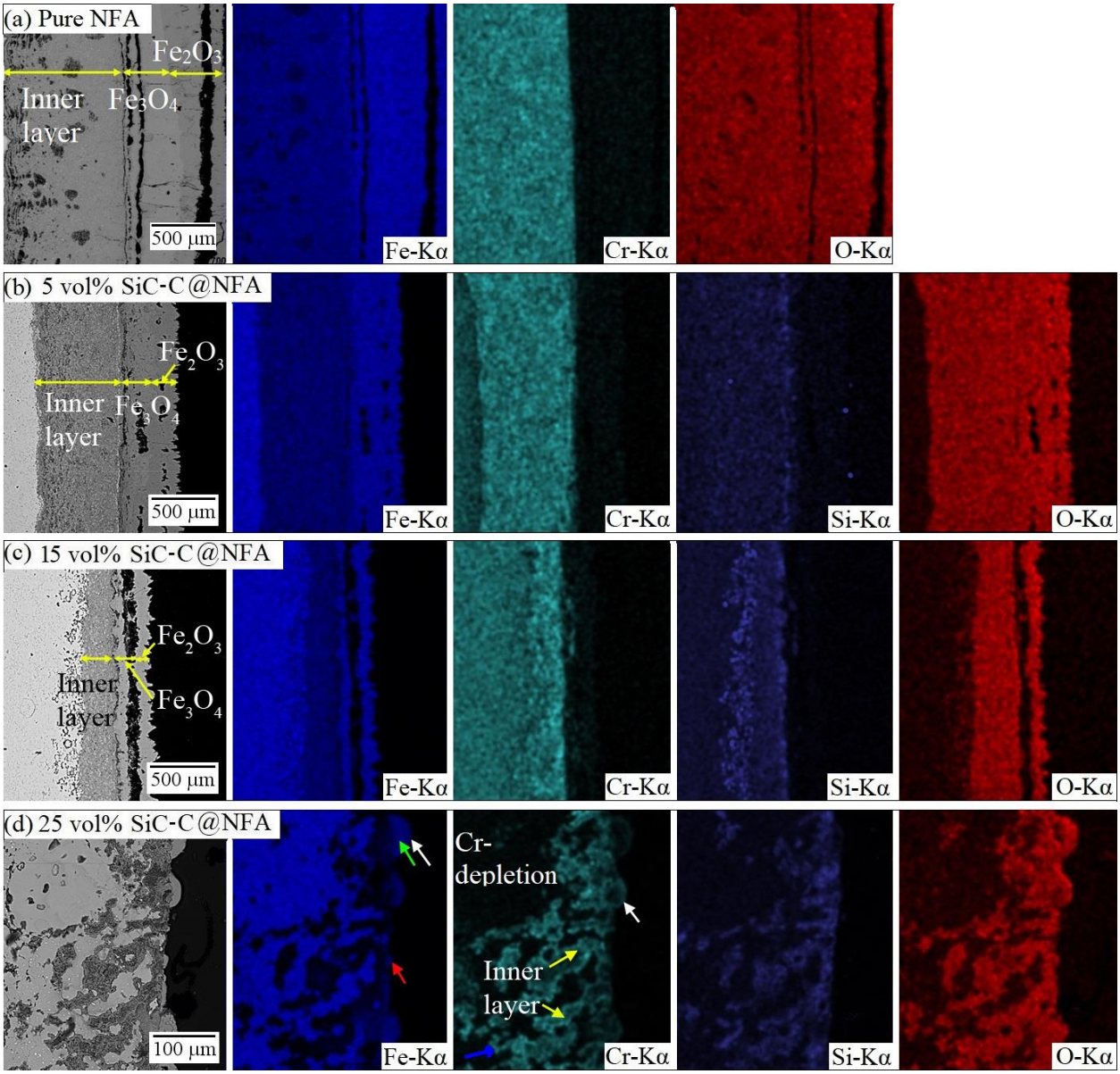

Fig. 5.8. EDS maps of the oxide layers for the 950°C sintered (a) pure NFA, (b) 5 vol% SiC-C@ NFA, (c) 15 vol% SiC-C@ NFA, and (d) 25 vol% SiC-C@NFA after the air+water vapor thermal treatment at 1000°C.

The SiC addition effect on the oxide layer thickness of the pure NFA and SiC-C@NFA composites after the thermal treatment in air+45 vol% H_2O at 1000°C is shown in Fig. 5.10, with the contributions from different phases shown. The thickness of the overall external oxidation layer shows decreasing trend with addition of SiC for both 850°C and 950°C sintered composites. The

thickness of the 850°C sintered samples is also higher than the 950°C counterparts. This can be explained by the smaller relative densities (refer Chapter 2, section 2.4.2) of the 850°C sintered samples relative to those of the 950°C ones, which promotes oxidation damage. The thickness of the outer Fe_2O_3 and middle Fe_3O_4 layers shows the similar decreasing trend with the addition of SiC. The inner layer of the 5 and 15 vol% SiC-C@NFA composites shows considerably smaller thickness for the 950°C sintered samples compared to the 850°C sintered ones. This is consistent with the relatively large difference in relative densities between the 850°C and 950°C sintered samples (87.42% vs 99.33% for the 5 vol% SiC-C@NFA; 89.83 vs 99.33% for the 15 vol% SiC-C@NFA). While the pure NFA and 25 vol% SiC-C@NFA samples show slightly larger thickness after sintering at 950°C than at 850°C. The difference between the relative densities of the 850°C and 950°C sintered pure NFA and 25 vol% SiC-C@NFA samples is relatively low (95.6% vs 98.7% for the pure NFA; 96.84% vs 99.6% for the 25 vol% SiC-C@NFA). Since the mass gain data show almost similar or slightly higher values for the 850°C sintered samples, the slightly higher thickness of the 950°C samples should be from the measurement errors. All the SiC-C@NFA composites have an internal oxidation region after the thermal treatment. While the pure NFA sample does not show any internal oxidation. This means that the SiC addition promotes the formation of the internal oxidation region beneath the external scale. The 5 vol% and 15 vol% SiC-C@NFA composites show internal oxidation throughout the sample. Thus the thickness of the internal oxidation related region in these samples is around 1500 μm for both 850°C and 950°C sintering temperatures. The 25 vol% SiC-C@NFA sample shows minimal internal oxidation thickness compared to the 5 vol% and 15 vol% SiC-C@NFA samples, meaning the strong resistance to oxidation. As shown from the EDS maps in Fig. 5.9b, the internal oxidation region consists of a mixture of SiO_2 and Cr_2O_3 phases.

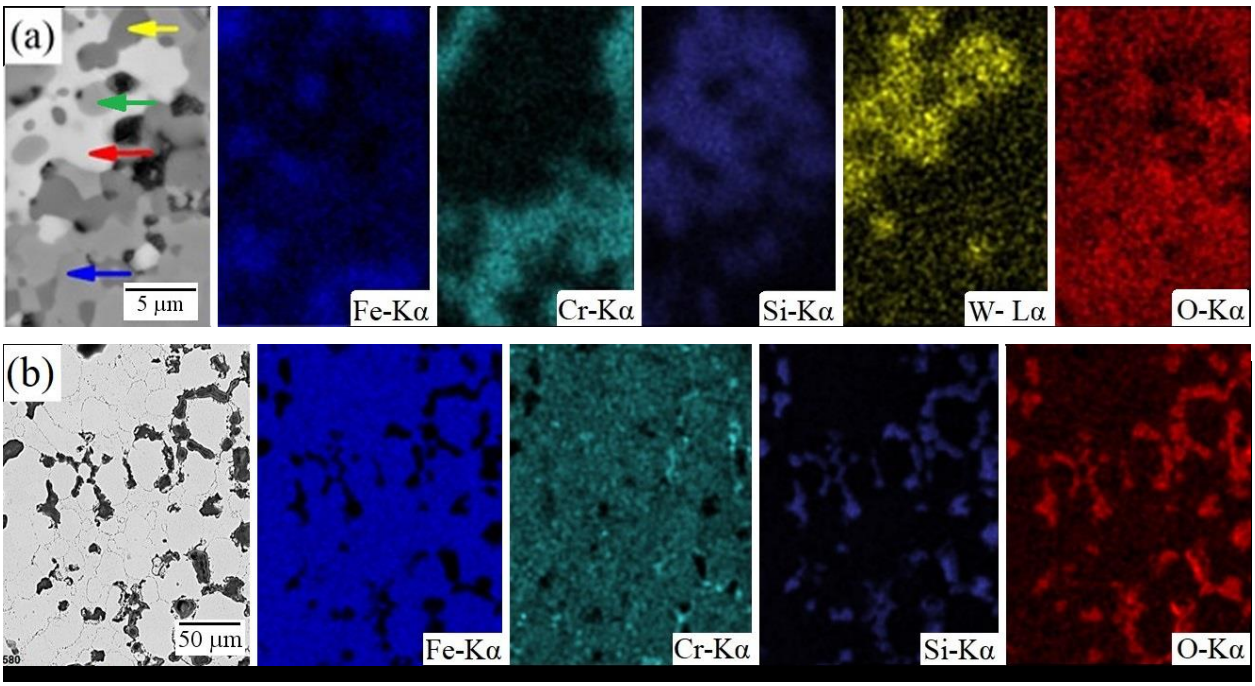

Fig. 5.9. EDS maps of the inner layer (a) and the internal oxidation region (b) in the 950°C sintered 15 vol% SiC-C@NFA composite after the air+water vapor thermal treatment at 1000°C.

5.3.5. Oxidation mechanisms

Fig. 5.11 shows the schematic of the layered structure in the pure NFA and 5-25 vol% SiC-C@NFA composites after the thermal treatment in air+45 vol% H_2O at 1000°C. The pure NFA shows the outer, middle, and inner tri-layer structure. An internal oxidation region is further produced beneath the inner layer for all the composites. Cr evaporation in the formation of $CrO_2(OH)_2$ due to the reaction between the protective chromia scale (Cr_2O_3) and water vapor is a major cause for the breakaway oxidation, as shown in Eq. (5.1). The Fe-rich outer/middle layer (Fe_2O_3 + Fe_3O_4) gradually forms due to the outward diffusion of Fe^{3+}/Fe^{2+} ions [154] after the breakdown of the protective Cr- rich layer. Eqs. (5.2) and (5.3) show the formation of the outer Fe_2O_3 layer and middle Fe_3O_4 layer due to the reactions with the water vapor containing atmosphere. The inner layers of the composites have a mixed phases of Fe_3O_4, $FeCr_2O_4$, Fe_2SiO_4, and $(Fe,Si)_2W$. The reaction of the substrate Fe and oxygen with the protective Cr_2O_3 and SiO_2

layers during the breakaway oxidation results in the formation of $FeCr_2O_4$ and Fe_2SiO_4 in the inner layer, respectively, as shown in Eqs. (5.4) and (5.5).

$$2Cr_2O_3(s) + 3O_2(g) + 4H_2O(g) = 4CrO_2(OH)_2(g) \quad (5.1)$$

$$2Fe\ (s) + O_2\ (g) + H_2O\ (g) = Fe_2O_3\ (s) + H_2\ (g) \quad (5.2)$$

$$9Fe\ (s) + 4O_2\ (g) + 4H_2O\ (g) = 3Fe_3O_4\ (s) + 4H_2\ (g) \quad (5.3)$$

$$2Fe + O_2\ (g) + 2Cr_2O_3\ (s) = 2FeCr_2O_4 \quad (5.4)$$

$$2Fe + O_2(g) + SiO_2 = Fe_2SiO_4(s) \quad (5.5)$$

Cracks/gaps and microchannels can be observed in the Fe-rich outer/middle layer of the pure NFA as well as the 5 vol% and 15 vol% SiC-C@NFA composites as shown in Fig. 5.11. The formation crack is usually a complicated process, which may be relate to phase separate, phase precipitation, phase growth and phase compositions. In this work, the phase compositions have been identified to be Fe_3O_4 and Fe_2O_3, and the crack is found to be between them due to the thermal expansion mismatch between the oxides (1.0×10^{-5}/ºC for Fe_2O_3, 1.5×10^{-5}/ºC for Fe_3O_4 at 1000ºC [155]). The thickness of the outer Fe-rich layers (Fe_2O_3+Fe_3O_4) is smaller than those of the inner layers for the pure NFA, 5 vol% and 15 vol% SiC-C@NFA composites. This is attributed to the presence of cracks/gaps in the samples, which hinder the diffusion of Fe^{2+}/Fe^{3+} ions required for the growth of these outer layer phases. The inner layer is sustained by a continuous supply of oxidizers such as O_2 and H_2O via microchannels and cracks in the outer/middle layer. The formation of volatile hydroxide species as shown in Eq. (5.1) should be the reason for the formation of the microchannels, which serve as its escape routes.

The 25 vol% SiC-C@NFA composite shows a relatively dense outer/middle layer without any cracks or gaps throughout the cross-section. The outer layer is a mixture of Fe_2O_3 and $(Fe,Cr)_2O_3$. There is significant Cr-depletion just beneath the oxide layer as shown in Fig. 5.8d, indicating that chromium evaporation occurs by Eq. (5.1). The continuous removal of chromium

from the alloy by evaporation requires diffusion of chromium from the composite bulk in order to maintain the protective chromia layer. Breakdown of the protective chromia layer will quickly expose Cr depleted (Fe-rich) region and promote rapid oxidation to the level equivalent to that of the pure NFA and 5-15 vol% SiC-C@ NFA composites. The Cr-depleted region signifies the considerable delay in the breakaway oxidation for the 25 vol% SiC-C@NFA composite.

Unlike the pure NFA sample, all the SiC-C@NFA composites after the thermal treatment in air+45 vol% H_2O at 1000^{o}C show an internal oxidation region comprised of SiO_2 and Cr_2O_3. The internal oxidation mechanism involves three stages. First, oxygen dissolves in the composite matrix at the external scale and substrate interface. Second, it diffuses inwards to form the reaction front for the nucleation of oxide precipitates. Third, the solute (Cr and Si) diffuses to this reaction front to ultimately nucleate SiO_2 and Cr_2O_3 [156]. Therefore, the higher solute (Cr and Si) diffusivities would bring the reaction front closer to the substrate surface and ultimately reduce internal oxidation depth. Thus, the kinetics of internal oxidation is related to both solubility and diffusivities of oxygen and solute species (Cr and Si) at the thermal treatment temperature. The general reaction for the formation of the internal oxidation is given as follows [157]:

$$M + \nu O = MO_\nu \tag{5.6}$$

where M is the solute that oxidizes internally (Si and Cr for this work), ν is a constant. For SiO_2, ν is 2; for Cr_2O_3, ν is 3/2. MO_ν is either SiO_2 or Cr_2O_3. The parabolic rate constant $k_p^{(i)}$ for the internal oxidation can be estimated using the following equation [157]:

$$k_p^{(i)} = \frac{\pi}{D_M}\left(\frac{D_O N_O}{2\nu N_M}\right)^2 \tag{5.7}$$

where N_O is the solubility of oxygen in the matrix (4.5×10^{-6} for α-BCC phase, 3.3×10^{-6} for γ-FCC phase [157]), D_O is the diffusivity of oxygen in the matrix (3.5×10^{-6} m^2/s for α-BCC phase, $7.3\times10^{-}$

^{6} m^2/s for γ-FCC phase [157]), D_M is the diffusivity of solute M in the matrix, N_M is the mole fraction of the solute in the matrix.

Table 5.1 shows the concentrations and diffusivities of Cr and Si in all the samples. The concentrations of Cr and Si are obtained by considering the contributions from NFA, C, and SiC in the composites. The diffusivities were obtained using the ThermoCalc-DICTRA MOBFE4 database. The diffusivities of Cr and Si in the 25 vol% SiC-C@NFA composites are almost two orders of magnitude higher than those in the pure NFA, as well as 5 vol% and 15 vol% SiC-C@NFA composites. The parabolic rate constants $k_p^{(i)}$ for both SiO_2 and Cr_2O_3 were calculated using the values in Table 5.1. The 25 vol% SiC-C@NFA composite shows a considerably smaller $k_p^{(i)}$ for both SiO_2 and Cr_2O_3 compared to the 5 vol% and 15 vol% SiC-C@NFA samples. This explains why there is less internal oxidation for the 25 vol% SiC-C@NFA composite. The accumulation and continuous lateral layered growth of Cr_2O_3 and SiO_2 instead of internal precipitate formation can result if $N_O D_O << N_M D_M$ [156]. For the 25 vol% SiC-C@NFA both diffusivities (D_M) and concentration (N_M) of solute species (Cr and Si) are relatively high. The EDS mapping in Fig. 5.8d does show some enrichment of Cr between the external scale and the substrate (blue dashed arrow). Such continuous film would likely improve oxidation resistance of the 25 vol% SiC-C@NFA composite by acting as a barrier for the diffusion of oxygen, which is required for both external and internal oxide growth. This explains the delay in breakdown oxidation for the 25 vol% SiC-C@NFA composite compared to other samples.

The aforementioned model considers lattice diffusivity, which is a reasonable assumption for high temperature of 1000^{o}C. However, the diffusivity of oxygen through grain boundaries will further enhance the inward movement of the reaction front and thereby the thickness of the internal oxidation region. The continuous protective layer growth due to enhanced solute diffusivities in the 25 vol% SiC-C@NFA sample would still effectively prevent inward oxygen movement.

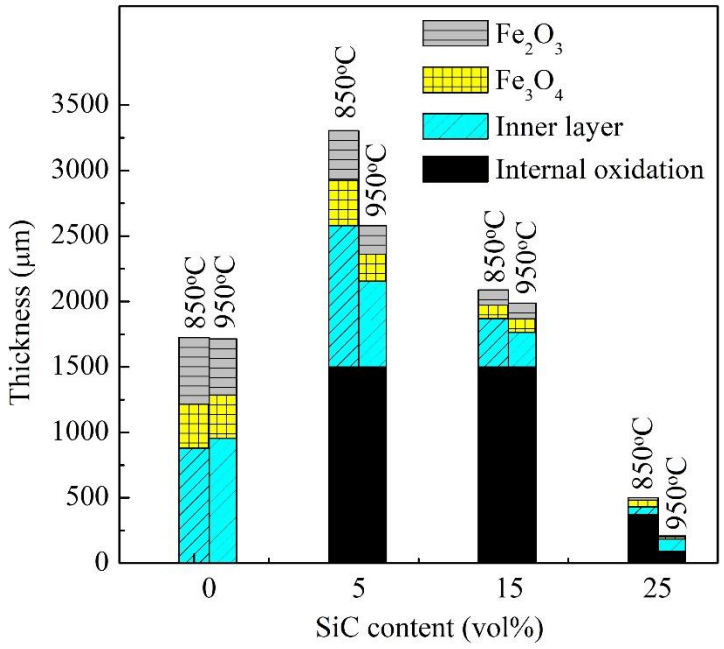

Fig. 5.10. Effect of SiC addition on the oxidation layer thickness of the 850°C and 950°C sintered pure NFA and the 5-25 vol% SiC-C@NFA composites after the air+water vapor thermal treatment at 1000°C.

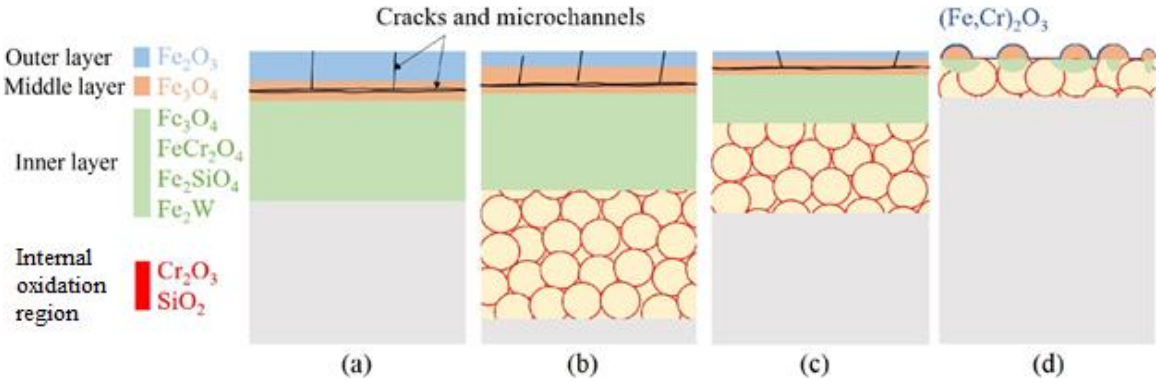

Fig. 5.11. Schematic representation of the oxidation behaviors for the pure NFA (a), 5 vol% SiC-C@ NFA (b), 15 vol% SiC-C@ NFA (c), and 25 vol% SiC-C@ NFA (d) under the air+water vapor thermal treatment condition at 1000°C.

Table 5.3. Concentration and diffusivity for Cr and Si, and the parabolic rate constant of $k_p^{(i)}$ for SiO_2 and Cr_2O_3 in the NFA and SiC-C@NFA composites during the thermal treatment at 1000°C.

Sample	**NFA**	**5 vol% SiC-C@NFA**	**15 vol% SiC-C@NFA**	**25 vol% SiC-C@NFA**
Majority phase	FCC	FCC	FCC	BCC
Cr concentration, N_{Cr} (mole fraction)	0.0973	0.0917	0.0807	0.0701
Cr diffusivity, D_{Cr} (m^2/s)	2.05×10^{-16}	2.32×10^{-16}	2.55×10^{-16}	6.65×10^{-14}
Si concentration, N_{Cr} (mole fraction)	0	0.0288	0.085	0.139
Si diffusivity, D_{Cr} (m^2/s)	/	1.35×10^{-15}	2.98×10^{-15}	2.37×10^{-13}
Parabolic rate constant $k_p^{(i)}$ for SiO_2 (m^2/s)	/	1.02×10^{-14}	5.28×10^{-16}	1.05×10^{-16}
Parabolic rate constant $k_p^{(i)}$ for Cr_2O_3 (m^2/s)	1.04×10^{-14}	1.04×10^{-14}	1.21×10^{-14}	2.64×10^{-15}

5.5. Conclusions

The oxidation behaviors of pure NFA and SiC-C@NFA composites at three different temperatures, 500^{o}C, 750^{o}C and 1000^{o}C in an air+45 vol% H_2O atmosphere, are studied. All the samples show negligible mass gain during the 500^{o}C and 750^{o}C treatments. The 25 vol% SiC-C@NFA composite shows the highest oxidation resistance during the 1000^{o}C treatment, 90% less than that of the pure NFA. The oxidized surfaces have a layered structure with two Fe-rich outer layers (Fe_2O_3, Fe_3O_4) and a Cr-rich inner layer (Fe_3O_4+$FeCr_2O_4$ +Fe_2SiO_4+$(Fe,Si)_2W$). A significant internal oxidation region is observed for the 1000^{o}C treated SiC-C@NFA composites due to the preferential oxidation of Cr- and Si-rich phases at the NFA grain boundaries. The improved oxidation resistance for the 25 vol% SiC-C@NFA composite is due to the high Cr and Si diffusivities and thus the SiO_2+Cr_2O_3 protective layer formation.

Chapter 6

High Temperature Oxidation Behavior of Chromium Carbide Coated Silicon Carbide – Nanostructured Ferritic Alloy Composites in Air+Water Vapor Environment

6.1. Abstract

This work focuses on the oxidation resistance of a new class of composites, chromium carbide coated silicon carbide-nanostructured ferritic alloy (Cr_3C_2@SiC-NFA) composite, in a water vapor containing atmosphere at 500-1000^{o}C. Oxidation temperature effects on surface morphologies, scale characteristics and cross-sectional microstructures are investigated and analyzed. The Cr_3C_2@SiC content in the composites is strongly associated with the oxidation resistance by forming a dense Cr- and Si-rich inner-layer, which can be explained based on the Thermo-Calc simulation. The fundamental understandings offer important guidance for the applications of this class of composites in nuclear reactors and high temperature moist environments.

6.2. Introduction

Previous work from our group focused on the high temperature water vapor oxidation behaviors of NFA-SiC and SiC-NFA composites without any reaction barrier layers on the two initial powders (NFA or SiC) [151, 158]. Previous chapter discussed oxidation behavior of SiC-C@NFA composites. In this chapter, the oxidation resistance of newly developed Cr_3C_2@SiC-NFA composites was studied in an air+H_2O(g) environment between 500^{o}C-1000^{o}C. Weight changes along with surface microstructures, morphologies, and phases were studied in order to understand the effects of temperature and Cr_3C_2@SiC content on the corrosion resistance and the mechanisms of oxidation for the Cr_3C_2@SiC-NFA composites.

6.3. Materials and methods

Cr_3C_2@SiC-NFA (Fe-9Cr-2W-0.4Ti-0.2V-0.12C-0.3Y_2O_3, wt%) composite samples with 5-25 vol% Cr_3C_2@SiC were prepared by spark plasma sintering (SPS) at 850^{o}C and 950^{o}C. Detailed information on the microstructures, densities, and hardness results of these composites are reported in a previous chapter. In this work, oxidation tests were performed in a tube furnace (1730-20 HT Furnace, CM Furnace Inc., Bloomfield, NJ). The gas flow mixture was composed of air (55 vol%)-water vapor (45 vol%) at the condition of ~1.2 L·min^{-1} and 1 atm pressure. All the thermal treatment experiments were conducted at three different temperatures, 500^{o}C, 750^{o}C, and 1000^{o}C, for 50 hrs. The weights of all the composites were measured before and after the thermal treatment. The weight changes were normalized with respect to the area of each specimen by physically measuring the composite dimensions.

Phase composition analysis was carried out using an X-ray diffractometer (XRD, PANalytical B.V., Almelo, Netherlands) with Cu-Kα radiation at operating condition of 45 kV/40 mA. Surface morphologies, cross-section microstructures, and elemental compositions were observed using scanning electron microscopy (SEM, FEG E-SEM QUANTA600, FEI Company, Hillsboro, OR, USA) and the attached energy dispersive spectroscopy (EDS) module.

Electron backscattered diffraction (EBSD, SEM-FEI Company, Hillsboro, OR, USA) was used to identify the phases in the oxidation layer. Measurements were performed at 70^o tilt angle with respect to the horizontal axis of the SEM at 30 kV accelerating voltage. The EDAX TEAM software was used to collect data and then match with the existing diffraction database.

Temperature effect on the phase fraction of the Cr_3C_2@SiC-NFA composites and the diffusivity of silicon (Si) and chromium (Cr) in NFA were calculated using the Thermo-Calc® software in order to obtain fundamental understanding of the oxidation mechanisms of the Cr_3C_2@SiC-NFA composites.

6.4. Results and discussion

6.4.1. Physical changes

Fig. 6.1 shows the (area) specific mass change and oxide layer thickness of different Cr_3C_2@SiC-NFA composites after the water vapor thermal treatment at 500ºC, 750ºC, and 1000ºC. As shown in Figs. 6.1a and 6.1c, the mass gains of the 5 vol% Cr_3C_2@SiC-NFA composites (~77 mg/cm^2) are 35 times higher than that of the 25 vol% Cr_3C_2@SiC-NFA composites (~2.2 mg/cm^2) after the treatment at 1000ºC for both the 850ºC and 950ºC sintered composites. The 15 vol% Cr_3C_2@SiC-NFA composite sintered at 850°C shows much higher mass gain than that sintered at 950°C after the 1000°C thermal treatment (26 vs. 8.4 mg/cm^2). The 500ºC and 750ºC treated composites with all Cr_3C_2@SiC contents show no significant difference (all within a range of 0.1-2.5 mg/cm^2) in mass gains. Figs. 6.1b and 6.1d show the Cr_3C_2@SiC content effect on the oxide layer thickness of the 1000ºC treated Cr_3C_2@SiC-NFA composites sintered at 850ºC and 950ºC respectively, which were calculated by dividing the area of the oxide layer by the corresponding length on the composite surface to take into consideration of the varying oxide layer thickness. The 25 vol% Cr_3C_2@SiC-NFA composites have significantly lower thickness (15-25 μm) than those of the 5 vol% Cr_3C_2@SiC-NFA composites (900-950 μm) for both 850ºC and 950ºC sintering temperatures. The 15 vol% Cr_3C_2@SiC-NFA composite sintered at 850°C shows much higher oxide layer thickness than that sintered at 950°C after the 1000°C thermal treatment (407 μm vs. 104 μm). The 500ºC and 750ºC treated composites of all Cr_3C_2@SiC contents show no significant difference (all within a range of 2-12 μm) in the oxide layer thickness. The thickness measurements in Figs. 6.1b and 6.1d correspond well with the mass gain results in Figs. 6.1a and 6.1c.

During the thermal treatment in an oxidizing environment, there are two causes for mass change: metal vaporization and/or spallation of the oxide layer for weight loss and uptake of oxygen from the air+H_2O atmosphere for mass gain. Mass gains have been observed for all the composites as shown in Figs. 6.1a and 6.1c. This means that metal vaporization and spallation are not as significant as metal oxidization. Ferritic alloys are less prone to spallation of oxide scales compared to austenitic or duplex alloys, due to the small difference between the thermal expansion

coefficients of the substrate and the corresponding oxides (~18.4×10^{-6} $^{o}C^{-1}$ for austenitic alloys and ~$4.8-15.6\times 10^{-6}$ $^{o}C^{-1}$ for ferritic alloys at 650–800^{o}C) [159]. The obvious increase in mass gains and oxide layer thicknesses for the 1000^{o}C thermally treated 5 vol% and 15 vol% Cr_3C_2@SiC-NFA composites, compared to the 25 vol% Cr_3C_2@SiC-NFA composites, can be attributed to the early onset of 'breakaway oxidation' for the lower Cr_3C_2@SiC composites. The breakaway oxidation involves localized cracking and spallation of the protective oxide layer, which are believed to create O_2 transport channels to the metal surface beneath the oxide layer and thus expose the NFA surface for intensified oxidation damage.

The addition of Cr_3C_2@SiC in the NFA has significantly delayed the breakaway oxidation and improved the high temperature oxidation resistance. The oxidation resistance of the 950^{o}C sintered 15 vol% Cr_3C_2@SiC-NFA composites is much better than that of the 850^{o}C sintered counterparts, as pointed out above. The 25 vol% Cr_3C_2@SiC-NFA composite is most oxidation resistance and the sintering temperature effect is negligible. It is believed that the higher Si content in the NFA matrix after the higher temperature sintering (Si/Fe ration of 0.03-0.08 for the 950°C sintered samples vs 0.01 for the 850°C sintered samples [160]) is beneficial for the formation of dense protective layers for oxidation resistance (to be further discussed in later sections). However, the 5 vol% Cr_3C_2@SiC-NFA composites are equally affected for both sintering temperatures, which means that 'breakaway oxidation' is more predominant due to the lower content of Cr_3C_2@SiC.

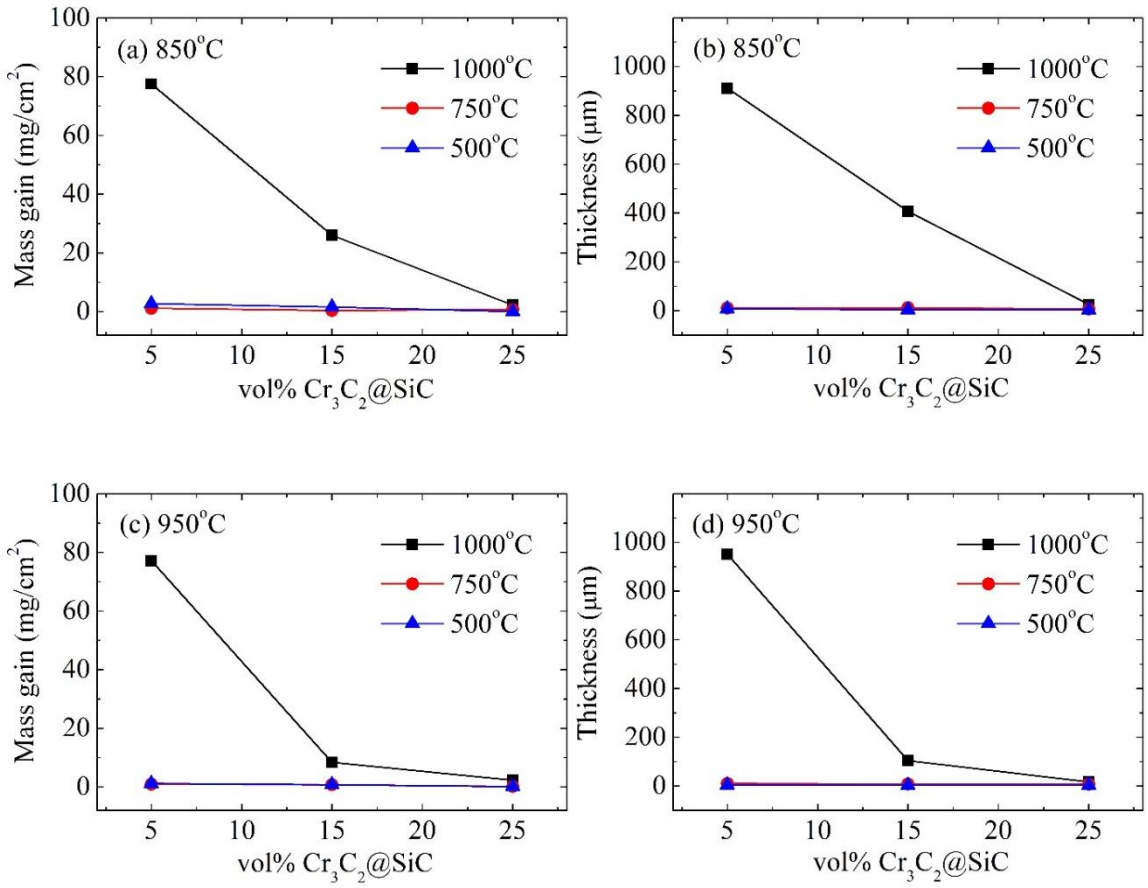

Fig. 6.1. Effect of Cr_3C_2@SiC content on the mass gain and oxide layer thickness of the water vapor treated Cr_3C_2@SiC-NFA composites sintered at 850°C (a and b) and 950°C (c and d). (The error bars for the mass gain and thickness are estimated within ±0.11 g/cm^2 and ±5 μm, respectively).

6.4.2. Phase compositions

Fig. 6.2 shows the XRD patterns of the 850°C (a) and 950°C (b) sintered composites after the thermal treatment at 500°C, 750°C, and 1000°C. The composites thermally treated at 500°C and 750°C show a mixture of hematite (Fe_2O_3) and α-Fe (BCC) phases. The α-Fe peaks are from the underlying NFA due to the thin oxide thickness on the surfaces, which is consistent with the low values of mass gain and thickness for the 500°C and 750°C treated composites shown in Fig.

6.1. The XRD patterns of the 1000°C treated composites show different phases as seen in Fig. 6.2. Both the 850°C and 950°C sintered 5 vol% Cr_3C_2@SiC-NFA composites show the hematite (Fe_2O_3) phase with high intensity (006) peaks. This indicates the presence of preferentially oriented hematite grains in the top layer of the thick oxide scale. The 850°C sintered 15 vol% Cr_3C_2@SiC-NFA composite exhibits hematite and magnetite (Fe_2O_3+ Fe_3O_4) phases, while the 950°C sintered 15 vol% Cr_3C_2@SiC-NFA composite shows preferentially oriented hematite phase with the (110) peak as the highest, different from the 5 vol% Cr_3C_2@SiC-NFA composite. The 850°C and 950°C sintered 25 vol% Cr_3C_2@SiC-NFA composites show Cr-rich $(Cr,Fe)_2O_3$ phase with some α-Fe peaks as shown in Fig. 6.2. The results indicate that higher Cr_3C_2@SiC content promotes the formation of the more protective Cr-rich $(Cr,Fe)_2O_3$ scale during the 1000°C water vapor thermal treatment. The presence of the α-Fe peaks also indicates a thinner oxide layer compared to those of the 5 and 15 vol% Cr_3C_2@SiC-NFA composites. With the thermal treatment temperature increase, the surface layer transitions from pure Fe_2O_3 to Fe_2O_3/$(Fe,Cr)_2O_3$+Fe_3O_4. However, higher Cr_3C_2@SiC-NFA content stops this change by inducing the Cr-rich $(Cr,Fe)_2O_3$ phase.

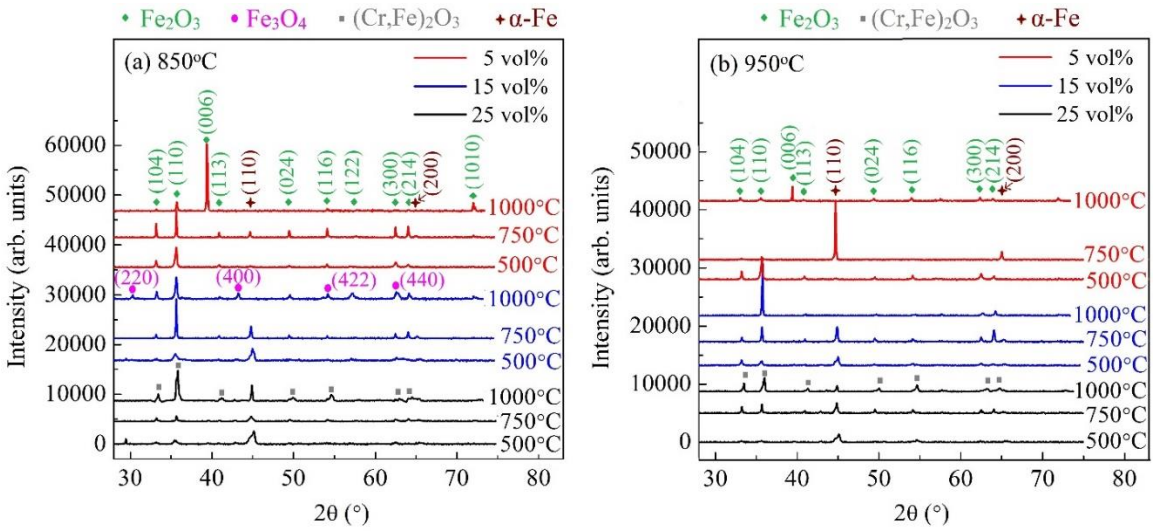

Fig. 6.2. XRD patterns of 850°C (a) and 950°C (b) sintered Cr_3C_2@SiC-NFA composites after the water vapor thermal treatment at 500°C, 750°C, and 1000°C.

6.4.3. Oxidation layer evolutions

Figs. 6.3 and 6.4 shows the surface morphologies of 850^{o}C and 950^{o}C sintered composites after the thermal treatment at 500^{o}C, 750°C, and 1000°C. The 850^{o}C sintered composites have similar morphologies and the discussion is omitted here for brevity (see Fig. 6.3). The 950^{o}C sintered 5 vol% Cr_3C_2@SiC-NFA composites show porous flake type structures throughout the sample surface as shown in Fig. 6.4a. The 15 vol% Cr_3C_2@SiC-NFA composites show regions with flake structures and regions without. The latter is thin oxidation layers, as indicated by the arrows in Fig. 6.4b. The uneven oxidation layers indicate less oxidation for the 15 vol% Cr_3C_2@SiC-NFA compared to the 5 vol% Cr_3C_2@SiC-NFA. This result is also consistent with the weight gain and oxidation layer thickness data in Fig. 6.1. The 25 vol% Cr_3C_2@SiC-NFA composite exhibits fine grained structure as shown in Fig. 6.4c. This surface structure is fairly dense (right image of Fig. 6.4c) and thus more protective compared to the porous flake structures in Figs. 6.4a and 6.4b.

Figs. 6.4d, 6.4e and 6.4f show the surface morphologies of the 950^{o}C sintered composites treated at 750^{o}C. All three composites show larger flake structures in the form of islands growing on a flat oxidation layer. The oxidation layer of the 5 vol% Cr_3C_2@SiC-NFA composite shows interconnected cracks as indicated in Fig. 6.4d. The 15 and 25 vol% Cr_3C_2@SiC-NFA composites exhibit denser and crack-free oxidation layers. The areas covered by the flake islands decrease and the flat oxidation regions increase with more addition of Cr_3C_2@SiC.

For all the 500^{o}C (Figs. 6.4a-6.4c) and 750^{o}C (Figs. 6.4d-6.4f) treated composites, even though the surface morphologies indicate lower damages with an increasing amount of Cr_3C_2@SiC, only marginal changes are observed for the mass gain and the oxidized layer thickness in Fig. 6.1. This means that no significant breakdown oxidation damages have commenced for both the 850^{o}C and 950^{o}C sintered Cr_3C_2@SiC-NFA composites.

The surface morphologies of the 950^{o}C sintered composites thermally treated at 1000^{o}C are shown in Figs. 6.4g-6.4i. The 5 vol% Cr_3C_2@SiC-NFA composite exhibits preferentially oriented rib-type morphology with small pores and cracks in Fig. 6.4g, which is consistent with the cracks in Fig. 6.4d as well as the appearance of the single highest intensity XRD peak of (006)

in Fig. 6.2b. The 15 vol% Cr_3C_2@SiC-NFA composite also shows preferentially oriented flakes, but with very large flake structures growing on crowded and deformed smaller flakes as shown in Fig. 6.4h, different from the 5 vol% Cr_3C_2@SiC-NFA composite. These flake structures are still believed to have the hematite structure, as shown from the highest intensity (110) XRD peak in Fig. 6.2b. Pores and microchannels can also be observed in the 15 vol% Cr_3C_2@SiC-NFA composite as indicated in Fig. 6.4h. It has been reported that H_2O dissociation facilitates transport of oxygen via pores and cracks and aids in oxidation damage [69, 161]. The evaporation of $CrO_2(OH)_2$ should have also contributed to the microchannel formation [151]. The surface morphology of the 25 vol% Cr_3C_2@SiC-NFA composite, however, shows bulky hemispherical island structures. Overall, no pores, cracks, or microchannels can be observed. Thus such phase should be more protective compared to the porous structures for the 5 vol% and 15 vol% Cr_3C_2@SiC composites (Figs. 6.4g and 6.4h). However, such a structure may derive from the early stage of breakaway oxidation (part of the region with breakaway), where the bulky hemispherical islands form from the heavy oxide nucleation sites. The right side of Fig. 6.4i shows magnified structures of both the flat areas (right top) and the hemispherical islands (right bottom). Faceted grains with 1-2 μm size can be observed on the hemispherical islands, while the flat areas show fine-grained structures with few sparsely distributed faceted grains. This means faceted islands and flat areas are different types of oxides. The faceted grains are believed to be Fe_3O_4 type oxide with some Cr diffused in it [162]. The flat areas should be the Cr-rich $(Cr,Fe)_2O_3$ phase, as confirmed by our XRD result in Fig. 6.2. The transport properties of such Cr-rich $(Cr,Fe)_2O_3$ layer can be considered similar to those of a protective chromia (Cr_2O_3) layer other than non-protective Fe-rich porous layers [163]. Thus, the addition of 25 vol% Cr_3C_2@SiC in the composites promotes the formation of protective Cr-rich layers and greatly retards breakaway oxidation, leading to the thinnest oxidation layer (see Figs. 6.1b and 6.1d).

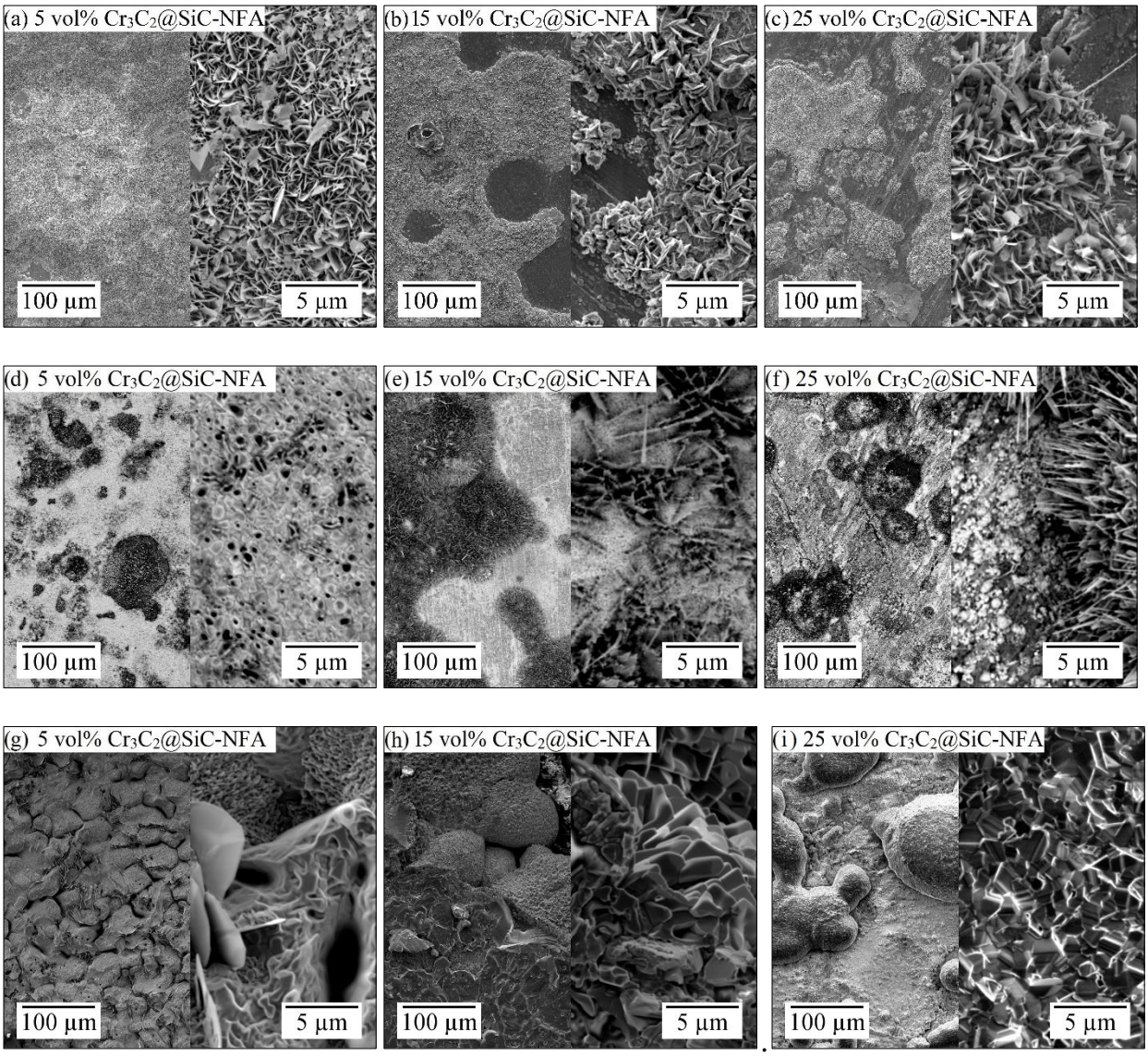

Fig. 6.3. Surface morphologies of the 850°C sintered Cr_3C_2@SiC-NFA composites thermally treated at 500°C (a, b, and c), 750°C (d, e, and f), and 1000°C (g, h, and i). (Right image is the magnified version of left image).

The cracks observed in the oxidation layers for the 750°C treated composite in Fig. 6.4d and for the 1000°C treated composite in Fig. 6.4g for the same 5 vol% Cr_3C_2@SiC-NFA composite show obvious difference. The cracks in Fig. 6.4d occur in some tiny regions and are predominately on the surface, which are probably caused by the relatively high inhomogeneous stress accumulated in some local regions at 750°C. The cracks in Fig. 6.4g locate in-between the grains,

and the crack gaps are relatively large. This is because sintering of the oxidation products on the sample surface happens at 1000ºC. Some grains shrink while others preferentially grow, and finally gaps appear in some areas as observed.

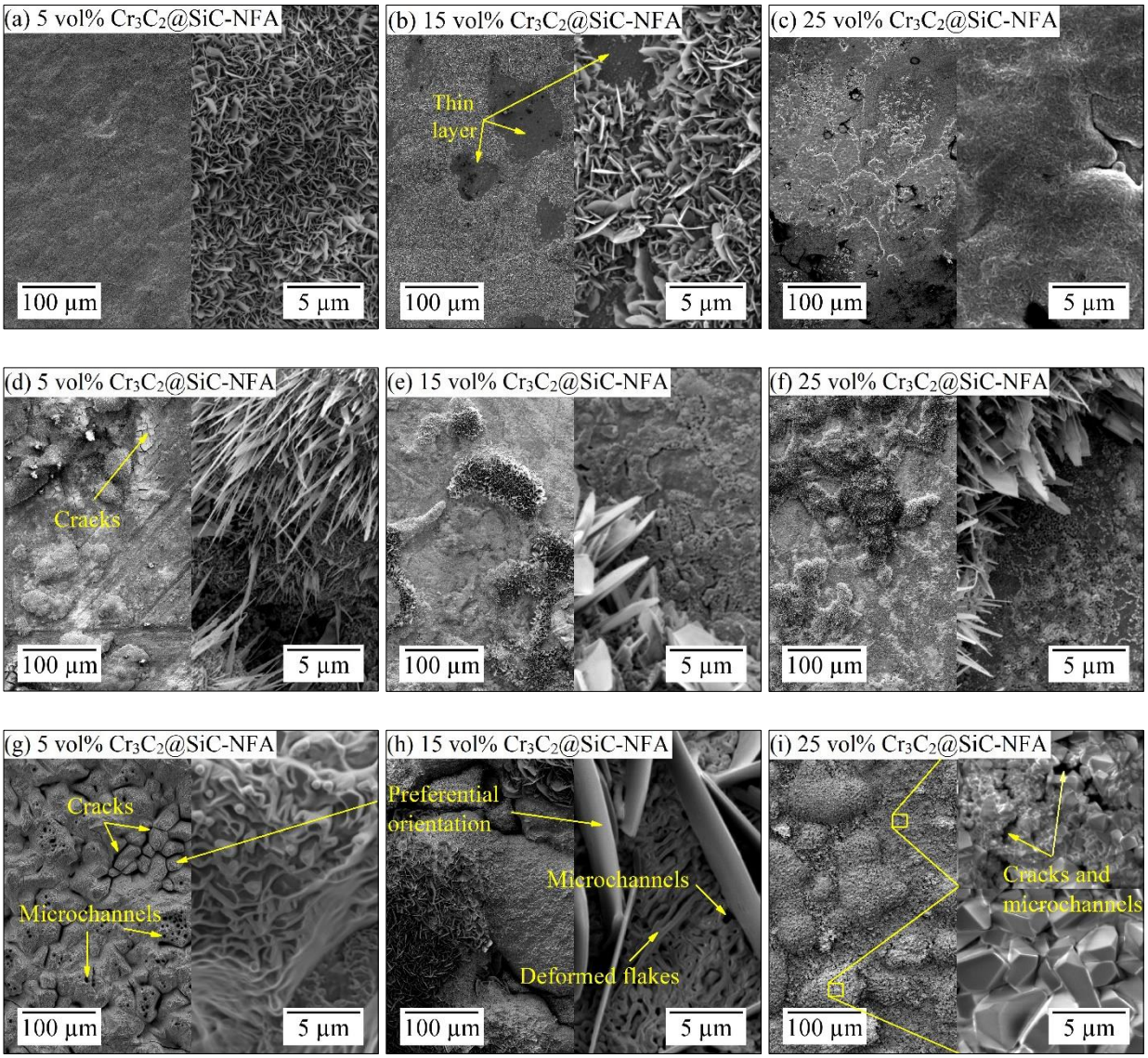

Fig. 6.4. Surface morphologies of the 950ºC sintered Cr_3C_2@SiC-NFA composites thermally treated at 500°C (a, b, and c), 750°C (d, e, and f), and 1000°C (g, h, and i). (Right image is the magnified version of left image).

Fig. 6.5 shows the cross-section microstructures of the 850°C and 950°C sintered Cr_3C_2@SiC-NFA composites treated at 1000°C. Continuous oxide layers are observed for the 850°C and 950°C sintered 5 vol% Cr_3C_2@SiC composites (Figs. 6.5a and 6.5d) and for the 850°C sintered 15 vol% Cr_3C_2@SiC composite (Fig. 6.5b). This means that these composites have undergone considerable oxidation. The islands from the early oxidation stage have merged to form dense and continuous two-layer structures. The enlarged images of the inner oxide layer (bottom images in Fig. 6.5) show three distinct phases with dark, gray, and bright contrast.

The 25 vol% Cr_3C_2@SiC-NFA composites for both sintering temperatures (Figs. 6.5c and 6.5f) and the 950°C sintered 15 vol% Cr_3C_2@SiC-NFA composite (Fig. 6.5e) show island-like structures, which are consistent with the surface morphologies in Figs. 6.4h and 6.4i. The islands for the 950°C sintered 15 vol% Cr_3C_2@SiC-NFA composites are 300-500 μm in width and 150 μm in thickness, while for the 950°C sintered 25 vol% Cr_3C_2@SiC-NFA composite the width and thickness are 80-100 μm and 30-50 μm, respectively. The 850°C sintered 25 vol% Cr_3C_2@SiC-NFA composite has surface island dimensions similar to those of the 950°C sintered sample (see supplement). The region between two islands shows the very thin oxidation layer (~4-5 μm). We conjuncture that the initial areas for the islands are more vulnerable to oxidation and lead to an aggressive growth of the oxidation layer. The island structures are a result of the breakaway oxidation. The smaller size of the islands with increasing Cr_3C_2@SiC content shows the significant delay in the onset of the breakaway oxidation by Cr_3C_2@SiC.

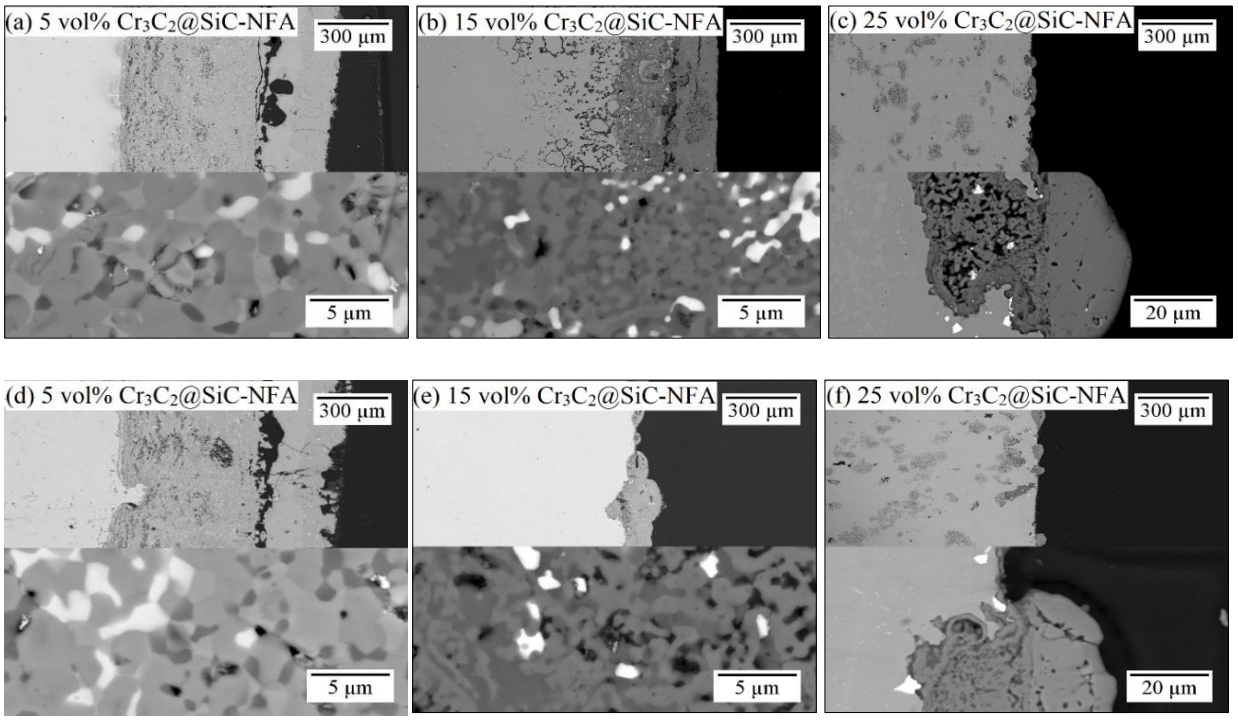

Fig. 6.5. Cross section microstructures of the Cr_3C_2@SiC-NFA composites treated at 1000^{o}C: (a), (b), and (c) 850°C sintered samples; (d), (e), and (f) 950°C sintered samples.

The elemental maps of the oxide layer for 850^{o}C and 950^{o}C sintered 5-15 vol% Cr_3C_2@SiC-NFA composites are shown in Figs. 6.6 and 6.7. The 850^{o}C sintered composites have similar elemental maps, therefore discussion is omitted here for brevity (see Fig. 6.6). Outer- and inner-layer structures can be observed within the oxide scale for all of the samples. For the 5 vol% Cr_3C_2@SiC-NFA composite in Fig. 6.7a, the outer-layer is predominantly Fe- and O-rich, while the inner-layer is Cr-, Si-, and O-rich as well as Fe-deficient. The Fe-rich outer-layer is composed of Fe_2O_3 and Fe_3O_4 phases as identified by the XRD patterns in Fig. 6.2, and the boundary between them can be seen through the slight difference in contrast as shown in Fig. 6.7a. The appearance of Fe_2O_3 and Fe_3O_4 phases has also been reported before for ferritic steels [58, 69]. At the bottom of the inner-layer, a very tiny layer shown in Fig. 6.8. This tiny layer is clearly Cr-, Si-, and O-rich, which is believed to be Cr_2O_3+SiO_2. For the 15 vol% Cr_3C_2@SiC-NFA composite in Fig. 6.7b, the outer-layer is Fe-, Cr-, and O-rich, and the inner-layer is Cr-, Si-, O-rich and Fe-deficient. Compared to the 5 vol% Cr_3C_2@SiC-NFA composite, the outer-layer close to the surface has more Cr diffusion, which is determined to be $(Cr,Fe)_2O_3$ from the XRD patterns in Fig. 6.2b. The outer-

layer away from the surface is believed to be Fe_3O_4, which is without Cr diffusion (Cr depletion). The inner-layer located at the bottom of the bump is much clearer, and has the same composition as the 5 vol% Cr_3C_2@SiC-NFA composite. For the 25 vol% Cr_3C_2@SiC-NFA composite in Fig. 6.7c, the inner-layer is Cr-, Si-, O-rich and Fe-deficient, similar to the 5 and 15 vol% Cr_3C_2@SiC-NFA composites. The outer-layer on the island appears to be Cr-rich and Fe-deficient. Based on the XRD patterns in Fig. 6.2b and the spinel type morphologies in Fig. 6.4i, this is determined to be Cr-rich $(Cr,Fe)_3O_4$. Between the two islands, the outer-layer in both the 15 and 25 vol% Cr_3C_2@SiC-NFA composites is Cr-rich as shown in Figs. 6.7b and 6.7c. This oxide layer is believed to be the highly protective Cr-rich $(Cr,Fe)_2O_3$ layer, consistent with the XRD patterns in Fig. 6.2b. The outer-layer away from the surface within the islands is Fe-rich, similar to that of the 15 vol% Cr_3C_2@SiC-NFA composite; this oxide layer is believed to be Fe_3O_4. The Cr-rich inner-layer is very thin, and can be seen clearly; it is believed that this inner-layer is very dense and has the same compositions as those of the 5 vol% and 15 vol% Cr_3C_2@SiC-NFA composites, which are responsible for the oxidation resistance. The area fraction of the protective thin $(Cr,Fe)_2O_3$ layer is significantly higher for the 25 vol% Cr_3C_2@SiC-NFA composite, consistent with the improved oxidation resistance of the 25 vol% Cr_3C_2@SiC composite. Both the 15 and 25 vol% Cr_3C_2@SiC-NFA composites also show a significant Cr-depletion layer (the outer-layer with Fe_3O_4 phase) away from the Cr-rich islands, ~200 μm and ~50 μm, respectively, as shown in Figs. 6.7b and 6.7c, indicating the source of Cr-enrichment in the islands.

To understand the phase composition for the inner-layer, which is responsible for the oxidation resistance, the EDS image of the inner-layer bottom from the 950°C sintered 5 vol% Cr_3C_2@SiC-NFA composite treated at 1000°C is shown Fig. 6.8, as mentioned during the above discussion. This tiny layer is Cr-, Si-, and O-rich, which is believed to be Cr_2O_3+SiO_2 phases. The EDS maps of the main inner-layer for the 950°C sintered 5 vol% Cr_3C_2@SiC-NFA composite treated at 1000°C are shown in Fig. 6.9. The 850°C sintered composites have similar elemental maps for the inner-layer and are omitted here for brevity (see supplement). The SEM image in Fig. 6.9a shows four types of phases in this inner-layer. The bright phase is W-, Si-rich, and O-deficient as determined from Figs. 6.9e, 6.9d and 6.9f, while the dark phase is Si- and Fe-rich and Cr-deficient as determined from Figs. 6.9d, 6.9b and 6.9c. Such bright phase has been observed by Abe et. al. [153] and identified as Fe_2W. The Si enrichment (in Fig. 6.9d) might be misleading with W enrichment (in Fig. 6.9e), as W and Si have very close EDS energy peaks (Si: Kα 1.739

eV, W: Mα 1.774 eV). The dark phase is believed to be Fe_2SiO_4, which forms due to the solid-state reaction of FeO and SiO_2 as to be discussed in later sections. The matrix of this inner-layer is also divided into two regions, Fe-rich and Cr-rich as shown in Fig. 6.9a. This inner-layer matrix is probably a mixture of Fe_3O_4 and $FeCr_2O_4$ [69]. The SEM image also shows that this inner-layer is dense compared to the outer-layer and can be effective in reducing the outward diffusion of metal cations (Fe^{2+}, Fe^{3+}, Cr^{3+}).

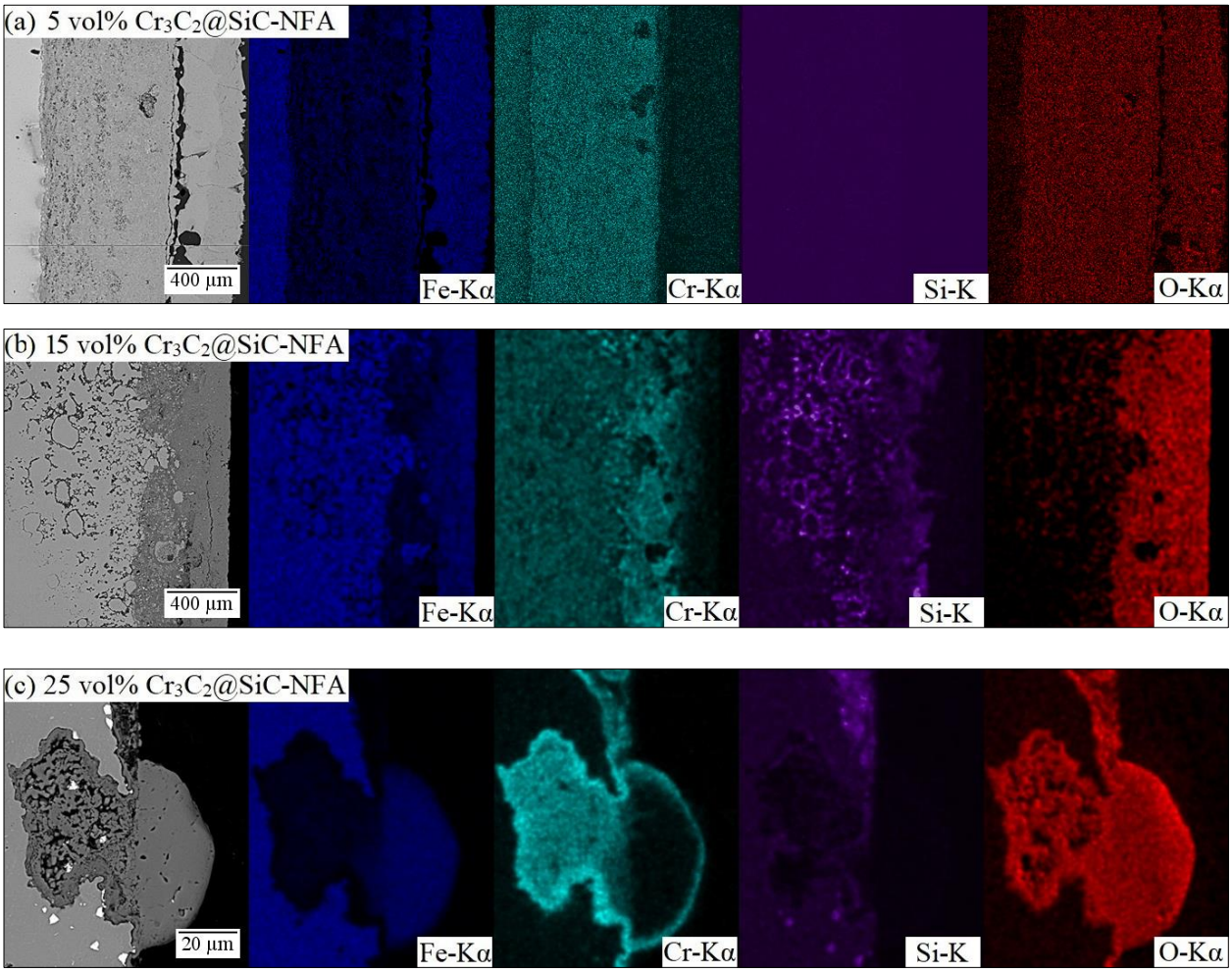

Fig. 6.6. EDS maps of the oxide layer of the 1000°C treated (a) 5 vol%, (b) 15 vol%, and (c) 25 vol% Cr_3C_2@SiC-NFA composites sintered using SPS at 850°C.

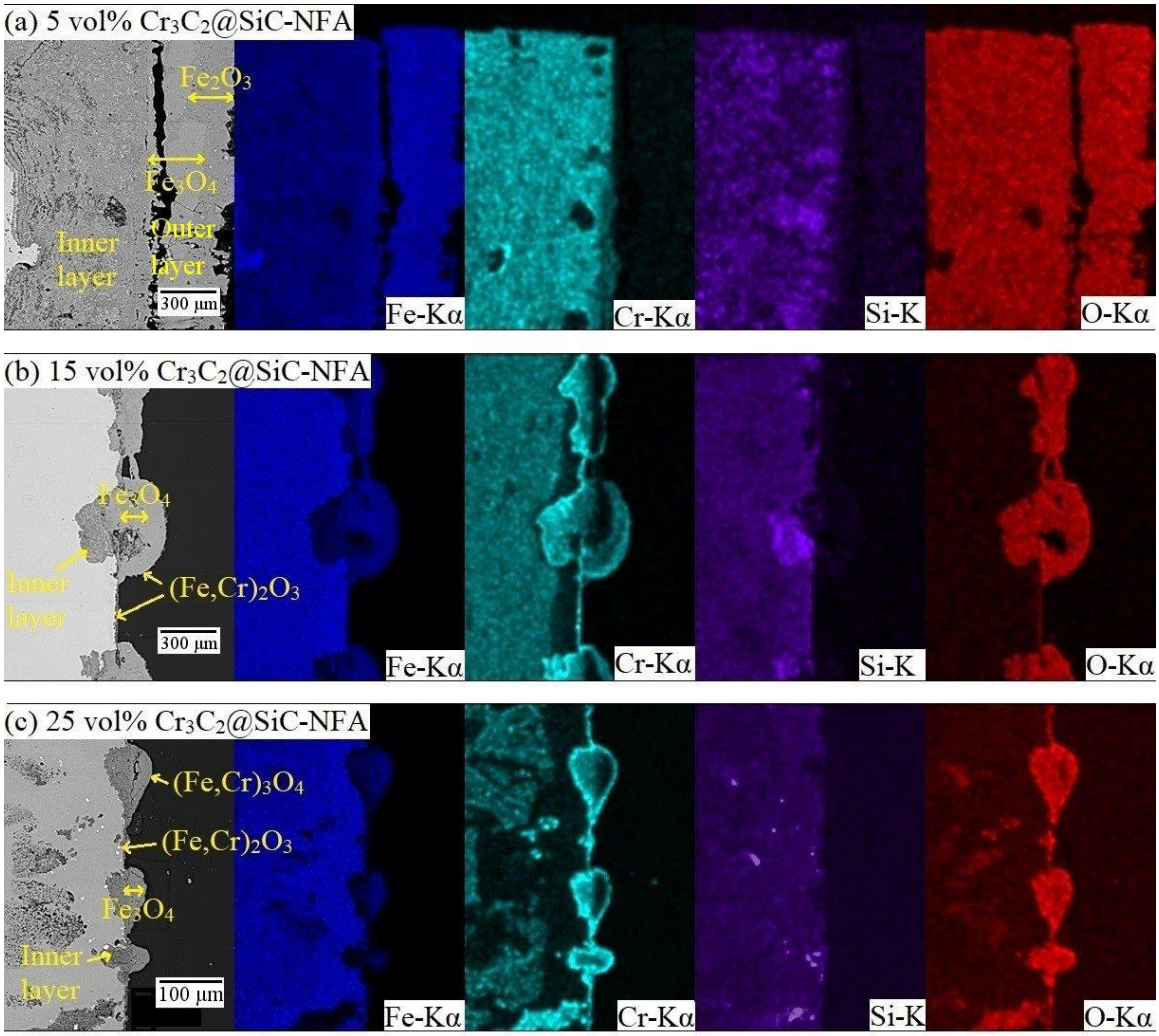

Fig. 6.7. EDS maps of the oxide layers of the 1000ºC treated (a) 5 vol%, (b) 15 vol%, and (c) 25 vol% Cr_3C_2@SiC-NFA composites sintered at 950ºC.

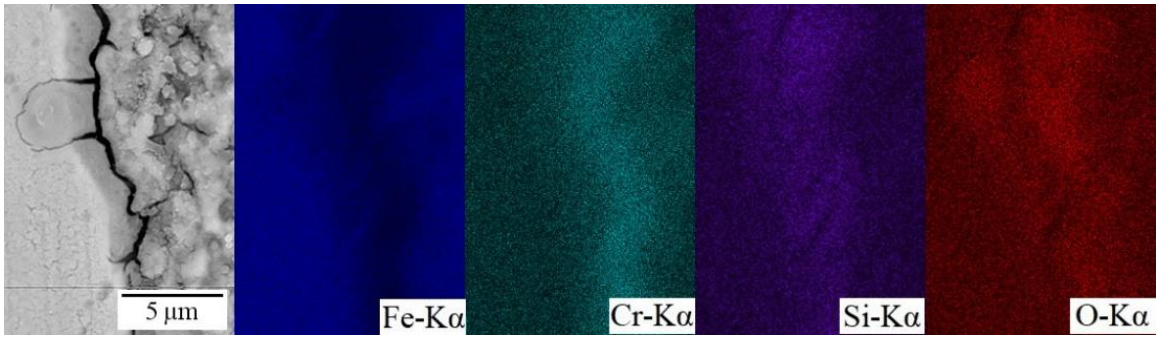

Fig. 6.8. EDS image from the bottom of the inner-layer for the 1000ºC treated 5 vol% Cr_3C_2@SiC-NFA with sintering temperature of 950ºC.

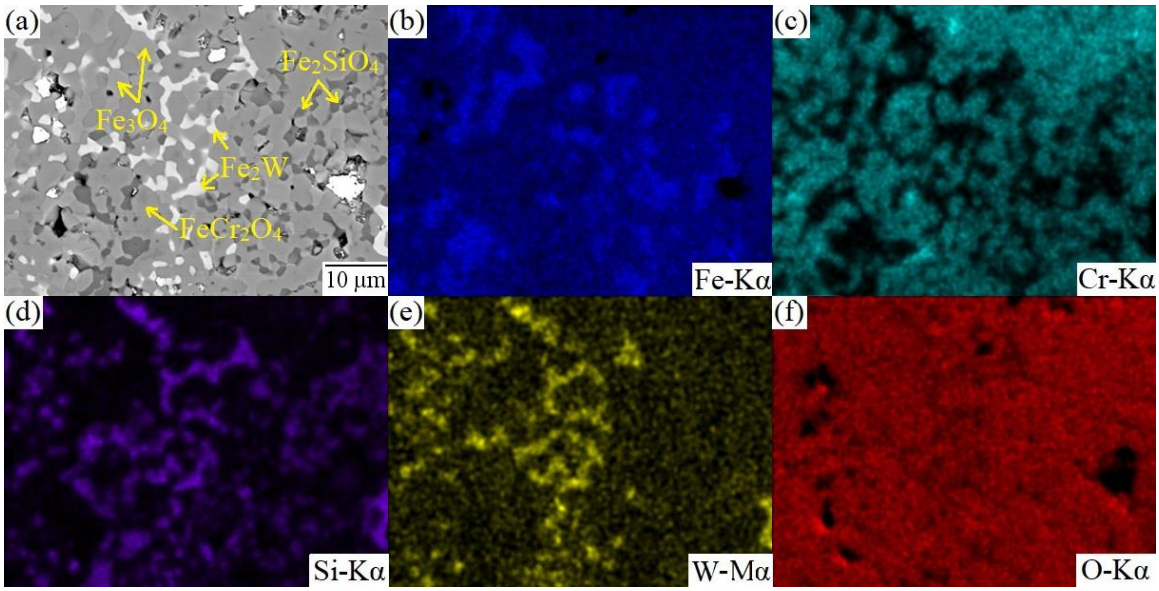

Fig. 6.9. EDS maps of the main inner-layer of the 950ºC sintered 5 vol% Cr_3C_2@SiC-NFA composite after the 1000ºC thermal treatment.

6.4.4. Fundamental understanding of oxidation resistance

Based on our observation and analysis, Fig. 6.10 shows the schematic illustration of the oxide scale growth during the 1000ºC water vapor thermal treatment for the Cr_3C_2@SiC-NFA composites. The oxide scale can be divided into an Fe-rich outer-layer and a Cr-rich inner-layer.

The outer-layer forms due to the outward diffusion of Fe cations (Fe^{2+} and Fe^{3+}) from the bulk, which is believed to happen after the initially formed Cr_2O_3 layer is broken as commonly understood for the high Cr NFA alloy. Since Cr ions diffuse slower than Fe ions [164], the outer-layer is Fe-rich oxide. Cr tends to be oxidized internally to form a Cr-rich inner-layer. The 5 vol% Cr_3C_2@SiC-NFA composite shows the least oxidation resistance and hence forms a very thick oxide scale as shown in Fig. 6.10a. The outer-layer of the Fe-rich scale is as predicted. The outer-layer with Fe_2O_3 and Fe_3O_4 phases are due to the reactions between the water vapor/oxygen (from air) and the composite bulk [151] as follows:

$$2Fe\ (s) + O_2\ (g) + \ H_2O\ (g) = Fe_2O_3\ (s) + H_2\ (g) \tag{6.1}$$

$$3Fe\ (s) + \frac{4}{3}O_2\ (g) + \ \frac{4}{3}H_2O\ (g) = Fe_3O_4\ (s) + \frac{4}{3}H_2\ (g) \tag{6.2}$$

At low Cr_3C_2@SiC content, the main inner-layer contains four different phases: Fe_3O_4 and $FeCr_2O_4$, Fe_2SiO_4, and Fe_2W. The $FeCr_2O_4$ and $FeSi_2O_4$ phases are due to the following solid state reactions of short lived FeO with stable oxides such as Cr_2O_3 and SiO_2 respectively [69, 165]:

$$FeO\ (s) + Cr_2O_3\ (s) = \ FeCr_2O_4(s) \tag{6.3}$$

$$2FeO\ (s) + SiO_2(s) = Fe_2SiO_4(s) \tag{6.4}$$

As stated earlier (from Fig. 6.9), the main inner-layer is a mixture with the major $FeCr_2O_4$ and Fe_3O_4 phases. Such metastable mixed layer [69, 165] is related to the inherent inhomogeneous distribution of Cr and its low diffusivity. Fe_2SiO_4 appears in the form of precipitates but not as a continuous layer as shown in Fig. 6.9. Therefore, even though the diffusion of Fe cations is much slower in Fe_2SiO_4 [166], it is unlikely to contribute much towards oxidation resistance. The bright

phase in the main inner-layer is W-rich and Fe-, C-, O-deficient. A presence of Fe_2W-laves phase is matches well with the literature [153].

The inner-layer of the 15 and 25 vol% Cr_3C_2@SiC-NFA composites shows similar phase compositions of Fe_3O_4 and $FeCr_2O_4$, Fe_2SiO_4, and Fe_2W (as illustrated in Figs. 6.10b and 6.10c). At the bottom of the inner-layer, it is believed that there is a tiny Cr_2O_3+SiO_2 layer, which happens for all the three composites. This tiny Cr_2O_3+SiO_2 layer is the first barrier for oxidation resistance of the Cr_3C_2@SiC-NFA composites, and its formation capability and healing ability are dependent on diffusivities of Cr and Si contents in the composites during the treatment, which will be discussed later.

One of the major effects of the water vapor is the formation of volatile species after the reaction with the oxide layers. Asteman et. al. [167] showed that the reaction between the protective chromia scale and water is one of the main reasons triggering breakaway oxidation:

$$\frac{1}{2}Cr_2O_3 + \frac{3}{4}O_2(g) + H_2O(g) = CrO_2(OH)_2(g) \quad (6.5)$$

Cracks and microchannels are observed for the Fe-rich scale of the 1000ºC treated 5 vol% Cr_3C_2@SiC-NFA composite as shown in Fig. 6.4g. The microchannels end at the gap in the magnetite (Fe_3O_4) layer as shown in Fig. 6.10a. The water vapor reacts with the scale to form volatile products and leads to cracks as well as microchannels in the outer-layer [69, 163]. The microchannels indicate an outward evaporation path of the volatile products. The reactions are as follows:

$$Fe_2O_3 + 2H_2O(g) = 2Fe(OH)_2(g) + \frac{1}{2}O_2(g) \quad (6.6)$$

$$Fe_3O_4 + 3H_2O(g) = 3Fe(OH)_2(g) + \frac{1}{2}O_2(g) \quad (6.7)$$

The gap in the magnetite (Fe_3O_4) phase of the outer-layer can stop the Fe^{2+} and Fe^{3+} diffusion required for the further growth of the outer-layer. Fig. 6.7a shows that the outer-layer is far thinner than the inner-layer. This means that the inner-layer keeps growing despite of the gap. The dissociation of water vapor in this gap is the major contributor of oxygen for the enhanced growth of the inner-layer in Fe-Cr alloys [69]. The cracks and microchannels in the outer-layer also facilitate the direct access of water vapor and oxygen to the inner-layer [57, 58, 69, 163, 168].

The top regions of the outer-layers of the 1000^{o}C treated 15 and 25 vol% Cr_3C_2@SiC-NFA composites are Cr-rich as illustrated in Figs. 6.10b and 6.10c. This is due to the protective Cr_2O_3+SiO_2 layer between the oxide and the composite, which decreases the Fe^{2+} and Fe^{3+} migration to the outer-layer. EDS maps in Figs. 6.7b and 6.7c show that the top regions of the outer-layers in the 15 vol% Cr_3C_2@SiC-NFA composite are both Fe- and Cr-rich while that of the 25 vol% Cr_3C_2@SiC-NFA is only Cr-rich. With the increase in Cr_3C_2@SiC content, Fe cation (Fe^{2+} and Fe^{3+}) migration is greatly retarded. Due to the lower supply of Fe cations (Fe^{2+} and Fe^{3+}) for the 25 vol% Cr_3C_2@SiC-NFA composite, the formation of the $(Cr,Fe)_2O_3$ phase is suppressed, leaving the top region of the outer-layer as the Cr-rich $(Cr,Fe)_3O_4$ phase. Another reason for the Cr-rich top region of the out-layer can be back-deposition of gaseous $CrO_2(OH)_2$ in the form of Cr_2O_3. Since the 5 vol% Cr_3C_2@SiC sample does not have the Cr-rich outer-layer, the Cr depletion below the oxide layers in the 15 vol% and 25 vol% Cr_3C_2@SiC samples is an evidence of Cr evaporation in the water vapor atmosphere. Some of this $CrO_2(OH)_2$ might redeposit back to the surface by the reverse reaction of Eq. (6.5), while most of it is lost in the flowing gas. This explains net reduction in Cr with the enhancement in breakaway oxidation.

Even though the presence of SiO_2 in the protective inner-layer cannot be observed in the current work, such layer is likely to form because of the relatively high concentration of Si (2-13 wt%) in the composites, based on the EDS observation from Fig. 6.8. The failure to directly detect SiO_2 is due to the very small thickness of such film, as observed in previous work on NFA-SiC composites (~330 nm) [160]. A very thin amorphous SiO_2 layer between the oxide and substrate interface during the oxidation of Si containing steels has also been reported elsewhere (~200 nm) [79, 153]. Such Cr_2O_3 + SiO_2 protective layer (observed from Fig. 6.8) is believed to be responsible for the oxidation protection due to the low diffusivities of both cation (Fe^{3+}, Fe^{2+}, Cr^{3+}) and anion (O^{2-}) species.

The growth rate of the protective Cr_2O_3/SiO_2 layer for the 5 vol%, 15 vol%, and 25 vol% Cr_3C_2@SiC-NFA composites can be expressed as follows [165]:

$$z\frac{dz}{dt} = \frac{D(\overline{X} - X_{interface})^2}{2(X_{oxide} - X_{interface})(X_{oxide} - \overline{X})} \quad (6.8)$$

where X_{oxide}, $X_{interface}$, and $\bar{X}$ refer to the mole fractions of the cation species (Cr or Si) in the oxide, oxide-substrate interface, and substrate, respectively. D is the diffusivity of Cr or Si in the NFA matrix. If assuming X_{oxide}, $X_{interface}$, and $\bar{X}$ stay constant, the growth rate in Eq. (6.8) can be determined from the diffusivity D. Higher diffusivity leads to higher oxide layer growth rate.

The diffusivity D varies with the matrix phases, which are strongly affected by the thermal treatment temperature. The Thermo-Calc® simulation results (Fig. 6.11) demonstrate different α (BCC) and γ (FCC) mass fractions at different thermal treatment temperatures. α-Fe (BCC) is the major phase for all the Cr_3C_2@SiC-NFA composites at 500°C and 750°C treatment temperatures. However, at 1000°C treatment temperature only the 25 vol% Cr_3C_2@SiC-NFA composite has α-Fe (BCC) as the major phase while the 5 vol% and 15 vol% Cr_3C_2@SiC-NFA composites mainly contain γ-Fe (FCC) phase.

The concentrations of Cr and Si in the NFA matrix of the composites can be obtained by considering the elemental contributions of the starting Cr_3C_2@SiC-NFA composite as shown in Fig. 6.12a. The concentration of Cr decreases marginally with the addition of Cr_3C_2@SiC, while the concentration of Si increases significantly with the addition of Cr_3C_2@SiC. The diffusivities of Si (D_{Si}) and Cr (D_{Cr}) in the NFA matrix can be obtained from the Thermo-Calc® software as shown in Fig. 6.12b. The diffusivities of Cr and Si in the 15 and 25 vol% Cr_3C_2@SiC-NFA composites at the 1000°C treatment condition are almost 2 orders of magnitude higher than those in the 5 vol% Cr_3C_2@SiC-NFA composite. This means that the 15 and 25 vol% Cr_3C_2@SiC composites have higher capability forming the protective Si/Cr oxide layers when the breakaway oxidation happens, thus quicker healing ability before extensive damage proceeds.

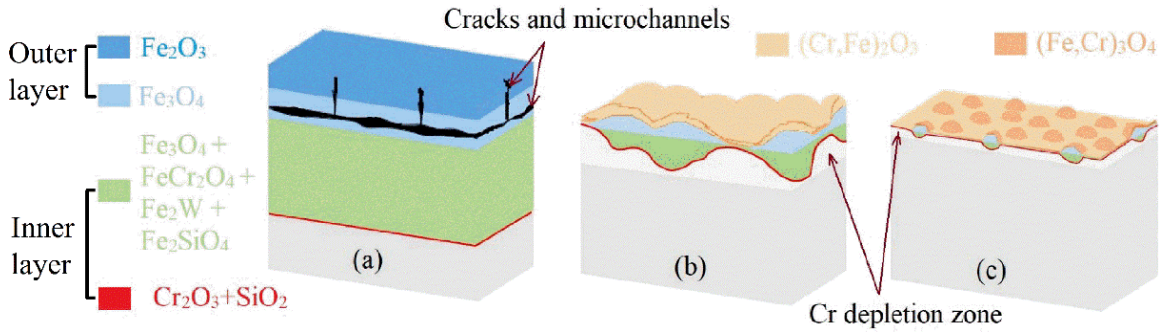

Fig. 6.10. Schematic representation of the oxide scale growth during the water vapor thermal treatment at 1000°C with increasing volume fraction of Cr_3C_2@SiC in the Cr_3C_2@SiC-NFA composites, (a) low Cr_3C_2@SiC content, (b) intermediate Cr_3C_2@SiC content

The thin oxidation outer-layer between two islands in both the 15 and 25 vol% composites is the Cr-rich $(Cr,Fe)_2O_3$ layer. Significant Cr depletion can be observed beneath this film (Figs. 6.10b and 6.10c), likely through Cr evaporation by reaction with water vapor (Eq. (6.5)). The cracks and microchannels in the thin oxidation layer (Fig. 6.4) also support this explanation. Thus during the breakdown of such protective film with oxidation, the matrix will not be able to supply enough Cr to allow the regrowth of such protective film. The Fe-rich regions then undergo heavy oxidation, similar to the 5 vol% Cr_3C_2@SiC-NFA composite. Therefore, Cr_3C_2@SiC can only delay the breakaway oxidation but not completely stop it.

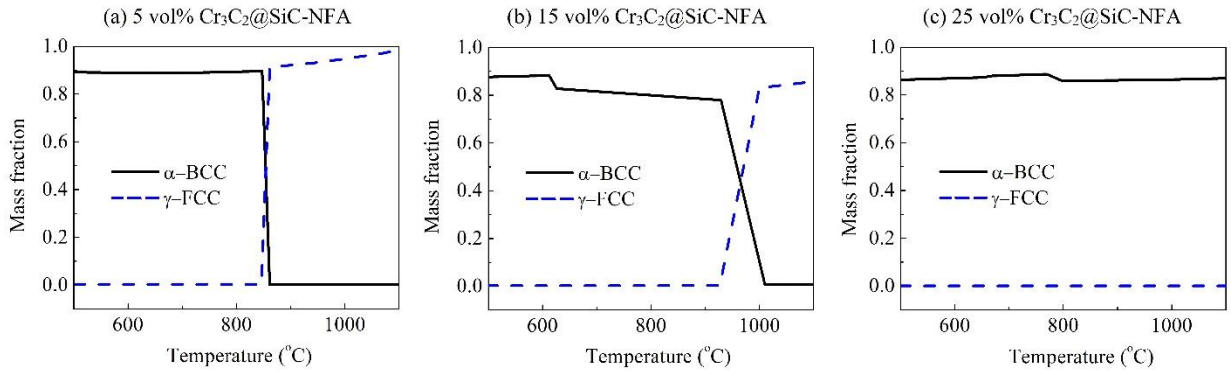

Fig. 6.11. Mass fraction of α and γ Fe phases with temperature for (a) 5 vol%, (b) 15 vol%, (c) 25 vol% Cr_3C_2@SiC-NFA composites based on the Thermo-Calc® simulation.

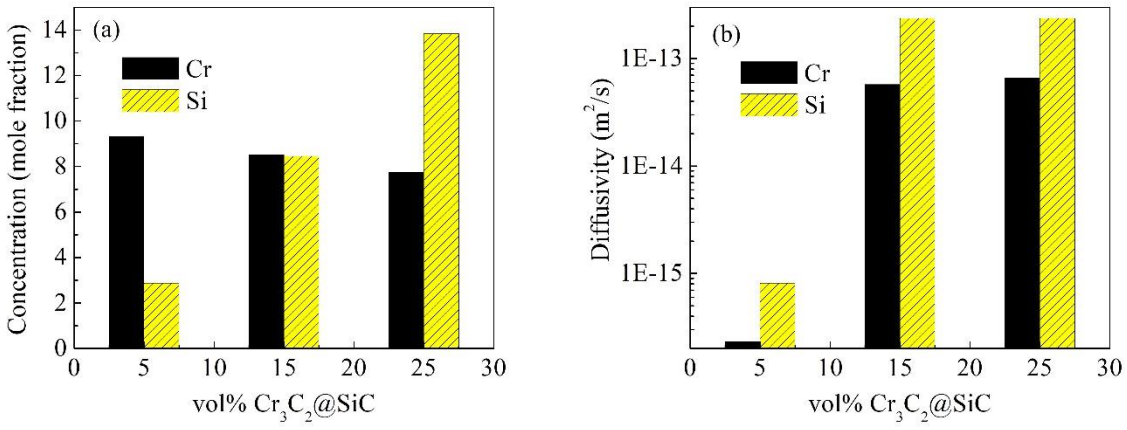

Fig. 6.12. Effect of Cr3C2@SiC addition on (a) concentration of Cr and Si, and (b) diffusivity of Cr and Si in the NFA matrix at 1000°C thermal treatment condition.

6.5. Conclusions

In this work, NFA with 5, 15 and 25 vol% Cr_3C_2@SiC addition has been thermally treated at 500°C, 750°C and 1000°C in the presence of water vapor. The 5 vol% Cr_3C_2@SiC sample shows almost 40 times more oxidation damage than the 25 vol% Cr_3C_2@SiC samples with porous surface morphology. The oxidation layer is predominantly hematite for the 500°C and 750°C treated samples. At 1000°C thermal treatment, the samples show more protective Cr-rich layers with increasing Cr_3C_2@SiC content. The multi-layer structures for each composition is systematically analyzed. The improved oxidation resistance for the 1000°C treated 15 and 25 vol% Cr_3C_2@SiC-NFA is attributed to higher diffusivities of Cr and Si in the α-Fe phase, which significantly boost the healing ability of the breakaway protective Cr- and Si-rich layer (Cr_2O_3 + SiO_2) and thus delay the onset of breakdown oxidation. The results show promising applications of the Cr_3C_2@SiC-NFA composites for harsh water vapor containing environments, especially as nuclear cladding materials.

Chapter 7

Microstructural Evolution of a Silicon Carbide – Carbon Coated Nanostructured Ferritic Alloy Composite during In-Situ Kr Ion Irradiation at 300ºC and 450ºC

7.1. Abstract

Silicon carbide and carbon coated nanostructured ferritic alloy (SiC-C@NFA) composites are promising cladding materials for next-generation reactors. In this study, this material system was irradiated with 1 MeV Kr ions up to 10 dpa at 300 and 450ºC. Microstructures and defect evolution were studied in-situ at the IVEM-Tandem facility at Argonne National Laboratory. The effects of ion irradiation on various phases such as α-ferrite matrix, $(Fe,Cr)_7C_3$, and (Ti,W)C precipitates were evaluated. The α-ferrite matrix showed a continuous increase in dislocation density along with spatial ordering of dislocation loops (or loop strings) at >5 dpa. The size of the dislocation loops at 450ºC was larger than that at 300ºC. The nucleation and growth of new (Ti,W)C precipitates in α-ferrite grains were enhanced with the ion dose at 450ºC. This study provides new insight into the irradiation resistance of the SiC-C@NFA system.

7.2. Introduction

Understanding microstructure and property changes due to irradiation is very important in order to ensure the safety of reactors as well as to provide guidance for the design of novel irradiation resistant materials. Heavy ion irradiation can generate cascade type damage, similar to that observed in neutron irradiation [169-171]. Ion irradiation experiments are inexpensive and can provide better control over temperature, dose rate, and damage level. Absence of residual radioactivity in irradiated materials also makes it much easier to handle the specimens and characterize the microstructures [169, 172]. The displacement cascade damage results in the

formation of defect clusters, dislocation loops, and voids, which can be studied either after irradiation (ex-situ) or during irradiation (in-situ) [170]. In-situ observation of various defects and dislocations provides valuable real-time information on the evolution of these defects and their interactions at different temperatures, dose rates, and damage levels [171, 173].

This work is focused on the in-situ Kr ion irradiation of the SiC-C@NFA material at 300^{o}C and 450^{o}C using the IVEM-Tandem facility at Argonne National Laboratory. The microstructural evolution of various phases in the SiC-C@NFA system during the ion irradiation was characterized.

7.3. Materials and methods

The NFA powder was made by arc melting of a ferritic steel powder (Fe-9Cr-2W-0.4Ti-0.2V-0.18C, in wt%) with 0.3% Y_2O_3 in an argon atmosphere (~15 μm average size, provided by Dr. T. S. Byun from Pacific Northwest National Laboratory). The SiC powder (Grade UF-15, α-SiC, ~1.25 μm average size, H.C. Starck, Karlsruhe, Germany) was coated with carbon as detailed in our earlier work [126]. A 25 vol% SiC-C@NFA mixture was sintered using SPS at 950^{o}C. The details of the sintering process and the resultant properties can be found elsewhere [126]. In brief, the microstructure contained a Si-diffused NFA (NFA_{Si}) matrix, various carbides (e.g., $(Fe,Cr)_7C_3$ and (Ti,W)C), and graphite precipitates due to the reactions between SiC and C@NFA. For TEM examination, the SiC-C@NFA sample was cut using a low speed saw (Isomet, Beuhler, IL, USA) to obtain a 300 μm thick foil. This foil was further ground to ~60 μm thickness using 1200 grit papers. An ultrasonic disc cutter (Model 170, E.A. Fischione Instruments, PA, USA) was used to obtain multiple discs with 3 mm in diameter. Further thinning was carried out using a low angle ion milling machine (Model 1010 Low Angle Ion Mill, E.A. Fischione Instrument, PA, USA). An argon ion source with 3 kV voltage and 5 mA current was used to thin the sample at 12^{o} angle.

In-situ Kr ion irradiation was performed at the IVEM-Tandem TEM facility at Argonne National Laboratory (ANL). The Kr ion energy was 1 MeV. The acceleration voltage for the in-situ TEM analysis was kept at 300 kV. The TEM analysis was performed on the un-irradiated (0 dpa) SiC-C@NFA sample and the ion irradiated sample at dose levels of 0.2, 0.5, 1, 2, 5, and 10

dpa. Further analysis was performed at the end dose of 10 dpa using energy dispersive spectroscopy (Bruker EDS, MA, USA) and electron diffraction techniques on a TEM (Model 2100, JEOL, MA, USA) with 200 kV accelerating voltage. The dislocation loop density was measured manually using ImageJ software (with cell counter plug-in). The thickness of the TEM foil was estimated to be 100 nm.

SRIM simulation was performed with a 1 MeV Kr ions and the $NFA|_{Si}$ (Si dissolved α-BCC matrix) phase as the target using the SRIM-2013 (Stopping and Range of Ions in Matter) software [174]. In total, 50,000 incident ions were used for the simulation. The results were used to estimate the irradiation dose level in terms of displacement per atom (dpa) from the in-situ Kr ion irradiation with the corresponding fluence.

Figs. 7.1a and 7.1b show the Kr ion range and dpa levels plotted against the TEM foil thickness obtained using the SRIM simulation. The ion range plot in Fig. 7.1a shows Kr ion concentration in the sample, indicating that most of the ions leave the TEM foil. The dpa level can be calculated using the target vacancy data obtained by the SRIM simulation (d_v), using the same irradiation flux as in our irradiation experiment ($f=5.21\times10^{11}$ ions$\cdot s^{-1}\cdot cm^{-2}$), atomic density ($d_a=8.225\times10^{22}$ atoms/cm^3), and irradiation time (t) according to Eq. (7.1). Fig. 7.1b shows the damage level obtained for the fluences used in this experiment, i.e., 6.25×10^{14} ion/cm^{-2}, 1.88×10^{15} ion/cm^{-2}, 3.13×10^{15} ion/cm^{-2}, 6.25×10^{15} ion/cm^{-2}, etc. The SRIM simulation results in Fig. 7.1b suggest that the average damage accumulated in the TEM foil for these fluences is 1, 3, 5 and 10 dpa respectively.

$$\mathrm{dpa} = \mathrm{ftd_v}/\mathrm{d_a} \tag{7.1}$$

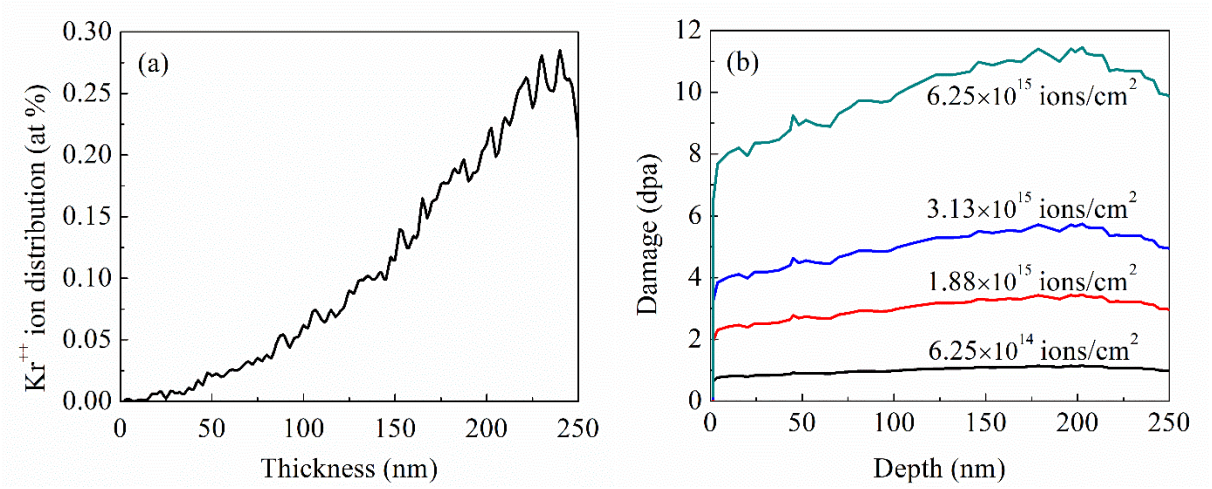

Fig. 7.1. SRIM simulation results showing (a) Kr ion distribution and (b) dpa damage plotted against the TEM foil thickness.

7.4. Results and Discussion

7.4.1 Microstructural evolution in α-ferrite phase during ion irradiation

Fig. 7.2 shows the TEM images of the α-ferrite phase of the 25 vol% SiC-C@NFA material obtained during the in-situ Kr ion irradiation at 300ºC. All images were obtained using kinematic bright field TEM mode with g=(110) diffraction condition and near the zone axis=[121]. The TEM image before the ion irradiation (Fig. 7.2a, 0 dpa) shows the α-ferrite matrix and precipitates such as $(Fe,Cr)_7C_3$ and (Ti,W)C. Some surface damage was observed before the ion irradiation, due to the ion milling during the sample preparation. The sample irradiated to 3 dpa (Fig. 7.2b) shows some new dislocation loops in the α-ferrite matrix (see the black dots pointed by yellow arrows). Alignment of these black dots can also be seen (green arrow in Fig. 7.2b). The average size of

dislocation loops is 9.6 nm after the 3 dpa irradiation. Fig. 7.2c shows the TEM bright field image of the irradiated sample after 5 dpa irradiation. There are a mix of new black dot dislocations (yellow arrow) and some fully evolved dislocation loops (yellow circle). In addition, there is a significant increase in the alignment of dislocation loops in a particular direction (blue arrow). The average dislocation loop size shows a considerable increase to 16.5 nm after 5 dpa. The alignment of black dot dislocations (or loop strings) is a commonly observed phenomenon in irradiated materials [175-179], attributed to elastic interactions of dislocation loops. Such alignment only occurs when dislocation loop density reaches a certain level where the distance between loops is small enough for effective elastic interactions between them. As the irradiation dose increases, the black dot dislocations inside loop strings eventually realign their Burgers vector to form fully evolved dislocation loops [176, 178], which can be observed at high irradiation doses (e.g., yellow circles at 5 and 10 dpa doses in Figs. 7.2c and 7.2d respectively). The TEM image after 10 dpa irradiation in Fig. 7.2d shows heavy radiation damage consisting of high-density of dislocation loops. The average size of the dislocation loops shows a significant increase to 27.3 nm after 10 dpa irradiation. This means that the marginal decrease in the dislocation density is a result of dislocation loop growth. The sample after 10 dpa irradiation shows fully evolved dislocation loops as opposed to black dots in the low dose samples. These results indicate that at high irradiation doses the newly generated point defects and small clusters may prefer to join nearby existing loops (because their density is high at high doses) instead of nucleating new ones.

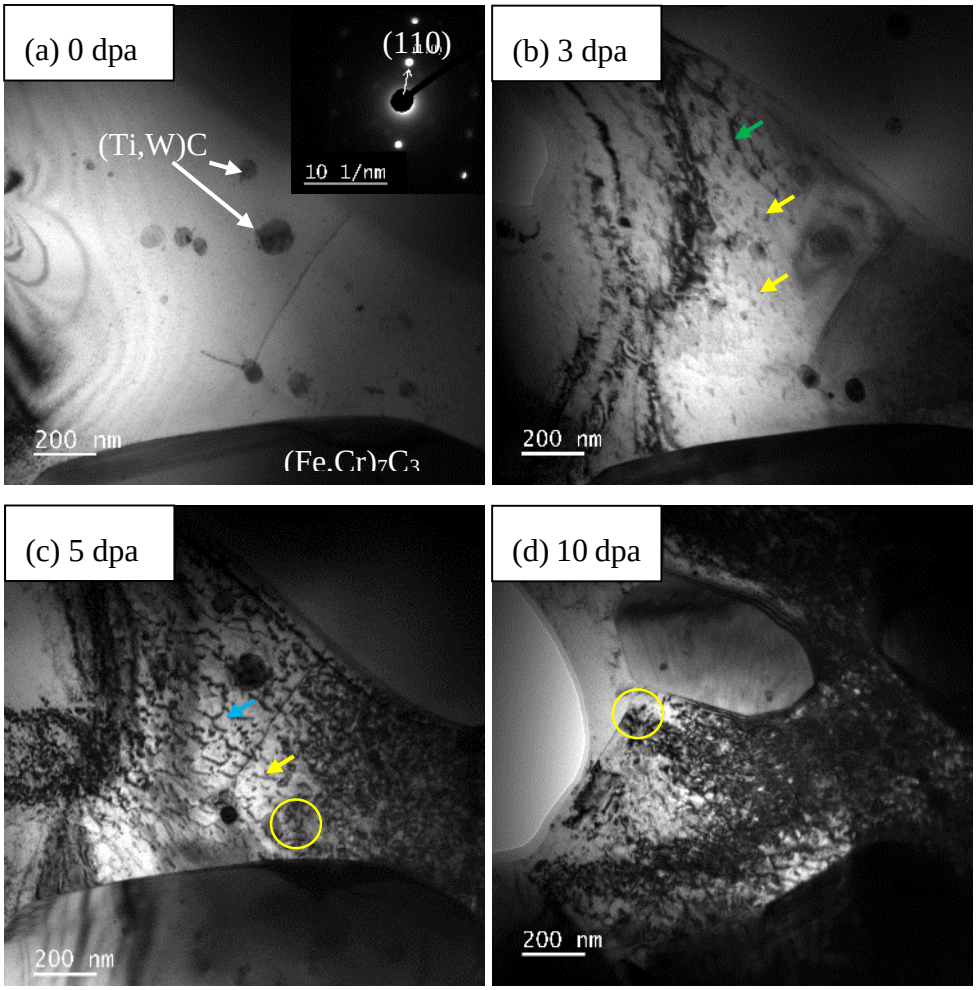

Fig. 7.2. Bright field TEM images of the SiC-C@NFA composite with g=(110) condition (zone axis =[121] after in-situ ion irradiation at 300oC at different dose levels: (a) 0 dpa, (b) 3 dpa, (c) 5 dpa, and (d) 10 dpa.

Fig. 7.3 shows the TEM images of the 25 vol% SiC-C@NFA sample before and after the in-situ ion irradiation at 450^{o}C. Before the ion irradiation, Fig. 7.3a shows mainly precipitates ($(Fe,Cr)_7C_3$ and (Ti,W)C) in the α-ferrite matrix. Unlike the sample at 300^{o}C irradiation, surface damage due to ion milling cannot be observed, maybe as a result of annealing during in-situ heating at 450^{o}C. The samples after both 3 and 5 dpa irradiation show considerable dislocations in the

thicker regions of the sample. The microstructure of the thicker region for the sample after 5 dpa irradiation is shown in the insert of Fig. 7.3c. Fully grown dislocation loops can be clearly seen. The corresponding dislocation loop sizes are 14.6 nm and 19.4 nm respectively. The sample after 10 dpa ion irradiation has been characterized using g=(002) diffraction condition near the <100> zone axis. The kinematic bright field and weak beam dark field images in Figs. 7.4a and 7.4b show fully evolved dislocation loops. The average dislocation loop size is around 35.8 nm, which is significantly higher than that of the samples after 3 and 5 dpa ion irradiation.

At 3 dpa (Fig. 7.3b), the SiC-C@NFA sample also shows the formation of spherical, very fine (Ti,W)C type precipitates (red circle). The TEM image of the 5 dpa sample in Fig. 7.3c shows an increased number density of the fine, spherical precipitates. The 10 dpa sample (Fig. 7.3d) shows both increased number density and coarsening of these fine spherical precipitates. This behavior is explained separately in section 7.4.3.

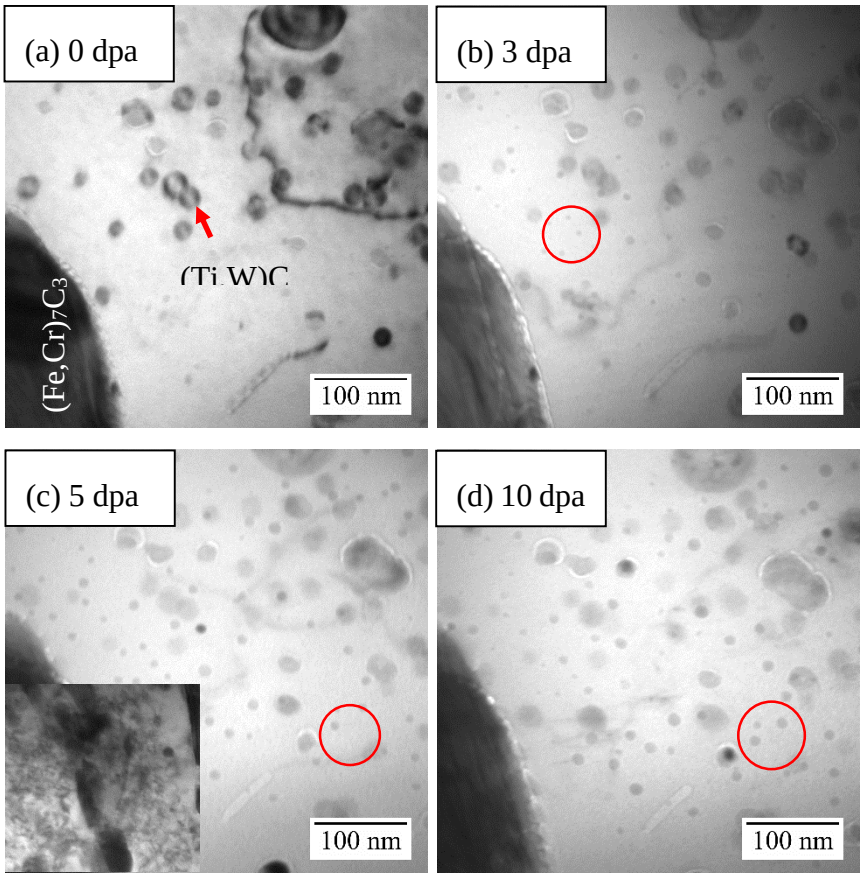

Fig. 7.3. TEM images of the 25 vol% SiC-C@NFA sample after in-situ ion irradiation at 450ºC using different dose levels: (a) 0 dpa, (b) 3 dpa, (c) 5 dpa, and (d) 10 dpa.

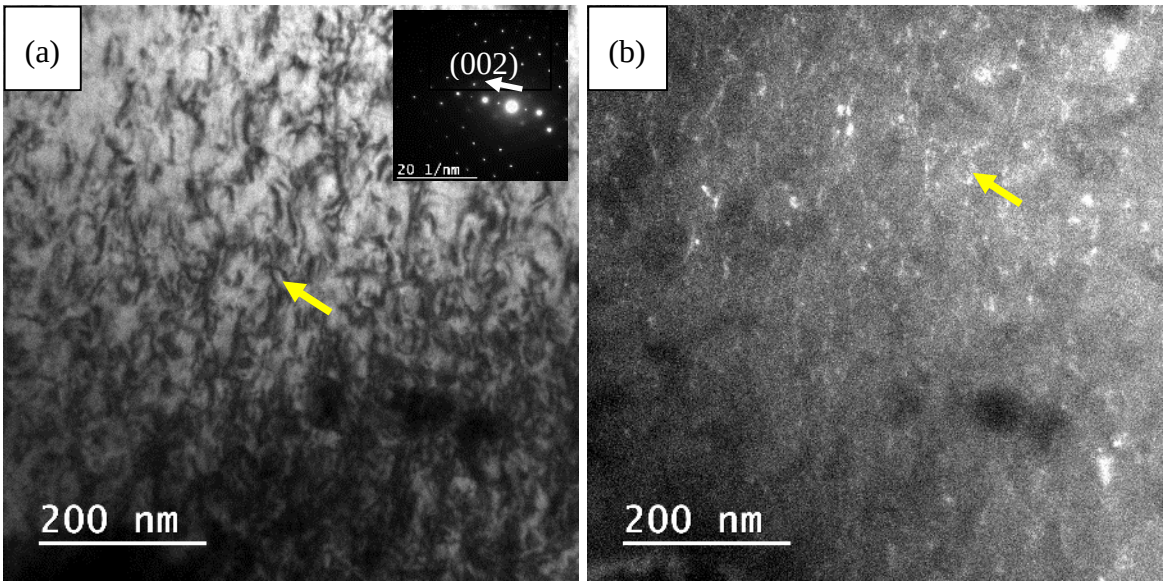

Fig. 7.4. (a) Kinematic bright field and (b) weak beam dark field TEM images with g=(002) condition near the [100] zone of the SiC-C@NFA composite after 10 dpa ion irradiation at 450^{o}C.

7.4.2. Dislocation loop evolution

Fig. 7.5 shows the comparison between dislocation loop sizes after 300^{o}C and 450^{o}C ion irradiation. At 300^{o}C the loops have very small sizes (<10 nm) at lower dose levels (0-2 dpa), which correlates with the black dot dislocations observed in Fig. 7.2b. The loop size increases up to 27.3 nm and 35.8 nm at high dose levels (10 dpa) for the 300^{o}C and 450^{o}C ion irradiation conditions, respectively. This behavior correlates with fully evolved dislocation loops observed in Fig. 7.2d and Fig. 7.4a. The dislocation loop size is larger for the 450^{o}C irradiation as compared to that of 300^{o}C irradiation at all dose levels.

During the ion irradiation, high-energy Kr ions displace atoms from their lattice sites in the target material, generating many Frenkel pairs (known as collision cascade event or primary damage [180]). The accumulation of surviving interstitials from the primary damage can grow into new, highly mobile defect clusters and eventually evolve into dislocation loops [176, 181-184]. Since the dislocation loop density is low at lower dose levels, loop nucleation becomes predominant over growth. Therefore, an increase in the loop density at low irradiation dose (<3-5

dpa) during both 300°C and 450°C ion irradiation can be observed (see Figs. 7.2b,c and 7.3b,c). At high irradiation doses, the dislocation loop density is also high. However, the newly generated defects/clusters from cascade events prefer to coalesce with nearby existing dislocation loops. This leads to loop growth with increasing irradiation dose, which is evident in Fig. 7.5. Previous literature shows that new clusters usually coalesce with large loops by climbing and reorienting their Burgers vector in accordance with large loops [178, 185].

The increase in irradiation temperature can significantly increase the mobility of defects/clusters. This phenomenon could have two effects. First, it can result in an increase in vacancy-interstitial recombination and lead to a smaller loop density at high temperatures. Second, it can lead to an early balance between nucleation rate and annihilation rate and result in enhanced loop growth at high temperatures as observed in Fig. 7.5.

Both dislocations and precipitates act as sinks for interstitials and vacancies generated during the cascade events. The corresponding sink strengths for dislocations and precipitates are given by Eqs. (7.2) and (7.3) respectively [181, 186]. Therefore, higher precipitate density can attract more interstitials than dislocations and thus decrease overall loop density.

$$k_{i,d}^2 = Z_i \rho_d \tag{7.2}$$

Where $k_{i,d}^2$ is sink strength due to dislocations, Z_i is absorption efficiency (typically it is larger for interstitials than vacancies), and ρ_d is dislocation density (m^{-2}).

$$k_{i,n}^2 = 4\pi R_n N_n \tag{7.3}$$

Where $k_{i,n}^2$ is sink strength due to precipitates, R_n is average radius of precipitates (m), and N_n is number density of precipitates (m^{-3}).

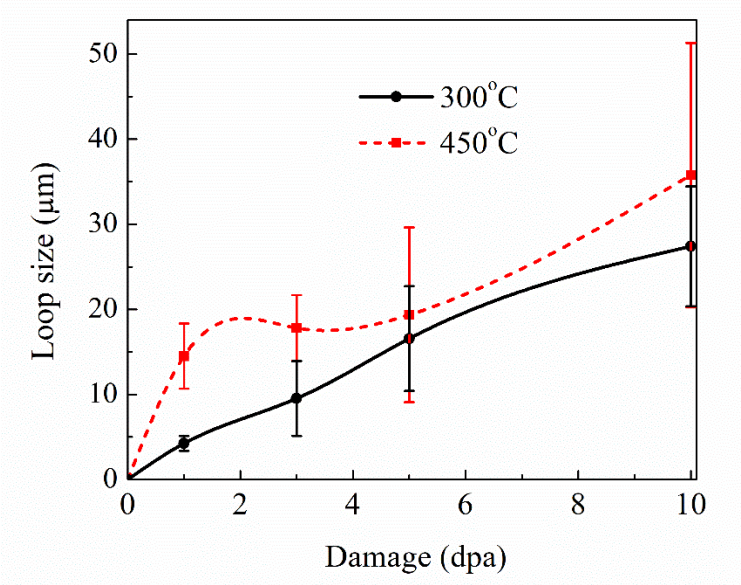

Fig. 7.5. Dislocation loop sizes in the α-ferrite matrix during the in-situ Kr ion irradiation.

7.4.3. Radiation induced precipitation

EDS mapping was performed for the SiC-C@NFA sample after irradiation to 10 dpa at 450°C. Fig. 7.6 shows large precipitates with Cr enrichment, which must be from the $(Fe,Cr)_7C_3$ precipitate as observed in Chapter 4. The spherical precipitates in the α-ferrite matrix show Ti- and W-enrichment. These precipitates must be (Ti,W)C carbides. Some small-sized precipitates (red circle) with similar Ti- and W-enrichment can be observed along with the existing (Ti,W)C precipitates. This means that the new fine spherical precipitates in Figs. 7.3b, 7.3c, and 7.3d are indeed (Ti,W)C type carbides. During irradiation at 300°C, such precipitation was not observed.

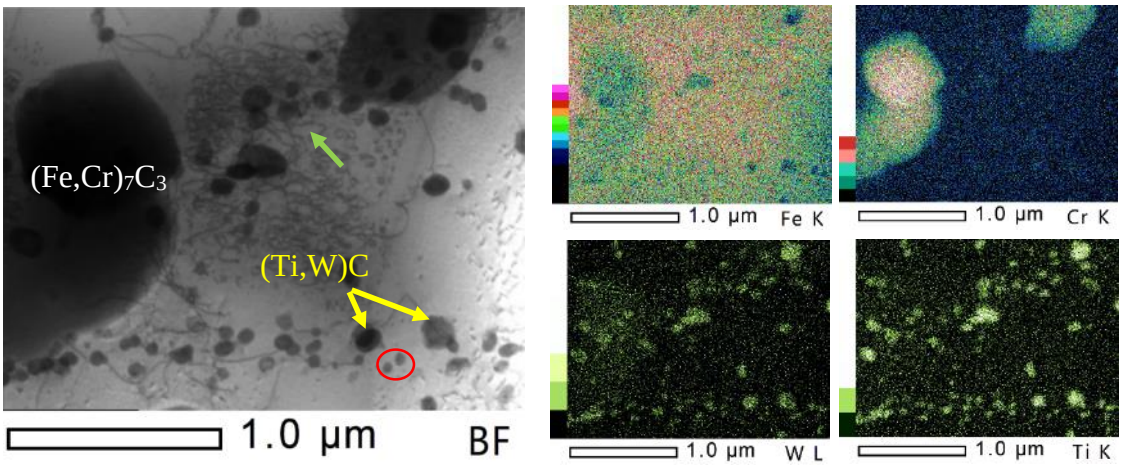

Fig. 7.6. EDS mapping of the SiC-C@NFA composite after 10 dpa ion dose at 450°C.

Fig. 7.7 shows the size distribution of the (Ti,W)C precipitates at 450°C. At 0 dpa (Fig. 7.7a), the precipitate size is 15 nm to 55 nm. Figs. 7.7b, 7.7c and, 7.7d show the formation of new precipitates with sizes less than 12 nm. Fig. 7.8 shows that a large number of new precipitates have already formed at 3 dpa as compared to the original precipitates of >15 nm size. At 3 dpa, the size distribution is bimodal with peaks at 4 nm and 25 nm respectively. The subsequent results after 5 and 10 dpa ion irradiation (Fig. 7.7c and 7.7d respectively) show similar size distribution as after 3 dpa ion irradiation; however, some coarsening of the new precipitates occurs. This behavior can be correlated with coarsened new precipitates observed in Figs. 7.3c and 7.3d. The precipitate number density and average size are plotted against the dose level as shown in Fig. 7.8. The number density of (Ti,W)C shows a significant increase after the ion irradiation. The average size of the precipitates shows a sharp decrease after irradiation at 3 dpa. This must be due to the sudden increase in the number density of the new precipitates with size < 12 nm. The average sizes of (Ti,W)C after 5 and 10 dpa irradiation remains similar to that after 3 dpa irradiation. These results indicate that the number density of the (Ti,W)C precipitates becomes saturated at high dose levels. They also suggest that the coarsening of these carbides, even though present, is not significant in our study.

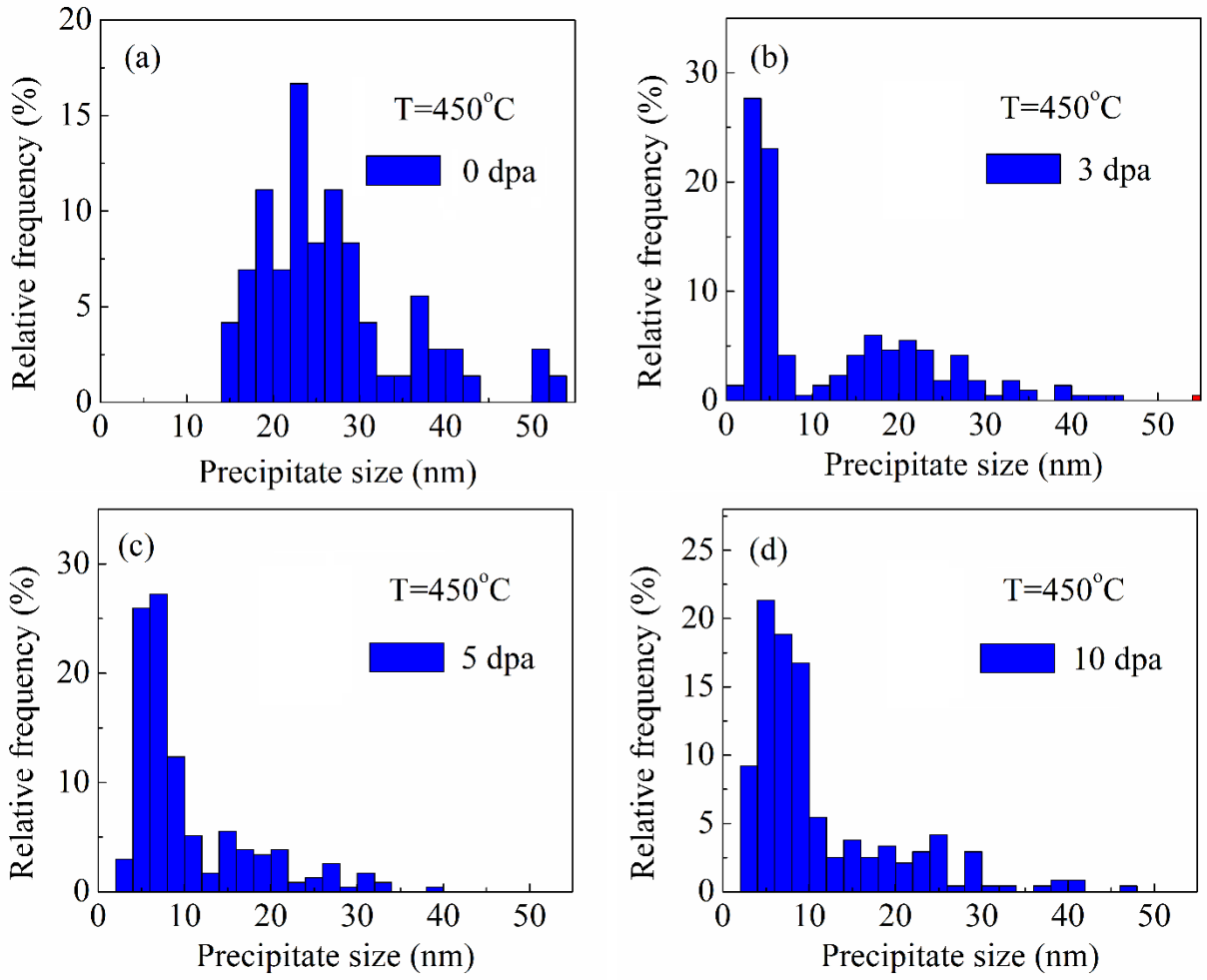

Fig. 7.7. Precipitate size distribution in the SiC-C@NFA sample after irradiation at 450ºC with an ion dose of (a) 0 dpa, (b) 3 dpa, (c) 5 dpa, and (d) 10 dpa.

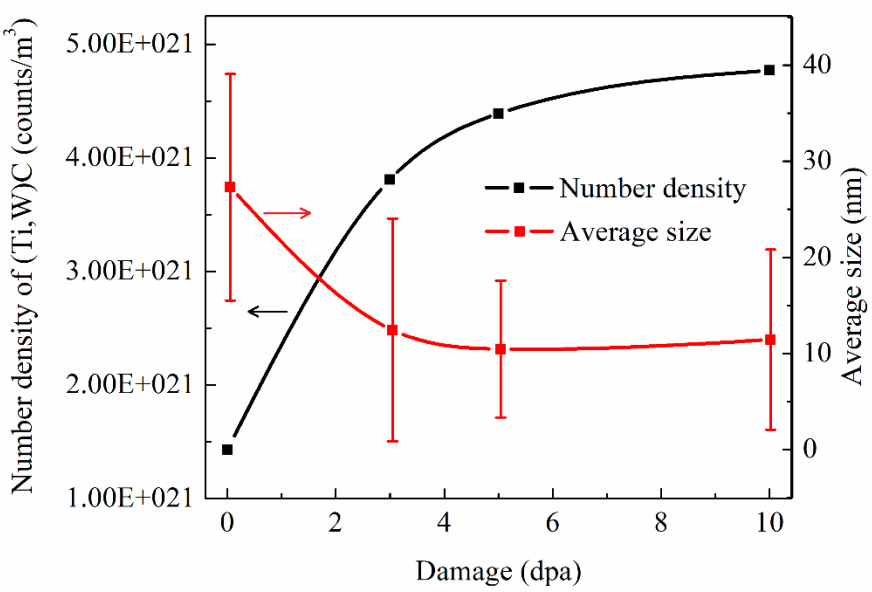

Fig. 7.8. Number density and average size of (Ti,W)C precipitates with increasing dose level.

The TTT diagram acquired using the ThermoCalc software (Fig. 7.9) indicates that nucleation of the new (Ti,W)C takes more than 10^6 seconds (~280 hours) at 450^{o}C in the absence of irradiation. Therefore, it can be concluded that irradiation-induced precipitation is in effect and the impact of ion irradiation on the nucleation of new (Ti,W)C precipitates is significant. Bachhav et al. [187] proposed two mechanisms for irradiation-induced precipitation. First, irradiation induced point-defect supersaturation can provide abundant carriers for the diffusion of solute atoms and result in an increased rate of precipitation as compared to that observed in thermal equilibrium conditions. Similar radiation-enhanced precipitation mechanism was also proposed for Cu precipitation in ferritic Fe under irradiation [188]. Second, solute atoms and migrating point defects can couple with increasing irradiation dose and result in the formation of non-equilibrium precipitates. The TTT diagram in Fig. 7.9 shows that (Ti,W)C precipitates are thermodynamically favorable at a certain temperature. Therefore, it is most likely that the first mechanism, i.e., irradiation-enhanced precipitation, is predominant in the current experiments.

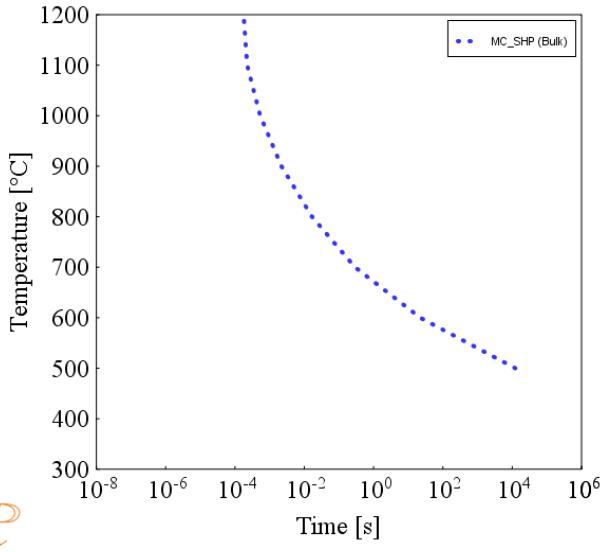

Fig. 7.9. TTT diagram of the (Ti,W)C phase in an α-BCC iron matrix.

7.4.4. Irradiation response of $(Fe,Cr)_7C_3$ phase

Fig. 7.10 shows the TEM images of the $(Fe,Cr)_7C_3$ phase before and after 10 dpa ion irradiation at 300°C and 450°C. After the 10 dpa dose irradiation at 300°C, the $(Fe,Cr)_7C_3$ phase does not show any discernable damage (Fig. 7.10b). This means that the M_7C_3 phase is highly resistant to irradiation as compared to α-ferrite at 300°C. After the 10 dpa dose irradiation at 450°C, the $(Fe,Cr)_7C_3$ phase shows some Kr bubbles (see the inset in Fig. 7.10c). Large size Kr bubbles can be seen at the interface between the $(Fe,Cr)_7C_3$ phase and the α-ferrite matrix (yellow arrow in Fig. 7.10c). The Kr bubbles cannot be observed in the α-ferrite matrix. The TEM images under underfocus and overfocus conditions in Figs. 7.11a and 7.11b respectively confirm the presence of bubbles (see yellow arrow). It is possible that some bubbles are annihilated as the Kr gas from the α-ferrite matrix travels towards the precipitate-matrix interfaces [189].

Bubbles form due to the interaction between vacancy clusters and incoming Kr^{++} ions. Even though the majority of Kr^{++} ions have penetrated through our samples, some Kr^{++} ions may be trapped in the samples. Pagano et al. [190] showed the formation of bubbles during the Kr^{++} ion irradiation in Zr-based alloys. In the presence of noble gas ions, vacancies in Zr form bubbles as opposed to vacancy dislocation loops. The bubbles either grow by the accumulation of incoming

Kr^{++} ions or by agglomeration of other bubbles (if mobile). The immobile bubbles often have homogeneous size distributions as opposed to mobile ones [190]. The bubbles formed in the $(Fe,Cr)_7C_3$ phase at 450°C in this study are likely immobile considering their homogenous size distribution and large size. In addition, bubbles cannot be observed in the samples irradiated at 300°C. This is likely because the bubble formation is often controlled by Kr atom mobility. Therefore, it can be argued that at 450°C Kr atom diffusion is fast enough to form stable bubbles as compared to that at 300°C.

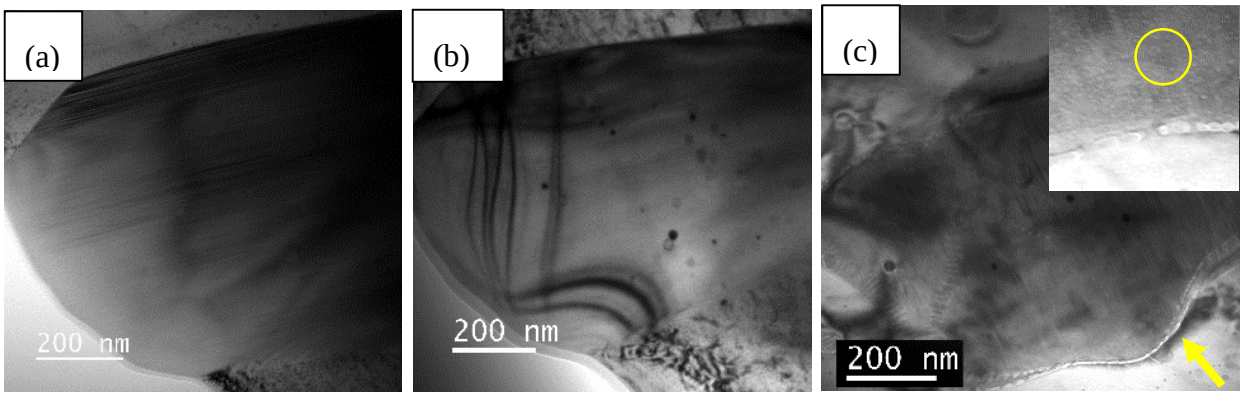

Fig. 7.10. Bright field TEM images of $(Fe,Cr)_7C_3$ precipitate at (a) 0 dpa, (b) 10 dpa at 300°C and (c) 10 dpa at 450°C.

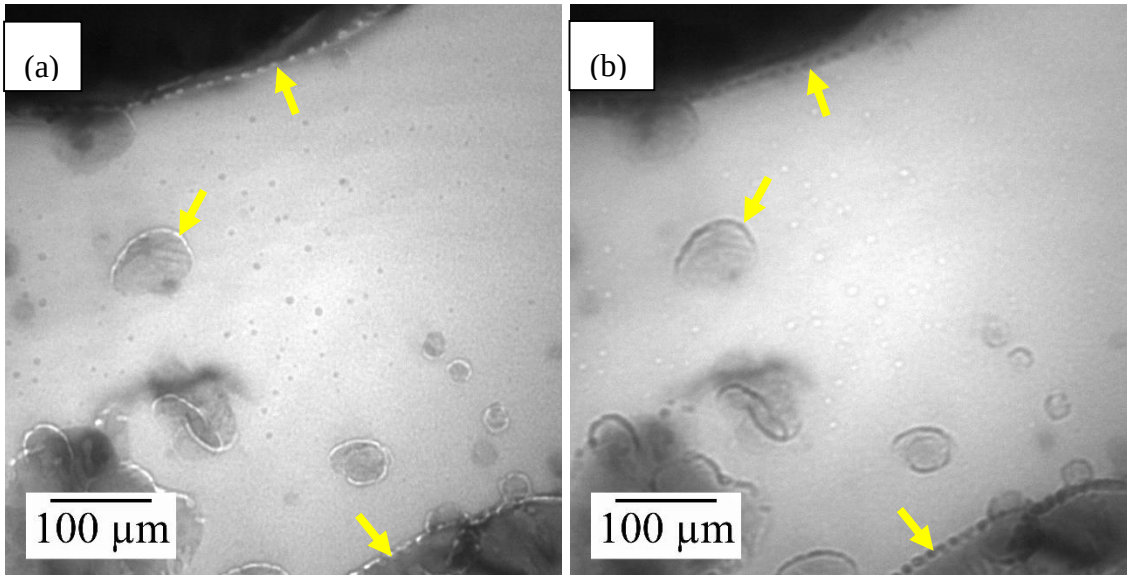

Fig. 7.11. Bright field TEM images of SiC-C@NFA in (a) underfocus and (b) overfocus imaging conditions after irradiation at 450ºC up to 5 dpa.

7.5. Conclusions

This study focuses on the in-situ Kr ion irradiation study of a newly developed SiC-C@NFA system at 300°C and 450°C to a maximum ion dose of 10 dpa. Ion irradiation at 300°C shows the evolution of dislocation loops and loop string formation in the α-ferrite phase above 5 dpa dose levels. The microstructure of the 300°C ion irradiated sample at 10 dpa shows heavy damage in the α-ferrite phase. The sample irradiated at 450°C shows much larger dislocation loops compared to that at 300°C. Ion irradiation at 450°C and above 3 dpa results in nucleation of new (Ti,W)C precipitates. The $(Fe,Cr)_7C_3$ phase is highly resistant to the Kr irradiation damage during the ion irradiation at both 300°C and 450°C temperatures.

Chapter 8

In-Situ TEM Study of Microstructural Evolution in NFA and Chromium Carbide Coated SiC – Nanostructured Ferritic Alloy Composite during Ion Irradiation

8.1. Abstract

In this work, the ion irradiation responses of a Fe-based nanostructured ferritic alloy or 'NFA' (Fe-9Cr-2W-0.2V-0.4Ti-0.3Y_2O_3) and a Cr_3C_2@SiC-NFA composite were assessed. *In-situ* ion irradiation with TEM observation was carried out by using 1 MeV Kr^{++} ions at doses of 0, 1, 3, 5, 10 dpa and temperatures of 300°C and 450°C. Both the NFA and Cr_3C_2@SiC-NFA samples showed significant dislocation density after 10 dpa at 300°C. However, the Cr_3C_2@SiC-NFA composite showed a significantly lower dislocation loop density and a smaller average loop size during the irradiation at 450°C as opposed to the NFA. At 300°C, 1/2<111> type dislocation loops were observed in both the NFA and Cr_3C_2@SiC-NFA samples. Interestingly, at 450°C, <100> type loops were dominant in the NFA sample while 1/2<111> type loops were still dominant in the Cr_3C_2@SiC-NFA sample. The results were discussed based on the large surface sink effects and enhanced interstitial-vacancy recombination at higher temperatures. The additional Si element in the Cr_3C_2@SiC-NFA sample might have played a significant role in determining the dominant loop types.

8.2. Introduction

Neutron and ion irradiation studies on body-centered-cubic (BCC) Fe-based ferritic alloys have shown the formation of two kinds of dislocation loops with Burgers vector $b=a/2<111>$ and $b=a<100>$ [84, 191], where a is the BCC lattice constant. They are referred as ½<111> and <100> loops in this study, respectively. Relative quantities and sizes of the two types of loops strongly

depend on alloy compositions and irradiation conditions (e.g., temperature). During neutron irradiation of pure iron, 1/2<111> loops are mostly observed between 30-90^{o}C [87, 88]. However, at temperatures above 300^{o}C, <100> loops become predominant [89, 90]. It is well known that 1/2<111> loops are highly mobile while <100> loops are almost immobile [191]. Therefore, the observed predominance of <100> loops at high temperatures could be an outcome of the loss of mobile 1/2<111> loops at defect sinks. However, in Yao's in-situ ion irradiation experiment [191] in which the samples were oriented carefully to prevent the loss of 1/2<111> loops to surface sink, ½<111> and <100> loops were found to be dominant below 300^{o}C and above 500^{o}C, respectively. At 400^{o}C, the two types of loops had nearly equal fractions. Field et al. [192] calculated contributions of ½<111> and <100> dislocations to radiation-induced hardening for ferritic Fe-Cr-Al alloys using linear superposition of a DBH (dispersed barrier hardening) model. It was concluded that <100> loops are much stronger obstacles to dislocation motion as compared to ½<111>. This behavior was correlated with the sessile nature of <100> loops as compared to the glissle nature of ½<111> loops. Alloy composition can also affect the relative abundance of the two types of loops [193]. Fe-Cr alloys show a strong affinity to the formation of Cr-interstitial clusters, mainly along b=a/2<111> type dislocations [90, 194]. This leads to the mobility decrease of 1/2<111> loops [185, 195-198]. Therefore, Cr addition can influence relative fractions of 1/2<111> and <100> loops. However, the exact correlation between the Cr content and the dominance of these loops has not been fully established yet [84]. The α-ferrite matrix of the Cr_3C_2@SiC-NFA material contains mainly Fe, Cr, and Si elements. The additional Si element could have interesting effects on the dislocation loop evolution during ion irradiation as compared to the NFA.

This study focuses on the evolution of irradiation-induced dislocation loops in the NFA and Cr_3C_2@SiC-NFA materials using the IVEM-Tandem facility at Argonne National Laboratory. The irradiation was performed at 300^{o}C and 450^{o}C to identify the effect of temperature on dislocation loop properties (size, density, and Burgers vector) in these materials. The comparison between the irradiation responses of the NFA and the Cr_3C_2@SiC-NFA is conducted and the differences are discussed.

8.3. Materials and methods

The NFA powder (~15 μm average size) was prepared using mechanical alloying of ferritic steel powder (Fe-9Cr-2W-0.4Ti-0.2V-0.18C wt%) with 0.3% Y_2O_3 in an argon atmosphere (powder provided by Dr. T. S. Byun and Dr. David Hoelzer from Oak Ridge National Laboratory). SiC particles (Grade UF-15, α-SiC, ~1.25 μm average size, H.C. Starck, Karlsruhe, Germany) were coated with Cr_3C_2 using a melt salt method followed by reduction treatment at high temperatures. The NFA and 25 vol% Cr_3C_2@SiC-NFA composite were sintered using SPS at 950^{o}C. The details of the sintering process, densities, and microstructural evolution of the resultant material can be found in chapter 3 and 4. Thin sections of the NFA and Cr_3C_2@SiC-NFA samples were cut using a low speed saw (Isomet-Low speed precision cutter, Beuhler, IL, USA). This section was further polished into 60 μm thickness foils using diamond papers with sizes in the following order: 30 μm, 15 μm, 10 μm, 3 μm, and 1 μm. These foils were then cut using a Gatan disc punch system to obtain discs with ~3 mm diameter. The discs were thinned using a twin-jet electropolisher system (Model 110, E. A. Fischione Instruments, Inc., PA). A solution of 5% perchloric acid ($HClO_4$)+95% methanol was used as an electrolyte for the twin jet electropolishing. For the NFA sample, the temperature and voltage used were -30^{o}C and 20 V respectively. For the Cr_3C_2@SiC-NFA sample, the electropolishing was kept at -60^{o}C using liquid nitrogen and a voltage of 40 V was applied until a hole was obtained. The low electropolishing temperature allowed the use of a higher voltage without an increase in current. In order to increase observable area of TEM sample during in-situ experiments, further thinning was carried out using a low angle ion mill (Model 1010 Low Angle Ion Mill, E. A. Fischione Instruments, Inc., PA). An argon ion source with 3 kV voltage and 5 mA current was used to thin the sample at a 12^o angle for 1 hour.

In-situ Kr^{++} ion irradiation with TEM observation was conducted at 300^{o}C and 450^{o}C using an Intermediate Voltage Electron Microscope (Hitachi-9000) attached with an ion accelerator. The electron and Kr^{++} ion energies were 300 keV and 1 MeV respectively. The irradiation was performed up to a fluence of 6.25×10^{15} ions/cm^2 (~10 dpa according to SRIM simulation). The irradiation was stopped for detailed TEM analysis after fluences of 6.25×10^{14} ions/cm^2 (~1 dpa), 1.875×10^{15} ions/cm^2 (~3 dpa), 3.125×10^{15} ions/cm^2 (~5 dpa), and 6.25×10^{15} ions/cm^2 (~10 dpa).

Dislocation loops were counted manually using the cell counter plugin in ImageJ software. Dislocation loop number density (m^{-3}) was calculated by assuming the TEM foil thickness at 100 nm for all the samples. All the dislocations present in the given image were counted (number ranges from 15-30 in 450^{o}C irradiated Cr_3C_2@SiC-NFA up to 250-300 in 300^{o}C irradiated NFA). The procedure was repeated for 2-3 TEM images from different regions of the same sample to get average loop number density and standard deviation. Dislocation loop sizes were measured using ImageJ software. For elliptically shaped loops, the major diameter was measured. For loop strings/rafts, the width was reported as loop size. Sizes were measured for nearly all dislocations in the current TEM image. The data was used to get average loop size and standard deviation as well as loop size distribution.

Dislocation burgers vector (b=a/2<111> and b=a<100>) was identified for specimens with 10 dpa irradiation dose where the shape of most of the dislocation loops was clearly visible. The shape of the dislocation was matched with simulated projections of ½<111> and <100> loops at [100] zone axis. This method is discussed in detail in later sections.

To investigate whether lattice contraction due to the dissolution of Si in the Fe matrix can significantly modify the relative stability of 1/2<111> and <100> loops in Fe, molecular dynamics (MD) simulations were conducted to study the effects of isotropic compressive and dilative strains on the formation energies of the two types of dislocation loops in pure Fe. The MD simulations were conducted using LAMMPS software [199] and the M07 interatomic potential [200] for Fe was used.

8.4. Results

8.4.1. Dislocation evolution in NFA

Fig. 8.1 shows the kinematic bright field (BF) and weak beam dark field (DF) TEM images of the NFA sample after the ion irradiation at 300^{o}C. The dislocations observed at 0 dpa (see Fig. 8.1a) are likely from the mechanical polishing during the sample preparation. Some surface damage from the final ion milling preparation method can also be observed in Fig. 8.1a. Small

dislocation loops (black dots in BF, white dots in DF) can be observed after irradiation at 3 dpa and 5 dpa as shown in Figs. 8.1b and 8.1c respectively (see yellow circles). The loop density shows a significant increase from 2.2×10^{21} m^{-3} at 3 dpa to 5.26×10^{21} m^{-3} at 5 dpa. The average loop size also shows an increase from 4.4±1.5 nm at 3 dpa to 5±2 nm at 5 dpa. Finally, at 10 dpa, Fig. 8.1d shows a mixture of small dislocations (black dots in BF) and large dislocation loops (the green arrow in BF). This indicates simultaneous loop growth and nucleation events during the ion irradiation. The loop density and size increase significantly to 7.26×10^{21} m^{-3} and 9±6.3 nm, respectively, after the 10 dpa ion irradiation.

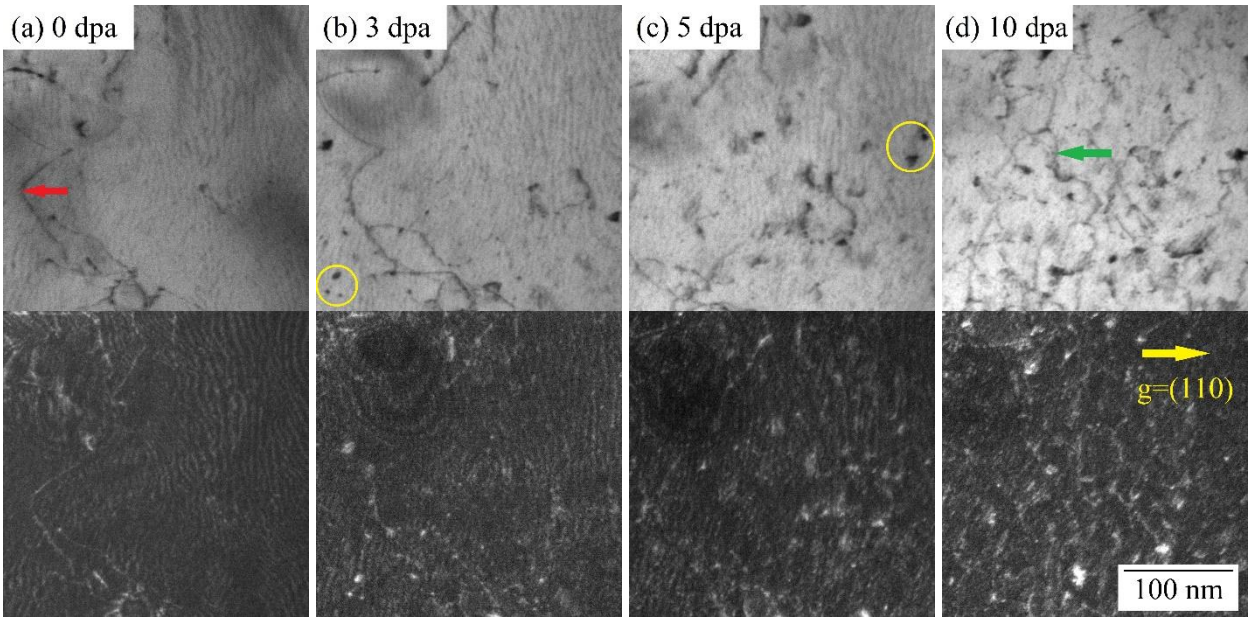

Fig. 8.1. Kinematic bright field (top) and weak beam dark field (bottom) TEM images of the NFA sample (zone axis=[001]) after the in-situ Kr^{++} ion irradiation at 300°C: (a) 0 dpa, (b) 3 dpa, (c) 5 dpa, (d) 10 dpa.

Fig. 8.2 shows kinematic bright field and weak beam dark field TEM images of the NFA sample irradiated with various dose levels (0-10 dpa) at 450°C. The 0 dpa image shows dislocation lines from mechanical damage during the sample preparation. Unlike the 300°C unirradiated NFA sample (Fig. 8.1a), the surface damage due to the ion milling is non-existent for the 450°C unirradiated NFA sample. It is possible that most of the surface damage from ion milling has been

annealed out at 450^{o}C. After 3 dpa irradiation (Fig. 8.2b), TEM image shows several small dislocation loops (black dots in the BF image) as well as fully evolved dislocation loops. At 5 dpa, a similar mixture of small loops (black dots) and fully evolved dislocation loops can be observed (see Fig. 8.2c). The dislocation loop density shows a slight increase from 4×10^{21} m^{-3} at 3 dpa to 4.5×10^{21} m^{-3} at 5 dpa. However, the dislocation loop size shows a significant increase from 11±8.2 nm at 3 dpa to 19±16.3 nm at 5 dpa. This means that the combination of high irradiation dose and high temperature has led to the rapid loop growth as well as nucleation of new loops. The fully evolved dislocation loops are elliptical in shape and aligned mostly in the same direction as shown in the BF image in Fig. 8.2c (45^{o} with g=(110)). The kinematic bright field image in Fig. 8.2d shows very heavy radiation damage with a large number of small dislocation loops (black dots) and elliptical dislocation loops after 10 dpa irradiation. The dislocation loop density increases to 5.9×10^{21} m^{-3} after 10 dpa ion irradiation as compared to 4.5×10^{21} m^{-3} at 5 dpa. However, the average loop size shows a decrease to 13.3±9.1 nm at 10 dpa as compared to 19±16.3 nm at the 5 dpa dose level. The decrease in the average loop size for the 10 dpa dose level may be due to an increased nucleation rate for the dislocation loops vs. loop growth (refer to section 8.5.1). This behavior also explains the increase in the dislocation loop density with the dose level.

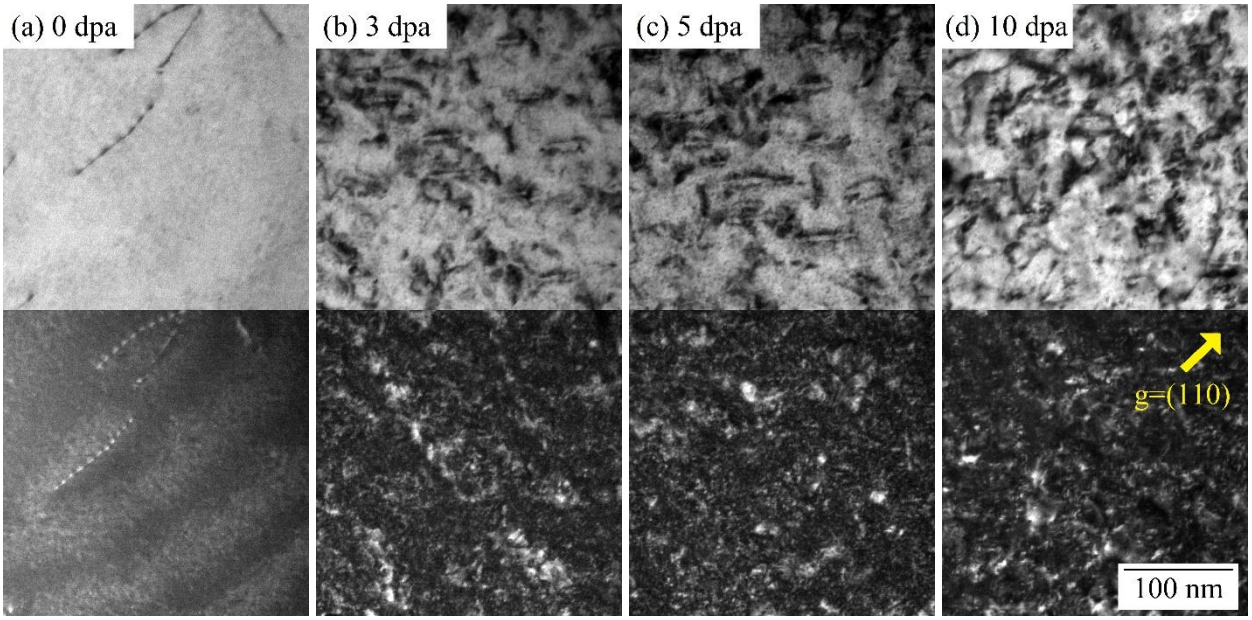

Fig. 8.2. Kinematic bright field (top) and weak beam dark field (bottom) TEM images of the NFA sample (zone axis=[001]) after the in-situ Kr^{++} ion irradiation at 450ºC: (a) 0 dpa, (b) 3 dpa, (c) 5 dpa, (d) 10 dpa.

8.4.2. Dislocation evolution in Cr_3C_2@SiC-NFA

Fig. 8.3 shows kinematic bright field and weak beam dark field TEM images of the Cr_3C_2@SiC-NFA sample irradiated with various dose levels (0-10 dpa) at 300ºC. Fig 8.3a and 8.3c clearly shows existence of (Ti,W)C and $(Fe,Cr)_7C_3$ precipitates respectively in the α-ferrite matrix. Similar to the unirradiated NFA sample at 300ºC, the dark field image at 0 dpa in Fig. 8.3a shows some surface damage due to ion milling during the sample preparation. At 3 dpa, the presence of mainly small dislocation loops, some of which align in a particular direction to form 'loop strings [179, 201, 202]', can be seen in Fig. 8.3b (blue arrow in the DF image). Note such loop strings are not observed for both 300ºC and 450ºC irradiated NFA samples. At 5 dpa, an increased density of such loop strings can be observed as shown in Fig. 8.3c (blue arrow in the DF image). The loop density shows an increase from 4.8×10^{21} m^{-3} at 3 dpa to 6×10^{21} m^{-3} at 5 dpa. The loop size also shows a considerable increase from 5.7±1.4 nm at 3 dpa to 11.3±3 nm at 5 dpa. After 10 dpa irradiation, the TEM image in Fig. 8.3d shows heavy damage with predominantly fully

evolved dislocation loops. The dislocation density and size increase to 7.2×10^{21} m^{-3} and 13.8±3.5 nm, respectively. The TEM images for this sample were taken at g=(020), unlike all the other samples where g=(110) was used. According to g·b=0 invisibility criteria, all variants of ½<111> and [010] loop are visible, while [100] and [001] type loops are invisible when g=(020) is used.

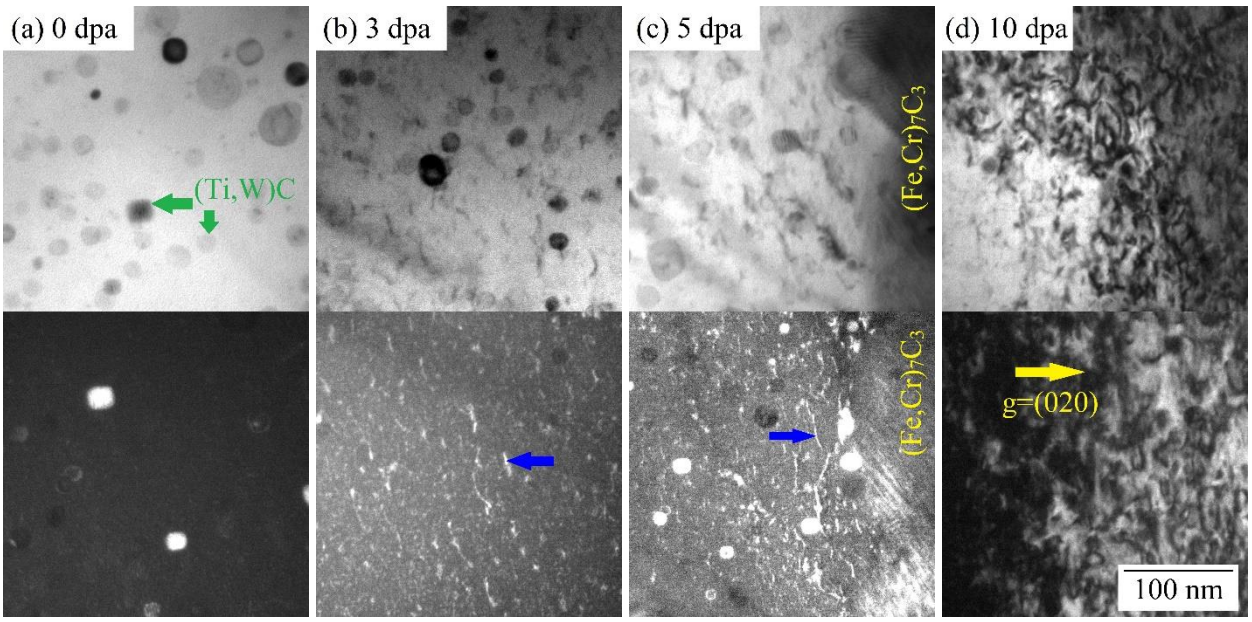

Fig. 8.3. Kinematic bright field (top) and weak beam dark field (bottom) TEM images of the Cr_3C_2@SiC-NFA sample (zone axis=[001]) after the Kr++ ion irradiation at 300°C: (a) 0 dpa, (b) 3 dpa, (c) 5 dpa, and (d) 10 dpa.

Fig. 8.4 shows kinematic bright field and weak beam dark field TEM images of the Cr_3C_2@SiC-NFA samples irradiated at 450°C. The spherical precipitates observed in Fig. 8.4 are (Ti,W)C carbides [203]. At 0 dpa, the TEM image in Fig. 8.4a again does not show any surface damage from the ion milling, which is similar to the unirradiated NFA sample at 450°C shown in Fig. 8.2a. The kinematic bright field TEM images of the Cr_3C_2@SiC-NFA sample irradiated to 3, 5, and 10 dpa show a surprisingly small number of dislocation loops (red arrows). The loop density after 3, 5 and 10 dpa dose levels is 0.15×10^{21} m^{-3}, 0.33×10^{21} m^{-3}, and 0.66×10^{21} m^{-3}, respectively.

The size of the dislocation loops (~7 nm) is also much smaller compared to all other samples investigated here at the same irradiation conditions (see Figs. 8.1, 8.2, and 8.3).

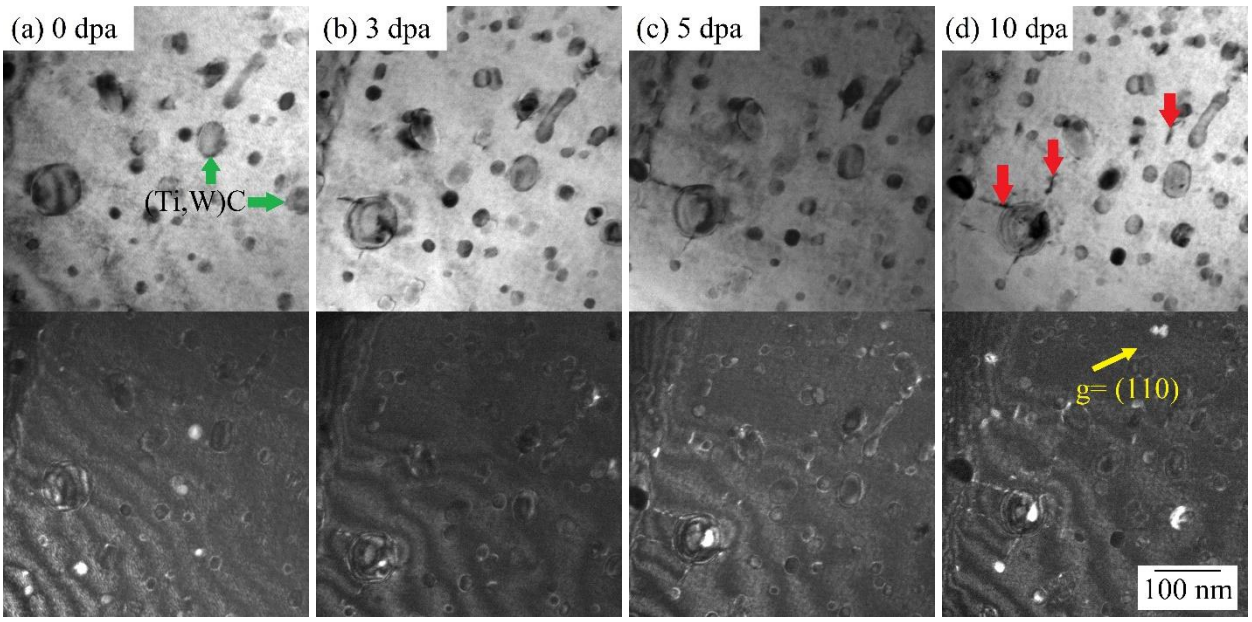

Fig. 8.4. Kinematic bright field (top) and weak beam dark field (bottom) TEM images of the Cr_3C_2@SiC-NFA sample (zone axis=[001]) after the ion irradiation at 450°C: (a) 0 dpa, (b) 3 dpa, (c) 5 dpa, and (d) 10 dpa.

8.4.3. Dislocation loop size and density

Figs. 8.5a-8.5c show loop size distributions for the NFA sample after the ion irradiation at 300°C to 3, 5, and 10 dpa dose levels. At 3 dpa, the loop size distribution is unimodal (Fig. 8.5a) with a very small size range (~1-10 nm), which corresponds to small black dots in Fig. 8.1b. The loop size distribution at 5 dpa (Fig. 8.5b) also shows a unimodal distribution with mostly small dislocations (<10 nm) and very few in the range of 10-20 nm size. This means that some dislocation loops have started to grow with the increasing dose. The loop size distribution after 10 dpa irradiation (Fig. 8.5c) shows some dislocations of larger size (~10-35 nm), and most are within 2-10 nm size. This indicates considerable loop growth along with extensive nucleation of new small

loops. This behavior corresponds well with the mixture of small (black dots) and large (fully evolved) loops observed in Fig. 8.1d. The loop size distributions of the NFA sample after the irradiation at 450^{o}C are shown in Figs. 8.5d-8.5f. After 3 and 5 dpa irradiation at 450^{o}C, the NFA sample shows a bimodal loop size distribution, indicating concurrent loop nucleation and growth. The bimodal distribution could be also due to surface effect where point defects or small clusters can migrate to the surface at this temperature. In this case, small loops form close to the surface and large loops stay in deeper regions. This phenomenon is typically more effective at high temperatures due to the increased defect/cluster mobilities. At 10 dpa, the loop size distribution is still unimodal. The small dislocation loops (<10 nm) constitute the major fraction of the total loops in all the samples. The peaks for the large dislocations loops (>20 nm) are located at ~20 nm, ~25 nm, and ~30 nm for the NFA sample irradiated up to 3, 5, and 10 dpa at 450^{o}C respectively. This indicates continuous loop growth with increasing ion dose. At 10 dpa, an increase in the number of loops with 10-20 nm size can be observed as compared to those at 3 and 5 dpa. This indicates growth of small loops that form during the 3 and 5 dpa dose irradiation, nucleation of new small loops, and also the growth of existing large loops (>20 nm, see Fig. 8.5f) after the 10 dpa irradiation. These results correspond well with the presence of large elliptical loops and small black dot dislocation loops as shown in Figs. 8.2b-8.2d. Clearly, the temperature has a significant effect on the size and distribution of dislocation loops. The 450^{o}C irradiated sample shows much larger loop sizes and a wider size distribution compared to the 300^{o}C irradiated ones.

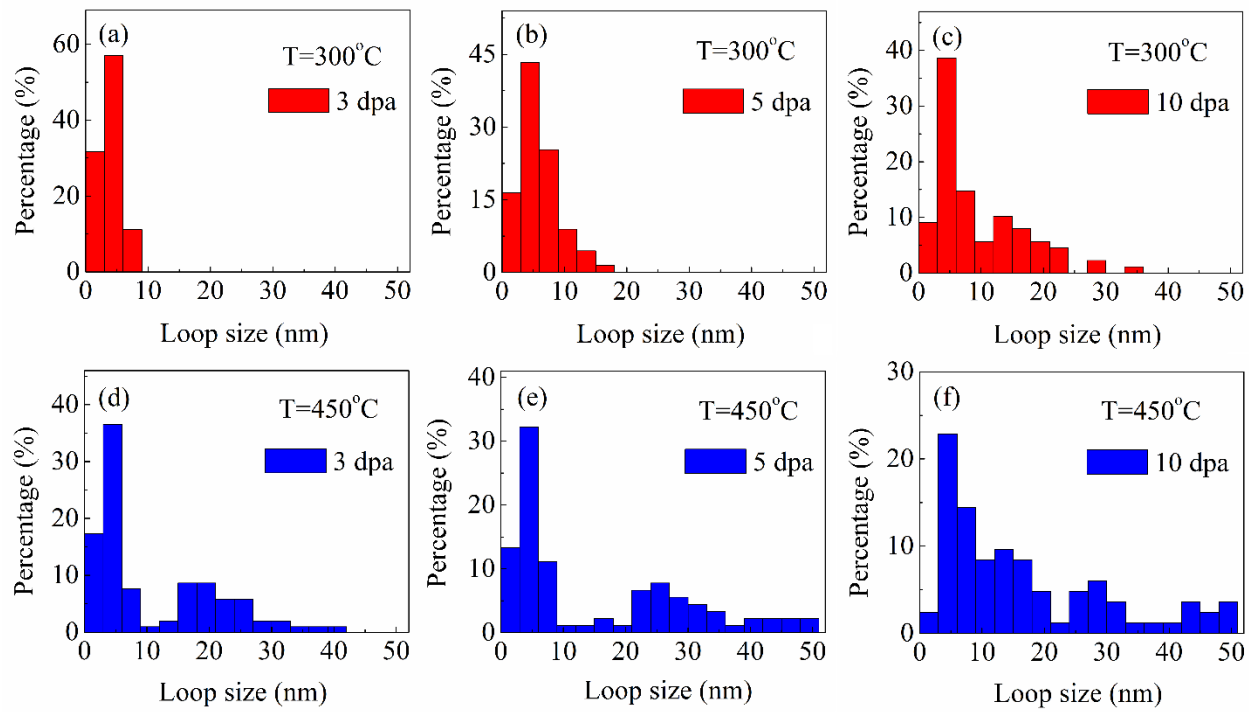

Fig. 8.5. Loop size distribution of the NFA sample irradiated at 300ºC (a, b, c) and 450ºC (d, e, f) with dose levels of 3 dpa, 5 dpa, and 10 dpa respectively.

Figs. 8.6a-8.6c show the dislocation loop size distributions for the Cr_3C_2@SiC-NFA sample after the ion irradiation at 300ºC with 3, 5, and 10 dpa dose. At 3 dpa, a unimodal loop size distribution with small dislocation loops (<10 nm) can be observed. However, at 5 dpa, the loop size distribution is approximately bimodal with peaks at 3-6 nm and 12-15 nm (Fig. 8.6b). This behavior suggests simultaneous loop nucleation and growth events. At 10 dpa, the loop sizes are less than 20 nm, different from the wide distribution of the 300ºC irradiated NFA sample (Fig. 8.5c). Overall, the increase in the dose level leads to the marginal increase in loop sizes. Interestingly, the 450ºC irradiated sample after 3, 5, and 10 dpa shows unimodal loop size distributions with the majority of the loops at <15 nm (Figs. 8.6d-8.6f). The absence of a bimodal size distribution at higher dose levels suggests that loop growth is suppressed. This behavior is very different from the 450ºC irradiated NFA sample (Figs. 8.5d-8.5f) where large dislocation loops (15-50 nm) and bimodal loop size distributions are observed. In stark contrast to the NFA

sample, increasing irradiation temperature leads to a decrease of average loop size for the Cr_3C_2@SiC-NFA sample.

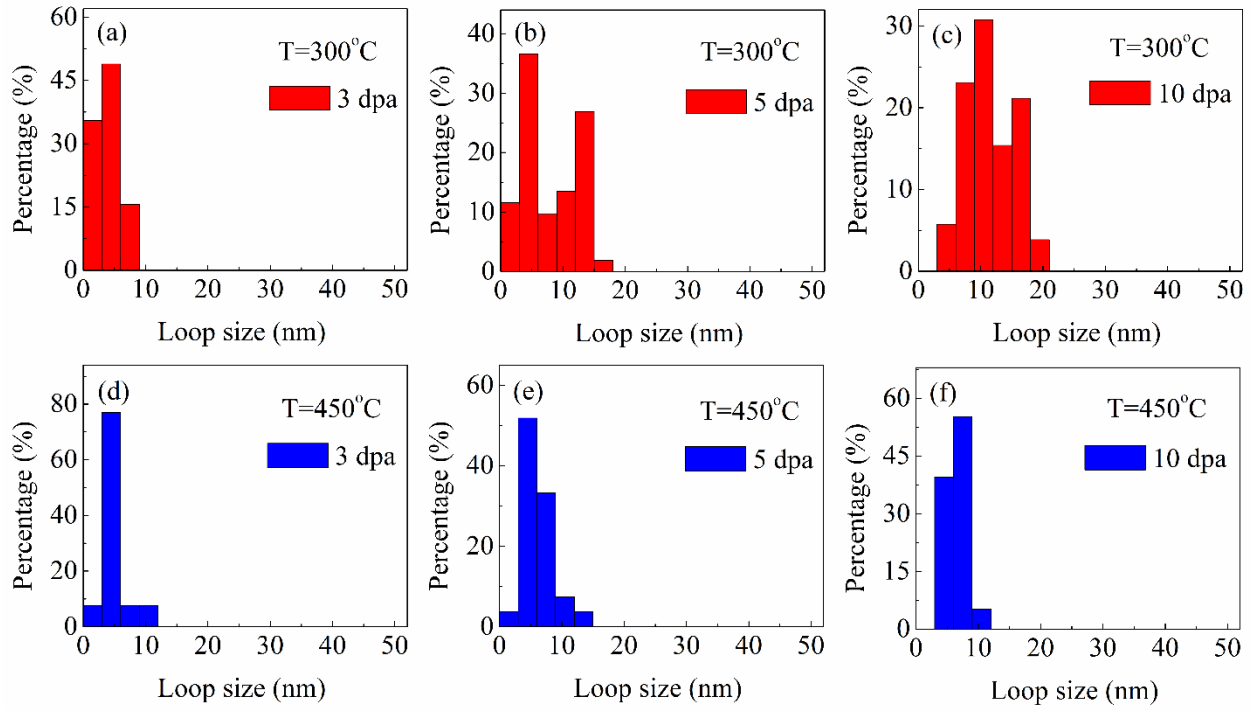

Fig. 8.6. Loop size distribution in the α-ferrite matrix of the Cr_3C_2@SiC-NFA sample irradiated at 300°C (a, b, c) and 450°C (d, e, f) with dose levels of 3 dpa, 5 dpa, and 10 dpa respectively.

Figs. 8.7a-8.7b show the dislocation loop density as a function of irradiation dose for the NFA and Cr_3C_2@SiC-NFA samples after the ion irradiation at 300°C and 450°C. For both materials, the loop density increases with increasing dose. For the NFA sample, the loop density for the 300°C irradiated sample is lower than that of the 450°C sample at low dose levels (below 3 dpa). At 5-10 dpa dose levels, the loop density of the 450°C sample is lower than that of the 300°C sample. For the Cr_3C_2@SiC-NFA material, the loop density of the 450°C irradiated sample is much lower as compared to that of the 300°C sample. For example, at 10 dpa, the loop density in the 450°C irradiated sample is nearly one order of magnitude lower than that in the 300°C irradiated sample. At 300°C irradiation, the loop density is comparable for the NFA and Cr_3C_2@SiC-NFA samples. At 10 dpa dose level, the decrease in the loop density with temperature

for the NFA sample is much smaller than that for the Cr_3C_2@SiC-NFA sample. Figs. 8.7c-8.7d show average loop sizes calculated using the data from the loop size distribution plots in Figs. 8.5 and 8.6. For both NFA and Cr_3C_2@SiC-NFA materials, the average loop size shows an increasing trend with the dose level at low doses. At high doses, the average loop size shows a continuous increase, saturated, or even decrease trend. For the NFA sample, the average loop size in the 450^{o}C sample is larger than that of the 300^{o}C sample at all dose levels. For the Cr_3C_2@SiC-NFA sample, however, the average loop size in the 450^{o}C sample is smaller than that of the 300^{o}C sample at all dose levels. At the same irradiation temperature, the average loop sizes in the NFA are marginally smaller than those in the Cr_3C_2@SiC-NFA sample at 300^{o}C. The smaller average loop sizes in the 300^{o}C irradiated NFA sample are probably due to the continuous increase in the fraction of small dislocations (<10 nm) even at higher dose levels. After the 450^{o}C irradiation, the average loop sizes in the NFA sample are much larger compared to those of the Cr_3C_2@SiC-NFA material, indicating extensive loop growth in the NFA sample. In general, the NFA sample shows a "normal" irradiation behavior with temperature: the dislocation loop density decreases and the average loop size increases with temperature. However, the Cr_3C_2@SiC-NFA sample shows an "abnormal" behavior: the loop density decreases by about one order of magnitude from 300^{o}C to 450^{o}C and the average loop size also decreases with increasing temperature. The possible causes for this "abnormal" behavior are discussed in the next section.

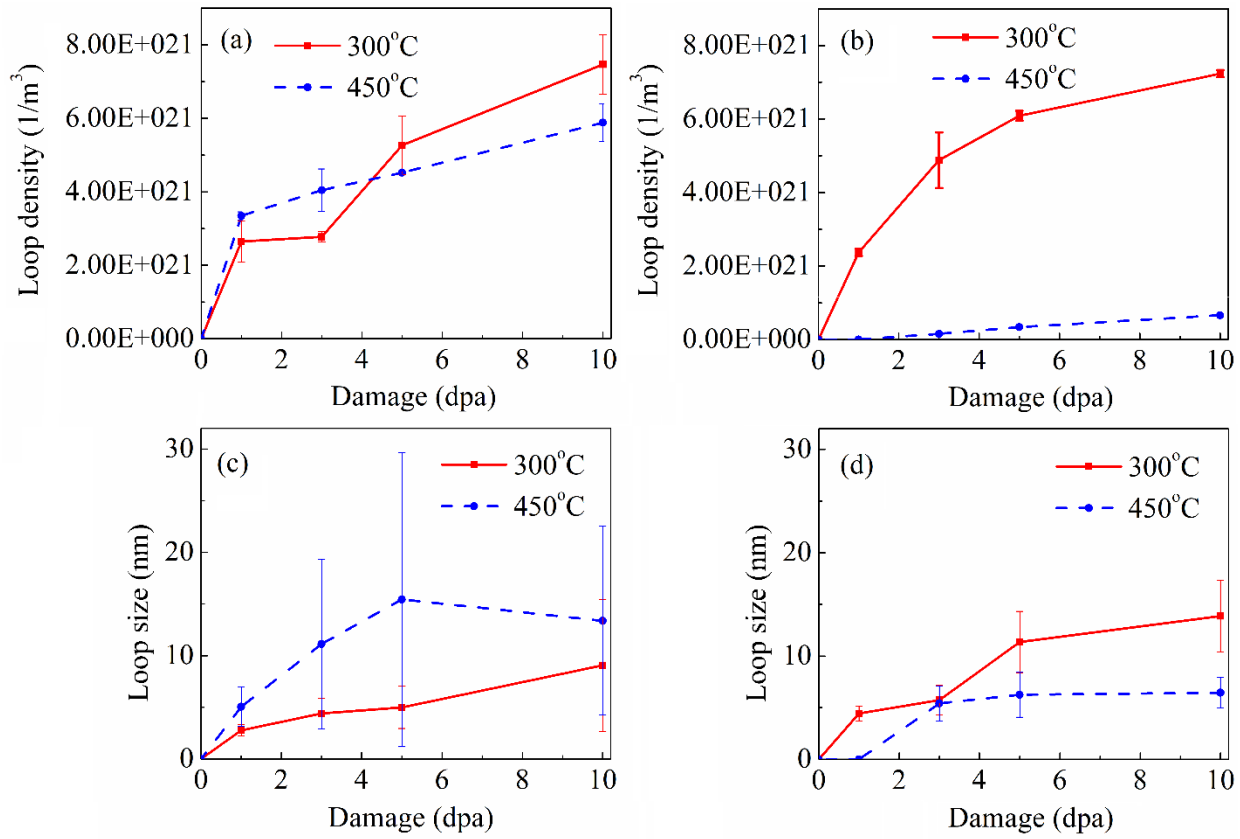

Fig. 8.7. Dislocation loop density (a, b) and average loop size (c, d) after the ion irradiation for the NFA and Cr3C2@SiC-NFA samples respectively (the lines joining two consecutive data points are simply guide for eyes).

8.5. Discussion

8.5.1. Effect of irradiation dose

The dislocation loop evolution behaviors in the NFA and Cr_3C_2@SiC-NFA materials show some differences, in particular at 450°C. Regardless of the irradiation temperature, initially both NFA and Cr_3C_2@SiC-NFA materials show an increasing trend in loop density with the dose level (see Figs. 8.7a-8.7b). At high doses, the loop density seems to become saturated in most cases except for the Cr_3C_2@SiC-NFA sample at 450°C. It is well known that irradiation creates Frenkel

pairs (interstitials and vacancies) and their clusters. The evolution of surviving defects can lead to the formation of interstitial loops and voids. Since voids are not observed in this work, it is reasonable to assume that migration energies of interstitials/clusters much lower than while vacancies/clusters at the temperatures studied in this work. In BCC Fe or Fe-based alloys, both sessile <100> and glissle ½<111> loops can exist and their relative abundance depends on temperature [191]. At low dose levels, the dislocation density is small. Therefore, the nucleation of new dislocation loops is predominantly observed. These irradiation-induced crowdion bundles [182, 204, 205] and loops can act as either sinks or nucleation centers for newly generated defects and clusters, depending on whether they have the same or opposite defect types. This phenomenon leads to two competing and simultaneously operating mechanisms, i.e., loop nucleation/growth and annihilation/coalescence [176, 182, 184]. Therefore, the slower increasing loop density rate with the dose level can be observed (see the slopes of the loop density plots in Figs. 8.7a-8.7b). At a particular threshold loop density, annihilation/coalescence becomes comparable with nucleation, which can lead to saturation of loop densities in materials [206], as observed in Figs. 8.7a and 8.7b).

The increase in the average loop size with irradiation dose is also observed (Figs. 8.7c and 8.7d). This is because the absorption of mobile defect clusters into dislocation loops leads to an increase in loop size [182]. For example, loops can grow by coalescence of two dislocation loops or crowdion bundles. The small loops/crowdions can assimilate with the larger loops by climbing and realigning their Burgers vector with those of the larger ones [176, 178].

8.5.2. Loop string formation

The alignment of the small black dot dislocations (i.e., the formation of loop strings) can be observed during the ion irradiation of the Cr_3C_2@SiC-NFA material at 300^{o}C (Figs. 8.3b-8.3c, blue arrow). Such alignment is attributed to the combination of elastic interactions of dislocation loops and their encounter probabilities. Therefore, this phenomenon is only observed when the local dislocation loop density reaches a certain level at which the distance between loops is small enough for effective elastic interactions [176, 179, 201, 202]. Since the loop alignment requires migration of dislocation loops, it is likely that the loops in the loop strings observed in the 300^{o}C

irradiated Cr_3C_2@SiC-NFA sample are of 1/2<111> type. The loop strings can also act as nucleation sites for larger, fully evolved loops. The dislocations in loop strings can reorient their Burgers vectors to create a large, single dislocation [176, 178]. This phenomenon is evident in Fig. 8.8c where fully evolved dislocation loops (see red arrow) can be observed for the 300°C irradiated Cr_3C_2@SiC-NFA material after 10 dpa, while loop strings can be observed in the same material with 3 and 5 dpa irradiation (Figs. 8.3b and 8.3c). Note that in NFA, loops strings have not been observed at both 300°C and 450°C. It is not obvious to us why they can form in the Cr_3C_2@SiC-NFA but not in the NFA.

8.5.3. Effect of irradiation temperature

Irradiation temperature can influence the mobility of loops and crowdion clusters. In this work, it is found that the balance between loop nucleation and annihilation/coalescence rates can be achieved at low dose levels and high temperatures. The TEM image of the NFA sample after 3 dpa dose at 450°C shows fully evolved dislocation loops as compared to small black dot loops during 300°C irradiation at the same dose (see Fig. 8.1b and Fig. 8.2b), indicating enhanced loop growth at high temperatures. At 10 dpa, the loop density of the NFA irradiated at 450°C is lower than that of the 300°C sample (Fig. 8.7a), while the average loop size has the opposite trend (Fig. 8.7c). The increased tendency of loop growth with temperature could be due to the high mobilities of point defects and defect clusters at 450°C as compared to 300°C. Therefore, point defects and defect clusters prefer to join existing loops than nucleating a new one. The loops can also grow by coalescence of two or more loops, which is also more effective at high temperatures. The decrease in nucleation rate at high temperature leads to a reduction in loop density. It should be noted that the loop density at lower dose levels shows higher values for the 450°C condition than the 300°C condition (see Fig. 8.7a). Previously, Chen's [207] work on neutron irradiated Fe-Cr model alloys reported similar results in which a sample irradiated at 450°C showed higher loop density than the 300°C counterparts for doses between 0.01 and 0.1 dpa. This is because the coalescence of defect loops is not significant at low doses. Therefore, the higher mobilities of point defects and small defect clusters lead to nucleation of more small dislocation loops at the higher temperature than at the low temperature.

The irradiation temperature can also influence the type of dislocation loops in the material. Many experiments on Fe-based ferritic alloys have confirmed the presence of <100> loop dominated microstructures at temperatures ≥400^{o}C and 1/2<111> loop dominated microstructures at temperatures ≤300^{o}C [191, 198, 208-210]. Theoretical analysis suggests that the reduction in the shear stiffness constant with temperature makes <100> loops energetically more favorable than 1/2<111> loops above 300^{o}C in BCC Fe [209]. The formation mechanisms of <100> loops in BCC Fe are still controversial. Several possible mechanisms have been proposed, such as reaction of two 1/2<111> loops of similar sizes [210, 211], transformation from C15 Laves phase interstitial clusters [212], or direct formation from collision cascades [213]. Therefore, it is of great interest to analyze the dominant type of loops in the NFA and Cr_3C_2@SiC-NFA irradiated samples at both 300^{o}C and 450^{o}C. In the present experiments, the dislocation loop type can be identified using the shapes of dislocations. Yao et al. [214] simulated the projections of 1/2<111> and <100> type loops at different zone axes and g-vector conditions. At zone axis=[100] and g=(110), <100> type loop is always highly elliptical with its major axis parallel to g={200}. Figs. 8.8a and 8.8b show the magnified TEM images of the 300^{o}C and 450^{o}C irradiated NFA samples at 10 dpa, respectively. The majority of the loops in the 450^{o}C irradiated NFA sample (Fig. 8.8b) show an elliptical shape with the major axis parallel to g=(020) and at 45^{o} to g=(110). Therefore, according to the g·b=0 invisibility criterion, these loops must be of [010] type. On the other hand, the 300^{o}C-irradiated NFA sample (Fig. 8.8a) shows regular elliptical loops instead of highly elongated loops. These regular elliptical loops must of ½<111> type based on simulated shapes reported in Yao et al.'s [214] work. It is difficult to ascertain Burgers vector of small dot dislocations using current experimental results due to a lack of discernible shape. Literature reports on similar ion irradiated Fe-Cr alloys show ½<111> dominated microstructures at 300^{o}C [170, 191, 196]. Overall, the temperature dependence of the predominant loop types in the NFA sample is consistent with many previously reported trends in Fe-based ferritic alloys: 1/2<111> and <100> loops are dominant at 300^{o}C and 450^{o}C, respectively.

For the 300^{o}C irradiated Cr_3C_2@SiC-NFA sample, the formation of loop strings after the 3 and 5 dpa irradiation (Figs. 8.3b and 8.3c) and the presence of regular elliptical loops (Fig. 8.8c) instead of highly elliptical ones after 10 dpa irradiation indicate predominantly 1/2<111> type loops. Fig. 8.8d shows a magnified kinematic bright field TEM image of the 450^{o}C irradiated Cr_3C_2@SiC-NFA. The significantly lower loop density and small average loop size (Figs. 8.7b

and 8.7d) in the Cr_3C_2@SiC-NFA sample during the 450°C irradiation is intriguing. This observation may be explained using the surface sink effect of the TEM foil. The TEM images in this experiment were captured using the [001] zone axis. At this zone axis, the Burgers vector of all variants of 1/2<111> type loops has components parallel to the surface normal [182, 191, 215]. This means that mobile 1/2<111> loops or crowdions can escape to the surface by traveling a very short distance (i.e. TEM foil thickness). At 450°C, the mobilities of 1/2<111> crowdions or loops are expected to be high. Therefore, most of 1/2<111> small loops or crowdions may have escaped to the surface before they coalesce with each other to form larger loops. This also explains the small size of 1/2<111> loops observed in this material at 450°C (Fig. 8.7d). To further elucidate the surface sink effect, the microstructure in thicker regions of the Cr_3C_2@SiC-NFA sample is analyzed, as shown in the kinematic bright field image in Fig. 8.9. Many dislocation loops can be observed in the thick region, much closer to the top invisible portion. The shape of these loops is not elliptical or aligned parallel to the g=(020) vector, thus confirming that they are 1/2<111> type loops. The thinner portions at the image bottom are nearly denuded of loops (see Fig. 8.9). This analysis confirms that the surface sink effect is operational in thinner regions of the sample, thus providing low loop densities. However, the results also indicate that the predominant loop type in the Cr_3C_2@SiC-NFA sample at 450°C is ½<111> type, which is different from the predominance of <100> loops in the NFA sample and other Fe-based alloys at similar temperatures. Therefore, the surface sink effect alone cannot explain the negligible fraction of <100> loops in the Cr_3C_2@SiC-NFA sample at 450°C. Since <100> loops are sessile, they should be visible even in thinner regions if they form, such as in the 450°C irradiated NFA sample in which the surface sink effect also exists.

Recent in-situ ion irradiation studies on F/M steel (HT-9) [216] and model Fe-Cr-Al alloys [182] have shown up to 50% and 50-80% proportion of ½<111> loops. The high level of predominance of ½<111> loops and negligible fraction of <100> loops observed in 450°C irradiated Cr_3C_2@SiC-NFA sample is intriguing. In comparison of the NFA and Cr_3C_2@SiC-NFA materials, the main difference is that the Cr_3C_2@SiC-NFA matrix contains around 6-7 wt% Si (due to the reaction between SiC and Fe) while the NFA does not. Therefore, it is likely that the addition of Si causes this interesting behavior.

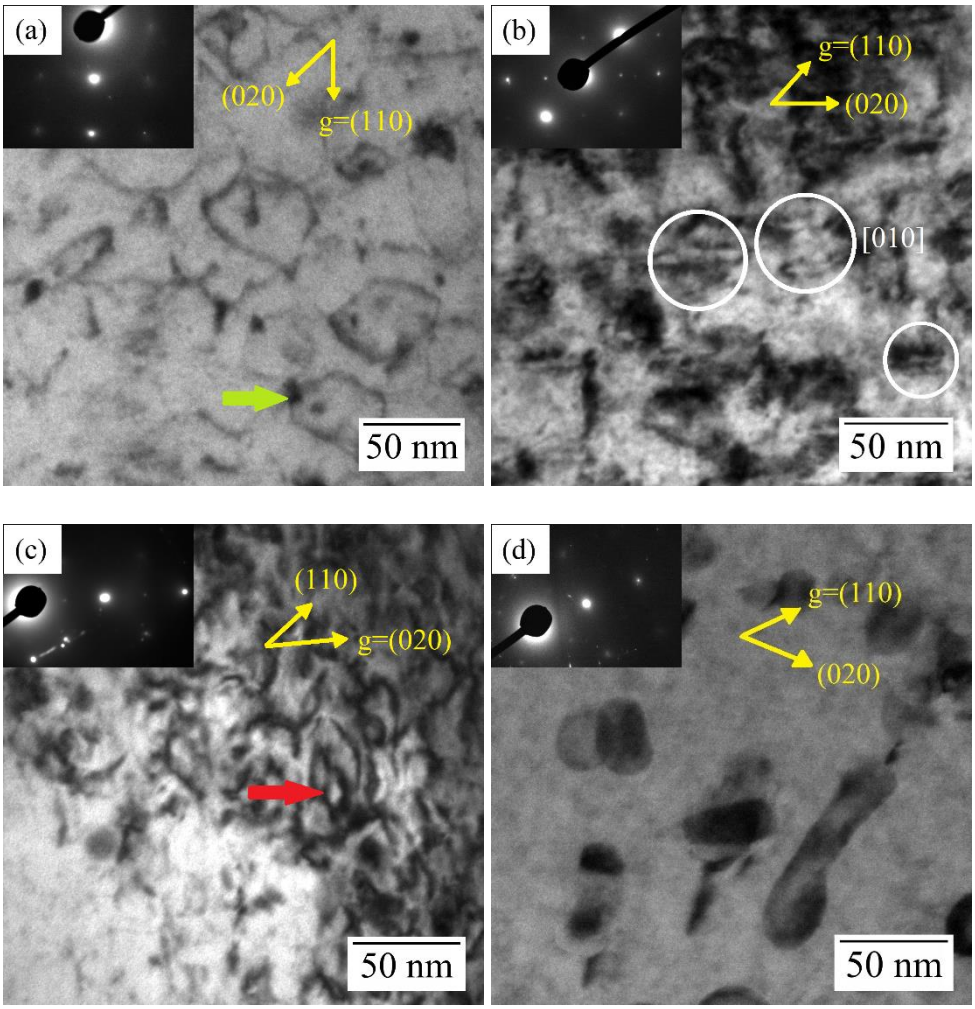

Fig. 8.8. Magnified kinematic bright field TEM images (Z.A.=[001]) showing dislocations in the NFA (a, b) and Cr_3C_2@SiC-NFA (c, d) materials after the ion irradiation up to 10 dpa at 300°C (left) and 450°C (right) respectively.

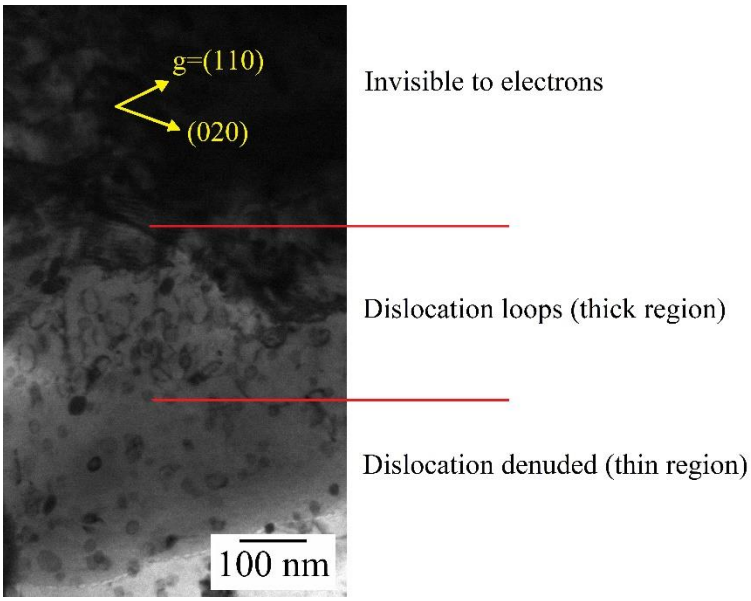

Fig. 8.9. Kinematic bright field TEM image (Z.A.=[001]) of different thickness regions in the Cr_3C_2@SiC-NFA material after the ion irradiation up to 3 dpa at 450°C.

8.5.4. Effect of dissolved silicon

(The molecular dynamics simulations in this section were performed by Prof. Xian-Ming Bai)

One effect of dissolving Si in Fe is the reduction of the lattice constant of the solid solution Fe-Si alloy. It has been experimentally shown that the lattice constant of an Fe-Si alloy decreases nearly linearly with Si concentration up to 10 at% Si [112]. The reduction of the lattice constant can cause an isotropic compressive strain in the Fe matrix. In BCC Fe, the habit plane for 1/2<111> loop is still controversial. Experimentally, researchers found that the habit planes of ½<111> loops are {111} [214]; or {110}, {111}, and {211} [217]; or between {111} and {110} [208]; or close to {111} [176]. In computer modeling, the habit plane of ½<111> loop was found to be mainly {110} [212, 218]. For <100> loops, the {100} habit plane was mainly observed experimentally. However, when the loop contains less than 65-70 interstitials, computer simulation showed that the <100>{110} loops are more stable than <100>{100} loops [218]. In our modeling work, the habit plane of {110} is used for both ½<111> and <100> loops, aiming at studying the early-stage loop formation. Using this approach, both ½<111> and <100> loops contain exactly the same

number of interstitials. Therefore, the change in the formation energy due to a hydrostatic strain can be unambiguously compared for the two types of loops. To create a loop, a circular disk of atoms parallel to a {110} plane is inserted in a Fe single crystal that contains 16,000 atoms. The Burgers vector of the disk is either a/2<111> or a<100>, depending on the loop type to be created. Note that a perfect dislocation loop in Fe may have either a square (for <100> loops) or hexagonal shape (for ½<111> loops) that corresponds to a magic number (interstitial arranged in polygon shaped clusters with sides corresponding to closed packed directions in the habit plane) of interstitials in the loop [212, 218]. Here an initial circular shape is used for both types of loops simply because we want to compare their formation energies at exactly the same loop size (in terms of the number of interstitials they contain). After a loop is created, it is relaxed at 300 K for 60 picoseconds in an NVT ensemble (constant number of atoms, volume, and temperature) and then energy minimization is conducted at 0 K. Figs. 8.10a and 8.10b show the relaxed loop structures at zero strain for the <100> and 1/2<111> loops that each contains 55 interstitials. The Burgers vectors of the two loops are confirmed by the dislocation analysis (DXA) algorithm [219] available in the OVITO software. The loop formation energy per atom is calculated by:

$$\mathrm{E_f} = (\mathrm{E_1} - \mathrm{E_0})/\mathrm{n} \tag{8.1}$$

where E_1 is the total energy of a loop-containing system, E_0 is the energy of the single crystal that contains the same number of atoms as in the loop-containing system, and n is the number of interstitials in the loop (termed as loop size here).

Loops with sizes ranging from 35 to 77 interstitials are created in this work. To study the strain effect, both -0.01 and +0.01 hydrostatic strains are applied to the loop containing systems. The same strains are also applied to the reference single crystal in order to calculate the formation energies correctly. Fig. 8.10c shows the formation energies of <100> and ½<111> dislocation loops as a function of loop size at 0, -0.01, and +0.01 hydrostatic strains. At zero strain, the results show that ½<111> loops are slightly more stable than <100> loops, which are consistent with many previous studies [212, 218]. At the compressive strain (-0.01), the absolute formation energies of both types of loops increase, which is expected. However, the energy difference between the two types of loops remains almost the same (strictly, increases slightly). At a dilative

strain (+0.01), the formation energies of both types of loops decrease slightly. Again, the energy difference between the two types of loops changes very little. At this strain level, which is already much larger than that induced by the lattice contraction in the Cr_3C_2@SiC-NFA sample in this work, an isotropic strain is not expected to significantly modify the relative stability between the <100> and ½<111> loops. Therefore, we can rule out the effect of lattice contraction due to dissolved Si in Fe on the absence of <100> loops in the Cr_3C_2@SiC-NFA sample at 450^{o}C.

The kinetic Monte Carlo simulation work by Xu et al. [210] has shown that interactions between two 1/2<111> type loops of similar size can form either <100> type loops or larger 1/2<111> type loops. If this is the dominant mechanism for <100> loop formation, the additional Si element in the Cr_3C_2@SiC-NFA material should have increased the formation probability of 1/2<111> type loops as compared to <100> type loops. However, this mechanism cannot be deduced from current experimental results.

Another possible effect is the increased vacancy mobility due to the presence of Si in Fe. Previously, it has been shown that the addition of Si in Ni or Fe-Ni-Cr stainless steel can enhance the effective vacancy diffusivity due to the fast diffusion of Si through the vacancy exchange mechanism [220]. In BCC Fe, vacancies usually migrate much slower than interstitials. At high temperatures, Si-assisted vacancy diffusion in the Cr_3C_2@SiC-NFA may be more active than the vacancy diffusion in the NFA if Si has a similar effect in Fe as in stainless steels. If this is the case, the Si-assisted vacancy diffusion may enhance the interstitial-vacancy recombination and thus decrease the overall loop density and size [221, 222]. This provides another possible explanation for the low loop density in the Cr_3C_2@SiC-NFA at 450^{o}C even in the deeper region (Fig. 8.9). If <100> loops form mainly through the mechanism of reaction of two ½<111> loops of similar size [210, 211], the enhanced recombination may reduce the available interstitials to form mobile ½<111> loops and thus suppress the formation of <100> loops. However, even if this is the case, it is expected that some <100> loops may still be observed. However, <100> loops have not been observed in the Cr_3C_2@SiC-NFA at 450^{o}C. Here we use Fig. 8.11 to schematically illustrate our hypotheses of dislocation loop evolution mechanisms in both NFA and Cr_3C_2@SiC-NFA samples at 450^{o}C. It shows the possible effects of Si-assisted vacancy-interstitial recombination and surface sink on the dislocation loop evolution. The hypotheses, however, need to be validated in the future.

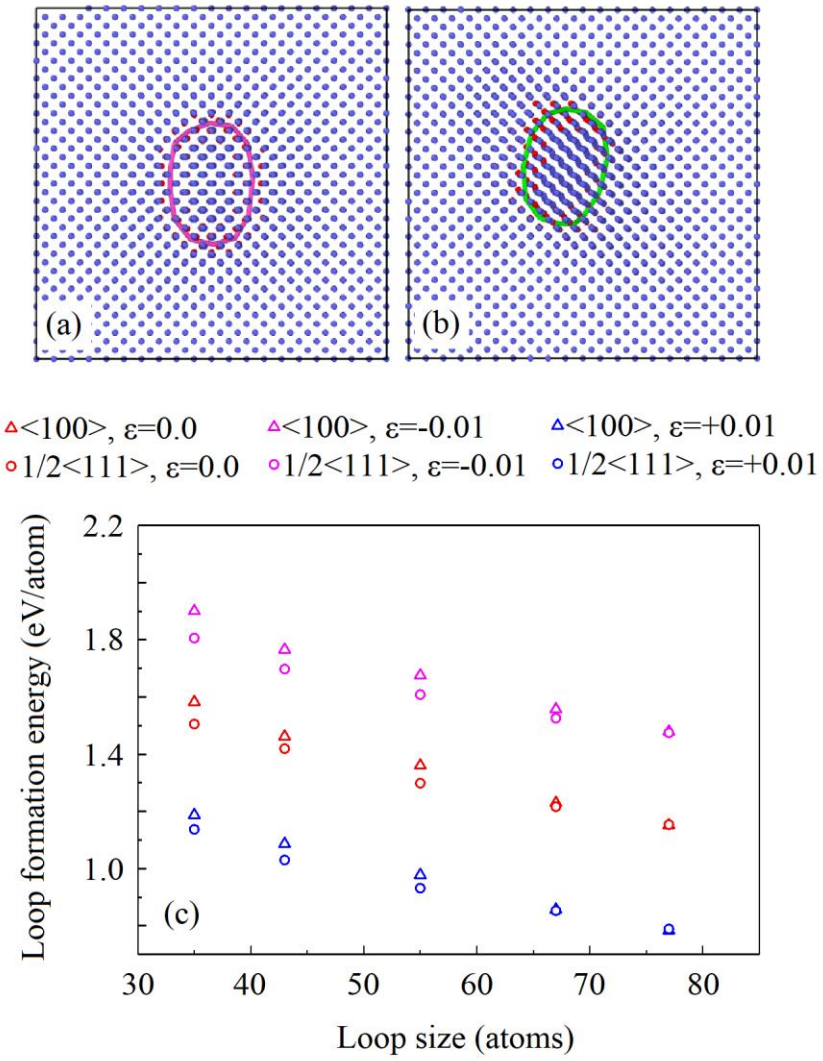

Fig. 8.10. MD calculations of strain effects on the dislocation loop formation energies in BCC Fe. (a) <100>{110} loop containing 55 interstitials, (b) 1/2<111>{110} loop containing 55 interstitials, and (c) Dislocation loop formation energy as a function of loop size at zero, -0.01, and +0.01 isotropic strains. Here the two snapshots are projected along the [100] direction. The blue and red spheres represent BCC and non-BCC atoms identified by DXA, respectively. The purple and green lines are <100> and ½<111> dislocation lines identified by DXA, respectively (courtesy: Prof. Xian-Ming Bai – co-author in this manuscript).

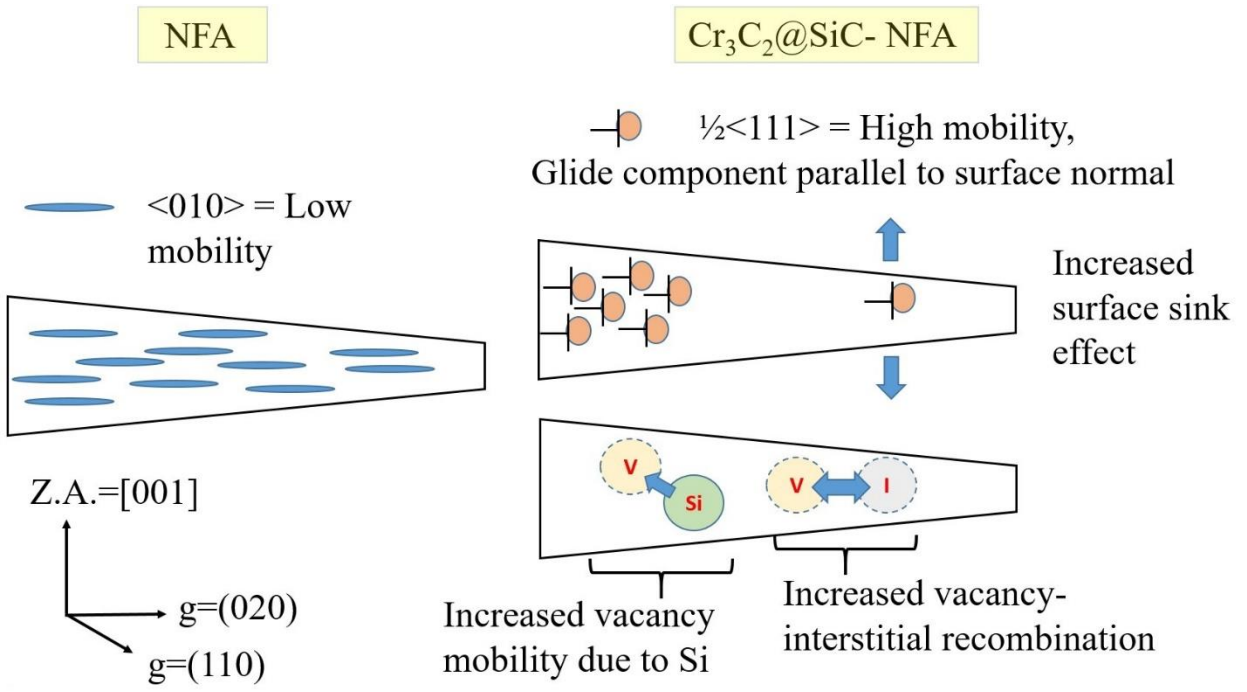

Fig. 8.11. Schematic illustrations showing irradiation behaviors of the NFA and Cr_3C_2@SiC-NFA samples at 450ºC (dislocation types shown are the predominant ones).

8.5.5. Effect of precipitates

The NFA sample in this work consists of Y-Ti-O complex nanoclusters (~10^{24} m^{-3} [59]), while the Cr_3C_2@SiC-NFA sample contains additional (Ti,W)C precipitates (~3×10^{21} m^{-3}). The sink strength due to precipitates can be calculated using following equation:

$$\text{Sink strength} = 4\pi r N_p \quad (8.2)$$

Where, r=radius of precipitates, Y-Ti-O= ~1.5 nm [59]

(Ti,W)C=~10 nm (measured)

N_p=number density of precipitates, Y-Ti-O=~10^{24} m^{-3} [59]

(Ti,W)C=~3×10^{21} m^{-3} (measured)

The sink strength values for NFA and Cr_3C_2@SiC-NFA composite are 1.88×10^{16} m^{-2} and 1.92×10^{16} m^{-2} respectively. This means sink strength of Cr_3C_2@SiC-NFA composite is just marginally higher than NFA. Therefore, precipitate sink effect may be another factor to slightly enhance defect/crowdion/loop annihilation rates in the Cr_3C_2@SiC-NFA, thereby reducing the loop densities and sizes. However, the precipitate sink effect still cannot explain the key differences in dislocation behaviors of the NFA and Cr_3C_2@SiC-NFA materials during irradiation at 450^{o}C, such as the negligible fraction of <100> loops in the latter sample.

8.6. Conclusions

In-situ Kr^{++} ion irradiation was used to study the microstructural evolution in spark plasma sintered NFA and newly developed Cr_3C_2@SiC-NFA composite at 300^{o}C and 450^{o}C temperatures. Irradiation at 300^{o}C creates high loop densities in both NFA and Cr_3C_2@SiC-NFA materials. The predominant loop type is 1/2<111> type in both materials at this temperature. At 450^{o}C ion irradiation, the NFA sample shows extensive damage with mostly <100> type loops as opposed to very minimal damage for the Cr_3C_2@SiC-NFA sample with predominantly 1/2<111> type loops. The significantly lower loop density and smaller loop size in the Cr_3C_2@SiC-NFA sample at 450^{o}C is attributed to the surface sink effect (for thin region), as well as possible enhanced interstitial-vacancy recombination due to Si-assisted vacancy diffusion and presence of precipitate sinks. The negligible fraction of <100> loops in the Cr_3C_2@SiC-NFA at 450^{o}C could be caused by the presence of Si element. However, MD simulations show that the compressive strain due to Si-induced crystal lattice contraction does not change the relative stability between two types of loops significantly, and therefore the lattice contraction of the Fe matrix due to dissolved Si is unlikely to be the cause for the negligible fraction of <100> loops in the Cr_3C_2@SiC-NFA at 450^{o}C. It is possible that other effects due to the presence of Si cause this phenomenon and more studies are needed in the future to understand this interesting behavior.

Chapter 9

Summary and Future Work

6.1. Summary of the findings

This study deals with the processing-structure-property relationship of SiC-NFA composites with C and Cr_3C_2 interfacial barrier layers. C and Cr_3C_2 interfacial barriers have successfully suppressed silicide formation, however, could not retain SiC in the system. Instead, the final microstructure consisted of graphite, carbides such as $(Fe,Cr)_7C_3$ and (Ti,W)C in the α-ferrite (NFA) matrix. The dissolved Si in α-ferrite and presence of carbides have imparted unique oxidation and irradiation properties to these composites. Following are some of the important findings from the current work:

- Detailed microstructure studies on SiC-C@NFA and Cr_3C_2@SiC-NFA using SEM-EDS, STEM-EDS, and EBSD techniques revealed unique microstructure with graphite, $(Fe,Cr)_7C_3$ and (Ti,W)C in α-ferrite (NFA) with varying amounts in both samples. Cr_3C_2@SiC-NFA samples had a much higher number density of (Ti,W)C carbides than SiC-C@NFA. While SiC-C@NFA had a higher volume fraction of graphite with much more homogeneous distribution throughout the microstructure than Cr_3C_2@SiC-NFA. In both SiC-C@NFA and Cr_3C_2@SiC-NFA composites, the matrix was rich in Si, due to the dissolution of SiC during the spark plasma sintering process. These differences in microstructures of NFA, SiC-C@NFA, and Cr_3C_2@SiC-NFA helped understand the processing-microstructure-properties relationship.
- The effect of long term (50 hours) thermal treatment at 1000^{o}C was assessed using advanced microstructural characterization techniques. Thermal treatment resulted in a simultaneous increase in volume fraction and sizes of $(Fe,Cr)_7C_3$ and (Ti,W)C carbides. ThermoCalc precipitation and coarsening simulations reasonably predicted precipitate size and matched well with experimental values.

- SiC-C@NFA composite showed a significant decrease in weight gain after high temperature oxidation under water vapor containing atmosphere. However, the microstructures of 5 and 15 vol% samples consisted of significant internal oxidation. 25 vol% SiC-C@NFA samples showed around 90% increase in oxidation resistance during 1000^{o}C thermal treatment as compared to NFA sample. Cr_3C_2@SiC-NFA also composites showed a 97% improvement in oxidation performance (in terms of weight gain) as compared to the NFA sample at 1000^{o}C. Unlike SiC-C@NFA, no internal oxidation was observed for Cr_3C_2@SiC-NFA composites. Such a huge leap in oxidation performance was attributed to the formation of Cr_2O_3+SiO_2 protective oxidation layer. Diffusion simulations using ThermoCalc software confirmed improved kinetics of Cr_2O_3+SiO_2 protective layer formation with increasing Cr_3C_2@SiC content.
- SiC-C@NFA composite showed significant damage after 10 dpa irradiation at 300^{o}C. 'Loop strings', i.e. spatial ordering of black dot dislocation loops and fully evolved loops were observed at high irradiation dose levels (5 and 10 dpa respectively). At 450^{o}C, high dislocation damage was observed in the thicker regions of the sample. While, thinner regions were largely devoid of any dislocation damage, indicating large scale migration of defects towards surface sinks soon after their nucleation. New precipitation and growth of (Ti,W)C carbides were observed with increasing irradiation dose. TTT diagram plotted using the ThermoCalc diagram predicted a very long time (~280 hours) for the formation of (Ti,W)C precipitates at 450^{o}C. This confirmed the irradiation assisted precipitation of (Ti,W)C carbides in SiC-C@NFA samples.
- NFA samples showed heavy irradiation damage at 300^{o}C and 450^{o}C. Dislocation loop densities were lower for samples irradiated at 450^{o}C than at 300^{o}C, in contrast, loop sizes were higher for 450^{o}C than at 300^{o}C. The microstructure of NFA was predominant in ½<111> loops after 300^{o}C irradiation up to 10 dpa. At 450^{o}C, NFA showed predominantly <100> type loops. This behavior was in agreement with results observed in literature for similar ODS, ferritic and ferritic-martensitic steels.
- Cr_3C_2@SiC-NFA samples showed heavy irradiation damage after irradiation at 300^{o}C. However, at 450^{o}C, dislocation loop density and size were surprisingly low. TEM investigations of thicker regions showed primarily ½<111> type loops, unlike the NFA sample. Formation energies of ½<111> and <100> calculated using molecular dynamics simulations

showed only a marginal difference for NFA and Cr_3C_2@SiC-NFA composites. The additional dissolved Si element in the α-ferrite matrix of Cr_3C_2@SiC-NFA could have been an important factor behind this interesting behavior.

6.2. Future work

Future work of this research may focus on two aspects: (1) Better understanding of high temperature corrosion and irradiation aspects of SiC-C@NFA and Cr_3C_2@SiC-NFA composites, (2) Development of processing methods for SiC-NFA composites with improved microstructure, i.e. higher volume fraction of SiC and negligible reaction products and development of pathways for proposed gradient SiC-NFA composites. The brief description of future work is as follows:

- Better understanding of the oxidation behavior of these composites can be gained by tracking oxide scale evolution with time. It will be interesting to know the kinetics of oxidation reaction and growth laws (e.g. parabolic, linear, etc.) it follows. Thermogravimetric analysis can be useful to achieve these goals. SEM and TEM analysis of oxide scales at different times can provide important information on the mechanism of oxide growth.
- Analysis of vapors formed during the oxidation of these composites using gas chromatography can be useful. It can identify 'breakaway' events triggered by the volatilization of Cr_2O_3+SiO_2 protective layers during attack by water vapors at high temperatures.
- It will be interesting to know the corrosion response of these materials under more aggressive environments such as supercritical water or the combination of high pressure and high temperature conditions.
- Irradiation behavior showed interesting behavior for Cr_3C_2@SiC-NFA composites, in which ½<111> type dislocation loops were observed even at 450^{o}C, contrary to NFA and also most of the literature results on similar ferritic and ferritic martensitic alloys. It would be interesting to perform experiments at even higher temperatures such as 500^{o}C, 600^{o}C, and 700^{o}C to see at what temperature transition from ½<111> loops to <100> occurs.
- Future experiments on Cr_3C_2@SiC-NFA should also focus on dislocation loop evolution in thicker parts of the sample and during very early stages of irradiation such as 0, 0.1, 0.2, 0.3,…1

dpa. In these stages, dislocation loop density would be relatively low and therefore easier to quantify the damage. In this work, the zone axis for all in-situ irradiation experiments was [001], which is parallel to all the variants of ½<111>. This resulted in the easy escape of ½<111> loops to surface as they had to travel very short distances especially at thinner regions of the TEM sample. Therefore, in future experiments, the zone axis should be such that it will be difficult for most variants of ½<111> type loops to escape to surface easily.

- Simultaneous irradiation can accelerate corrosion damage in the sample. Future work may also consider simultaneous ion irradiation and corrosion experiments on SiC-C@NFA and Cr_3C_2@SiC-NFA composites.
- There is a need to improve processing methods to retain SiC particles inside the NFA matrix and achieve the lowest amounts of reaction products. These methodologies should include the development of new dense and crack-free reaction barrier coatings which can control the reaction between NFA and SiC. Our recent work on Y_2O_3 coatings on SiC using the molten salt technique successfully retained SiC particles in the NFA matrix during pressureless sintering. Future work may involve the consolidation of Y_2O_3 coated SiC using spark plasma sintering to achieve full density. The development of such coatings can be useful for the eventual fabrication of gradient SiC-NFA composites using spark plasma sintering technique.
- Some new solid-state processing techniques such as friction stir processing can be used for the fabrication of fully dense SiC-NFA samples.

Bibliography

[1] M.M. Abu-Khader, Recent advances in nuclear power: A review, Progress in Nuclear Energy 51(2) (2009) 225-235.

[2] C.R.F. Azevedo, Selection of fuel cladding material for nuclear fission reactors, Engineering Failure Analysis 18(8) (2011) 1943-1962.

[3] A. Huhtala, P. Remes, Quantifying the social costs of nuclear energy: Perceived risk of accident at nuclear power plants, Energy Policy 105 (2017) 320-331.

[4] I.N. Kessides, Nuclear power: Understanding the economic risks and uncertainties, Energy Policy 38(8) (2010) 3849-3864.

[5] A. Adamantiades, I. Kessides, Nuclear power for sustainable development: Current status and future prospects, Energy Policy 37(12) (2009) 5149-5166.

[6] S.J. Zinkle, K.A. Terrani, J.C. Gehin, L.J. Ott, L.L. Snead, Accident tolerant fuels for LWRs: A perspective, Journal of Nuclear Materials 448(1-3) (2014) 374-379.

[7] K. Bruninx, D. Madzharov, E. Delarue, W. D'Haeseleer, Impact of the German nuclear phase-out on Europe's electricity generation—A comprehensive study, Energy Policy 60 (2013) 251-261.

[8] Z. Ming, L. Yingxin, O. Shaojie, S. Hui, L. Chunxue, Nuclear energy in the Post-Fukushima Era: Research on the developments of the Chinese and worldwide nuclear power industries, Renewable and Sustainable Energy Reviews 58 (2016) 147-156.

[9] S.J. Zinkle, G.S. Was, Materials challenges in nuclear energy, Acta Materialia 61(3) (2013) 735-758.

[10] K.A. Terrani, S.J. Zinkle, L.L. Snead, Advanced oxidation-resistant iron-based alloys for LWR fuel cladding, Journal of Nuclear Materials 448(1-3) (2014) 420-435.

[11] F. Thomas, B. Stephan, Nuclear fuel, cladding and the discovery of Zirconium, Three Mile Island, Chernobyl and Fukushima: Curse of the nuclear genie-Springer (2016) 105-114.

[12] A.T. Motta, A. Couet, R.J. Comstock, Corrosion of zirconium alloys used for nuclear fuel cladding, Annual Review of Materials Research 45(1) (2015) 311-343.

[13] B. Rouben, Introduction to reactor physics, Atomic Energy of Canada Limited (AECL) (2002).

[14] P.A. Burr, Ab-initio modelling of Zr and Be alloys for nuclear applications, PhD thesis-Department of Materials, Imperial College London (2015).

[15] D.M. Carpenter, An assessment of silicon carbide as a cladding material for light water reactors, PhD thesis-Department of Nuclear Science and Engineering-Massachusetts Institute of Technology (2010).

[16] M.S. M. F. Ashby, Materials for nuclear power systems, Granta Materials Inspiration (2011).

[17] M.F. Ashby, M. Smidman, Materials for nuclear power systems, Granta Materials Inspiration 1.1 (2010).

[18] Control assembly materials for water reactors: Experience, performace and perspective Proceedings of a technical committee meeting, Vienna, International Atomic Energy Agency (1998).

[19] Y. Ishiwatari, Y. Oka, S. Koshizuka, A. Yamaji, J. Liu, Safety of super LWR, (I) safety system design, Journal of Nuclear Science and Technology 42(11) (2005) 927-934.

[20] T. Abram, S. Ion, Generation-IV nuclear power: A review of the state of the science, Energy Policy 36(12) (2008) 4323-4330.

[21] G. Locatelli, M. Mancini, N. Todeschini, Generation IV nuclear reactors: Current status and future prospects, Energy Policy 61 (2013) 1503-1520.

[22] J.E. Kelly, Generation IV International Forum: A decade of progress through international cooperation, Progress in Nuclear Energy 77 (2014) 240-246.

[23] A. Todd, B. Jeremy, M. Mitch, P. David, Materials challenges for nuclear systems, Materials Today 13(10) (2010) 14-23.

[24] Y. Katoh, L.L. Snead, I. Szlufarska, W.J. Weber, Radiation effects in SiC for nuclear structural applications, Current Opinion in Solid State and Materials Science 16(3) (2012) 143-152.

[25] P. Eddy S., A. Alfredo Y., G. Claudia, The quest for safe and reliable fuel cladding, 2015 International Nuclear Atlantic Conference - INAC 2015 (2015).

[26] J. Nikola, R. Vasile, N. Karl-Fredrik, Nuclear fuel cladding-Review of the Zircaloy cladding and basic analysis of the model with the single hydride, European Commision: Directorate General Joint Research Center-Institute of Energy (2008).

[27] A. Yacout, Nuclear Fuel, Energy engineering and systems analysis, Argonne National Laboratory (2011).

[28] L. Hallstadius, S. Johnson, E. Lahoda, Cladding for high performance fuel, Progress in Nuclear Energy 57 (2012) 71-76.

[29] G.R. Odette, M.J. Alinger, B.D. Wirth, Recent developments in irradiation-resistant steels, Annual Review of Materials Research 38(1) (2008) 471-503.

[30] G.R. Odette, Recent progress in developing and qualifying nanostructured ferritic alloys for advanced fission and fusion applications, JOM 66(12) (2014) 2427-2441.

[31] A. Kimura, R. Kasada, N. Iwata, H. Kishimoto, C.H. Zhang, J. Isselin, P. Dou, J.H. Lee, N. Muthukumar, T. Okuda, M. Inoue, S. Ukai, S. Ohnuki, T. Fujisawa, T.F. Abe, Development of Al added high-Cr ODS steels for fuel cladding of next generation nuclear systems, Journal of Nuclear Materials 417(1-3) (2011) 176-179.

[32] R.B. Rebak, Alloy selection for accident tolerant fuel cladding in commercial light water reactors, Metallurgical and Materials Transactions E 2(4) (2015) 197-207.

[33] S.F. Pugh, Beryllium as a nuclear fuel cladding material, Beryllium 1977 Fourth international conference on beryllium held at the Royal Society, London, 4-7 October 1977, United Kingdom, 1977, pp. 51/1-51/8.

[34] S.F. Pugh, J.E. Antill, B.W. Mott, Magnesium alloy cladding for nuclear fuels, J. Brit. Nucl. Energy Soc. 11-No. 4(313-30) (1972).

[35] B.A.P. Kurt A. Terrani, Chad M. Parish, Chinthaka M. Silva, Lance L. Snead,* and, Y. Katoh*, Silicon carbide oxidation in steam up to 2 MPa, J. Am. Ceram. Soc. 97(8) (2014) 2331-2353.

[36] D.L. Douglass, The metallurgy of zirconium, International Atomic Energy Agency, Vienna, 1971.

[37] R. Krishnan, M.K. Asundi, Zirconium alloys in nuclear technology, Proceedings of Indian Academy of Sciences 4(1) (1981) 41-56.

[38] C.A. Rusch, Nuclear fuel performance: Trends, remedies and challenges, Journal of Nuclear Materials 383(1-2) (2008) 41-44.

[39] K. Whittle, Mistakes made and lessons learnt, Nuclear Materials Science, IOP Publishing, 2016, pp. 9-1-9-21.

[40] D.K. Randall Gauntt, Jeff Cardoni, Jesse Phillips, Andrew Goldmann, Susan Pickering, Matthew Francis, Kevin Robb, Larry Ott, Dean Wang, Curtis Smith, Shawn St.Germain, David Schwieder, Cherie Phelan, Fukushima Daiichi accident study (Status as of April 2012), Sandia Reports - Sandia National Laboratories (2012).

[41] K. Barret, S. Bragg-Sitton, G. Danny, Advanced LWR nuclear fuel cladding system development trade off study, Light water reactor sustainability program - Idaho National Laboratory (2012).

[42] E. Alat, A.T. Motta, R.J. Comstock, J.M. Partezana, D.E. Wolfe, Multilayer (TiN, TiAlN) ceramic coatings for nuclear fuel cladding, Journal of Nuclear Materials 478 (2016) 236-244.

[43] B.R. Maier, B.L. Garcia-Diaz, B. Hauch, L.C. Olson, R.L. Sindelar, K. Sridharan, Cold spray deposition of Ti_2AlC coatings for improved nuclear fuel cladding, Journal of Nuclear Materials 466 (2015) 712-717.

[44] H. Yeom, B. Hauch, G. Cao, B. Garcia-Diaz, M. Martinez-Rodriguez, H. Colon-Mercado, L. Olson, K. Sridharan, Laser surface annealing and characterization of Ti2AlC plasma vapor deposition coating on zirconium-alloy substrate, Thin Solid Films 615 (2016) 202-209.

[45] B.A. Pint, K.A. Terrani, Y. Yamamoto, L.L. Snead, Material selection for accident tolerant fuel cladding, Metallurgical and Materials Transactions E 2(3) (2015) 190-196.

[46] I.J. van-Rooyen, Pre-irradiation testing and analysis to support the LWRS hybrid SiC-CMC-Zircaloy-4 unfueled rodlet irradiation, Idaho National Laboratory (2012).

[47] P. Dubuisson, Y.d. Carlan, V. Garat, M. Blat, ODS Ferritic/martensitic alloys for Sodium Fast Reactor fuel pin cladding, Journal of Nuclear Materials 428(1-3) (2012) 6-12.

[48] S. Ukai, M. Fujiwara, Perspective of ODS alloys application in nuclear environments, Journal of Nuclear Materials 307–311 (2002) 749–757.

[49] S. Ukai, M. Harada, H. Okada, M. Inoue, S. Nomura, S. Shikakura, K. Asabe, T. Nishida, M. Fujiwara, Alloying design of dispersion strengthened ferritic steel for long life FBRs core material, Journal of Nuclear Materials 204 (1993) 65-73.

[50] N. Baluc, J.L. Boutard, S.L. Dudarev, M. Rieth, J.B. Correia, B. Fournier, J. Henry, F. Legendre, T. Leguey, M. Lewandowska, R. Lindau, E. Marquis, A. Muñoz, B. Radiguet, Z. Oksiuta, Review on the EFDA work programme on nano-structured ODS RAF steels, Journal of Nuclear Materials 417(1-3) (2011) 149-153.

[51] J. Ren, L. Yu, Y. Liu, C. Liu, H. Li, J. Wu, Effects of Zr Addition on Strengthening Mechanisms of Al-Alloyed High-Cr ODS Steels, Materials 11(1) (2018).

[52] T.S. Byun, J.H. Kim, J.H. Yoon, D.T. Hoelzer, High temperature fracture characteristics of a nanostructured ferritic alloy (NFA), Journal of Nuclear Materials 407(2) (2010) 78-82.

[53] R.B. Rebak, Nuclear applications of oxide dispersion strengthened and nano-featured alloys: An introduction, JOM 66(12) (2014) 2424-2426.

[54] M.P. Brady, Y. Yamamoto, M.L. Santella, L.R. Walker, Composition, microstructure, and water vapor effects on internal/external oxidation of alumina-forming austenitic stainless steels, Oxidation of Metals 72(5-6) (2009) 311-333.

[55] B.A. Pint, K.A. Terrani, M.P. Brady, T. Cheng, J.R. Keiser, High temperature oxidation of fuel cladding candidate materials in steam–hydrogen environments, Journal of Nuclear Materials 440(1-3) (2013) 420-427.

[56] P. Yvon, F. Carré, Structural materials challenges for advanced reactor systems, Journal of Nuclear Materials 385(2) (2009) 217-222.

[57] E. Essuman, G.H. Meier, J. Żurek, M. Hänsel, W.J. Quadakkers, The effect of water vapor on selective oxidation of Fe–Cr alloys, Oxidation of Metals 69(3-4) (2008) 143-162.

[58] E. Essuman, G.H. Meier, J. Żurek, M. Hänsel, L. Singheiser, W.J. Quadakkers, Enhanced internal oxidation as trigger for breakaway oxidation of Fe–Cr alloys in gases containing water vapor, Scripta Materialia 57(9) (2007) 845-848.

[59] T.S. Byun, J.H. Yoon, D.T. Hoelzer, Y.B. Lee, S.H. Kang, S.A. Maloy, Process development for 9Cr nanostructured ferritic alloy (NFA) with high fracture toughness, J Nucl Mater 449(1-3) (2014) 290-299.

[60] M.K. Miller, C.M. Parish, Role of alloying elements in nanostructured ferritic steels, Materials Science and Technology 27(4) (2013) 729-734.

[61] M.K. Miller, D.T. Hoelzer, E.A. Kenik, K.F. Russell, Stability of ferritic MA/ODS alloys at high temperatures, Intermetallics 13(3-4) (2005) 387-392.

[62] R. Kasada, S.G. Lee, J. Isselin, J.H. Lee, T. Omura, A. Kimura, T. Okuda, M. Inoue, S. Ukai, S. Ohnuki, T. Fujisawa, F. Abe, Anisotropy in tensile and ductile–brittle transition behavior of ODS ferritic steels, Journal of Nuclear Materials 417(1-3) (2011) 180-184.

[63] I. Hilger, X. Boulnat, J. Hoffmann, C. Testani, F. Bergner, Y. De Carlan, F. Ferraro, A. Ulbricht, Fabrication and characterization of oxide dispersion strengthened (ODS) 14Cr steels consolidated by means of hot isostatic pressing, hot extrusion and spark plasma sintering, Journal of Nuclear Materials 472 (2016) 206-214.

[64] K. Yueh, K.A. Terrani, Silicon carbide composite for light water reactor fuel assembly applications, Journal of Nuclear Materials 448(1-3) (2014) 380-388.

[65] C.P. Deck, H.E. Khalifa, B. Sammuli, T. Hilsabeck, C.A. Back, Fabrication of SiC–SiC composites for fuel cladding in advanced reactor designs, Progress in Nuclear Energy 57 (2012) 38-45.

[66] W.J. Quadakkers, J. Zurek, M. Hansel, Effect of water vapor on high-temperature oxidation of FeCr alloys, JOM 61(7) (2009) 44-50.

[67] H. Asteman, J.E. Svensson, L.G. Johansson, M. Norell, Indication of chromium oxide hydroxide evaporation during oxidation of 304L at 873 K in the presence of 10% water vapor, Oxidation of Metals 52(1-2) (1999) 95-111.

[68] D.J. Young, B.A. Pint, Chromium Volatilization Rates from Cr2O3 Scales into Flowing Gases Containing Water Vapor, Oxidation of Metals 66(3-4) (2006) 137-153.

[69] J. Ehlers, D.J. Young, E.J. Smaardijk, A.K. Tyagi, H.J. Penkalla, L. Singheiser, W.J. Quadakkers, Enhanced oxidation of the 9%Cr steel P91 in water vapour containing environments, Corros Sci 48(11) (2006) 3428-3454.

[70] S. Henry, A. Galerie, L. Antoni, Abnormal oxidation of stabilized ferritic stainless steels in water vapor, High Temperature Corrosion and Protection of Materials 369-372 (2001) 353-360.

[71] J. Żurek, E. Wessel, L. Niewolak, F. Schmitz, T.U. Kern, L. Singheiser, W.J. Quadakkers, Anomalous temperature dependence of oxidation kinetics during steam oxidation of ferritic steels in the temperature range 550–650 °C, Corrosion Science 46(9) (2004) 2301-2317.

[72] L. Mikkelsen, S. Linderoth, High temperature oxidation of Fe–Cr alloy in O2–H2–H2O atmospheres; microstructure and kinetics, Materials Science and Engineering: A 361(1-2) (2003) 198-212.

[73] J. Zurek, M. Michalik, F. Schmitz, T.U. Kern, L. Singheiser, W.J. Quadakkers, The effect of water-vapor content and gas flow rate on the oxidation mechanism of a 10%Cr-Ferritic steel in Ar-H_2O mixtures, Oxidation of Metals 63(5-6) (2005) 401-422.

[74] D.Q. Zhang, G.M. Liu, G.Q. Zhao, Y.J. Guan, Cyclic oxidation behavior of Fe-9Cr-1Mo steel in water vapor atmosphere, Journal of Central South University of Technology 16(4) (2009) 535-540.

[75] Z.F. Li, G.M. Cao, Y.Q. He, Z.Y. Liu, G.D. Wang, Effect of chromium and water vapor of low carbon steel on oxidation behavior at 1050 ^{o}C, Steel Research International 87(11) (2016) 1469-1477.

[76] H. Hooshyar, High temperature corrosion of stainless steels in low oxygen activity environments: The effect of H_2 and H_2O, Department of Chemistry and Chemical Engineering, Chalmers University of Technology Goteborg, Sweden, 2016, p. 98.

[77] G.-A.T. Laverde Dionisio, Castro Francisco, Continuous and cyclic oxidation of T91 ferritic steel under steam, Corrosion Science 46(3) (2004) 613-631.

[78] I. Kvernes, M. Oliveira, P. Kofstad, High-temperature oxidation of Fe-13Cr-xAl alloys in air-H_2O vapor mixtures, Corrosion Science 17(3) (1977) 237-252.

[79] I.Y. Ishitsuka T., Ogawa H., Effect of silicon on the steam oxidation resistance of a 9%Cr heat resistant steel, Oxid Met 61(1/2) (2004) 125-142.

[80] A. Fry, S. Osgerby, M. Wright, Oxidation of alloys in steam environments - A review NPL Report MATC(A)90 2002.

[81] K.A. Terrani, Y. Yang, Y.J. Kim, R. Rebak, H.M. Meyer, T.J. Gerczak, Hydrothermal corrosion of SiC in LWR coolant environments in the absence of irradiation, Journal of Nuclear Materials 465 (2015) 488-498.

[82] D.J. Tallman, On the potential of MAX phases for nuclear applications, PhD thesis-Drexel University (2015).

[83] G.S. Was, Fundamentals of radiation materials science: Metals and alloys, Springer-Verlag New York (2017).

[84] W.-Y. Chen, Irradiation damage in neutron irradiated Fe-Cr model alloys, PhD thesis-University of Illinois, Urbana-Champaign (2014).

[85] D. Terentyev, G. Bonny, C. Domain, G. Monnet, L. Malerba, Mechanisms of radiation strengthening in Fe–Cr alloys as revealed by atomistic studies, Journal of Nuclear Materials 442(1-3) (2013) 470-485.

[86] L.L. Snead, T. Nozawa, Y. Katoh, T.-S. Byun, S. Kondo, D.A. Petti, Handbook of SiC properties for fuel performance modeling, Journal of Nuclear Materials 371(1-3) (2007) 329-377.

[87] J.S. Bryner, A study of neutron irradiation damage in iron by electron-transmission microscopy, Acta Metallurgica 14(3) (1966) 323-&.

[88] B.L. Eyre, A.F. Bartlett, An electron microscope study of neutron irradiation damage in alpha-iron, The Philosophical Magazine: A Journal of Theoretical Experimental and Applied Physics 12(116) (1965) 261-272.

[89] L.L. Horton, J. Bentley, K. Farrell, A Tem Study of Neutron-Irradiated Iron, Journal of Nuclear Materials 108(1-2) (1982) 222-233.

[90] M. Matijasevic, W. Van Renterghem, A. Almazouzi, Characterization of irradiated single crystals of Fe and Fe–15Cr, Acta Materialia 57(5) (2009) 1577-1585.

[91] Y. Katoh, H. H. Kishimoto, A. Kohyama, The influences of irradiation temperature and helium production on the dimensional stability of silicon carbide, Journal of Nuclear Materials 307(311) (2002) 1221-1226.

[92] I.A. Ibrahim, F.A. Mohamed, E.J. Lavernia, Particulate reinforced metal matrix composites — a review, Journal of Materials Science 26(5) (1991) 1137-1156.

[93] T.C. Chou, A. Joshi, High temperature interfacial reactions of SiC with metals, Journal of Vacuum Science & Technology A 9(3) (1991) 1525-1534.

[94] T.C. Chou, A. Joshi, Selectivity of silicon carbide/stainless steel solid-state reactions and discontinuous decomposition of silicon carbide, Journal of the American Ceramic Society 74(6) (1991) 1364-1372.

[95] W.M. Tang, Z.X. Zheng, H.F. Ding, Z.H. Jin, Control of the interface reaction between silicon carbide and iron, Materials Chemistry and Physics 80(1) (2003) 360-365.

[96] M.K. Mani, G. Viola, M.J. Reece, J.P. Hall, S.L. Evans, Influence of coated SiC particulates on the mechanical and magnetic behaviour of Fe–Co alloy composites, Journal of Materials Science 49(6) (2013) 2578-2587.

[97] J. Li, B.Y. Zong, Y.M. Wang, W.B. Zhuang, Experiment and modeling of mechanical properties on iron matrix composites reinforced by different types of ceramic particles, Materials Science and Engineering a-Structural Materials Properties Microstructure and Processing 527(29-30) (2010) 7545-7551.

[98] J. Pelleg, Reactions in the matrix and interface of the Fe-SiC metal matrix composite system, Materials Science and Engineering a-Structural Materials Properties Microstructure and Processing 269(1-2) (1999) 225-241.

[99] T.D. Shen, C.C. Koch, K.Y. Wang, M.X. Quan, J.T. Wang, Solid-state reaction in nanocrystalline Fe/SiC composites prepared by mechanical alloying, Journal of Materials Science 32(14) (1997) 3835-3839.

[100] D.F. Johnson, E.A. Carter, Bonding and adhesion at the SiC/Fe interface, Journal of Physical Chemistry A 113(16) (2009) 4367-4373.

[101] Z.H. Hu, K.J. Ning, K. Lu, Study of spark plasma sintered nanostructured ferritic steel alloy with silicon carbide addition, Materials Science and Engineering a-Structural Materials Properties Microstructure and Processing 670 (2016) 75-80.

[102] Z.H. Hu, K.J. Ning, K. Lu, Spark plasma sintered silicon carbide ceramics with nanostructured ferritic alloy as sintering aid, Materials Science and Engineering: A 682 (2017) 586-592.

[103] W.D. Callister, D.G. Rethwisch, Fundamental of materials science and engineering. An integrated approach 4th ed., John Wiley & Sons Inc., Hoboken, NJ, 2012.

[104] A. Hirata, T. Fujita, Y.R. Wen, J.H. Schneibel, C.T. Liu, M.W. Chen, Atomic structure of nanoclusters in oxide-dispersion-strengthened steels, Nature Materials 10(12) (2011) 922-926.

[105] K.J. Ning, H.F. Jun, K. Bawane, K. Lu, Spark plasma sintering of silicon carbide-nanostructured ferritic alloy composites with chromium carbide barrier layer, Materials Science and Engineering: A 700 (2017) 183-190.

[106] X.M. Bai, A.F. Voter, R.G. Hoagland, M. Nastasi, B.P. Uberuaga, Efficient annealing of radiation damage near grain boundaries via interstitial emission, Science 327(5973) (2010) 1631-1634.

[107] T.S. Byun, J.H. Yoon, S.H. Wee, D.T. Hoelzer, S.A. Maloy, Fracture behavior of 9Cr nanostructured ferritic alloy with improved fracture toughness, Journal of Nuclear Materials 449(1-3) (2014) 39-48.

[108] J. Pelleg, Reactions in the matrix and interface of the Fe–SiC metal matrix composite system, Materials Science and Engineering: A 269(1) (1999) 225-241.

[109] W.D. Callister, D.G. Rethwisch, Fundamental of materials science and engineering, an integrated approach, John Wiley & Sons Inc. 4th Ed., Hoboken, NJ (2012) 403-404.

[110] Z. Hu, K. Ning, K. Lu, Study of spark plasma sintered nanostructured ferritic steel alloy with silicon carbide addition, Materials Science and Engineering: A 670 (2016) 75-80.

[111] J.C. Slater, Atomic Radii in Crystals, The Journal of Chemical Physics 41(10) (1964) 3199-3204.

[112] M. Polcarová, S. Kadečková, J. Brądler, K. Godwod, J. Bąk-misiuk, Lattice parameters of Fe-Si alloy single crystals, physica status solidi (a) 106(1) (1988) 17-23.

[113] F.C. Collins, G.E. Kimball, Diffusion-controlled reaction rates, Journal of Colloid Science 4(4) (1949) 425-437.

[114] J. Cermak, L. Kral, Carbon diffusion in carbon-supersaturated ferrite and austenite, Journal of Alloys and Compounds 586 (2014) 129-135.

[115] F.J. Bradshaw, G. Hoyle, K. Speight, Diffusion of Silicon in Ferrite, Nature 171 (1953) 488.

[116] D.M. Liu, B.W. Lin, Thermal conduction in Cr_3C_2/SiC Composite, Journal of Materials Science 30(3) (1995) 758-762.

[117] Y.L. Al'shevskii, O.N. Baklanova, A.I. Zaitsev, V.V. Mal'tsev, I.G. Rodionova, A.N. Rybkin, N.G. Shaposhnikov, Thermodynamic analysis of equilibria in Fe-Cr-C alloys and evaluation of their dusting stability in aggressive carboniferous atmospheres, Inorganic Materials 41(2) (2005) 133-139.

[118] K.J. Ning, Q.L. Zhang, D.M. Zhang, J.T. Fan, D.L. Sun, X.F. Wang, Y. Hang, Crystal growth, characterization of NdTaO4: A new promising stoichiometric neodymium laser material, Journal of Crystal Growth 388 (2014) 83-86.

[119] T.R.G. Kutty, K. Ravi, C. Ganguly, Studies on hot hardness of Zr and its alloys for nuclear reactors, Journal of Nuclear Materials 265(1-2) (1999) 91-99.

[120] Z. Oksiuta, A. Ozieblo, K. Perkowski, M. Osuchowski, M. Lewandowska, Influence of HIP pressure on tensile properties of a 14Cr ODS ferritic steel, Fusion Engineering and Design 89(2) (2014) 137-141.

[121] M.E. Alam, S. Pal, K. Fields, S.A. Maloy, D.T. Hoelzer, G.R. Odette, Tensile deformation and fracture properties of a 14YWT nanostructured ferritic alloy, Materials Science and Engineering a-Structural Materials Properties Microstructure and Processing 675 (2016) 437-448.

[122] Z. Oksiuta, P. Olier, Y. de Carlan, N. Baluc, Development and characterisation of a new ODS ferritic steel for fusion reactor application, Journal of Nuclear Materials 393(1) (2009) 114-119.

[123] P. Fernandez, A.M. Lancha, J. Lapena, M. Serrano, M. Hernandez-Mayoral, Metallurgical properties of reduced activation martensitic steel Eurofer'97 in the as-received condition and after thermal ageing, Journal of Nuclear Materials 307 (2002) 495-499.

[124] Z. Oksiuta, M. Lewandowska, K.J. Kurzydlowski, Mechanical properties and thermal stability of nanostructured ODS RAF steels, Mechanics of Materials 67 (2013) 15-24.

[125] Z.H. Hu, K. Ning, K. Lu, Spark plasma sintered silicon carbide ceramics with nanostructured ferritic alloy as sintering aid, Materials Science and Engineering: A 682 (2017) 586-592.

[126] K. Ning, K. Lu, K. Bawane, Z. Hu, Spark plasma sintering of silicon carbide (SiC)-nanostructured ferritic alloy (NFA) composites with carbon barrier layer, Journal of Nuclear Materials 498 (2018) 50-59.

[127] K. Ning, H.-F. Ju, K. Bawane, K. Lu, Spark plasma sintering of silicon carbide-nanostructured ferritic alloy composites with chromium carbide barrier layer, Materials Science and Engineering: A 700 (2017) 183-190.

[128] K. Bawane, K. Ning, K. Lu, High temperature treatment of Cr_3C_2@SiC-NFA composites in water vapor environment, Corrosion Science 131 (2018) 365-375.

[129] K. Ning, K. Lu, Understanding ion irradiation resistance of a silicon diffused nanostructured ferritic alloy-chromium carbide–carbon composite, Composites Part B: Engineering 167 (2019) 746-753.

[130] C.P. Massey, D.T. Hoelzer, R.L. Seibert, P.D. Edmondson, A. Kini, B. Gault, K.A. Terrani, S.J. Zinkle, Microstructural evaluation of a Fe-12Cr nanostructured ferritic alloy designed for impurity sequestration, Journal of Nuclear Materials 522 (2019) 111-122.

[131] H. Kishimoto, M.J. Alinger, G.R. Odette, T. Yamamoto, TEM examination of microstructural evolution during processing of 14CrYWTi nanostructured ferritic alloys, Journal of Nuclear Materials 329-333 (2004) 369-371.

[132] X. Zhou, Y. Liu, L. Yu, Z. Ma, Q. Guo, Y. Huang, H. Li, Microstructure characteristic and mechanical property of transformable 9Cr-ODS steel fabricated by spark plasma sintering Materials and Design 132 (2017) 158-169.

[133] M.A. Auger, V. de Castro, T. Leguey, A. Muñoz, R. Pareja, Microstructure and mechanical behavior of ODS and non-ODS Fe–14Cr model alloys produced by spark plasma sintering, Journal of Nuclear Materials 436(1-3) (2013) 68-75.

[134] J.H. Yoon, Y. Lee, S.H. Kang, T.S. Byun, D.T. Hoelzer, Effects of partial phase transformation on characteristics of 9Cr nanostructured ferritic alloy, Current Nanoscience 10(1) (2014) 47-50.

[135] A. García-Junceda, M. Campos, N. García-Rodríguez, J.M. Torralba, On the role of alloy composition and sintering parameters in the bimodal grain size distribution and mechanical properties of ODS ferritic steels, Metallurgical and Materials Transactions A 47(11) (2016) 5325-5333.

[136] I. Hilger, F. Bergner, T. Weißgärber, D. Bouvard, Bimodal grain size distribution of nanostructured ferritic ODS Fe-Cr alloys, Journal of the American Ceramic Society 98(11) (2015) 3576-3581.

[137] H. Zhang, Y. Huang, H. Ning, C.A. Williams, A.J. London, K. Dawson, Z. Hong, M.J. Gorley, C.R.M. Grovenor, G.J. Tatlock, S.G. Roberts, M.J. Reece, H. Yan, P.S. Grant, Processing and microstructure characterisation of oxide dispersion strengthened Fe–14Cr–0.4Ti–0.25Y 2 O 3 ferritic steels fabricated by spark plasma sintering, Journal of Nuclear Materials 464 (2015) 61-68.

[138] X. Boulnat, M. Perez, D. Fabregue, T. Douillard, M.-H. Mathon, Y. de Carlan, Microstructure evolution in nano-reinforced ferritic steel processed by mechanical alloying and spark plasma sintering, Metallurgical and Materials Transactions A 45(3) (2013) 1485-1497.

[139] M. Hernández-Mayoral, M. Serrano, E. Oñorbe, A. García-Junceda, I. Hilger, B. Kloeden, T. Weissgaerber, A. Ulbricht, F. Bergner, B. Radiguet, A. Etienne, A. Shariq, C.D. Dewhurst, Microstructural and mechanical characterisation of ODS ferritic alloys produced by mechanical alloying and spark plasma sintering, Materials Science and Technology 30(13) (2014) 1669-1675.

[140] Z. Li, Z. Lu, R. Xie, C. Lu, C. Liu, Effect of spark plasma sintering temperature on microstructure and mechanical properties of 14Cr-ODS ferritic steels, Materials Science and Engineering: A 660 (2016) 52-60.

[141] R. Xie, Z. Lu, C. Lu, Z. Li, X. Ding, C. Liu, Microstructures and mechanical properties of 9Cr oxide dispersion strengthened steel produced by spark plasma sintering, Fusion Engineering and Design 115 (2017) 67-73.

[142] B. Srinivasarao, K. Oh-ishi, T. Ohkubo, K. Hono, Bimodally grained high-strength Fe fabricated by mechanical alloying and spark plasma sintering, Acta Materialia 57(11) (2009) 3277-3286.

[143] Z.A. Munir, U. Anselmi-Tamburini, M. Ohyanagi, The effect of electric field and pressure on the synthesis and consolidation of materials: A review of the spark plasma sintering method, Journal of Materials Science 41(3) (2006) 763-777.

[144] J.H. Jang, C.-H. Lee, Y.-U. Heo, D.-W. Suh, Stability of (Ti,M)C (M=Nb, V, Mo and W) carbide in steels using first-principles calculations, Acta Materialia 60(1) (2012) 208-217.

[145] A. Bjarbo, M. Hattestrand, Complex carbide growth, dissolution, and coarsening in a modified 12 pct chromium steel-an experimental and theoretical study, Metallurgical and Materials Transactions A 32A (2001) 19-27.

[146] S. Ohtsuka, Y. Yano, T. Tanno, T. Kaito, K. Tanaka, Microstructure characterization of oxide dispersion strengthened steels containing metallic chromium inclusions after high-temperature thermal aging, Materials Transactions 54(10) (2013) 2018-2026.

[147] A. Schneider, G. Inden, Simulation of the kinetics of precipitation reactions in ferritic steels, Acta Materialia 53(2) (2005) 519-531.

[148] S. Sovizi, M.E. Seraji, The densification behavior of metals and alloys during spark plasma sintering: A mini-review, Science of Sintering 51 (2019) 135-152.

[149] Y. Yamamoto, B.A. Pint, K.A. Terrani, K.G. Field, Y. Yang, L.L. Snead, Development and property evaluation of nuclear grade wrought FeCrAl fuel cladding for light water reactors, Journal of Nuclear Materials 467 (2015) 703-716.

[150] K.A. Terrani, B.A. Pint, C.M. Parish, C.M. Silva, L.L. Snead, Y. Katoh, Silicon carbide oxidation in steam up to 2 MPa, Journal of the American Ceramic Society 97(8) (2014) 2331-2352.

[151] K.J. Ning, K. Lu, Water vapor thermal treatment of silicon carbide-nanostructured ferritic steel alloy (SiC-NFA) composite materials Applied Surface Science 452 (2018) 248-258.

[152] K.J. Ning, K. Lu, K. Bawane, Z.H. Hu, Spark plasma sintering of silicon carbide (SiC)-nanostructured ferritic alloy (NFA) composites with carbon barrier layer, Journal of Nuclear Materials 498 (2018) 50-59.

[153] F. Abe, H. Kutsumi, H. Haruyama, H. Okubo, Improvement of oxidation resistance of 9 mass% chromium steel for advanced-ultra supercritical power plant boilers by pre-oxidation treatment, Corrosion Science 114 (2017) 1-9.

[154] Y.N. Chang, F.I. Wei, High-temperature oxidation of low-alloy steels, Journal of Materials Science 24(1) (1989) 14-22.

[155] M. Takeda, T. Onishi, S. Nakakubo, S. Fujimoto, Physical properties of iron-oxide scales on Si-containing steels at high temperature, Materials Transactions 50(9) (2009) 2242-2246.

[156] N. Birks, G.H. Meier, F.S. Pettit, Introduction to high temperature oxidation of metals, Cambridge University Press 2nd edition (2006) 104-110.

[157] D.J. Young, High temperature oxidation and corrosion of metals, Elsevier Corrosion Series 1 (2008) 260-267.

[158] K. Ning, K. Lu, Water vapor thermal treatment effects on spark plasma sintered nanostructured ferritic alloy-silicon carbide systems, Journal of the American Ceramic Society 101(6) (2018) 2208-2215.

[159] B.A.P. R. Peraldi, Effect of Cr and Ni contents on the oxidation behavior of ferritic and austenitic model alloys in air with water vapor, Oxidation of Metals 61(5/6) (2004) 463-483.

[160] K.J. Ning, H.F. Ju, K. Bawane, K. Lu, Spark plasma sintering of silicon carbide-nanostructured ferritic alloy composites with chromium carbide barrier layer, Materials Science and Engineering: A 700 (2017) 183-190.

[161] N.K. Othman, N. Othman, J. Zhang, D.J. Young, Effects of water vapour on isothermal oxidation of chromia-forming alloys in Ar/O_2 and Ar/H_2 atmospheres, Corrosion Science 51(12) (2009) 3039-3049.

[162] Y. Chen, K. Sridharan, S. Ukai, T.R. Allen, Oxidation of 9Cr oxide dispersion strengthened steel exposed in supercritical water, Journal of Nuclear Materials 371(1-3) (2007) 118-128.

[163] J.-E.S. H. Asteman, M. Norell, L.-G. Johansson, Influence of water vapor and flow rate on the high-temperature oxidation of 304L; Effect of chromium oxide hydroxide evaporation, Oxidation of Metals 54(1/2) (2000) 11-26.

[164] J. Bischoff, A.T. Motta, Oxidation behavior of ferritic-martensitic and ODS steels in supercritical water, Journal of Nuclear Materials 424(1-3) (2012) 261-276.

[165] E.J. Song, D.W. Suh, H.K.D.H. Bhadeshia, Oxidation of silicon containing steel, Ironmaking & Steelmaking 39(8) (2013) 599-604.

[166] K.Y. Shigeji Taniguchi, Daisuke Megumi, Toshio Shibata, Characteristics of scale/substrate interface area of Si-containing low-carbon steels at high temperatures, Materials science and Engineering A 308 (2001) 250-257.

[167] H. Asteman, J.E. Svensson, L.G. Johansson, Oxidation of 310 steel in H_2O/O_2 mixtures at 600 ^oC: The effect of water-vapour-enhanced chromium evaporation, Corrosion Science 44(11) (2002) 2635-2649.

[168] D.H.H. Graham H.C., Oxidation/vaporization kinetics of Cr_2O_3, Journal of the American Ceramic Society 54(2) (1971) 89-93.

[169] Z. Yao, K.H. Zhang, Z. Zhou, M.R. Daymond, S. Jublot-Leclerc, O. Kaitasov, In situ heavy ion irradiation in ferritic/martensitic ODS steels at 500°C, Materials Science and Technology 34(1) (2017) 42-46.

[170] X. Liu, Y. Miao, M. Li, M.A. Kirk, S.A. Maloy, J.F. Stubbins, Ion-irradiation-induced microstructural modifications in ferritic/martensitic steel T91, Journal of Nuclear Materials 490 (2017) 305-316.

[171] M. Li, M.A. Kirk, P.M. Baldo, D. Xu, B.D. Wirth, Study of defect evolution by TEM within situion irradiation and coordinated modeling, Philosophical Magazine 92(16) (2012) 2048-2078.

[172] E. Getto, K. Sun, A.M. Monterrosa, Z. Jiao, M.J. Hackett, G.S. Was, Void swelling and microstructure evolution at very high damage level in self-ion irradiated ferritic-martensitic steels, Journal of Nuclear Materials 480 (2016) 159-176.

[173] M.A. Kirk, M. Li, D. Xu, B.D. Wirth, Predicting neutron damage using TEM with in situ ion irradiation and computer modeling, Journal of Nuclear Materials 498 (2018) 199-212.

[174] J.F. Ziegler, M.D. Ziegler, J.P. Biersack, SRIM – The stopping and range of ions in matter (2010), Nuclear Instruments and Methods in Physics Research Section B: Beam Interactions with Materials and Atoms 268(11-12) (2010) 1818-1823.

[175] S.L. Dudarev, K. Arakawa, X. Yi, Z. Yao, M.L. Jenkins, M.R. Gilbert, P.M. Derlet, Spatial ordering of nano-dislocation loops in ion-irradiated materials, Journal of Nuclear Materials 455(1-3) (2014) 16-20.

[176] M. Hernández-Mayoral, Z. Yao, M.L. Jenkins, M.A. Kirk, Heavy-ion irradiations of Fe and Fe–Cr model alloys Part 2: Damage evolution in thin-foils at higher doses, Philosophical Magazine 88(21) (2008) 2881-2897.

[177] W.-Y. Chen, X. Liu, Y. Chen, J.-W. Yeh, K.-K. Tseng, K. Natesan, Irradiation effects in high entropy alloys and 316H stainless steel at 300^{o}C, Journal of Nuclear Materials 510 (2018) 421-430.

[178] M. Wen, N.M. Ghoniem, B.N. Singh, Dislocation decoration and raft formation in irradiated materials, Philosophical Magazine 85(22) (2005) 2561-2580.

[179] Y. Xiaoou, J. Michael L., K. Marquis A., Z. Zhongfu, R. Steven G., In-situ TEM studies of 150 keV W^{+} ion irradiated W and W-alloys: Damage production and microstructural evolution, Acta Materialia 112 (2016) 105-120.

[180] Y. Zhang, D. Schwen, X.-M. Bai, Effects of solute-SIA binding energy on defect production behaviors in Fe-based alloys, Journal of Nuclear Materials 509 (2018) 124-133.

[181] G.S. Was, Fundamentals of radiation in materials science: Metals and alloys, Springer, Berlin (2007).

[182] J.C. Haley, S.A. Briggs, P.D. Edmondson, K. Sridharan, S.G. Roberts, S. Lozano-Perez, K.G. Field, Dislocation loop evolution during in-situ ion irradiation of model FeCrAl alloys, Acta Materialia 136 (2017) 390-401.

[183] D. Xu, B.D. Wirth, M. Li, M.A. Kirk, Combining in situ transmission electron microscopy irradiation experiments with cluster dynamics modeling to study nanoscale defect agglomeration in structural metals, Acta Materialia 60(10) (2012) 4286-4302.

[184] X. Yi, M.L. Jenkins, K. Hattar, P.D. Edmondson, S.G. Roberts, Characterisation of radiation damage in W and W-based alloys from 2 MeV self-ion near-bulk implantations, Acta Materialia 92 (2015) 163-177.

[185] Z. Yao, M. Hernandez-Mayoral, M.L. Jenkins, M.A. Kirk, Heavy-ion irradiations of Fe and Fe-Cr model alloys Part 1: Damage evolution in thin-foils at lower doses, Philosophical Magazine 88(21) (2008) 2851-2880.

[186] K. Ning, X. Bai, K. Lu, Study of self-ion irradiated nanostructured ferritic alloy (NFA) and silicon carbide-nanostructured ferritic alloy (SiC-NFA) cladding materials, Nuclear Instruments and Methods in Physics Research Section B: Beam Interactions with Materials and Atoms 427 (2018) 44-52.

[187] M. Bachhav, G.R. Odette, E.A. Marquis, alpha ' precipitation in neutron-irradiated Fe-Cr alloys, Scripta Materialia 74 (2014) 48-51.

[188] X.M. Bai, H. Ke, Y. Zhang, B.W. Spencer, Modeling copper precipitation hardening and embrittlement in a dilute Fe-0.3at.%Cu alloy under neutron irradiation, Journal of Nuclear Materials 495 (2017) 442-454.

[189] O. El-Atwani, J.A. Hinks, G. Greaves, J.P. Allain, S.A. Maloy, Grain size threshold for enhanced irradiation resistance in nanocrystalline and ultrafine tungsten, Materials Research Letters 5(5) (2017) 343-349.

[190] L. Pagano, A.T. Motta, R.C. Birtcher, The formation of bubbles in Zr alloys under Kr ion irradiation, Journal of Nuclear Materials 244(3) (1997) 295-304.

[191] Z. Yao, M.L. Jenkins, M. Hernández-Mayoral, M.A. Kirk, The temperature dependence of heavy-ion damage in iron: A microstructural transition at elevated temperatures, Philosophical Magazine 90(35-36) (2010) 4623-4634.

[192] K.G. Field, X. Hu, K.C. Littrell, Y. Yamamoto, L.L. Snead, Radiation tolerance of neutron-irradiated model Fe–Cr–Al alloys, Journal of Nuclear Materials 465 (2015) 746-755.

[193] R. Schaublin, B. Decamps, A. Prokhodtseva, J.F. Loffler, On the origin of primary 1/2 a(0) <111> and a(0) <100> loops in irradiated Fe(Cr) alloys, Acta Materialia 133 (2017) 427-439.

[194] L. Malerba, A. Caro, J. Wallenius, Multiscale modelling of radiation damage and phase transformations: The challenge of FeCr alloys, Journal of Nuclear Materials 382(2-3) (2008) 112-125.

[195] A. Prokhodtseva, B. Decamps, A. Ramar, R. Schaublin, Impact of He and Cr on defect accumulation in ion-irradiated ultrahigh-purity Fe(Cr) alloys, Acta Materialia 61(18) (2013) 6958-6971.

[196] M. Hernandez-Mayoral, C. Heintze, E. Onorbe, Transmission electron microscopy investigation of the microstructure of Fe-Cr alloys induced by neutron and ion irradiation at 300 degrees C, Journal of Nuclear Materials 474 (2016) 88-98.

[197] D. Terentyev, L. Malerba, Diffusivity of solute atoms, matrix atoms and interstitial atoms in Fe-Cr alloys: a molecular dynamics study, Journal of Nuclear Materials 329 (2004) 1161-1165.

[198] S. Xu, Z. Yao, M.L. Jenkins, TEM characterisation of heavy-ion irradiation damage in FeCr alloys, Journal of Nuclear Materials 386-88 (2009) 161-164.

[199] S. Plimpton, Fast parallel algorithms for short-range molecular-dynamics, Journal of Computational Physics 117(1) (1995) 1-19.

[200] L. Malerba, M.C. Marinica, N. Anento, C. Bjorkas, H. Nguyen, C. Domain, F. Djurabekova, P. Olsson, K. Nordlund, A. Serra, D. Terentyev, F. Willaime, C.S. Becquart, Comparison of empirical interatomic potentials for iron applied to radiation damage studies, Journal of Nuclear Materials 406(1) (2010) 19-38.

[201] S.L. Dudarev, K. Arakawa, X. Yi, Z. Yao, M.L. Jenkins, M.R. Gilbert, P.M. Derlet, Spatial ordering of nano-dislocation loops in ion-irradiated materials, (2014).

[202] C. Wei-Ying, L. Xiang, C. Yiren, Y. Jien-Wei, T. Ko-Kai, N. Krishnamurti, Irradiation effects in high entropy alloys and 316H stainless steel at 300^{o}C, Journal of Nuclear Materials 510 (2018) 421-430.

[203] K. Bawane, K. Lu, Microstructure evolution for nanostructured ferritic alloy with and without Cr_3C_2 coated silicon carbide at high temperatures, Journal of Materials Science and Technology (Accepted) (2020).

[204] X. Yi, M.L. Jenkins, M.A. Kirk, Z. Zhou, S.G. Roberts, In-situ TEM studies of 150 keV W + ion irradiated W and W-alloys: Damage production and microstructural evolution, Acta Materialia 112 (2016) 105-120.

[205] Y. Matsukawa, S.J. Zinkle, One-dimensional fast migration of vacancy clusters in metals, Science 318(5852) (2007) 959-962.

[206] I.M. Robertson, M.A. Kirk, W.E. King, Formation of dislocation loops in iron by self-ion irradiations at 40K, Scripta Metallurgica 18 (1984) 317-320.

[207] W.-Y. Chen, Irradiation damage in neutron irradiated Fe-Cr model alloys, PhD thesis-University of Illinois at Urbana-Champaign (2014).

[208] K. Arakawa, M. Hatanaka, E. Kuramoto, K. Ono, H. Mori, Changes in the Burgers vector of perfect dislocation loops without contact with the external dislocations, Physical Review Letters 96(12) (2006) 125506.

[209] S.L. Dudarev, R. Bullough, P.M. Derlet, Effect of the alpha-gamma phase transition on the stability of dislocation loops in bcc iron, Phys Rev Lett 100(13) (2008) 135503.

[210] H. Xu, R.E. Stoller, Y.N. Osetsky, D. Terentyev, Solving the puzzle of <100> interstitial loop formation in bcc Iron, Phys Rev Lett 110(26) (2013) 265503.

[211] J. Marian, B.D. Wirth, J.M. Perlado, Mechanism of formation and growth of <100> interstitial loops in ferritic materials, Physical Review Letters 88(25) (2002).

[212] Y.F. Zhang, X.M. Bai, M.R. Tonks, S.B. Biner, Formation of prismatic loops from C15 Laves phase interstitial clusters in body-centered cubic iron, Scripta Materialia 98 (2015) 5-8.

[213] Q. Peng, F.J. Meng, Y.Z. Yang, C.Y. Lu, H.Q. Deng, L.M. Wang, S. De, F. Gao, Shockwave generates < 100 > dislocation loops in bcc iron, Nature Communications 9 (2018).

[214] B. Yao, D.J. Edwards, R.J. Kurtz, TEM characterization of dislocation loops in irradiated bcc Fe-based steels, Journal of Nuclear Materials 434(1-3) (2013) 402-410.

[215] C.A. English, M.L. Jenkins, Molecular ion irradiations of molybdenum, Philosophical Magazine 90(7-8) (2010) 821-843.

[216] C. Zheng, S. Maloy, D. Kaoumi, Effect of dose on irradiation-induced loop density and Burgers vector in ion-irradiated ferritic/martensitic steel HT9, Philosophical Magazine 98(26) (2018) 2440-2456.

[217] J. Chen, N. Gao, P. Jung, T. Sauvage, A new mechanism of loop formation and transformation in bcc iron without dislocation reaction, Journal of Nuclear Materials 441(1-3) (2013) 216-221.

[218] J. Marian, B.D. Wirth, R. Schäublin, J.M. Perlado, T. Díaz de la Rubia, 〈100〉-Loop characterization in α-Fe: comparison between experiments and modeling, Journal of Nuclear Materials 307-311 (2002) 871-875.

[219] A. Stukowski, V.V. Bulatov, A. Arsenlis, Automated identification and indexing of dislocations in crystal interfaces, Modelling and Simulation in Materials Science and Engineering 20(8) (2012).

[220] B. Esmailzadeh, A. Kumar, F.A. Garner, The influence of silicon on void nucleation in irradiated alloys, Journal of Nuclear Materials 133-134 (1985) 590-593.

[221] D. Chen, K. Murakami, K. Dohi, K. Nishida, N. Soneda, Z. Li, L. Liu, N. Sekimura, Depth distribution of Frank loop defects formed in ion-irradiated stainless steel and its dependence on Si addition, Nuclear Instruments and Methods in Physics Research Section B: Beam Interactions with Materials and Atoms 365 (2015) 503-508.

[222] D. Chen, K. Murakami, K. Dohi, K. Nishida, N. Soneda, Z. Li, L. Liu, N. Sekimura, Radiation defects formed in ion-irradiated 316L stainless steel model alloys with different Si additions, Materials Transactions 56(9) (2015) 1549-1552.

List of Scientific Communications

Journal articles:

1) **Kaustubh Bawane**, Kathy Lu, Xian-Ming Bai, Wei-Ying Chen, Meimei Li, *In-situ TEM study of microstructural evolution in NFA and Cr_3C_2@SiC-NFA composite during ion irradiation*, Materialia, 7 (100412), 2019
2) **Kaustubh Bawane**, Kaijie Ning, Kathy Lu, *High temperature treatment of Cr3C2@ SiC-NFA composites in water vapor environment*, Corrosion Science, 131, 2018, pp. 365-375.
3) **Kaustubh Bawane**, Kathy Lu, Quan Li, Rajendra Bordia, *High temperature oxidation behaviors of SiON coated AISI 441 in $Ar+O_2$, $Ar+H_2O$, and $Ar+CO_2$ atmospheres*, Corrosion Science (Accepted).
4) **Kaustubh Bawane**, Donald Erb, Kathy Lu, *Carbon content and pyrolysis atmosphere effects on phase development in SiOC systems*, Journal of European Ceramic Society, 39 (9), 2019, pp. 2846-2854.
5) **Kaustubh Bawane**, Kathy Lu, *Microstructure evolution for nanostructured ferritic alloy with and without Cr_3C_2 coated silicon carbide at high temperatures*, Journal of Materials Science and Technology (Accepted).
6) **Kaustubh Bawane**, Kathy Lu, Xian-Ming Bai, Jing Hu, Meimei Li, Edward Ryan, *Microstructural evolution of silicon carbide-carbon coated nanostructured ferritic alloy system during in-situ Kr^{++} ion irradiation at 300^{o}C and 450^{o}C* (Under review – Composites Part B).
7) **Kaustubh Bawane**, Kaijie Ning, Kathy Lu, *High temperature oxidation behavior of silicon carbide-carbon coated nanostructured ferritic alloy composites in air+water vapor environment*, Corrosion Science, 139, 2018, pp. 206-214.
8) Kathy Lu, **Kaustubh Bawane**, Donald Erb, Ni Yang, *Comparison of traditional and flash pyrolysis of different carbon content silicon oxycarbides*, Journal of European Ceramic Society, 39 (10), 2019, pp. 3035-3041.

9) Kaijie Ning, Kathy Lu, **Kaustubh Bawane**, Zhihao Hu, *Spark plasma sintering of silicon carbide (SiC)-nanostructured ferritic alloy (NFA) composites with carbon barrier layer*, Journal of Nuclear Materials 498, 2018, pp. 50-59.
10) Kaijie Ning, Hong-fei Ju, **Kaustubh Bawane**, Kathy Lu, *Spark plasma sintering of silicon carbide-nanostructured ferritic alloy composites with chromium carbide barrier layer*, Materials Science and Engineering A:700, 2018, pp. 183-190.

Conferences:

1) Kathy Lu, **Kaustubh Bawane**, Kaijie Ning, *Nanostructured ferritic alloy (NFA) – SiC composites for nuclear applications,* TMS–Annual Meeting and Exhibition 2019, San Antonio, TX, USA, March, 2019 (Invited talk by Prof. Kathy Lu).
2) **Kaustubh Bawane**, Kathy Lu, Xian-Ming Bai, Wei-Ying Chen, Jing Hu, Meimei Li, *In-situ Kr ion irradiation of SiC-NFA composites for nuclear applications*, International Conference on Advanced Ceramics and Composites (ICACC-2019), Daytona Beach, Florida, USA, January, 2019 (Oral presentation).
3) **Kaustubh Bawane**, Kaijie Ning, Kathy Lu, *Breakaway oxidation behavior of Cr_3C_2@SiC-NFA composites,* Materials Science and Technology (MST-2017), Pittsburgh, USA, October 2017 (Oral presentation).
4) Kathy Lu, **Kaustubh Bawane**, *Microstructure evolution for nanostructured ferritic alloy with and without Cr_3C_2 coated silicon carbide at high temperatures,* Materials Science and Technology (MST-2018), Columbus, October 2018 (Presenter: Kathy Lu).
5) Kathy Lu, **Kaustubh Bawane**, *Microstructural evolution of SiC-C@NFA during in-situ irradiation at 300^{o}C and 450^{o}C,* Materials Science and Technology (MST-2019), Portland, October 2018 (Presenter: Kathy Lu).
6) **Kaustubh Bawane**, Lauren M. Garrison, John Echols, *Microstructural evolution of AISI 347 stainless steels for applications in novel fission-fusion hybrid medical isotope generation facilities*, The Oak Ridge Postdoctoral Association (ORPA) Research Symposium, ORNL, Oak Ridge, TN, USA, August 2019 (Poster presentation)